Simulation of industrial granular flow and its effects on the sinter plant operation.

Bridgeman, Lee

Bridgeman, Lee (2010) *Simulation of industrial granular flow and its effects on the sinter plant operation..* thesis, Swansea University.
http://cronfa.swan.ac.uk/Record/cronfa42559

Swansea University
Prifysgol Abertawe

corus

Simulation of Industrial Granular Flow and its Effects On the Sinter Plant Operation

Lee Bridgeman

Submitted to the University of Wales in fulfilment of
the requirements for the Degree of
Doctor of Engineering

Academic Supervisor: Professor S.G.R Brown

Materials Research Centre
School of Engineering
Swansea University
Swansea, SA2 8PP

Submitted 2010

EPSRC

Engineering & Physical
Sciences Research Council

DECLARATION

This work has not previously been accepted in substance for any degree and is not being concurrently submitted for candidature for any degree.

Signed .. .. (candidate)

Date ...23/12/10...

STATEMENT 1

This thesis is the result of my own investigations, except where otherwise stated.

Other sources are acknowledged by footnotes giving explicit references. A bibliography is appended.

Signed .. .. (candidate)

Date ...23/12/10...

STATEMENT 2

I hereby give consent for my thesis, if accepted, to be available for photocopying and for inter-library loan, and for the title and summary to be made available to outside organisations.

Signed .... (candidate)

Date ...23/12/10...

ABSTRACT

The supply and bulk handling of raw materials is of fundamental importance in many facets of the manufacturing community, the scope of which ranges from mining to pharmaceuticals and critical aspects of steel production. This thesis is based on the development of a 3D spherical "Discrete Element Method" (DEM) modelling code to assist in the computer simulation of granular flow through a steelworks industrial environment. Presented in this work is a thorough evaluation and review of DEM techniques, highlighting the variety of discrete elements, contact special searches and contact interaction forces. Also addressed here is a validation of the current DEM Fortran code, using the effects of frictional forces on particulate flowing behaviour, in terms of "Angles of Repose".

The introduction of these forces followed a "Linear Spring Dash-pot" (LSD) method and "Soft Sphere" approach where contact penetration is small in comparison with element diameter. Both surface and boundary deformations were neglected during contact interaction and boundary conditions were implemented using a "Solid Works" 3D design package.

The results of the validation and frictional inputs in this modelling case were used as a calibration to set initial parameters of the discrete elements when simulating different material size distributions, and inter-particulate bonding scenarios due to the influence of moisture. To introduce attractive force due to moisture a "Toriodal Approximation" was used in conjunction with the "Soft Sphere" method that showed novelty in contact interactions between elements of differing radii.

The model was ultimately applied to practical material flow situations that exhibit system deterioration and inter-particulate degradation leading to atmospheric dust suspension. To express quantitive information kinetic energy transfer was recorded at boundary impact scenarios to isolate regions of severe momentum change and high intensity flow rates.

The resulting energy trend examinations relating to extensive theoretical application of the current model correlated strongly with actual equipment damage and material flow patterns. The acquisition of data in this format delivers a 3D insight into the internal dynamics of material flow through a domain and could be essential in developmental optimisation.

FOR YOU “EMMA”

ACKNOWLEDGEMENTS

The completion of this work marks the end of a second educational journey that has taken me to my absolute limits and back. All in all, it has been an incredible challenge that has given me many highs and just as many lows but has never forced me into giving up. This I can safely attribute to a number of factors, the strong academic and industrial support, the camaraderie between all of the student groups that I have been part of and the encouragement of close family and friends.

On the academic side I would like thank Prof Wiltshire for giving me the chance to enter the Engineering Doctorate scheme and to Prof Dave Worsley for just being Dave, it’s been a pleasure. Special thanks has to go to my academic supervisor Prof S.G.R Brown “Steve” for his unwavering support, his computational expertise and his passion for the project work that kept me pushing forward. At this point it would also be appropriate to thank EPSRC for their funding over the course of the project.

For the industrial element, I have had a great deal of support from Corus and they have been instrumental in project development by driving its content into practical applications where it seems to belong. For this I would like to thank to my industrial supervisor Dr Stuart Southern for his depth of knowledge and to Tony Jones for his effortless intellect and his friendship.

As for the camaraderie, I have been blessed with many good colleagues long the way who have shared my anguish in learning and my bizarre sense of humour, but none more than the EngD team who I have had the privilege to work with and who have unquestionably enhanced my life. They are Sarah Barnes, Dean Flynn, Ian Mabbett, Dave Mumford, David Warren, Bruce Philip, Samantha Cashmore, Michael James, Chris Weirman and Piia. However, special attention has to be given to the close bond that I have always had with the original crazy gang Dai, Mumf, Cash, Bruce and Deano, thanks guys, you are priceless.

As for the friends who have always been around, there are simply too many to mention but special consideration has to be given to the Parry's for "Par-Bridge", for their prayers and the numerous ignited candles on my behalf, you are very special.

In the case of my family where do I start, they have all been touched by this journey and those in close contact have been affected the most. Therefore my appreciation and thanks for being part of things goes out to my mother in law Marion and her late husband Bill who we lost along the way, my ever present parents Diane and Daron for all their love and support, my late Grand Mother Emma whom I know is very proud of me and to my wonderful children Luke, Niomi and Corey who will never know how much I love them and on occasions, how sorry I've been for not being mentally around.

And last but not least, I owe everything to a very special lady who has stood by me every step of the way and that's my wife "Beverley". Without her support it would not have been possible to get here, but more importantly, it would not have been worth getting here without her.

Bev, thanks for always being there and I love you from the bottom of my heart

Contents..Page N°

Index of Figures

Index of Graphs

Index of Tables

1. AIMS OF THE PROJECT

The key objectives of this project were:

1. To make an investigation into the bulk material handling systems used to supply mineral particulates as raw material into the Corus (Tata Group) iron making infrastructure.
2. To develop a Discrete Element Method (DEM) modelling technique into a usable non-invasive diagnostic tool to assess on-plant efficiency in terms of industrial granular flow.
3. To validate the DEM program against scientific publications and to relate simulated energy transfer predictions to observable systematic deterioration of on-plant equipment.

1.1 Introduction

The development and growth of any industrial concern is usually reflected in an increased productivity while maintaining both product quality and cost. Steel production is no exception to the rule and reduction in overheads to generate larger profit margins are a constant challenge. A major contributing factor in realising productions targets without large capital expenditure has been the minimisation of plant "down-time" and effective maintenance to offset plant failure.

This project was implemented to reinforce the drive for systems optimisation by introducing computer simulation techniques into the engineering framework. The main features of the project investigation focussed on the physical phenomenon behind the movement and distribution of mineral particulates as a raw material for the production of steel. The interests in this case were on the areas prior to mechanical or chemical processing, where the majority of the raw materials were in their basic mineral form. In essence, the research criteria took an objective view on the existing material transport operations with the intention of highlighting areas that required improvement.

1.2 Project Overview

The initial concepts behind this project were drawn from "Continuous Improvement" (CI) meetings that were keen to address basic on-plant issues. The business units involved in these forums are collectively described as the "Burdening Department". This area comprises an import facility and stock yards, a sintering plant, a coal granulation plant and a coke making department. These all feed into a pair of blast furnaces that are used as reactors to release iron compounds from mineral iron oxide. In 2006 when the primary research commenced on this project, the raw material requirements needed to supply the demand for steel was in the region of 15 million tonnes per annum. Approximately 87% of this tonnage came in through the deep water harbour facility and was distributed via a conveyor belt and transfer station network.

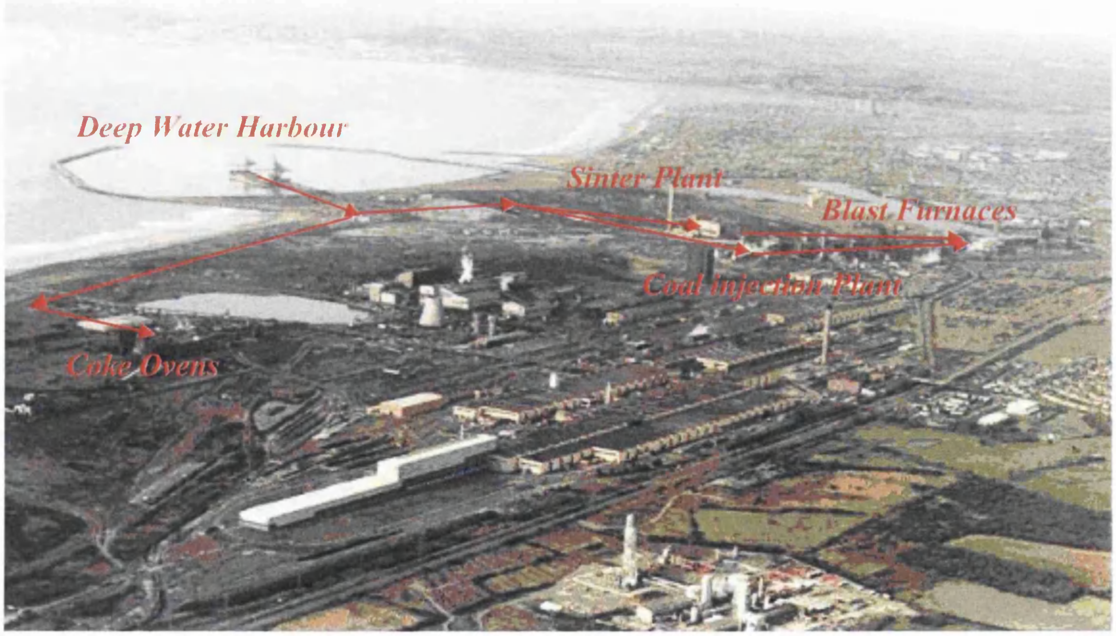

Figure 1: Aerial view of Port Talbot integrated steel works showing raw material conveyor belt distribution links

Figure 2: Conveyor belt transfer stations used to redirect raw material flow

If one considers the movement of material along a conveyor belt it can be viewed as low complexity, and an overall efficient method of bulk handling. However, to accommodate plant logistics the conveyor belt systems are required to change direction, and this is achieved by a transfer station infrastructure at key locations on the conveyor route.

These positions are critical for interlinking systems but are prone to internal structural damage and raw material spillage. The underlying reasons for this type of deterioration and material escape are mainly found in the volume of material handled, the composition and condition (moisture content), and the extremes in particulate size distribution.

The following figures indicate the variations in material size distribution but must be viewed as a basic guideline:

- Iron Ore (rubble): 5mm ~ 70mm
- Iron Ore (Fines): 0.1mm ~ 3mm
- Iron Ore (concentrates): $O(\mu m)$
- Coal: $O(\mu m) \sim 80mm$
- Coke: 50mm ~ 100mm

To produce 3.6 million tonnes of hot metal in 2006 the blast furnaces received ~15.5 million tonnes of burden (raw material and fluxes) and the composition is displayed in *Table 1*.

No4 Blast Furnace		No5 Blast Furnace	Total	Raw Mat
Hot Metal (HM) 1574KT Per Year		Hot Metal (HM) 2046KT Per Year	Hot Metal (HM) 3620KT Per Year	
Material	kg/THM	kg/THM	kg/THM	kT
Pellets	448	441	889	3218.18
Sinter/fines	1046	1042	2088	7558.56
Ore	103	116.5	219.5	794.59
Others	9.4	8.9	18.3	66.246
Coal	133	131	264	955.68
Coke	388	390	778	2816.36
Oil	0.01	0.55	0.56	2.0272
			Total Raw Material Input	15411.6432

Table 1: Raw material supplied to No's 4&5 blast furnaces in 2006

From the data displayed in Table 1 the major contributor in the raw material makeup is that of "Sinter/Fines". This product has good iron content and is cost effective but its size distribution renders it useless for direct furnace application. As a result, this product is processed in the sintering plant by a particulate fusion method.

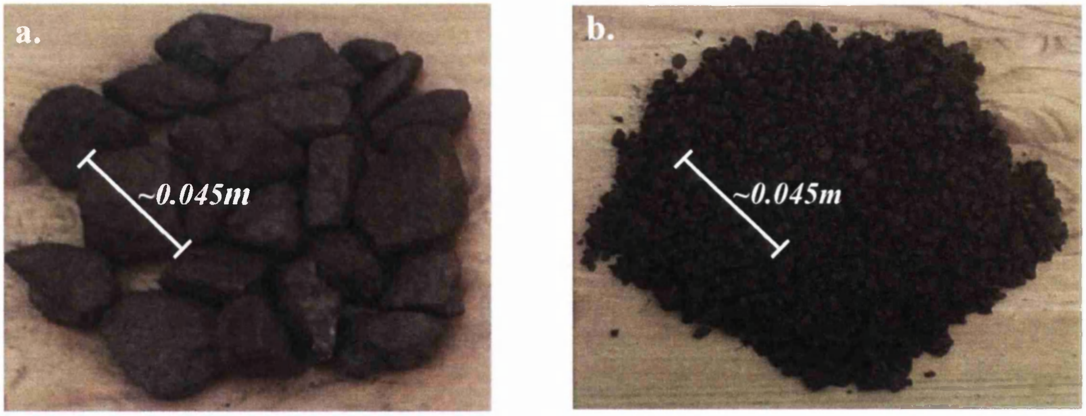

Figure 3: Examples of raw material iron ore in the form of (a)"Sishen" Lump and (b) fines

1.3 The Sinter Plant

In terms of the continuous improvement ethos set down by the Sinter Plant management team, one of the key issues highlighted over a rigorous systems investigation was internal material distribution. In particular, how the movement of material influenced the end product yield.

Sinter in Port Talbot makes up approximately 65-70% of the blast furnace burden and is highly beneficial in recycling process waste and controlling burden chemistry. However, the high production demands and throughput of fines ore has an effect on the plant and its equipment.

The main features of the project were created within this environment and are discussed at length in this section after a brief introduction to the sintering process.

1.4: Sinter Plant Background

The general function of a sinter plant is to process fines ore into agglomerate that becomes a usable blast furnace addition in the iron making process. Sintering is a heating procedure that stays below the constituent's melting point but encourages boundary fusion to take place. The mechanism employed at Port Talbot is a Dwight Lloyd sinter machine and comprises one sintering line known as a "Strand".

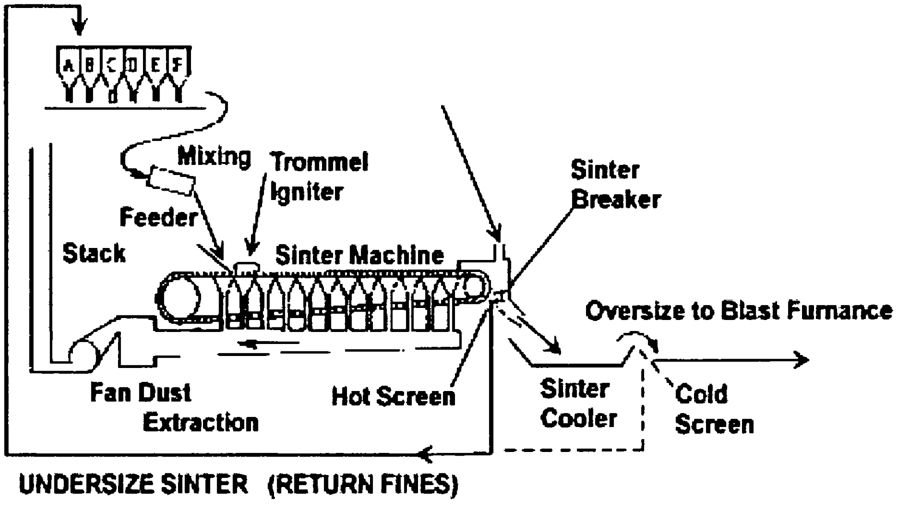

Figure 4: A schematic representation of a Dwight Lloyd travelling sinter strand

As shown in *Figure 4* the system consists of a raw material or sinter mix feeder on to a travelling sinter strand. The strand is a series of 135 mutually linked pallets (extending to 84m in length) that are circulated in a chain by a drive motor arrangement. Each section has vertical sides to contain the raw material, this is commonly described as the bed and each pallet has a porous grate base.

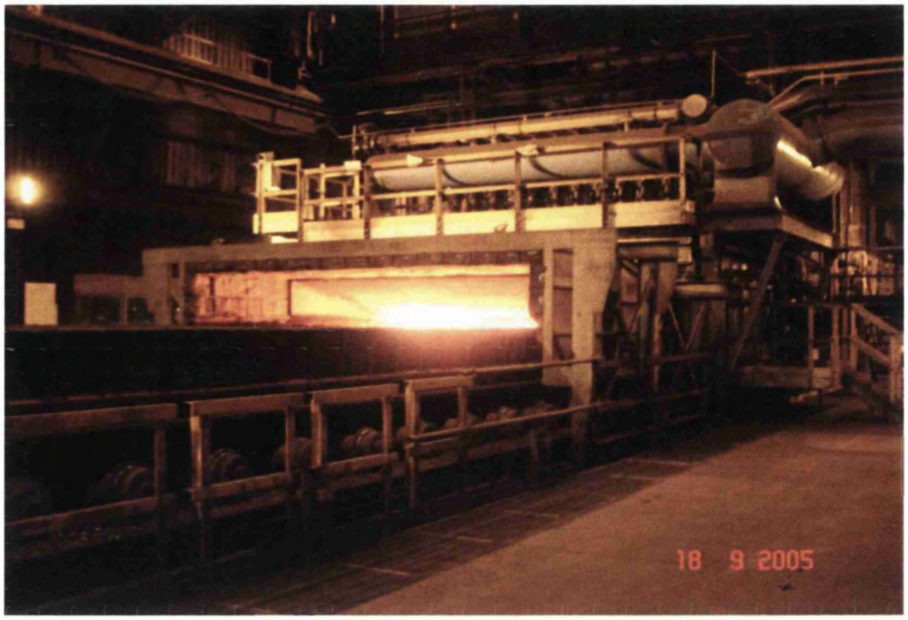

Figure 5: The ignition hood used to ignite the fuel blended within the raw mix

As the material is continuously fed onto the strand it travels under a gas fired ignition hood as shown in Figure 5. The fuel in the form of coke breeze (fine coke particles) is incorporated into the sinter mix and is ignited starting an agglomeration process. Two large suction fans draw air through the top of the mix which drives a narrow firing zone down through the bed. The fuel in the mix generates temperatures of 1200^{0}C to 1500^{0}C and this has the effect of preheating the air travelling through the bed, driving off moisture before the flame front.

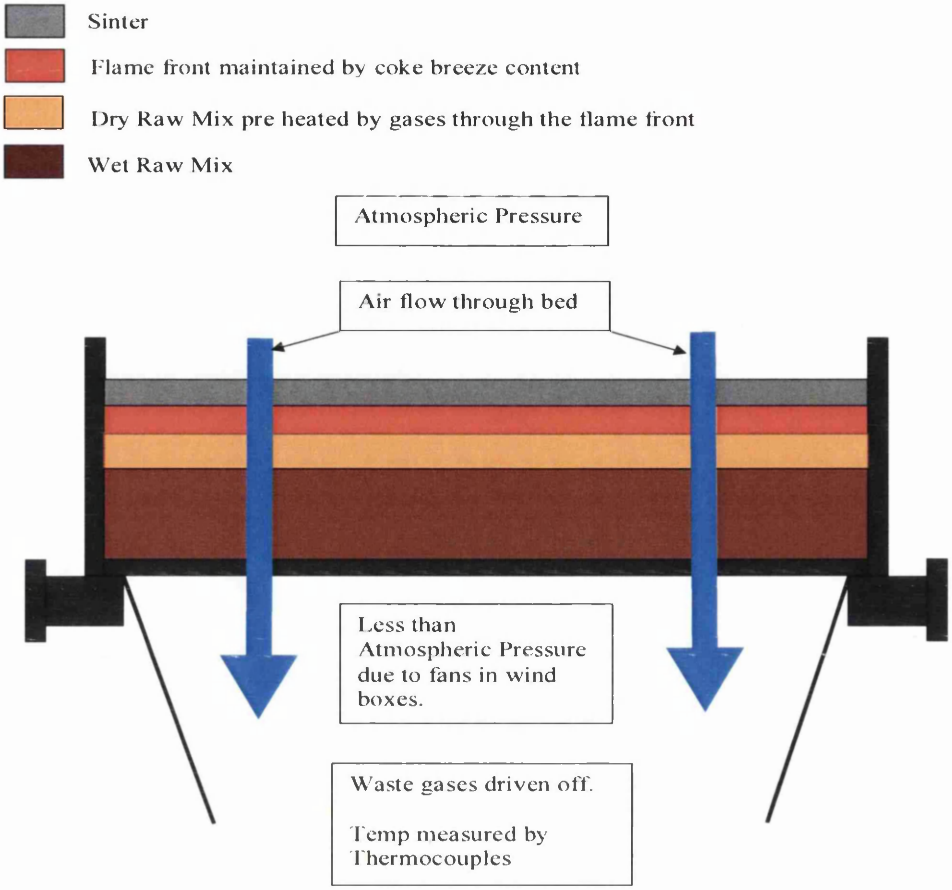

Figure 6: A cross-sectional image of a sinter pallet with raw mix

The key in this process is to ensure that the wedge shaped flame front reaches the pallet grating vertically before the end of the strand is reached. This is achieved by predicting the position of the flame front using temperature levels of the exhaust gases in the wind main. From this information, the strand speed can be varied accordingly by an operator in the control room.

Finally as the pallets return under the strand the fresh sinter is deposited onto a crash plate and is broken in a “sinter breaker”.

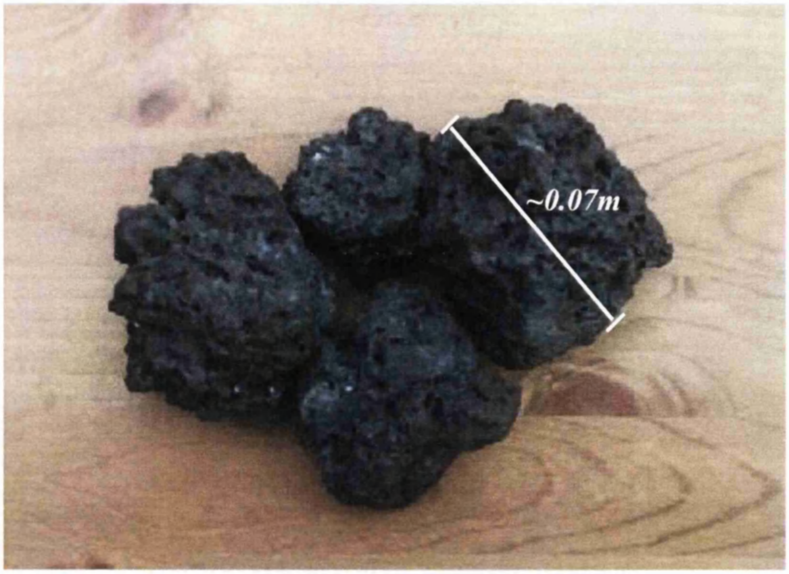

Figure 7: An example of sinter in comparison to the original fines ore shown in Fig 3b

If the flame front position is incorrectly estimated, the final sinter product at the end of the strand could either be over sintered and difficult to break or under sintered and returned through the process as raw mix blend.

In Port Talbot the apparatus used to distribute sinter mix onto the strand is a "Roll Feeder and Segregation Plate" type assembly and although simple in design it has been proven to be highly effective in its application. However, due to the raw material volume and abrasive nature, it is subjected to continuous surface wear issues that generate material hang ups resulting in destructive avalanche. The catalyst for this whole project was created here.

1.5: The "Roll Feeder and Segregation Plate" project investigation

The "Roll feeder and segregation plate" method of applying the raw mix onto the sinter strand has a number of world wide variations but in Port Talbot the system is relatively straight forward. However the importance of this piece of apparatus is without question and the search for improvement is an ongoing challenge.

This part of the plant has gradually evolved to accommodate the increase in sinter demand and to satisfy operational efficiency.

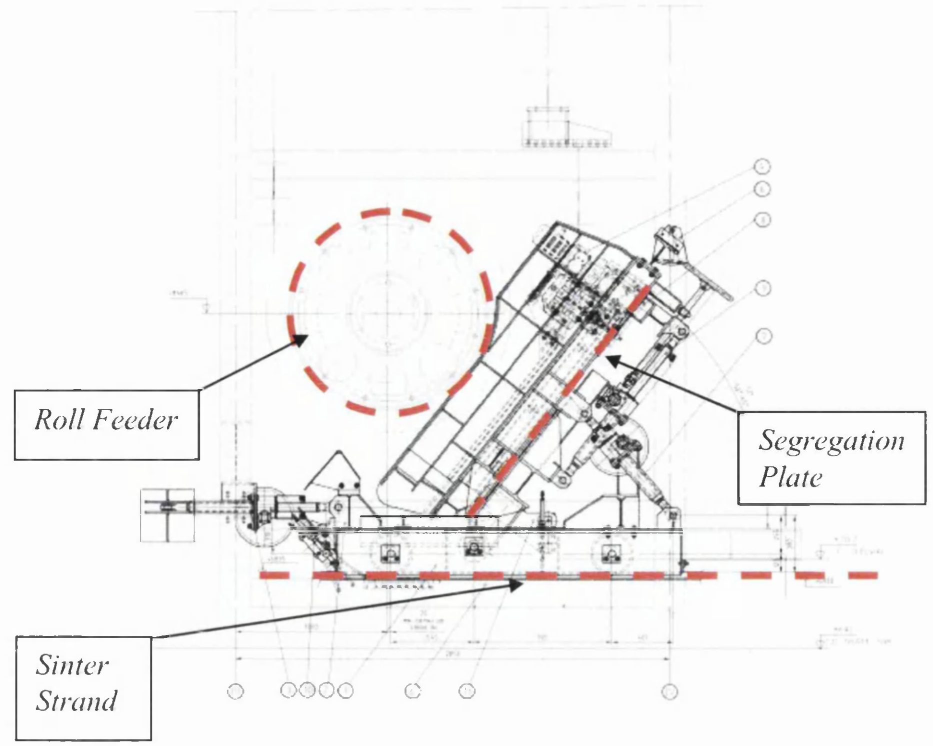

Figure 8: Shows a design drawing of the roll feeder and segregation plate

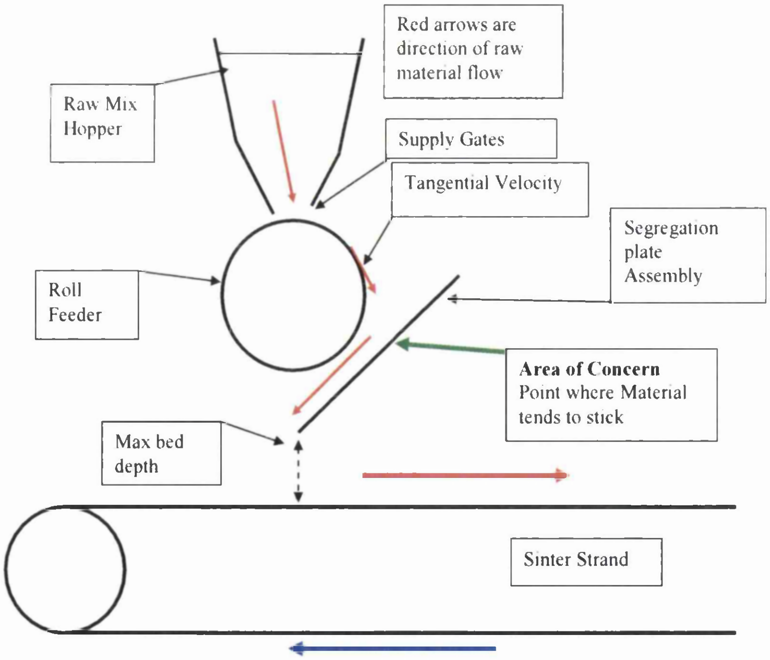

Figure 9: Shows a 2D schematic of the roll feeder and segregation plate (not to scale)

As shown in *Figure 9* the raw material flows from the material hopper through the supply gates onto the roller. The material is accelerated to the tangential velocity of the roller and is imparted onto the segregation plate. The material then flows down the segregation plate and falls off the end onto the strand.

The specific point of concern is highlighted by the green arrow and this is where sticking problems have a tendency to occur. This point is clearly the impact zone where the raw material first comes in contact with the segregation plate. The abrasive nature of the raw material eventually wears into the hard ceramic tiling causing a ridge which hinders the movement of the material down the inclined plate. This type of obstruction, although small, creates an area where the material compacts and therefore tends to stick.

The negative result of the material holding in this fashion is a build up of new material on old and an eventual avalanche that collapses onto the sinter strand. This undesirable action destroys the particulate micro structure by material compression and deforms the bed profile, in turn, affecting the ignition flame front. Both of these changes in the sinter bed have a direct bearing on the sinter productivity and sinter yield.

1.6: The "Roll Feeder and Segregation Plate" investigation results

The type of raw material running through this apparatus is highly abrasive and has a density of (3000-4000kgm^{-3}). Volumes of 100,000 tonnes / week are expected to travel though this system on a regular basis and this subjects the equipment to a punishing routine. Studying the dynamics of the material discharge from the hopper to the strand it was evident that the material transition impacted in one specific region causing a high intensity energy transfer.

18 9 2005

Figure 10: Shows the roll feeder with supply gates releasing raw mix

The roll feeder is 4m long cylinder with a diameter of 1.2m. It is driven by an electric motor and has a maximum of ten revolutions per minute. The basic function of the roller is to smoothly transfer an even distribution of raw material from the hopper onto the segregation plate.

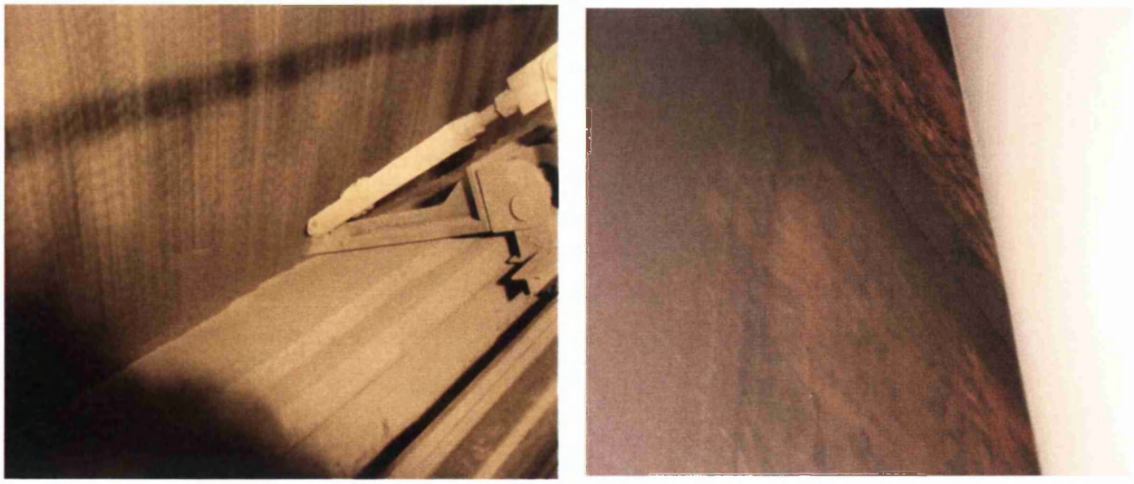

Figure 11: Shows the segregation plate with raw material flow and corresponding damage

The segregation plate is also 4m long and the surface is covered with a hard ceramic Alumina tile. The plate at Port Talbot is inclined at 48^0 to the horizontal. The basic functions of the segregation plate are:

1. To produce an even distribution of raw material on to the sinter strand
2. To improve/maintain inter-particulate bonding by:
    - Material segregation by encouraging large particle in the raw material to roll and gather at the bottom of the sinter bed with the smaller particle moving to the top. This action also promotes a green-balling effect although the time span on the plate is relatively short.
    - Prevention of material compression by reducing the impact velocity from the roll feeder to strand.

After detailed observation and data analysis, the conclusion was drawn that the basic shape of the inclined plate needed consideration. Reduction of energy transfer at the material impact point could be achieved by increasing the plate angle but this increased flow velocity over the surface and affected segregation, potentially increasing strand compression. Conversely reducing the plate angle increased the impact velocity of the material resulting in higher energy transfer. However, greater segregation was predicted with reduction in flow velocity along the plate which encouraged low material compression. Ideally, a combination of both results was a desirable outcome and the suggested solution to achieve this was the movement from a flat surface to one that had curvature.

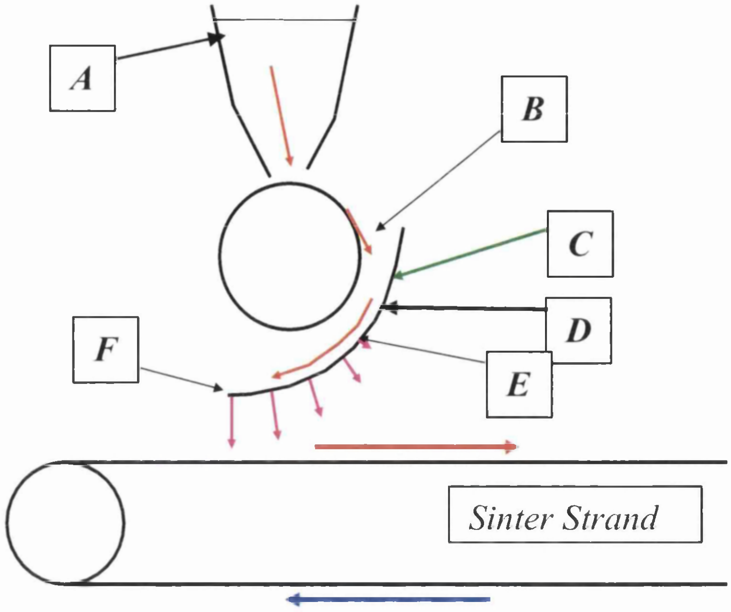

Figure 12: Schematic diagram depicting a curved segregation plate.

In *Figure 12* the key points have been highlighted and they are as follows:

A. The raw mix hopper is where the raw mix is stored prior to feeding on to the roll feeder. To promote a good feed and prevent large particles falling though the gates, the hopper is usually maintained at 70% full.

B. Due to the shape of the curve the segregation plate is brought in closer to the roller reducing the impact velocity.

C. The area of concern now has a higher gradient giving low energy into the plate. This reduces wear and material build up.

D. The shortest distance between any two points is a straight line. The curved segregation plate naturally increases the travelling distance between the impact point and the end of the plate while maintaining the same displacement. This produces a larger surface area for material segregation to occur.

E. The acceleration vector into the plate grows, forcing the material onto the surface. Particles with a greater mass should experience the effect of this force more than particle with a smaller mass, therefore drawing them through the material as it flows. This should result in the desired type of segregation with larger particle gathering at the bottom of the strand and the smaller at the top.

F. The end of the segregation plate now has a low angle high reaction force. This slows down the material as it flows by forcing it into the plate and transferring the kinetic energy. The result of this is a decrease in velocity onto the strand reducing impact compression.

For the Sinter Plant to consider such a radical approach and a movement away from what was already a relatively successful arrangement there would have to be sizeable proof that a curved segregation plate would be effective. The challenge here was to show that issues concerning wear and material sticking could be eradicated from the impact zone while maintaining/improving segregation along the plate. To be successful in achieving these goals would undoubtedly result in a considerable improvement.

As a result "Discrete Element Method" computer simulation was introduced to initiate an investigation due to its suitability in modelling industrial granular flow.

The project originally started with a 2D Fortran program that was subsequently converted into to 3D version for extra dimensional data analysis and visual superiority. To facilitate program development, the technique was then applied to a number of industrial environments were bulk material movements are essential and the progression of the simulation results are discussed at length throughout this thesis.

2. DISCRETE ELEMENT METHOD SIMULATION

The desire to replicate the natural world or to investigate critical conditions in terms of engineering has been greatly assisted by the rapid advancement in computer technology. Keeping in touch with this relentless development has been the growth and sophistication of the mainstream computer simulation techniques. An example of this symbiotic relationship has been the successful introduction of "Finite Element Method" (FEM) as a diagnostic tool in solving complex elasticity and structural analysis problems, particularly in the fields of civil and aeronautical engineering.

However, the fundamental algorithms used in FEM are based on a continuum method and this was found to have limitations in describing phenomenon that related to conditions expressing a discontinuum nature. Examples of these types of situations are regions that exhibit general fracture propagation and fragmentation in structural deterioration. To overcome this, work originally proposed by Goodman in 1968[1] was subsequently developed in 1971 by Cundall into the foundations for modelling discontinuum media[2]. Essentially the original algorithm was developed around the interaction of jointed ridged rocks and their behaviour when introduced to external parameters. This technique was termed as "*Distinct Element Method*" and the evolutionary processes eventually incorporated fully deformable blocks into the algorithm giving birth to the "*Discrete Element Method*" terminology.

2.1 Introduction and Background

In 1979 work by Cundall and Strack[3] described the mechanical behaviour of assemblies of discs and spheres. The method was based on the use of a numerical scheme in which the interactions of the particles were monitored contact by contact and the motion of the particles modelled particle by particle.

These simulation techniques are called "Granular Dynamics" (GD)[4] as opposed to "Molecular Dynamics" (MD)[5] in fluids. The subtle differences between GD and MD are the involvement of gravitational and drag forces as well as frictional forces that dissipate energy.

The (GD) modelling technique can be classified into two specific categories:

1. The soft sphere approach[6][7]
2. The hard sphere approach[8]

2.1.1: The Soft Sphere Approach to DEM

The "Soft-Sphere" models are capable of handling multiple particle contacts and resolving the resultant equilibrium condition. This is important for handling simulations of dense and quasi static systems and is therefore ideally suited for simulating dense granular flows with large range deformations.

The particle-particle, particle-boundary interactions can be seen as a dynamic process that is driven by the states of equilibrium that are resolved between the internal forces of two contacting systems. Consequently, the simulated motion of discrete elements under these conditions derives from a propagation of disturbances throughout an assembly. The mechanical behaviour of the system is described by the movement of each particle and the force and moment acting at each contact.

The relationship between the force acting on each particle and the resulting motion is determined by "Newton's Laws of Motion".

2.1.2: The Hard Sphere Approach to DEM

The hard sphere (quasi rigid) model is an event driven method, where interaction forces are considered to be impulsive, and the particle collisions are assumed to be binary and instantaneous. The collisions are the only means of exchanging momentum. The spheres are assumed to move undisturbed until a collision or an event occurs. The post collision velocities of the spheres are based on impact/momentum transfer. Energy dissipation is introduced with the coefficient of restitution.

For the hard sphere model computation time (CPU load) is less of a problem than is the memory usage. Motion calculations of very dense granular material remain a challenge that limits the application of this modelling for engineering problems[8]. However some recent literature suggests that the hard sphere approach could be made more memory efficient by averaging the results of multiple binary collisions occurring within one time step[9].

For this project the simulation technique employed uses the "Soft Sphere" method as a collision reaction process to study the dynamics of industrial granular flow. Particle generation is also dealt with to invoke continuity to demonstrate flow, and boundary walls are mathematically applied to generate flow domains in static or moving form.

2.2: Applications of "Discrete Element Method"

To date the influence of "Discrete Element Method" (DEM) has migrated into many facets of scientific and industrial application. The most predominant are in terms of:

- **Geomechanics**
    - ➢ Jointed rocks[2][10]
    - ➢ Falling rocks[11]
    - ➢ Sand Simulations[12]
- **Impact Analysis**
    - ➢ Reinforced concrete slabs[13]
    - ➢ Composites[14]
    - ➢ Splash Functions (Material ejection processes)[15]
    - ➢ Rotational Mill Operation (Mixing Drums and Grinding)[16][17]
- **Granular Material**
    - ➢ Pharmaceutical and food industry[18][19]
    - ➢ Granular Segregation and sieves [20] [21][22]
    - ➢ Material Hopper Discharge[21][23][24][25][26][27][28][29]
    - ➢ Bulk material handling[30]
    - ➢ Particulate flow (chutes and Conveyors)[31][32][33]
- **Combinations with Particle Flow Codes (PFC), Computer Fluid Dynamics CFD and Finite Element (FE)**
    - ➢ Ship Design (Green water effect PFC)[34]
    - ➢ Cyclone Gas cleaning Processes[35]
    - ➢ Chute Design (CFD)[36]
    - ➢ Plate Foundation Deformable bodies[37]

The foundation code used at the start of this project was a 2D National Algorithm Group (NAG) Fortran 95 particle impact DEM process. The original code was written and modified by Graham Mustoe (*Graham Mustoe, Colorado School Of Mines, USA*) in 2003 and incorporated a:

- 2D finite difference code for a system of impacting particle with a linear contact spring model
- Search radius neighbouring scheme
- A global damping force and work/energy calculation
- Contact damping calculations

2.2.1: The Fundamental Sections of a DEM Code

In terms of an effective industrial application the above program was subsequently tailored into a 3D version and the developmental process was ongoing throughout the duration of the project. There are many similarities regarding the construction of a 2D and 3D code but key areas are markedly different. However, almost every DEM code has four fundamental sections to it.

1. **The Discrete Element:** Geometric Shape
2. **Contact Detection:** Examines the region for particle interaction and determine if contact has been made.
3. **Constitutive Forces:** Calculate the forces acting on each particle during inter-particle contact and particle boundary contact.
4. **Application of Newton's 2nd Law:** Summation of the resultant forces associated to the discrete element to determine motion.

The methods involved in the 3D conversion considered in this project are highlighted in this section along with alternative methods in literature.

2.3 DEM Constituents and Corresponding Review of Techniques

In this sub-section a review is conducted of the fundamental building blocks of a DEM simulation code. The structure of the review follows the four main features of a DEM program code as shown in *2.2.1* and discusses the variation in each topic.

2.3.1: Introduction

Clearly, when attempting to apply computer simulation to subjects such as granular material one encompasses a large, diverse and complex set of parameters that in many cases are incalculable. However, by applying strong physical assumptions and robust equations to determine the DEM motion and interaction, close proximity to real microscopic and macroscopic situations are very achievable[38]. The simulated motion of particulates has to incorporate, and consider, particle-particle interaction and particle-boundary interaction. These are the building blocks of a DEM algorithm and are discussed in great detail throughout this section.

2.3.2: The Discrete Element

The shape of the discrete elements can have a significant bearing on the simulation requirements. The types of element fall into two main categories, Rigid Bodies and Deformable Finite Element which are essentially meshed polygons.

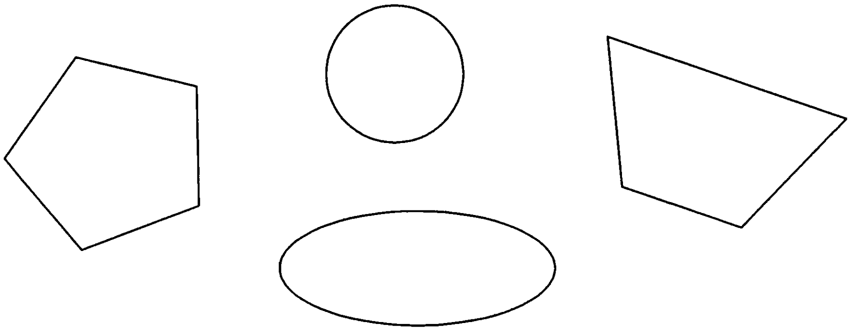

Figure 13: 2D Simplistic rigid discrete elements

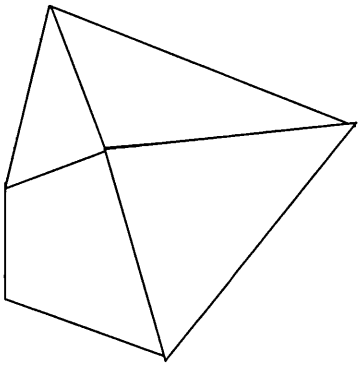

Figure 14: 2D deformable discrete elements showing finite element mesh

The elements shown in *Figures 13 & 14* are predominantly used for 2D simulation but their properties are insufficient when applied to simulating real physical conditions. One of the main drawbacks of using 2D analysis is data loss pertaining to the third dimension. As a result of this limiting factor, a great deal of emphasis has been focused on the development of 3D simulations using spherical elements and 3D meshed polygons.

2.3.3: The Spherical Discrete Element

Disk/spherical elements in DEM simulation have been the most commonly used element for modelling granular flow systems. The simple geometries in these shapes have been mathematically exploited in making particulate motion calculations.

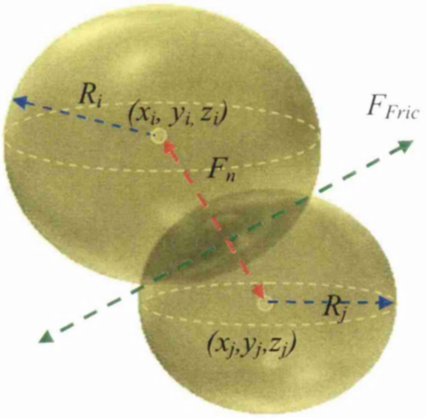

Figure 15: Spherical Discrete Elements in contact interaction

Spherical elements generated using the general equation of a sphere:

$$(x_{ij} - x_{ij0})^2 + (y_{ij} - y_{ij0})^2 + (z_{ij} - z_{ij0})^2 = r_{ij}^2 \tag{2.1}$$

The key components in the spherical element are the centre point and the magnitude of the radius, and these can be easily applied to the equations of rigid body dynamics with computational efficiency.

However, growth in this department has produced many new generations of element. Progress has been driven by the desire to create discrete elements that function in a more representative manner when applied to natural phenomena, such as density distribution and packing. The types of shapes generated to form solutions are ellipsoid[31][39], superquadric[40] tetrahedral[41] and others not considered here.

2.3.4: The Ellipsoid Discrete Element

Although there have been many DEM codes utilising disks and spheres to study granular regimes, questions have been directed at the effectiveness of the models when dealing with non-spherical material. Particle shapes have a significant effect on the mechanical behaviour of particulates and generate greater resistance to movement than spheres. In general disks and spheres tend to roll and rotate easily. A popular choice of shape in recent times to address this problem has been formed around elliptical equations as shown in *Figure 16*.

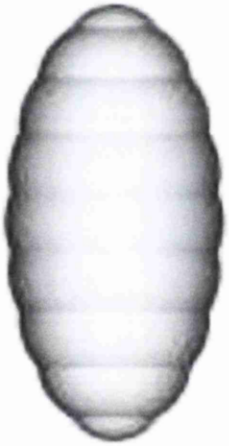

Figure 16: An example of an ellipsoid shape

This configuration has the advantage of having unique and continuous outward normal and no singularities along its surface. However, although this type of element has huge benefits in some applied DEM simulations 3D ellipsoids have only recently been adopted due to their difficult contact detection procedure. Significant work in improving the simulation performance has been carried out in the field of Soya bean flow and elliptical shape representation has been formed by the combination of spheres. For this case tangential force displacement models presented in previous work[42][31][43] have brought reliability in DEM simulation results

The basic function used to produce an ellipsoid shape:

$$\frac{x^2}{a^2}+\frac{y^2}{b^2}+\frac{z^2}{c^2}=1 \tag{2.2}$$

2.3.5: Superquadric elements

Superquadrics are 3D shapes derived from quadric surface functions and are generated by raising the exponent value of the variable terms in a quadric equation to values other than *2*. A quadric equation of the form:

$$Ax^2+By^2+Cz^2+Dxy+Exz+Fyz+Gx+Hy+Iz+J=0 \tag{2.3}$$

Considering the families of superquadric elements the most popular are the super ellipsoids

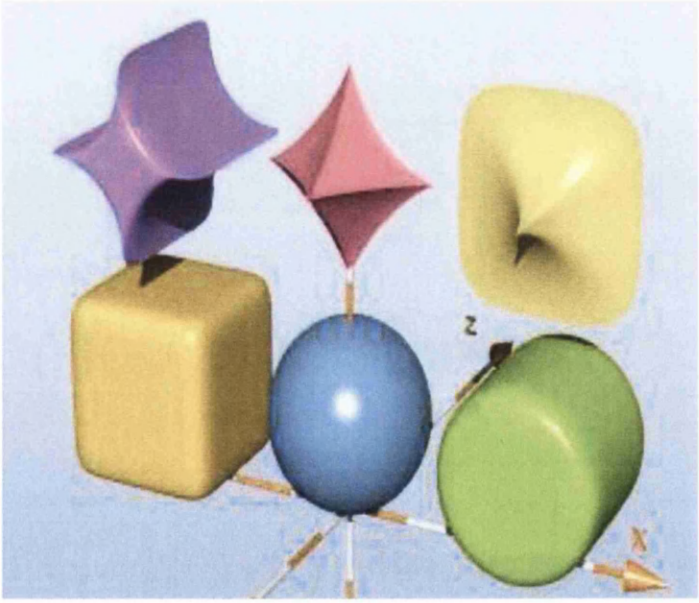

Figure 17: An assembly of Superquadric ellipsoid elements

The basic expression for a super ellipsoid can be shown as:

$$f(x,y,z)=\left[\left(\frac{x}{a_1}\right)^{\frac{2}{e}}+\left(\frac{y}{a_2}\right)^{\frac{2}{e}}\right]^{\frac{e}{n}}+\left(\frac{z}{a_3}\right)^{\frac{2}{n}} \tag{2.4}$$

Where:

(a_1,a_2,a_3) are the dimensions of the superquadric semi-major axes extents and are real numbers and determine the shape[44].

e and n are the roundness/squareness parameters of the function in two perpendicular directions respectively.

When an object is formed using (2.4) one can determine surface normal, surface curvature and relevant moments. The function $f(x,y,z)$ provides a measure of the distance of the point x,y,z from the surface of the superquadric. This property provides an extremely useful check, sometimes called an inside-outside check on whether a point lies inside or outside the surface. This check provides information as to whether an element is in contact with another element in a contact detection algorithm.

2.3.6: Tetrahedral elements

Tetrahedral polygons and polyhedrons[45] represent a very sophisticated discrete element but have highly complex geometries and are particularly suited to developments in rock, soil and concrete mechanics.

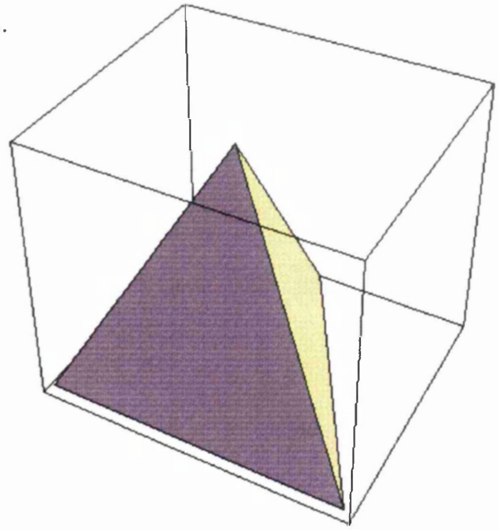

Figure 18: An example of a 3D tetrahedral element

Application of these shapes can be problematic due to contact detection, force and torque calculation were edge-edge, edge-corner, corner-corner contacts are apparent. This is compounded when extending from 2D to 3D and particle bonding is required; this can be complicated and computationally expensive. Similarly the same types of limitations are apparent when applying these shapes to the simulation of flow dynamics when considering particulate motion. However, previous works have presented a number of algorithms for DEM modelling of polyhedral particles for dealing with the complex nature of the motion calculation[46].

2.3.7: The spherical cluster Discrete Element

Alternatives to the complex structures of the ellipsoids and tetrahedra can be found by using clusters of spheres[47][48][49] formed into representative shapes.

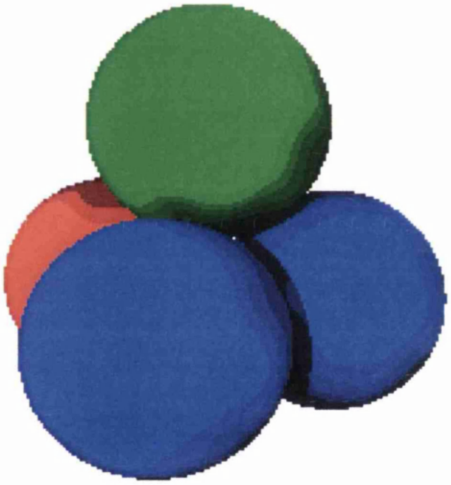

Figure 19: Example of a discrete element produced from a cluster of four spheres

The main advantages in using spherical clusters as an alternative solution to spherical elements are the resistance to rolling that is present and the maintenance of a simplistic contact prediction. In comparisons with the more exotic ellipsoid, superquadric and tetrahedral configurations the cluster compares well and the calculation times to simulate motion are reasonable. Except that, large numbers of individual elements are required in these processes and when mathematically joined together surface friction becomes difficult to evaluate. It has also been recorded that methods of multi-sphere generation can have limitations when used to replicate spherical bodies and will therefore face difficulty when applied to other arbitrary shapes[50]. However, previous work introducing cubic[51] elements have shown good representation of hopper flow issues, particularly in terms of discharge velocity. Three-dimensional particle shape descriptors for computer simulation of non-spherical particulate assemblies can also generate cubic clusters, using eight spherical elements in the construction and although computer expensive could draw closer to simulation reality[52].

For the aims of this project the decision was made to use the geometric benefits of spherical discrete elements in the required simulations. As stated, the simulation objective was to study the dynamic nature of compact particulate flow through an industrial environment and to assess the effects of energy transferred from the material to the system. As published[53] the effect of particle shape on flowing behaviour is very small providing there is high flow density. With the correct parameters introduced a spherical element can be used for the simulation of non-spherical particle flow. As a result of this the sphere-sphere and sphere boundary interaction are the primary concern and variations along this theme are critically evaluated.

2.4: Contact Spatial Search

Contact detection in terms of a DEM simulation is a mathematical process used to determine the probability of an impact/interaction between individual discrete elements within a region. The fundamental process is known as a 'Geometric Intersection Search' and in multi-body analysis the procedure becomes a significant computational task. The simplest form of contact search that one can implement over a region would be a search that checked for contact with every other individual element within the system as shown in *Figure 20*[54].

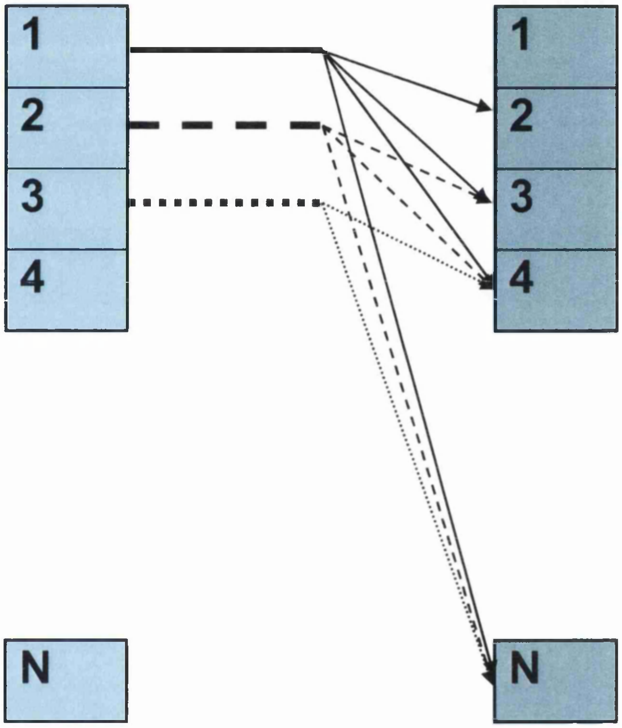

Figure 20: Individual element check with all others in the system

The table in *Figure 20* displays the simplistic search procedure that requires a link between each target body and the remaining contactor bodies. Although this method is legitimate, when considering a region with N (*number of particles*), the process becomes grossly inefficient as N become large. This is due to the fact that the number of operations required to detect all contacts between N bodies becomes proportional to:

$$N\frac{N-1}{2} \qquad (2.5)$$

This process becomes computationally expensive for large N.

More efficient methods of contact detection have reduced this proportionality down to factors of:

$$N \log_2(N) \tag{2.6}$$

The equations (2.5) & (2.6) represent extremes in search techniques however there are a number of alternative methods that have been introduced in recent years to address this critical area of research.

The mathematical principles implemented in contact detection methods strongly influence the computer processing unit (CPU) time for a given simulation and function effectively regarding element type. To minimise CPU demand for a fast efficient contact search and yet maintain data quality a balance has to be struck. The key components to a good 'General Global Search Algorithm' are ones that are efficient in dealing with large N (for both rigid and deformable bodies) and are applicable to close packed elements as well as those in rapid motion. However, due to the subtle changes in requirements, one single algorithm may fall short in achieving all targets and different approaches may be adopted for different applications[54]. Therefore, as a brief discussion, the variations in differing search algorithms are examined in this section.

2.4.1: Direct Checking Method

As highlighted above this method incorporates the simplest of techniques to search for potential contactors.

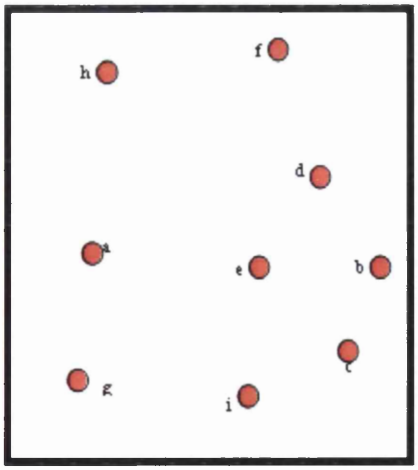

Figure 21: A 2D array of contactors in a domain

The basis of this technique links each body with every other body in the system and considering *N-1* potential contacts for assessment the number of operations becomes proportional to:

$$N\frac{N-1}{2} \tag{2.5}$$

2.4.2: Direct Evidence Search

In this technique the contact search area is reduced by only involving elements in close proximity to the target element. This produces a short list of contactors and is periodically updated as the incremental time step moves on.

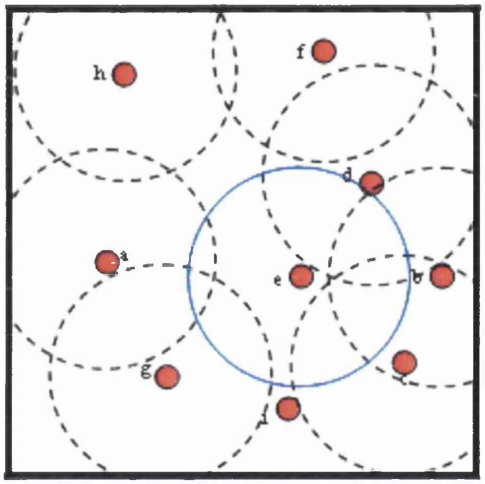

Figure 22: 2D contactors in a domain with 'Buffer Zone'

As shown in *Figure 22* a simple *'Buffer Zone'* has been created to select neighbouring particle for a short list of possible impactors. The buffer zone in this case is a radial distance and associated with each individual particle. For the calculation procedure the buffer zone can be applied and a short list of elements inside the zone recognised. By interpolating the velocities of the elements at each time step, a prediction can be made of expected contact time. If no contact is imminent the interaction can be ignored.

The creations of such short lists as shown in Figure 23 are generic in most of the developed search algorithms but methods can differ depending on the simulation requirements.

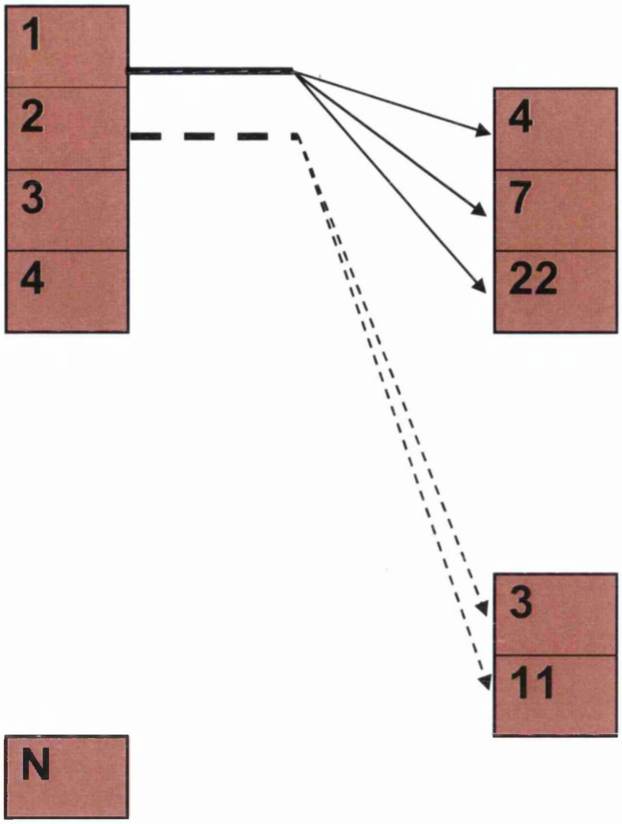

Figure 23: Short list of contactors[54]

2.4.3: Binary Tree Structure

A binary tree structure is a data sorting method that enables a program to easily add or delete information. Binary trees are one of the most important non-sequential types of data structures and they provide the basis for several searching algorithms[55]. The basic concept behind this technique is data storage in non-sequential locations of the computer memory.

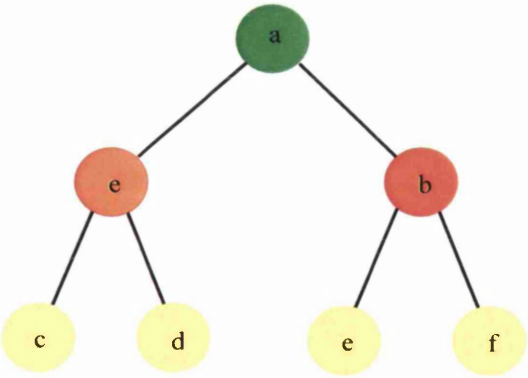

Figure 24: Simple binary tree structure

Each data item is extended by the addition of two integer values known as the *left* and *right* links and stored as a node in the tree formation. The construction of the data tree allows two nodes to be accessed from one higher in the hierarchy and for every node to be reached in this hierarchy it has only one link going to it. This is with the exception of the first node known as the *root*. A node without any branch (pointer) to another node is called a terminal node. *Figure 24* depicts how data can be stored when defining a simple binary tree. In addition each individual node of the tree can be designated with a binary number. Such as, each left branch recognised by 0 and each right branch by a 1 digit.

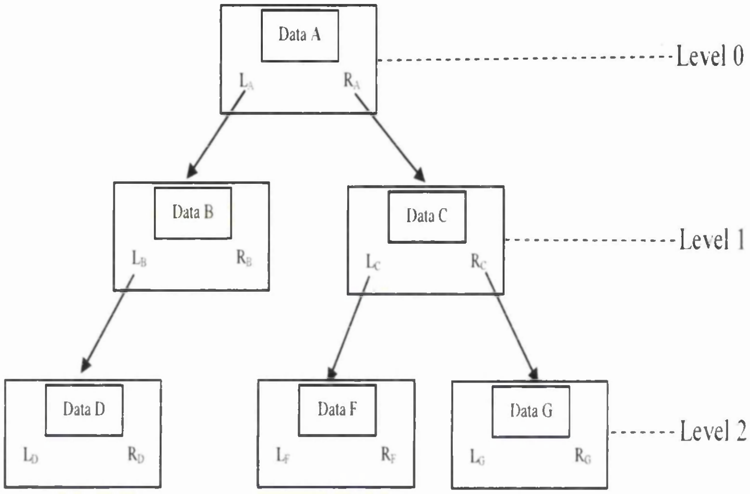

Figure 25: A binary tree structure with memory location

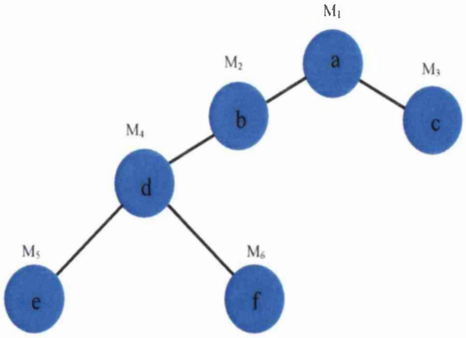

Left	Right	Node	Data	
M_2	M_3	A	x_A	y_A
M_4	M_6	B	x_B	y_B
M_5		C	x_C	y_C
		D	x_D	y_D
		E	x_E	y_E
		F	x_F	y_F

Figure 26: Data storage in a simple binary tree

To create a binary tree a root node is selected and adding new data points to the tree structure depends upon the program method of determining between left or right branch for insertion. Each new insertion then starts by checking the same method at the root node and traverses the tree until an empty place is found. The order of the new insertions determines the structure of the binary tree and the resulting shape has a major influence on computational cost of the global contact search procedure. To maximise the performance of this search method the tree structure is preferably well balanced and poor performance is produced when the tree is degenerated as shown in *Figure 27*.

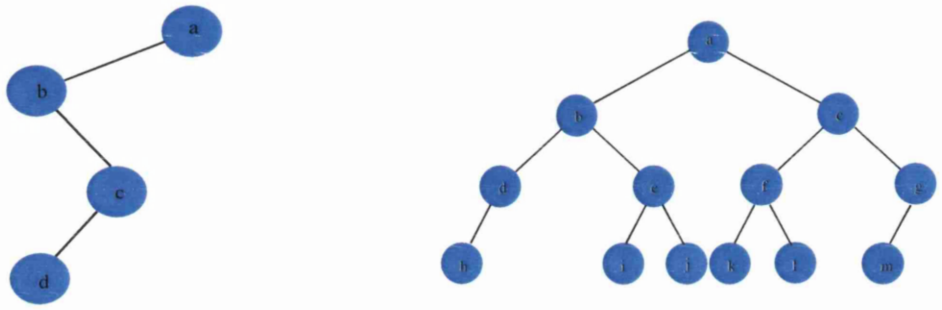

(a) Degenerate tree

(b) Well balanced tree

Figure 27: Degenerate and well balanced binary trees

2.4.4: Coordinate Based Space Decomposition

This method uses the coordinate axis to divide a region into finite intervals that are number associated. Each cell is defined as a set of points that have coordinates that belong to the same interval as shown in *Figure 28*

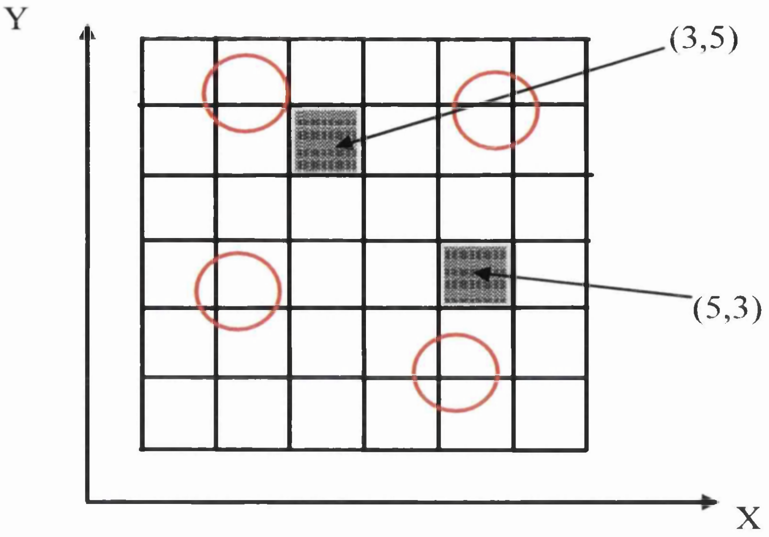

Figure 28: Coordinate based space decomposition in 2D

The numbering of the cells can have two coordinates for 2D and three coordinates for 3D, this number association can also be represented in binary terms. The 2D example in Figure 28 represents a square of dimensions $2a$ sub divided by N divisions on each edge to provide N^2 cells. The computer procedure generally requires two passes, the first is to associate each body or object with a single or several cells using coordinates and the second is to assemble a list of potential contactors for each target object from the list of objects associated with the cells containing the target[56].

The performance of the method is a function of the cell size relative to the size of the object/particle i.e. if the cell size is too large an excessively large number of potential contactors may be produced, however if the application allows an appropriate cell size an efficient algorithm may be developed. An example of a spatial search algorithm that is based on this concept is 'No Binary Search' (NBS).

2.4.5: Space Bisection Algorithm

This method can be used as an insertion criterion for the base node in constructing a digital tree. The region in question is systematically divided into two sections at each level.

Considering the situation depicted in *Figure 29* the space bisection algorithm approaches the body search as follows.

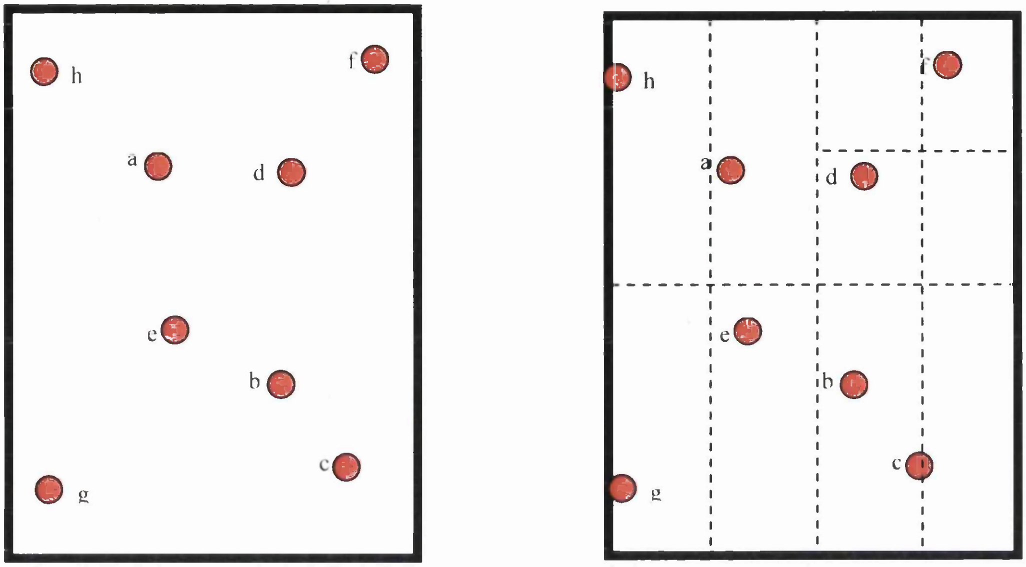

Figure 29: Bodies in a domain applied to space bisection algorithm

2.4.6: Body Based Cells

A derivative of the *'Buffer Zone* type method can be seen in the body based cells algorithm. In this case each element has a cell surrounding it that acts as a boundary detector.

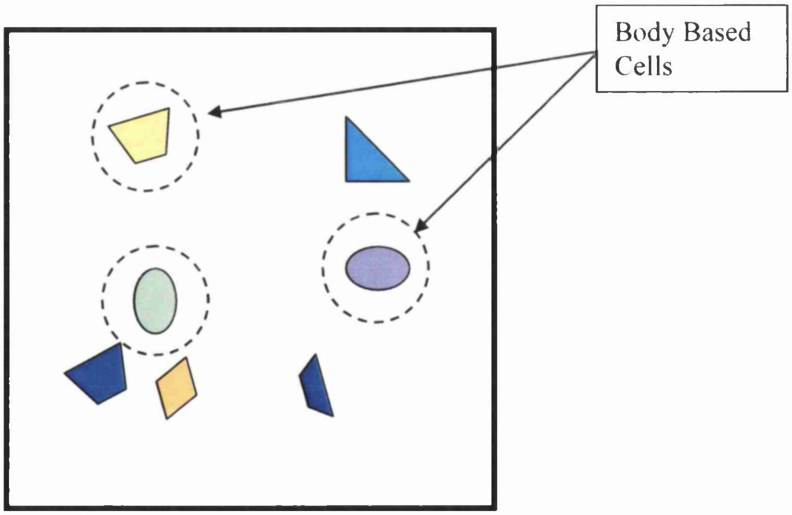

Figure 30: Space decomposition by body based cell approach

The element within the region will only be aware of elements within the scope of the bounding cell radius. Again any potential contactors are then recorded into a list of neighbours.

2.4.7: Neighbour Search

The 'Neighbour Search' is similar in design to the body based search procedure in that a bounding cell arrangement locates potential contactors and lists them. However, in this method the list of potential contactors is extended out to the nearest neighbours located within their bounding cell. The result of this is that the target body list is continually updated without a need for a further special search[57].

As stated the search grid is used to periodically build a particle near neighbour interaction list. Using only particle pairs in the near neighbour list reduces the force calculation to an $O(N)$ operation, where N is the total number of particles. Industrial simulations with 10 million particles are possible in reasonable time frames[30]

2.4.8: Alternating Digital Tree (ADT)

An alternating digital tree algorithm is used to determine which members of a set of n points in an N dimensional space lay inside a prescribed space subregion. This type of algorithm can be used for point searches but extends to handle finite sized objects such as soft-rigid elements.

In general terms an alternating digital tree search algorithm can be viewed as a binary tree where by a set of n points are stored following geometrical criteria. The criteria are based on conditions implemented in hierarchical node structure that flow through a parental branch configuration of a binary tree and a recursive bisection process. This method was introduced by Bonet & Peraire (1991)[58] and subsequently developed by Petrinic (1996)[58] and Yu (1999)[59].

An ADT algorithm is one of the most efficient available search algorithms and comprises of three key stages that provides a potential list of contacting objects in the spatial search:

- Body location mapping – representation of objects by bounding boxes
- Space bisection – construction of a binary tree containing all objects
- Bounding box intersection search – to compute the list of potential contacting objects

2.4.8.1: Body Location Mapping

In this type of global search algorithm a general shaped body is represented by a standard simple bounding box. The box circumscribes the body and its edges are parallel with the global coordinate system.

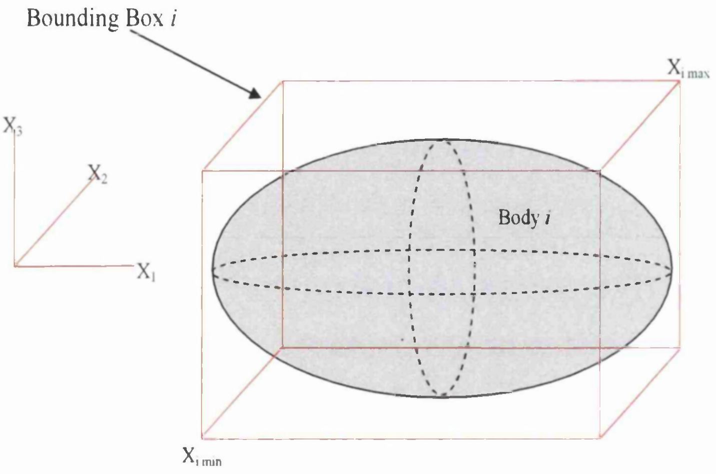

Figure 31: Bounding box around a 3D elliptical element[58]

In compliance with the point based space bisection algorithm, a body *i* from the R^n space can be represented by a point in the R^{2n} space via an invertible mapping $L : R^n \longrightarrow R^{2n}$ that combines the coordinate limits of the body's bounding box according to:

$$x_i = \left[x^1_{i,\min},\ldots,x^n_{i,\min},x^1_{i,\max},\ldots,x^n_{i,\max}\right]^T \qquad (2.7)$$

x_i is a unique location of an object in the R^{2n} space.

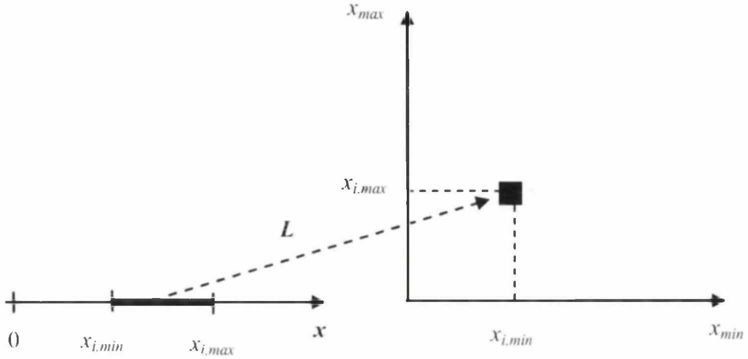

Figure 32: Mapping a 1D segment to a point in R^2 space[60]

2.4.8.2: ADT with Space Bisection and Binary Tree

The creation of an alternating digital tree utilises the body location mapping method in conjunction with the space bisection method and a binary tree structure as shown in *Figure 33*.

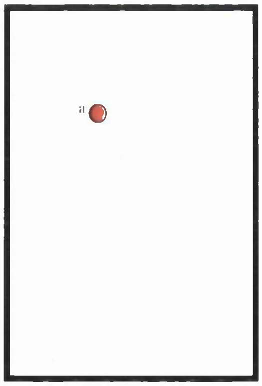

L	Node	R
	a	

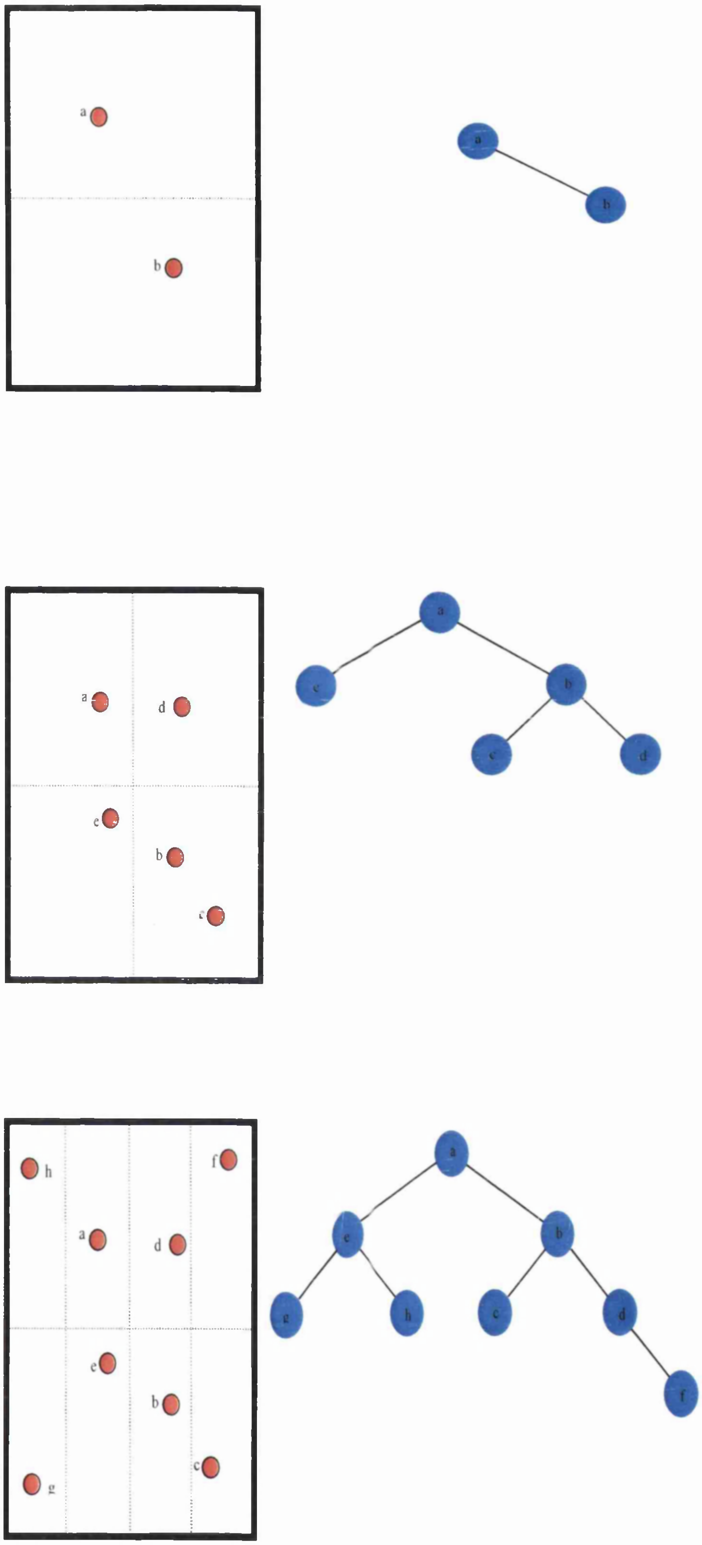

L	Node	R
	a	b
	b	

L	Node	R
e	a	b
c	b	d
	e	
	c	
	d	

L	Node	R
e	a	b
c	b	d
	e	
	c	
	d	f
	g	
	h	
	f	

Figure 33: ADT with space bisection, binary tree structure and memory storage[57]

2.5: Contact Interaction and Constitutive Forces

In a situation when contacting elements are selected through a spatial search algorithm, the contact interaction processes are initiated. The resulting collisional interactions predominantly occur between particles-particle, or particles encountering a boundary condition. Mathematically modelling these types of interactions require the manipulation of suitable contact force laws, and the implementation of the rules expressed in the equations of motion. There are many variations in DEM programming[61], however the fundamental concepts in the majority of programs are, by and large, generic and follow a similar structure. In this review a standard code is discussed as described by Cleary (1998)[62] where interactions are driven by the soft sphere method with no apparent element deformation.

2.5.1: Particle-Particle Point of Contact

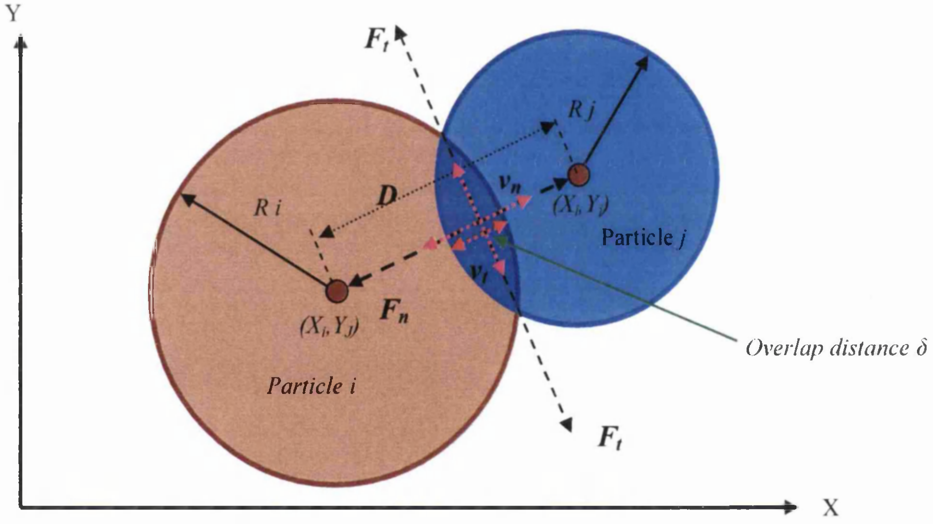

Figure 34: 2D particle-particle contact interaction

As shown in the 2D image in *Figure 34*, the contact force interaction laws are a function of the overlapping distance between the impacting particles. The depth of the overlap, signified by the value "δ", is dependent on the relative normal and tangential velocities and an associated time step.

The distribution of the forces generated during the interaction period can be viewed as a linear spring-dashpot diagram as shown in *Figure 35*. Surfaces are breached when a simple geometric relationship occurs. i.e.

$$D \leq \left(R_i + R_j\right) \tag{2.8}$$

Where: R_i, R_j are element radii and D is the centre-centre distance

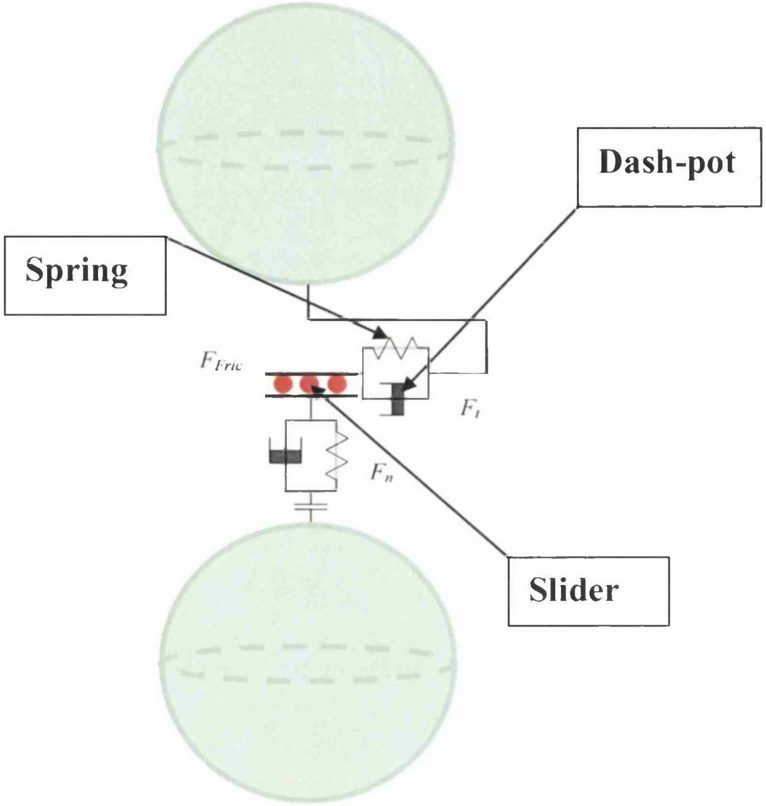

Figure 35: Forces during contact exchange expressed as a linear spring-dashpot (LSD) diagram

As shown in *Figure 35* the spring system in the schematic diagram stores the impact energy as a compressive repulsive force. The dashpot acts as a damping mechanism that dissipates the energy at contact and the magnitude of the dissipation is directly related to the applied coefficient of restitution. Along with the simulated energy transfer a velocity based damping mechanism is used to reduce a number of particle impacts (as in a granular flow) into a steady state[63].

2.5.1.1: Linear Spring Dash-pot (LSD) and Hertzian Spring Dash-pot (HSD) Systems

The schematic image shown in *Figure 35* highlights the simplified element contact interaction using a spring dash-pot arrangement to store and dissipate energy respectively. For the LSD model the viscoelastic contact interaction neglects element deformation at impact and 60% of DEM models use this method in contact interaction[64]. Where as, the HSD model functions by utilising material characteristics and represents a non-linear relationship[65][66].

As shown in *Figure 34* the magnitude of δ is the contact overlap distance and is a function of the spring constant k_{n}.. The stiffness of kn limits the overlap distance and affect the time step calculation, for the LSD model values in the order of 10^3-10^7 Nm^{-1} for 3D can be used.

For the HSD model the inter element/element boundary contact considers the plastic deformation at surface contact and is a function of the mechanical nature of the simulation material.

The equation to calculate k_n here is as follows:

Inter element:

$$k_n = \frac{4}{3}\sqrt{\frac{r_i r_j}{r_i + r_j}}\frac{E_i E_j}{\left(1-\nu_j^2\right)E_i + \left(1-\nu_i^2\right)E_j} \tag{2.9}$$

Element Boundary

$$k_n = \frac{4}{3}\sqrt{r_i}\frac{E_i E_w}{\left(1-\nu_w^2\right)E_i + \left(1-\nu_i^2\right)E_w} \tag{2.10}$$

Where:

E_i E_j are the Young's modulus of the elements (Nm^{-2})

r_i r_j the element radii (m)

k_n is the spring constant Nm^{-1}

v is Poisson's ratio of the element or boundary (-)

The non linearity of the HSD method is a more representative simulation technique but the k_n values produced using (2.9) and (2.10) can be large ($O(10^9)$)[67][68] due to material properties. This forces high k_n values producing very low time steps, and this is a major drawback as calculation time increased.[69][70].

In the case of the LSD model the linearity of the force calculation is preserved and follows Hooke's law if the contact overlap is small compared to the element radius. As a result of this F_n reduces to;

$$F_n = -k_n \delta_n \tag{2.11}$$

For the current program the LSD was the adopted model (due to its simplicity and effectiveness)[71] and applied to the interaction forces at contact. Further discussions on this topic are highlighted in *2.5.1.2 and 2.5.1.3.*

2.5.1.2: Normal Contact Force and Damping

In *Figure 35* the normal contact force has a vectorial element that links the centres of the contacting disk shaped objects. The spring represents a mechanism that generates a repulsive force and the dash-pot represents the dissipation of energy in terms of a damping coefficient. The maximum overlap between the disks (δ) is governed by the spring stiffness *"k"*. In the soft sphere model the overlap is designed to be small compared to the radial values of the discrete element in contact (values in the region of 0.1 and 1.0% of the radii are acceptable) and this can requires spring stiffness values of between 10^6–10^7 Nm^{-1} in 2D and 10^4–10^6 Nm^{-1} in 3D[72]. When this factor is realised the contact interaction behaves linearly (LSD) and follows Hooke's law. However, in some cases realistic particle motion is achievable while reducing computer time by limiting k_n to stiffness values in the region of 800-1000Nm^{-1}[67]. At this level the advantage of a larger time step is allowed to simulate a collision.[73][74][75]

The magnitude of the normal force is calculated using:

$$F_n = -k\delta_n - C_n v_n \tag{2.12}$$

Where:

k is the spring penalty stiffness (Nm^{-1}),($kg\ s^{-2}$)

δ_n is the overlap distance (m)

C_n is the tangential damping coefficient ($kg\ s^{-1}$)

v_n is the relative tangential velocity ($m\ s^{-1}$)

In terms of particle –particle interaction v_n is derived using:

$$\vec{v}_n = \left(\left(\vec{v}_f - \vec{v}_i\right)\bullet \hat{n}\right)\hat{n} \tag{2.13}$$

Where

v_f is the final velocity vector

v_i is the initial velocity vector

$\hat{n}$ is a unit vector

As highlighted the spring system depicted in *Figure 35* stores the impact energy in an incremental time frame before returning the energy to simulate an impact. The normal damping coefficient C_n is used in the same algorithm to limit the reaction force during the impact and acts as a dissipation of energy within the contact system.

$$C_n = 2\lambda\sqrt{m_{ij}k_n} \tag{2.14}$$

Where:

$$\lambda = -\frac{\ln(\varepsilon)}{\sqrt{\pi^2 + \ln^2(\varepsilon)}} \tag{2.15}$$

And

ε is an input variable of between 0 and 1 related to the coefficient of restitution

The application of Equation (2.14) during a collision event simulates the influence of the coefficient of restitution and its value is determined by input parameters used in Equation (2.15).

2.5.1.3: Tangential Contact Force and Friction

The tangential contact force is a force element generated perpendicular to the normal vector between the particle centres. The magnitude of the force is a function of the normal reaction force, the tangential velocity at contact and the damping coefficients apparent during the contact period.

$$F_t = -k\delta_t - C_t\vec{v}_t \tag{2.16}$$

Where:

k is the spring penalty stiffness *(Nm^{-1}),(kg s^{-2})*

δ_t is the overlap distance *(m)*

C_t is the tangential damping coefficient *(kg s^{-1})*

V_t is the relative tangential velocity *(m s^{-1})*

And:

$$C_t = 2\lambda\sqrt{m_{ij}k_n} \tag{2.17}$$

$$\vec{v}_t = \left(\left(\vec{v}_f - \vec{v}_t\right)\cdot\bar{s}\right)\bar{s} \tag{2.18}$$

Where:

$\bar{s}$ is the tangential shear unit vector

In this type of contact interaction the same values are used for both normal and tangential directions [74].

Frictional forces are introduced using "Sliders" to represent the shear between contactors in the linear spring-dashpot diagrams as shown in *Figure 35*. The fundamental principles behind the shear force contact components are governed by the "Coulomb Friction Model". This method incorporates a frictional coefficient, and a shear spring, to limit motion and store energy respectively in the tangential direction of contact. As in the normal reaction force energy is dissipated using a viscoelastic damping mechanism in the form of a tangential dashpot (as shown in *Figure 35b*). Energy dissipation of this nature could be associated to particle deformation due to shear, sound generation or impact wear. For this project these condition are briefly discussed but not embellished upon.

From this, the relative shear displacement δ_t in (2.14) is calculated by:

$$\delta_t = \vec{v}_t dt \tag{2.19}$$

During a contact interaction the "Coulomb Friction Model" introduces a slip criterion due to the magnitude of tangential velocity determining the tangential shear force. The slip frictional force is applied in the form of:

$$\vec{F}_{Fric} = -\mu \left| \vec{F}_n \right| \tag{2.20}$$

Where:

μ is the frictional coefficient of the impacting material types and is non-dimensional.

To enforce the slip criterion a comparison of the magnitude of the shear force from (2.16) is made with the frictional force in (2.20). If this value is greater, then the shear force is limited to the frictional force component. In this situation, the particles slip relative to one and other[76][77].

2.5.2: Particle-Boundary/Wall Contact

In the case of a particle-boundary interaction the contact force calculations that determine a reaction are dealt with in a very similar method to the particle-particle situation. However, the particle–particle interaction can be viewed as a "Binary" process and the boundary interaction seen as single particle with momentum encountering a static system.

The boundary wall implementation has a significant influence in the simulation process as a means of mathematically constructing a flow regime or a constraint to study packing conditions. In essence boundary conditions present themselves as limiting parameters that function to manoeuvre the passage of an element through a global domain.

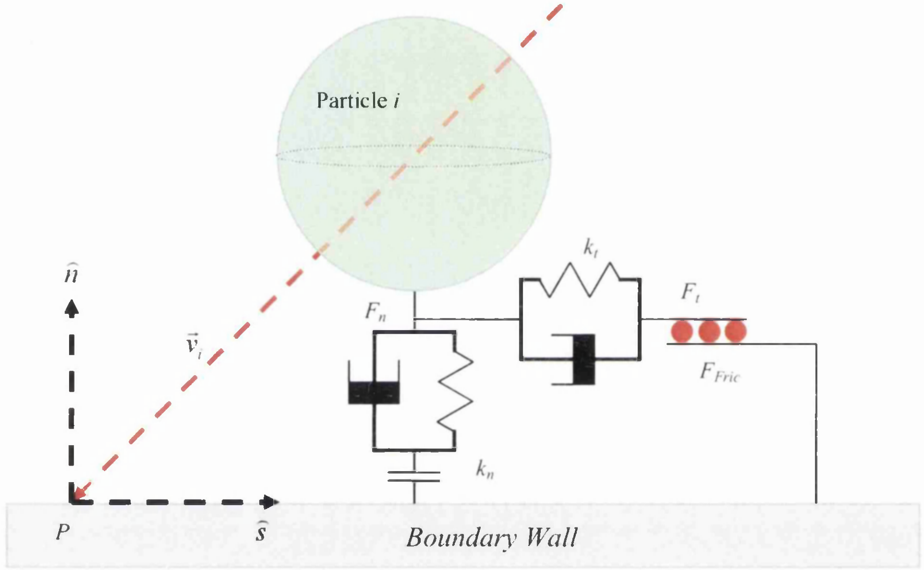

Figure 36: Normal and tangential forces between boundary and impacting particle

Where:

k_n & k_t *are the normal and tangential stiffness penalty value respectively* (Nm^{-1}),($kg\ s^{-2}$)

F_n & F_t *are the normal and tangential reaction forces respectively* (N)

F_{Fric} *is the frictional force between the boundary and the particle* (N)

$\vec{v}_i$ *is the velocity vector of the impacting particle* ($m\ s^{-1}$)

$\hat{n}, \hat{s}$ *are the normal and tangential unit vectors respectively*

P is the impact point of the incoming particle.

2.5.2.1: Basic 2D Boundary Wall Search

For the 2D case the boundary wall search mechanism utilises a geometric principle that uses the particle position in space and the boundary wall limits as a coordinate system.

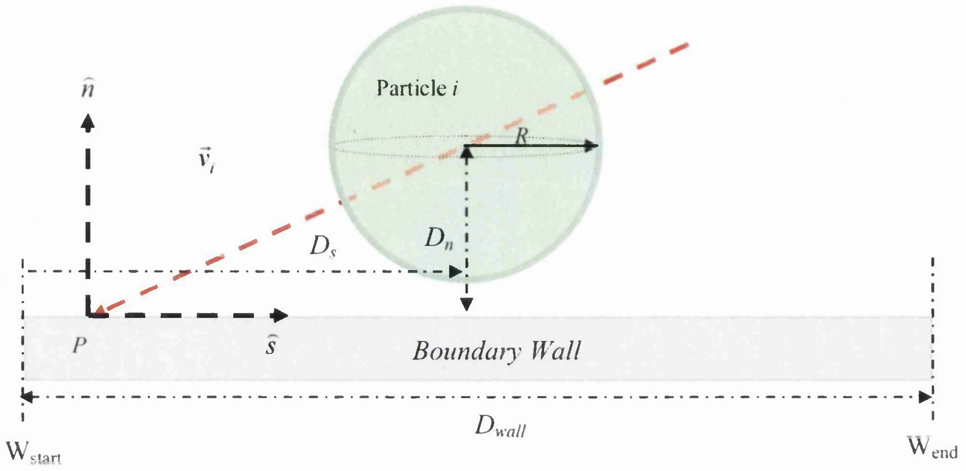

Figure 37: Particle with velocity approaching a boundary wall.

Where:

D_n is the perpendicular distance for the boundary surface to the centre of the particle
D_s is the tangential distance from the start of the wall to the D_n coordinate line
D_{wall} is the length of the boundary wall
W_{star} &, W_{end} are the start and end point of the wall respectively
R is the radius of the particle

As shown in *Figure 37* the particle is positioned over the surface of the boundary wall and is likely to make contact. From the schematic diagram the value of D_n is larger than the radial distance of the particle; therefore at this point the wall is not recognised. However, the key factors of the position of D_n over the boundary surface and distance D_s from the boundary coordinate W_{start} are critical in contact detection.

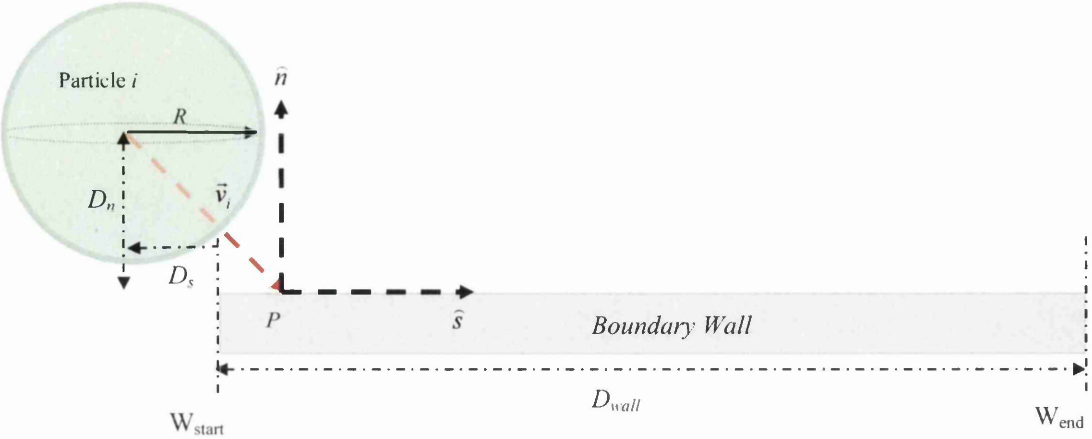

Figure 38: Here the distance $D_s < 0$ hence boundary is not recognised

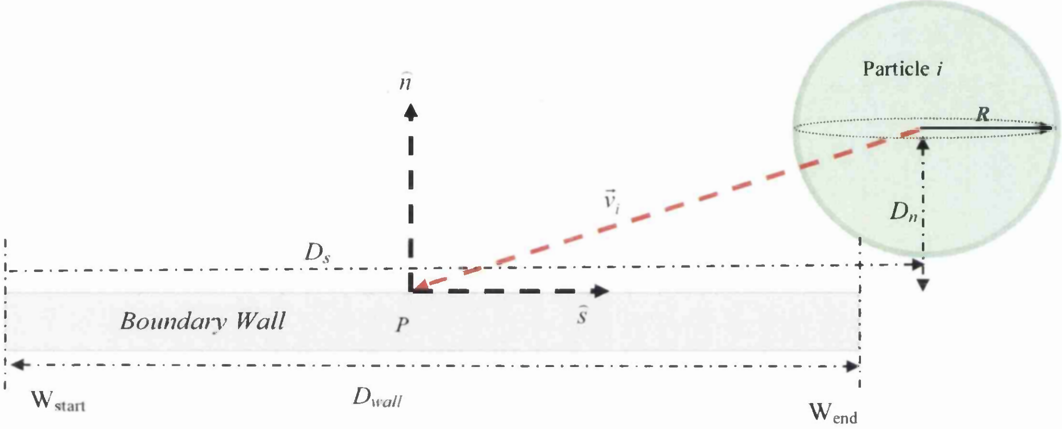

Figure 39: Here the distance $D_s > D_{wall}$ and again the wall is not recognised

In *Figures 38 & 39* the wall search conditions are not satisfied therefore the wall contact interaction process cannot take place. To initiate the contact algorithm:

$$D_n \leq R_{ij} \tag{2.21}$$

And:

$$0 \leq D_s \leq D_{Wall} \tag{2.22}$$

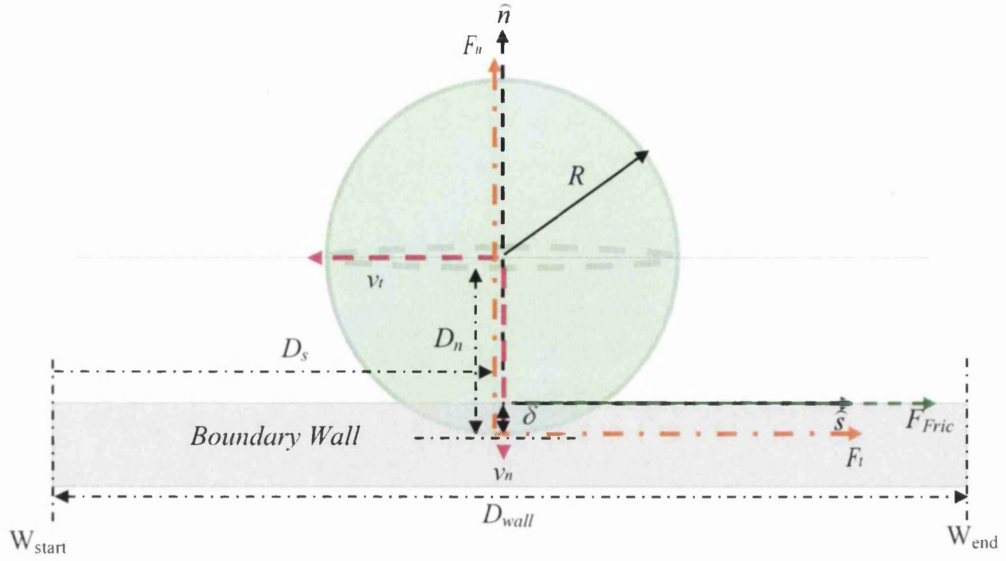

Figure 40: Particle in contact with the boundary surface and relevant conditions satisfied

Where:

v_t & v_n are the normal and tangential component velocities (ms^{-1})

F_n is the resultant normal reaction force (N)

F_t is the resultant tangential reaction force (N)

δ is the particle-boundary penetration depth (m)

$$\delta = R_i - D_n \tag{2.23}$$

2.5.2.1: Basic 2D Damping at Boundary Wall Contact

The details related to damping have been covered in the start of this section in terms of the particle-particle case. The damping mechanisms applied to boundary contact interaction are very similar and only differ in equation structure to determine force direction. The simple case of a particle impacting with a flat boundary is shown in *Figure 41*:

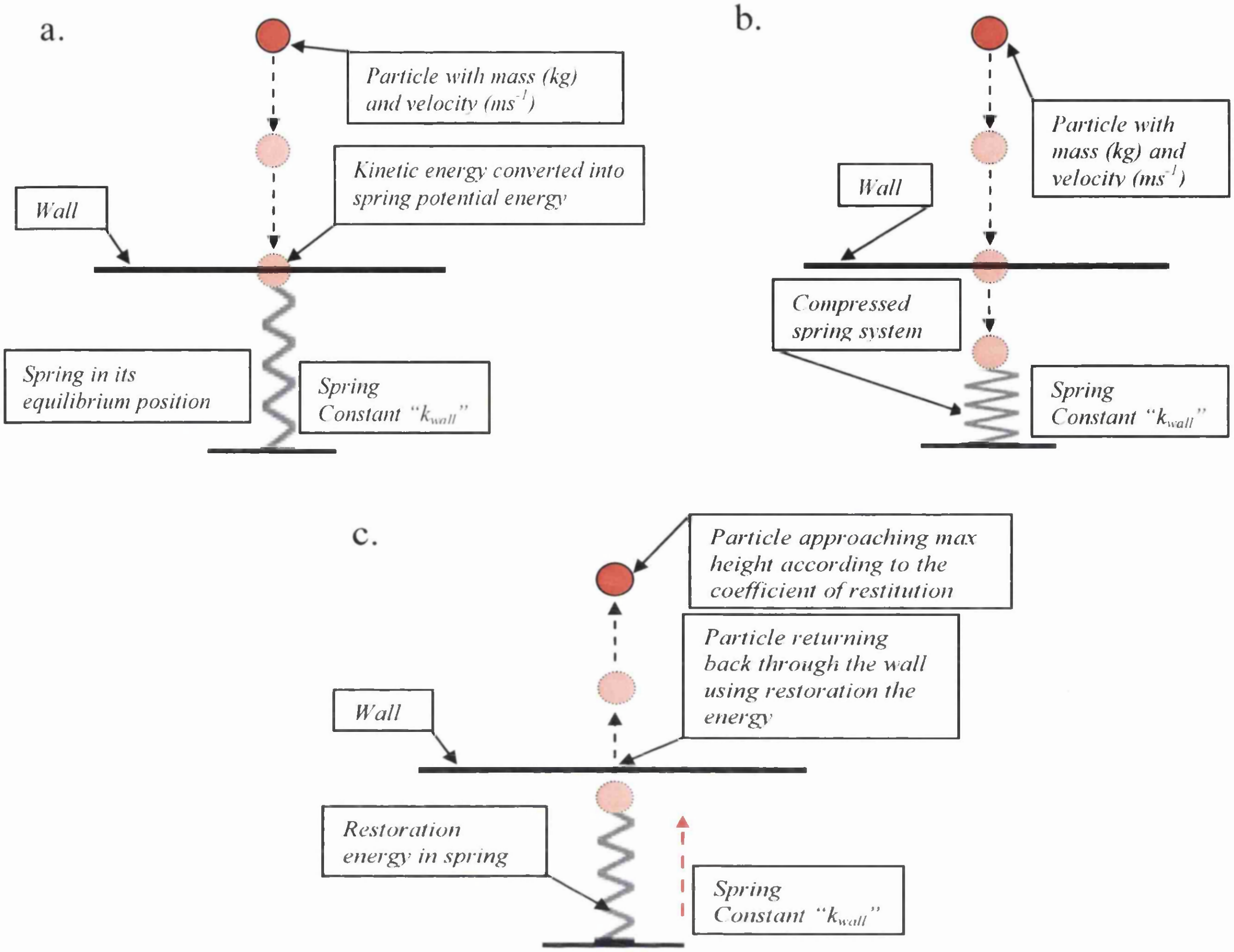

Figure 41: Simple case of particle falling under gravity and impacting with boundary condition

- In *Figure 41a* a particle with mass and velocity *v* is falling towards a flat boundary wall. As it makes contact with the wall the gain in kinetic energy is transferred into a spring potential energy.
- In *Figure 41b* the particle has breached the boundary surface and the theoretical spring becomes compressed. The amount of compression is a function of the particle mass, velocity and the penetration distance below the surface.
- Finally in *Figure 41c* the restoration energy stored in the compressed spring returns the particle back through the wall surface. A constant value for the coefficient of restitution is used generate a damping value and the particle returns physically to its expected height

2.5.2.2: Basic 3D Boundary Wall Search

In terms of a 3D boundary wall search the calculations to determine contact are similar to the 2D arrangements but the added dimension draws on vectorial mathematics of magnitudes and directions. For a particle encountering a boundary condition a distance to a plane in a given time step can be calculated by as follows[57]:

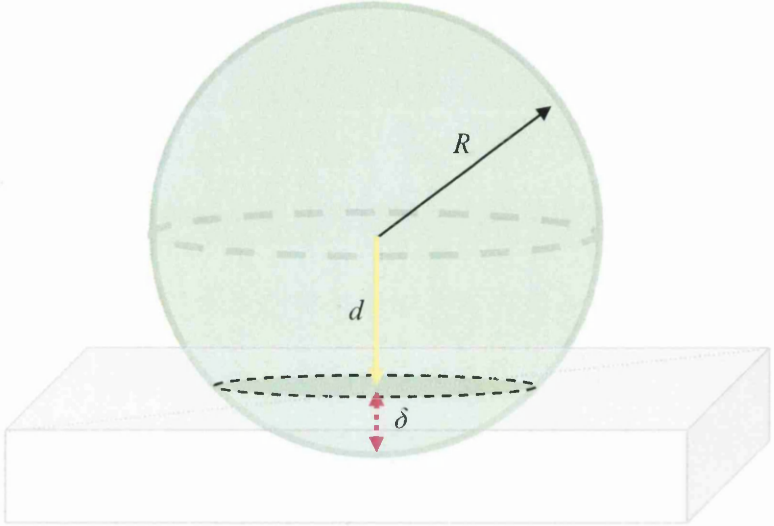

Figure 42: 3D sphere in contact with a boundary wall condition

$$r_i = \frac{abc}{4\Delta_{abc}} \tag{2.24}$$

$$0 \le d < R \tag{2.25}$$

$$\begin{aligned} A(x-x_1)+B(y-y_1)+C(z-z_1)=0 \\ A(x_2-x_1)+B(y_2-y_1)+C(z_2-z_1)=0 \\ A(x_3-x_1)+B(y_3-y_1)+C(z_3-z_1)=0 \end{aligned} \tag{2.26}$$

$$A^2+B^2+C^2=1 \tag{2.27}$$

$$\begin{vmatrix} x-x_1 & y-y_1 & z-z_1 \\ x_2-x_1 & y_2-y_1 & z_2-z_1 \\ x_3-x_1 & y_3-y_1 & z_3-z_1 \end{vmatrix} = 0 \tag{2.28}$$

$$(x-x_1)\begin{vmatrix} dy_{21} & dz_{21} \\ dy_{31} & dz_{31} \end{vmatrix} - (y-y_1)\begin{vmatrix} dx_{21} & dz_{21} \\ dx_{31} & dz_{31} \end{vmatrix} + (z-z_1)\begin{vmatrix} dx_{21} & dy_{21} \\ dx_{31} & dy_{31} \end{vmatrix} = 0 \tag{2.29}$$

$$\begin{aligned} a &= dy_{21} \cdot dz_{31} - dy_{31} \cdot dz_{21} \\ b &= dx_{31} \cdot dz_{21} - dx_{21} \cdot dz_{31} \\ c &= dx_{21} \cdot dy_{31} - dx_{31} \cdot dy_{21} \end{aligned} \tag{2.30}$$

$$A = \frac{a}{2S}, \quad B = \frac{b}{2S}, \quad C = \frac{c}{2S} \quad D = -Ax_1 + By_1 + Cz_1 \tag{2.31}$$

$$2S = \sqrt{a^2 + b^2 + c^2} \tag{2.32}$$

$$d = Ax_c + By_c + Cz_c + D \tag{2.33}$$

Contact with the boundary takes place if and only if *d* in (2.25) is satisfied.

2.5.3: Application of Newton's 2^{nd} Laws

As introduced previously in this section the constitutive forces at particle-particle / particle-boundary interactions are brought together in a summation to simulate motion. The calculations that are performed, alternate between Newton's second laws of motion to the element and the force displacement law at the contact area.[3]

- Newton's second law gives the motion of an element resulting from the forces acting on it.
- The force displacement law is used to find contact force from displacements

To determine the subsequent position of each element, Newton's Second Law of motion is twice integrating with respect to time. Along with that, individual elements move independently of one another with both translation and rotational motion considered.

Newton's 2^{nd} Law of Translational Motion

$$m_i \frac{d^2 x_i}{dt^2} = \sum_j f_i^j + m_i g \tag{2.34}$$

Newton's 2^{nd} Law of Rotational Motion

$$I_i \frac{d^2 \vartheta_i}{dt^2} = T_i \tag{2.35}$$

Where:

- *m_i is mass (kg)*
- *x is the location (m)*
- *g is the gravitational constant of acceleration (ms^{-2})*
- *I is the Inertia (kgm^2)*
- *ϑ is the angle of rotation due to the turning moment "T" (Radians)*
- *t is the time (s)*

2.5.3.1: Translational and Rotational Motion

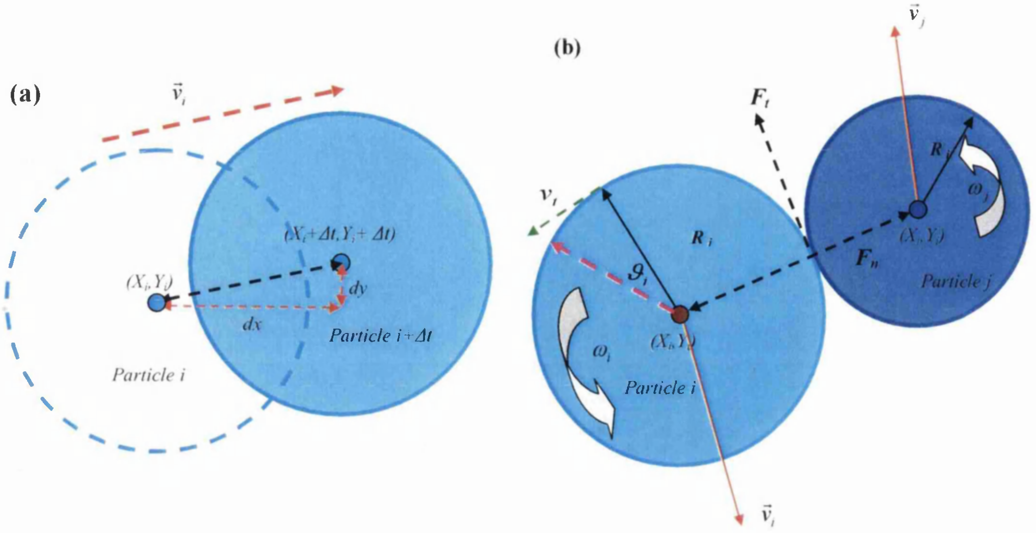

Figure 43: Elements in (a) & (b) in translational and rotational motion respectively

For the 2D case the translational motion of an element can be seen as the movement from an initial coordinate position to a final coordinate position in the x,y plane. In the 3D case the principles are same except that unit vectors are introduced to incorporate the third dimension. In rotation, inter-particle forces act over a contact region between the particles rather than the centre of mass of the particles and this generates a torque. The total torque includes two parts, one causing rotation from the tangential component and the other in a contribution from the normal component in terms of rolling friction[78].

If one considers the components of y and z to be constant, the one dimensional cases for translational and rotational motion are applied as follows:

$$m_i \ddot{x}_i = \sum F_i \tag{2.36}$$

$$I_i \ddot{\vartheta}_i = \sum M_i \tag{2.37}$$

In the soft sphere discrete element method the simulation is time stepped where the velocity and acceleration are assumed to be constant during each time step. Therefore $\ddot{x}$ and $\ddot{\vartheta}$ are constant over the period Δt and (2.36)&(2.37) become velocity expressions as shown in (2.38) & (2.39).

$$(\dot{x}_i)_{N+\frac{1}{2}} = (\dot{x}_i)_{N-\frac{1}{2}} + \left[\sum \frac{F_i}{m_i}\right]_N \Delta t \tag{2.38}$$

$$(\dot{\vartheta}_i)_{N+\frac{1}{2}} = (\dot{\vartheta}_i)_{N-\frac{1}{2}} + \left[\sum \frac{M_i}{I_i}\right]_N \Delta t \tag{2.39}$$

The formula in (2.38) & (2.39) are applied to each element and the corresponding velocity calculations are carried forward to the "Force Displacement Law" and this repeated over the number of elements *(N)* in the simulation and on every incremental time step.

$$(x_i)_{N+1} = (x_i)_N + (\dot{x}_i)_{N+\frac{1}{2}} \Delta t \tag{2.40}$$

$$(\vartheta_i)_{N+1} = (\vartheta_i)_N + (\dot{\vartheta}_i)_{N+\frac{1}{2}} \Delta t \tag{2.41}$$

The discrete element calculations in the discontinuum process shown in the above equations are achieved by the solution of partial differential equations using the *explicit finite difference*[3] method for continuum analysis.

2.4.3.2: Time Step Evaluation

In the soft sphere model for DEM simulation particle deformation is replicated by surface-surface overlap, although the overlaps are assumed to be small in relation to the particle size. This indicates that the collisions in this case are not instantaneous and develop over a finite time period. To maintain stability in the particle motion the integration time step between calculations must be correctly selected as an input and becomes a function of the force displacement law. To determine this value the DEM algorithm uses the relationship between the penalty stiffness value "*k*" and the characteristic natural frequency of a spring-mass oscillating system with mass m_i[3].

$$\tau_c = 2\pi\sqrt{\frac{m_i}{k}} \tag{2.42}$$

Where:

τ_c *is the critical time step(s)*

m_{ij} *is the effective mass* m_{eff} *(kg)*

k is the spring stiffness Nm^{-1}

$$m_{eff} = \frac{m_i m_j}{m_i + m_j} \tag{2.43}$$

As guidance, values that produce stable simulation time steps are in the region of 0.1% of the values generated in (2.42).

From (2.42) the critical time step for a calculation is dependent upon two main factors, spring stiffness and the particle mass. This implies that small hard particles with a low coefficient of restitution can prove to be computationally expensive.

Ultimately the above equations are introduced in sequence with a specific set of input parameters related to the simulation environment and material characteristics. The resulting output calculations produce an array of particle positions and velocities along with the forces at inter-particle contact, and contact with mathematical boundary conditions.

In general terms, the frictional forces are added to the normal forces and moments acting on the particles during contact. The particles velocity and position are then updated at each critical time step. This process continues at every positional increment until a pre-defined number of time steps have been reached.

3. DEM PROGRAM DEVELOPMENT

As discussed in Section 1, the original program applied to this granular flow investigation, was written as a 2D code. To stimulate growth and development within the program a conscious decision was made to apply it to real on-plant equipment, particularly those that had been identified as having material flow issues. Initially, the ideal candidate for application was the Sinter Plants "Roll feeder and segregation plate assembly". However, in terms of 2D, the resulting simulations returned limited information for data analysis and were visually uninspiring.

As a result of this, attention was drawn to more complex plant arrangements and 1004 to 1005 material transfer station and head chute was used as an alternative. This type of apparatus changes the direction of interconnecting conveyor belt systems through 90^0 and proved to be a demanding environment to control at the early stages. Primitive models were prone to simulation breakdown and the basic coding structure was mathematically developed at each failure to return a solution.

Throughout this section emphasis is drawn to the basic 2D mechanisms behind the motion and interaction of theoretical discs, with disc-disc and disc-boundary being considered.
Failures to generate suitable results for a 2D particulate simulation are highlighted and mathematical solutions to the inherent problems are offered.
Program application using plant designs are discussed to encourage and drive model improvement. The results of the coding development are presented as 2D working simulation renders.

3.1 Introduction

A primary concern with the original model was the failure of particle movement behind a boundary condition. To overcome this problem, a simplistic parametric equation was introduced into the code structure and a solution was obtained.

This developmental procedure ultimately produced a robust 2D modelling technique, but significant drawbacks were realised when 2D simulations were related to the actual flow regimes. The obvious disadvantages in these situations were critical data lose from the third dimension. As a result of this the program was systematically converted from 2D into 3D and progression to this stage is discussed at length throughout this section.

3.2: First Introduction to DEM

From the image in Figure 44 one can clearly see the type of particulate interaction that occurs in a DEM simulation with an element size distribution

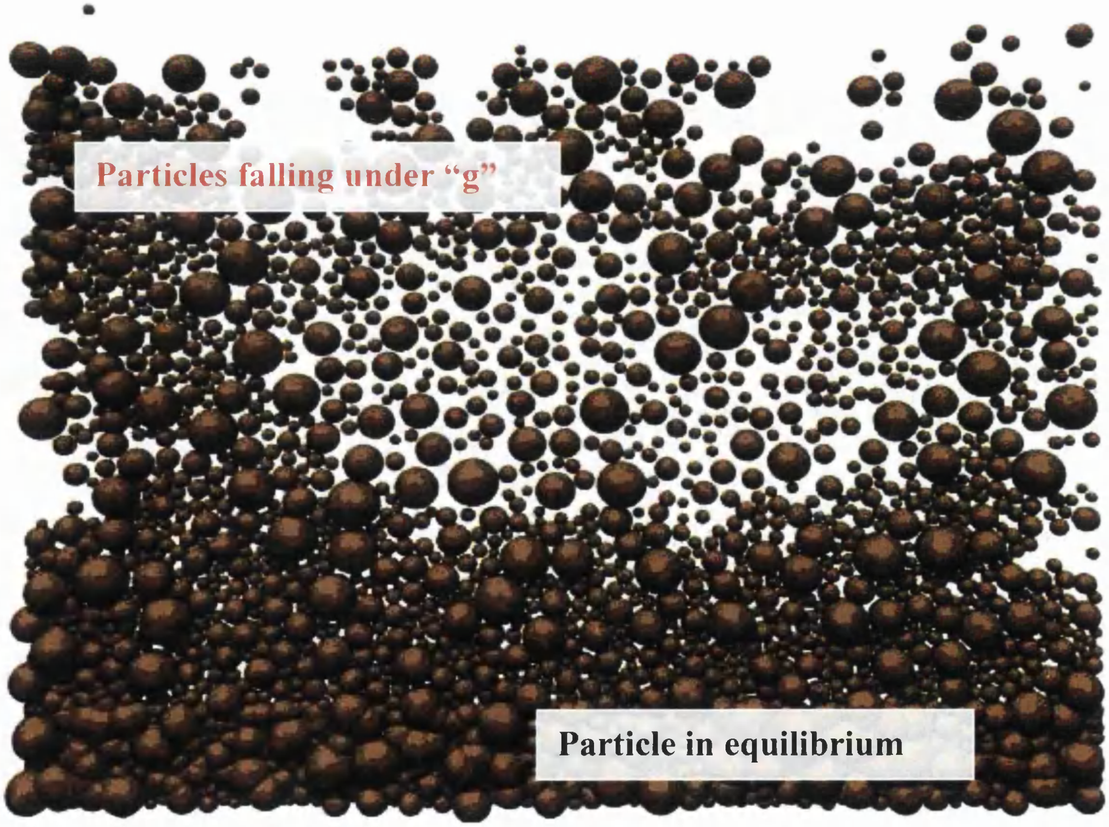

Figure 44: Discrete Elements packed into a global domain falling under gravity

. The image presented here is a snap shot of a global domain packed with discrete elements that are allowed to fall under gravity with varying degrees of global damping. As the elements settle and interact, contact forces are initiated at the surface overlap until equilibrium is achieved.

3.2.1: Particle-Particle Position Relation

The relative positions of potential contacting elements are calculated by a geometric 2D coordinate method.

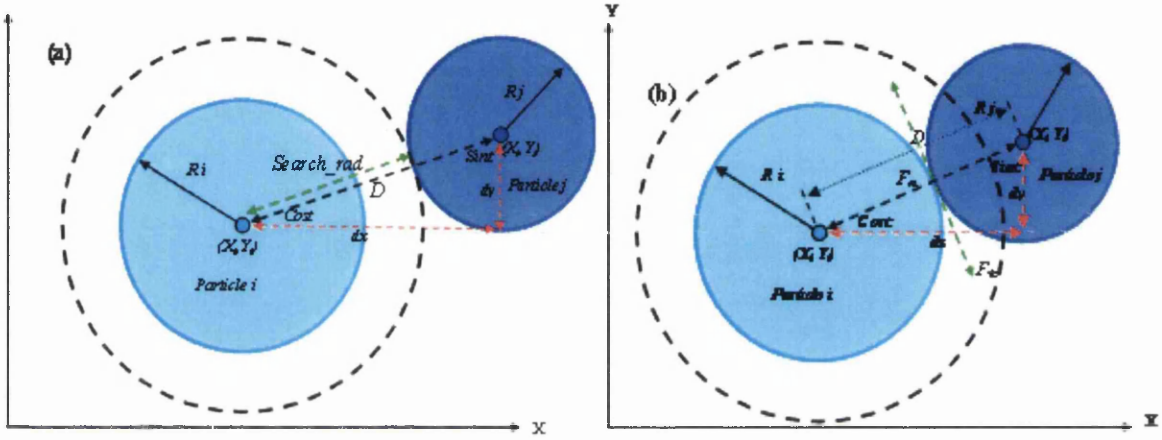

Figure 45: Relative positions calculate using 2D coordinate geometry

Where:

(x_i, y_i), (x_j, y_j) are the particle centres and R_i, R_j are the particle radii

$$dx = x_j - x_i \tag{3.1}$$

$$dx = y_j - y_i \tag{3.2}$$

$$D = \sqrt{\left(dx^2 + dy^2\right)} \tag{3.3}$$

$$Cost = \frac{dx}{D} \tag{3.4}$$

$$S\text{int} = \frac{dy}{D} \tag{3.5}$$

And:

$$D_{rad} = D - \left(R_i + R_j\right) \tag{3.6}$$

As shown in *Figure 45* the relative particle positions are determined by the centre coordinates and magnitude of the vector linking them. The *"Search_rad"* (*Figure 45a*) is an input variable that produces a search region to implement a *"Nearest Neighbour"* contact algorithm to predict potential contactor.

When $D_{rad} < Search\_rad$ the particle concerned is added to a contactor list array

The "Normal" forces components are directed between the particle centres using *Cosine Functions*. These are used to generate a "Tangential" force vector as shown in *Figure 45*.

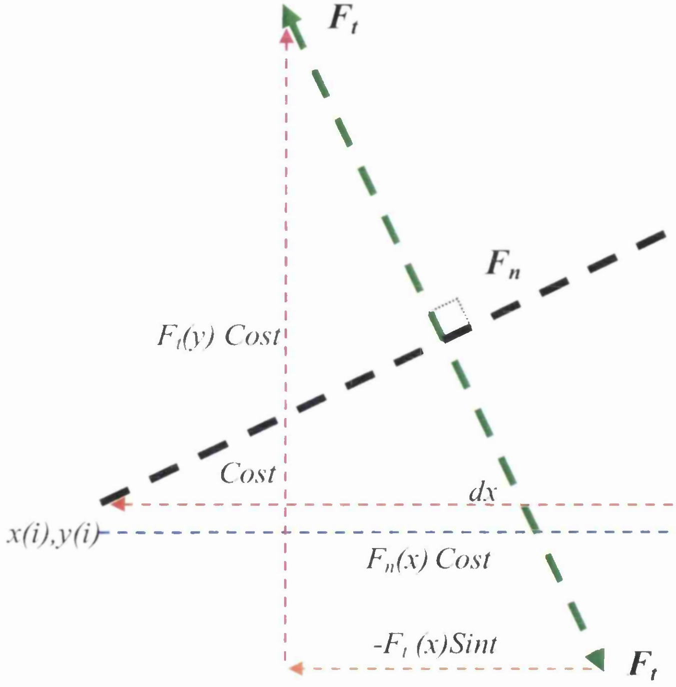

Figure 46: Normal and Tangential force directions produced in 2D using geometric and trigonometric functions

3.2.2: Particle-Boundary Position Relation and Wall Search

In addition to the global domain where particles fill the whole region, sub-regions of particle generation are introduced by limiting particle production to a specific coordinate system. As shown in *Figure 47*:

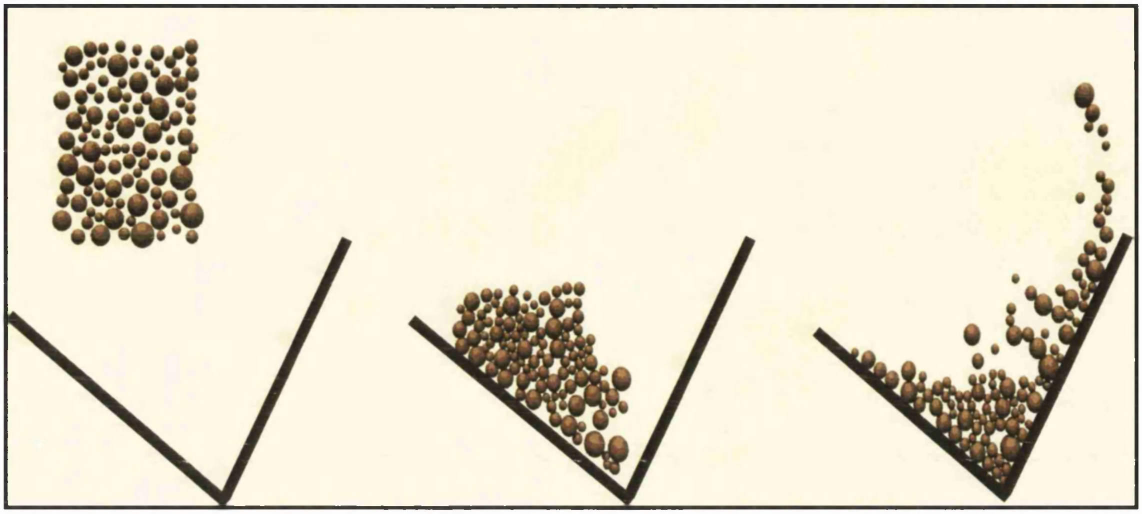

Figure 47: 2D simulation slides showing a region of particle generation falling onto a boundary condition

The snap shot diagram in *Figure 47* shows a number of discrete elements falling under gravity into a simple boundary wall arrangement. In the original 2D program code the boundary interaction procedure was calculated in a similar manner to the method discussed in Section 2 where distances are functions of positions in a coordinate system.

3.2.2.1: Particle-Boundary Contact Interaction

The schematic diagram in *Figure 48* shows a particle moving adjacent to a boundary wall. The perpendicular distance dn_n is the key factor and determines the point of contact with the boundary surface.

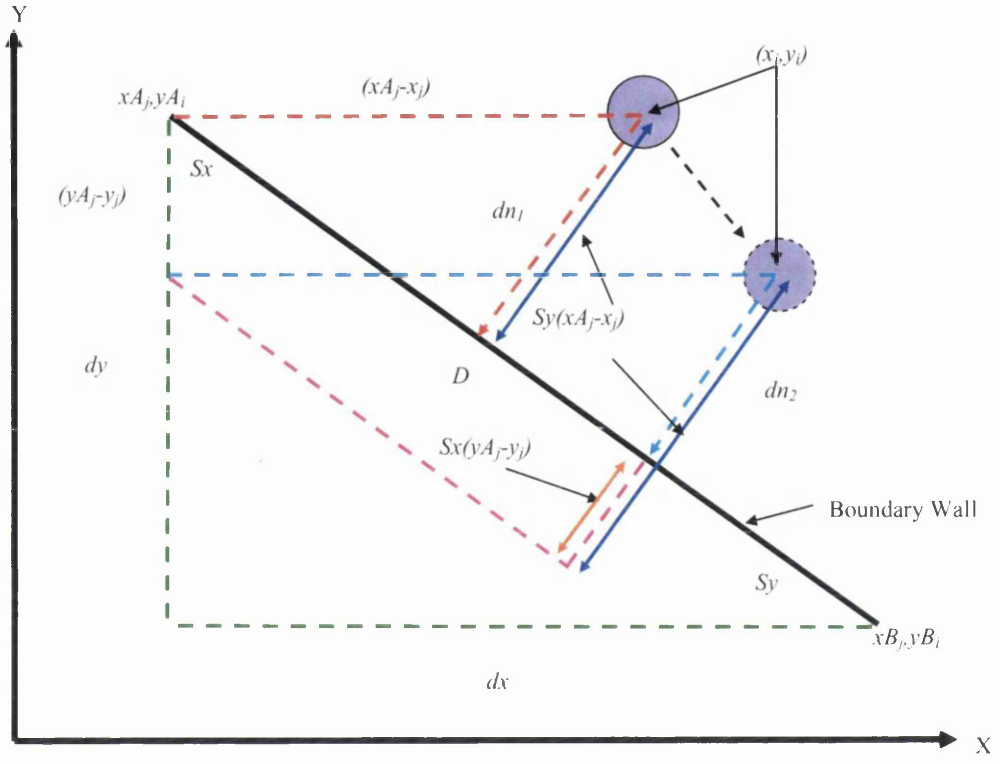

Figure 48: Particle motion over a boundary surface and corresponding calculations

Here the equations are formed as:

$$dx = xB_j - xA_j \tag{3.7}$$

$$dy = yB_j - yA_j \tag{3.8}$$

$$D_{wall} = \sqrt{\left(dx^2 + dy^2\right)} \tag{3.9}$$

$$sx = \frac{dx}{D_{wall}} \tag{3.10}$$

$$sy = \frac{dy}{D_{wall}} \tag{3.10a}$$

$$dn = sy \cdot (xA_j - x_i) - sx \cdot (yA_j - y_i) \tag{3.11}$$

$$ds = -sx \cdot (xA_j - x_i) - sy \cdot (yA_j - y_i) \tag{3.12}$$

$$\delta_{wall} = R_i - dn \tag{3.13}$$

Where:

xA_j, xB_j, yA_j, yB_j are end coordinates of the boundary wall

x_i, y_i, are the centre coordinates of the particle

dn is the normal distance from the particle centre to the boundary wall

ds is the distance from the boundary start point along the boundary perpendicular to the boundary normal

The equation used to calculate *dn* can be viewed as an equation with two separate parts:

$$dn = \underbrace{sy\,(xA_j - x_i)}_{\text{Part 1}} - \underbrace{sx\,(yA_j - yx_i)}_{\text{Part 2}}$$

Equation (3.11) can be seen as the key equation in 2D boundary detection and brings all the relevant formulae together. Part 1 remains dominant until the impacting particle encounters the boundary surface and Part 2 becomes larger. At this point $dn < 0$ contact interaction process takes place.

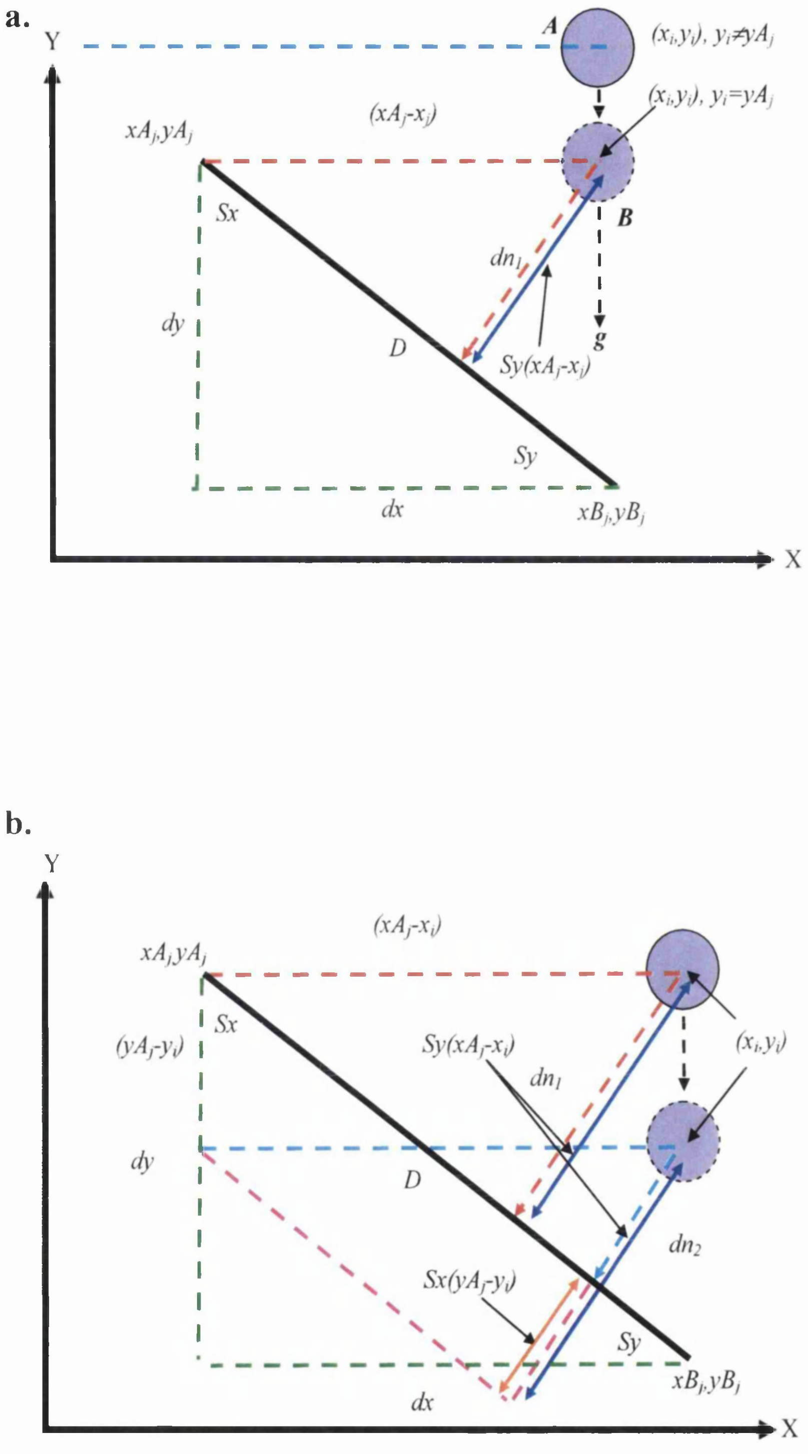

Figure 49: Slides *a* and *b* show a particle falling under gravity towards a boundary condition

In *Figure 49a*, at the highlighted position "***A***", y_i hasn't reached the yA_j co-ordinate and the particle has no relation to the wall.

At position "***B***" however, y_i and yA_j are the same and a "Wall Search" algorithm is switched on. Part 1 of Equation (3.11) at this stage is dominant and sets the *dn* value, if the particle is considered to be falling vertically (for simplicity) then this value remains constant.

In *Figure 49b* the particle draws closer to the wall and the perpendicular distance changes. The calculation from the wall search still exists but the Part 2 of Equation (3.13) comes into play to produce the actual distance.

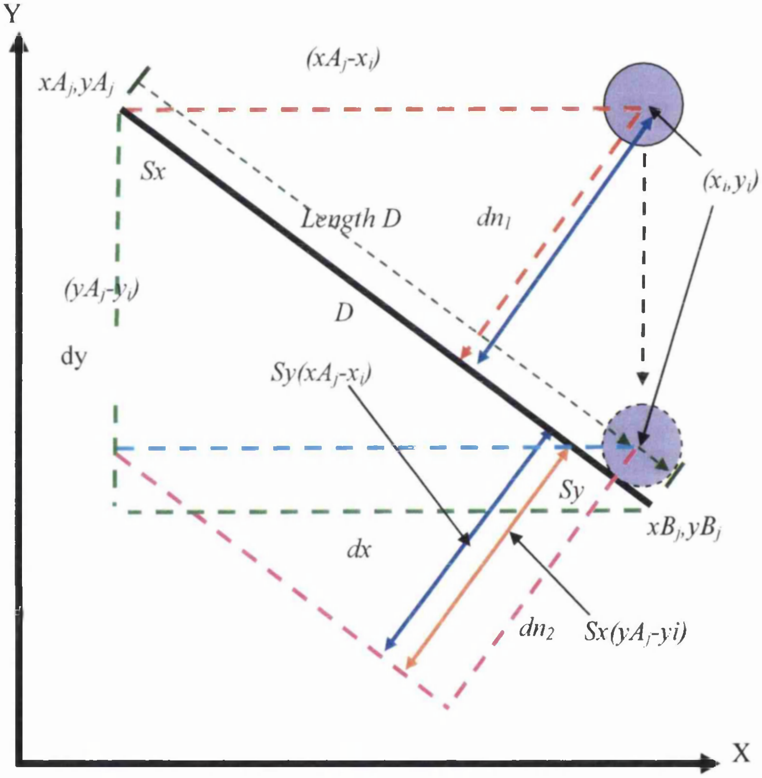

Figure 50: Particle comes in contact with the boundary with Part 2 of (3.13) dominant

In *Figure 50*, Part 2 of Equation (3.11) now becomes dominant and *dn* approaches zero. At this point the particle and the wall are now in contact. A force calculation takes place to determine the reaction force and the particle bounces physically, possibly leaving the confines of the wall.

3.3: Initial Program Application 1004 Material Transfer Head Chute

As discussed in the introduction to this section, applying the program to on-plant equipment was used as a method of indicating program weakness. In the case of 1004 the plans were obtained and a simulation domain was constructed to mathematical scale.

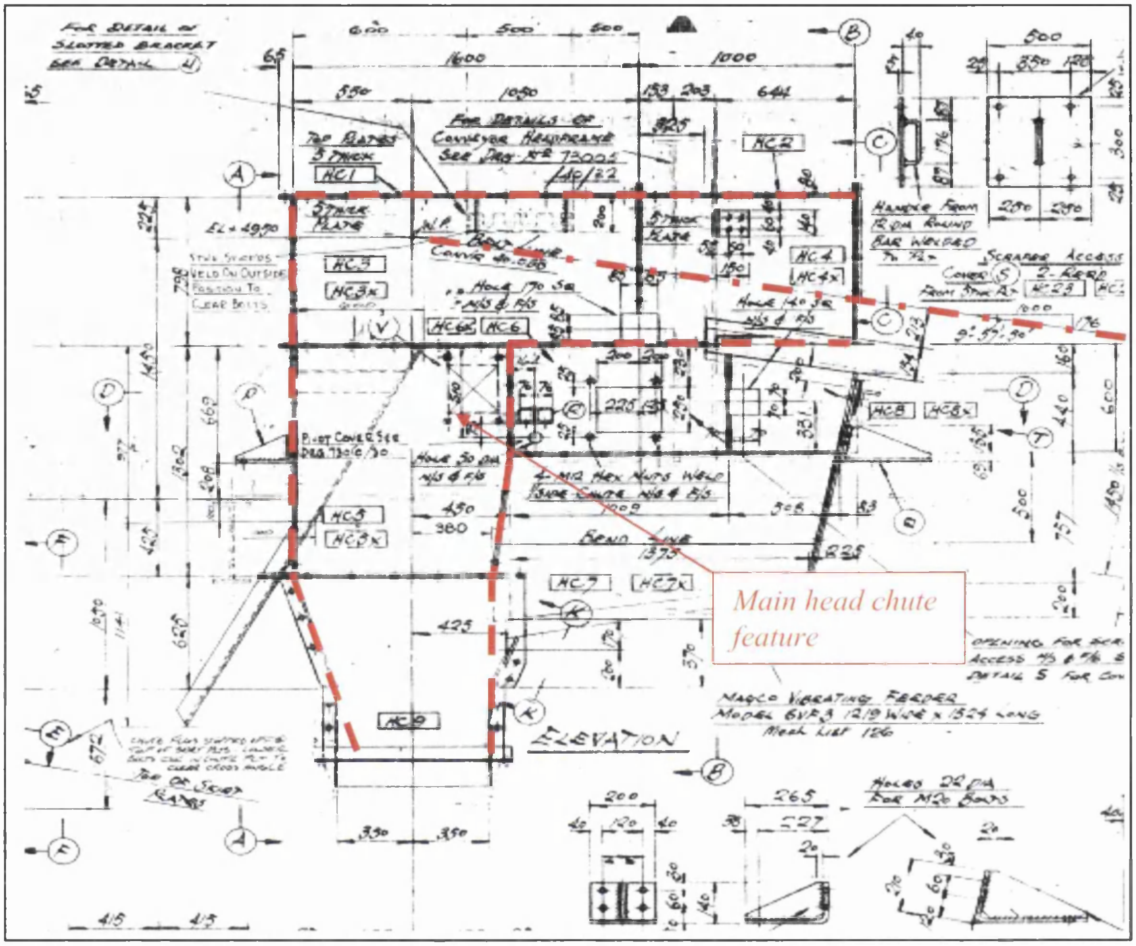

Figure 51: Design drawing front elevation of 1004 head chute showing a basic 2D domain.

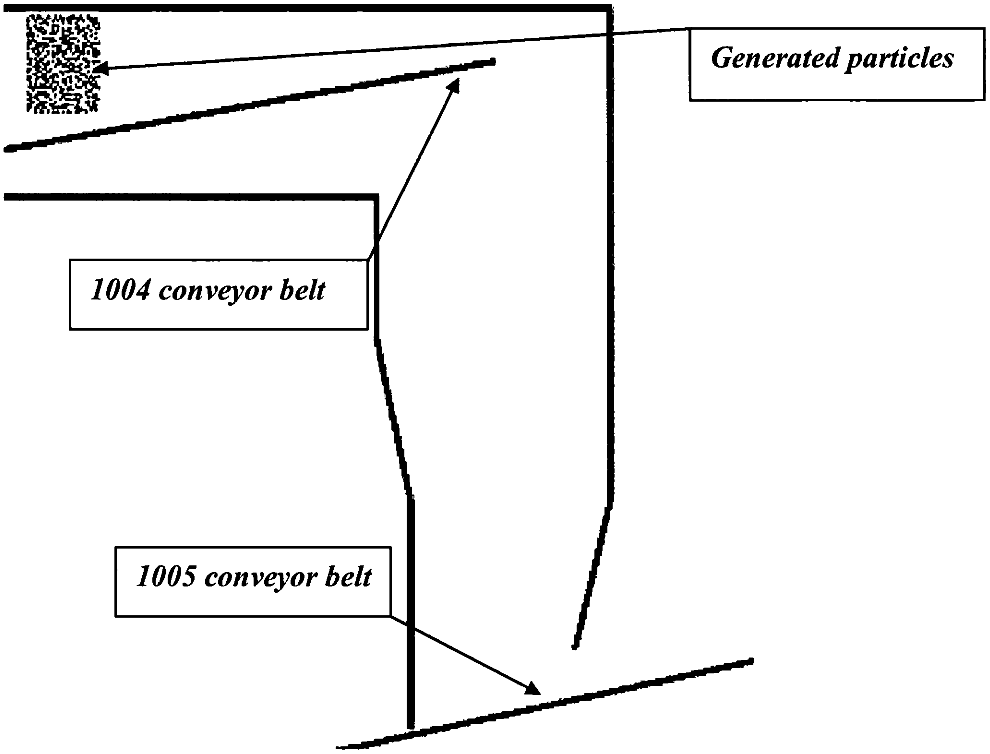

Figure 52: Full 2D 1004 simulation domain in mirror image as scaled per drawing in metres

The initial attempts at running simulation through the domain shown in *Figure 52* were unsuccessful and lead to repeated simulation breakdown. The simple requirement for this simulation was the transition of the generated particle along the 1004 moving wall/conveyor and through onto the 1005 conveyor.

3.3.1: Simulation Breakdown Explanation and Solution

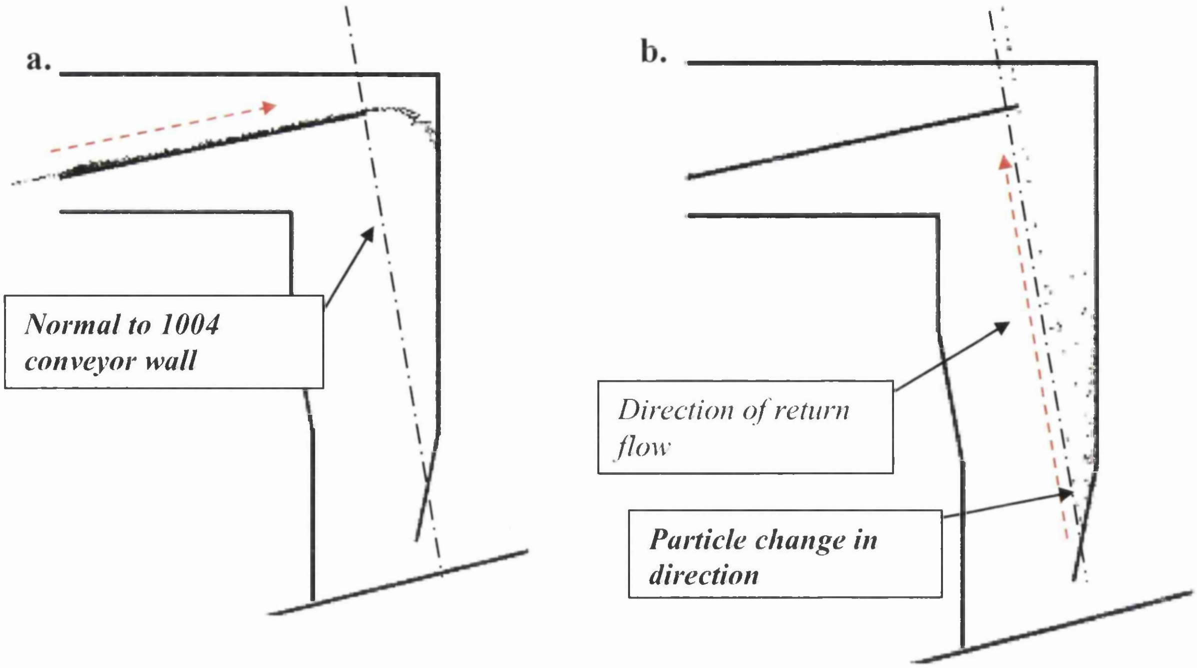

Figure 53: Simulated particle flow through 1004 head chute showing return flow along normal

In the case of the simulation slide shown in *Figure 53a* the particle motion follow an expected path along the moving conveyor wall and is distributed off the end into the main body of the domain.

As shown in *Figure 53b* the particles fall under gravity after a boundary impact and are returned at high velocity back along the normal to the wall in the positive Y direction.

Clearly the problem in this situation could be attributed to particles inability to pass under a boundary wall condition. Further data analysis revealed that this situation only arose with particles that had been related to a specific wall via the "Wall Search Algorithm" and then were unable to pass behind it. This lead to the conclusion that particles impacting with a boundary wall remain switched on to that wall and the rapid return was related to the reaction force calculation having a considerably high penetration depth.

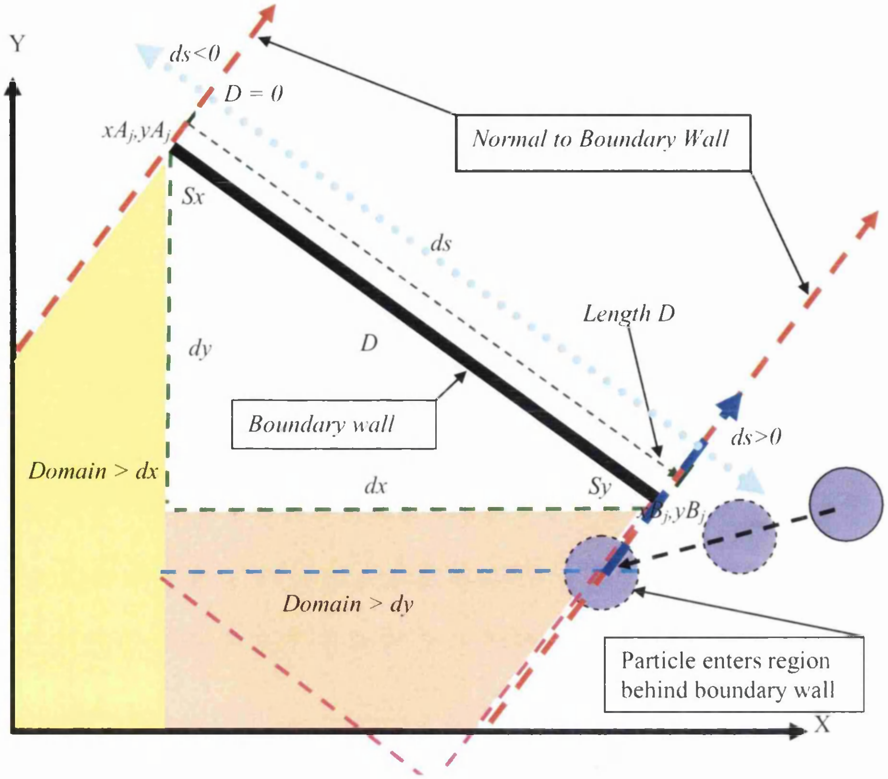

Figure 54: Particle entering restricted mathematical region

The key to addressing this problem was to ensure that as the particle departed from the wall domain, it stepped out of the wall search calculation. From there it would then be disassociated from the wall and be allowed to move through any point in the co-ordinate system.

3.3.2: Solution using the combination of two parametric equations of a line.

From the original wall search *'ds'* determines the point at which any particle is released from the end of the wall domain. However the program prefers not to allow particles behind a boundary wall when they are still related to it. The key to the solution was to ensure that as any particle passes the end co-ordinate of any wall that it automatically switches itself off. Furthermore, if any particle were to be deflected behind any wall domain it would recognise its position as being acceptable and carry on through the simulation.

3.3.2.1.: Solution in Parametric form

In this section a mathematical solution to the failure of particle motion behind a boundary wall is offered and the subsequent equations are related to the schematic image in *Figure 55*.

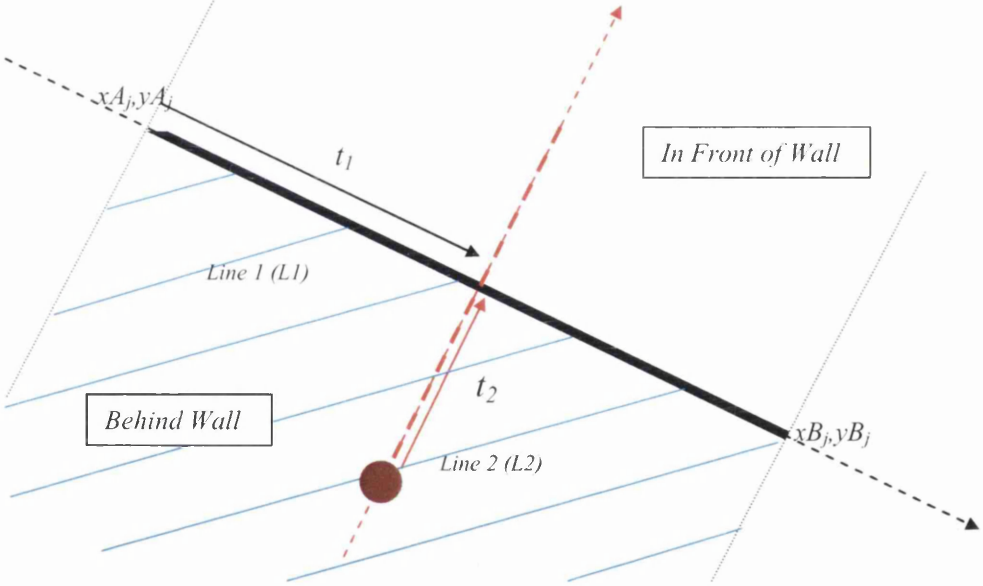

Figure 55: Shows a combination of two parametric equations of a line

From *Figure 55* the solution was produced as follows:

Parametric equation of line L_1:

1. $$L_1 = \left(\frac{xA(j)}{yA(j)}\right) + t_1\left[\left(\frac{xB(j)}{yB(j)}\right) - \left(\frac{xA(j)}{yA(j)}\right)\right]$$

Parametric equation of line L_2:

2. $$L_2 = \left(\frac{x(i)}{y(i)}\right) + t_2\left[\left(\frac{-yB(j)}{xB(j)}\right) - \left(\frac{-yA(j)}{xA(j)}\right)\right]$$

Combine 1&2 (i.e. $L_1 = L_2$)

3. $$\left(\frac{xA(j)}{yA(j)}\right) + t_1\left[\left(\frac{xB(j)}{yB(j)}\right) - \left(\frac{xA(j)}{yA(j)}\right)\right] = \left(\frac{x(i)}{y(i)}\right) + t_2\left[\left(\frac{-yB(j)}{xB(j)}\right) - \left(\frac{-yA(j)}{xA(j)}\right)\right]$$

4. $$\left(\frac{xA(j)}{yA(j)}\right) - \left(\frac{x(i)}{y(i)}\right) = t_2\left[\left(\frac{-yB(j)}{xB(j)}\right) - \left(\frac{-yA(j)}{xA(j)}\right)\right] - t_1\left[\left(\frac{xB(j)}{yB(j)}\right) - \left(\frac{xA(j)}{yA(j)}\right)\right]$$

Split 4 into two equations:

5. $(xA(j) - x(i)) = t_2(yB(j) - yA(j)) - t_1(xB(j) - xA(j))$

6. $(yA(j) - y(i)) = t_2(xB(j) - xA(j)) - t_1(yB(j) - yA(j))$

Find t_1 from 5

7. $t_1 = \left[\frac{t_2(yA(j) - yB(j)) - (xB(j) - x(i))}{(xB(j) - xA(j)} \right]$

Use 7 in 6

8.

$$\left(yA(j) - y(i)\right) = t_2(xB(j) - xA(j)) - \left[\frac{t_2(yA(j) - yB(j)) - (xB(j) - x(i))}{(xB(j) - xA(j)} \right](yB(j) - yA(j))$$

From 8 rearrange in terms of t_2

9.

$$\left(yA(j) - y(i)\right) = t_2(xB(j) - xA(j)) - \left[\frac{t_2(yA(j) - yB(j))(yB(j) - yA(j)) - (xB(j) - x(i))(yB(j) - yA(j))}{(xB(j) - xA(j)} \right]$$

10.

$$\left(yA(j) - y(i)\right) = t_2(xB(j) - xA(j)) - \left[\frac{t_2(2yA(j)yB(j) - yA^2(j) - yB^2(j)) - (xA(j)yB(j) - xA(j)yA(j) - x(i)yB(j) + yA(j)x(i))}{(xB(j) - xA(j)} \right]$$

From 10 Let:

11 & 12.

$$\alpha = (2yA(j)yB(j) - yA^2(j) - yB^2(j))$$
$$\beta = (xA(j)yB(j) - xA(j)yA(j) - x(i)yB(j) + yA(j)x(i))$$

Then:

13. $$(yA(j) - y(i))(xB(j) - xA(j) = t_2(xB(j) - xA(j))(xB(j) - xA(j) - t_2\alpha + \beta$$

And

14.

$$(yA(j)xB(j) - yA(j)xA(j) - y(i)xB(j) + y(i)xA) = t_2\left[(xB^2(j) - 2xA(j)xB(j) + xA^2(j)) - \alpha\right] + \beta$$

From 14 Let:

15 & 16.
$$\begin{aligned}\chi &= (yA(j)xB(j) - yA(j)xA(j) - y(i)xB(j) + y(i)xA)\\ \delta &= (xB^2(j) - 2xA(j)xB(j) + xA^2(j))\end{aligned}$$

Therefore:

17. $$t_2 = \frac{\chi - \beta}{\delta - \alpha}$$

Hence:

18.

$$t_2 = \frac{(yA(j)xB(j) - yA(j)xA(j) - y(i)xB(j) + y(i)xA) - (xA(j)yB(j) - xA(j)yA(j) - x(i)yB(j) + yA(j)x(i))}{(xB^2(j) - 2xA(j)xB(j) + xA^2(j)) - (2yA(j)yB(j) - yA^2(j) - yB^2(j))}$$

Finally deriving to:

The above equations applied to addressing the failure of particle motion behind a boundary wall were offered it terms of a parametric solution. The subsequent introduction into the model code resulted in a satisfactory outcome where particle motion behind a boundary wall was mathematically acceptable. The results of the coding additions are discussed in the next section.

3.3.2.2.: Results of program additions

In this section the application of the 2D parametric equations shown in *3.3.2.1* are discussed and the resulting simulation improvements are presented.

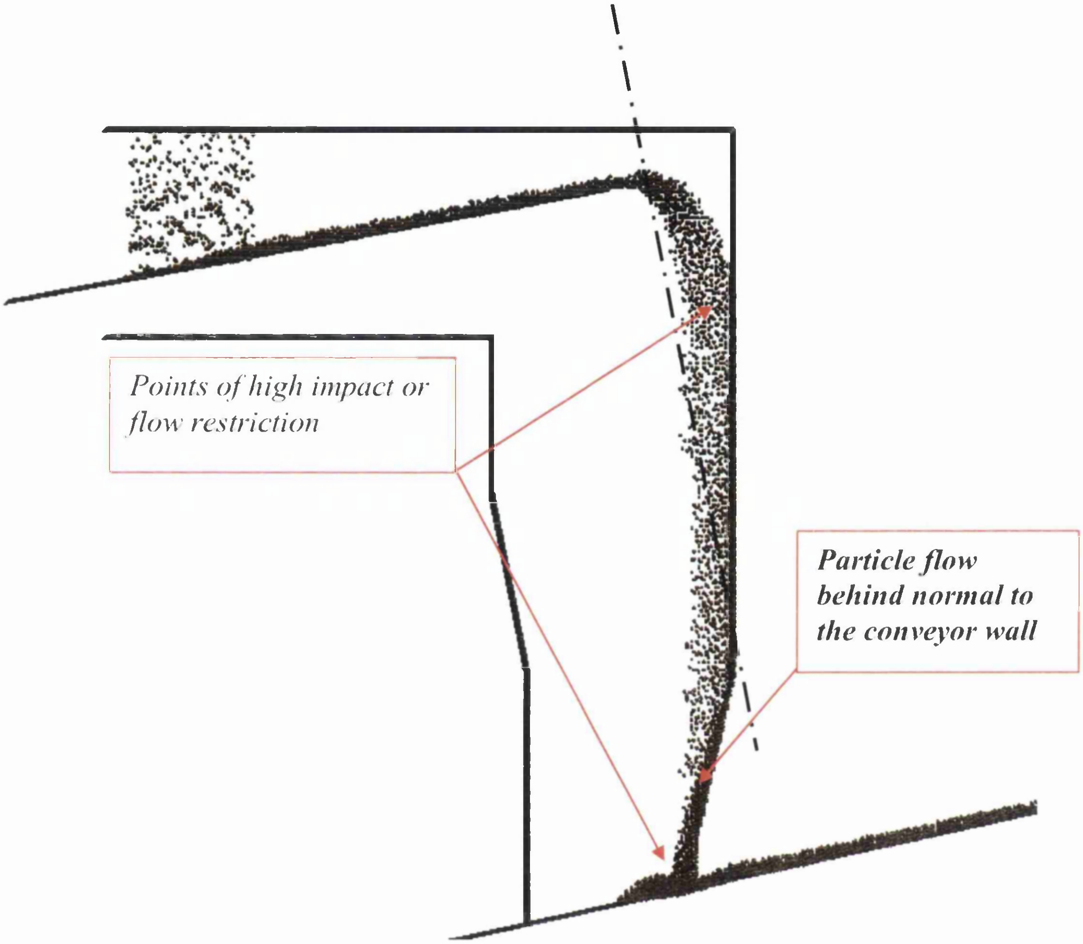

Figure 56: 2D Simulation of particulate flow through 1004 head chute

In applying the parametric equation into the code structure removed many of the breakdown anomalies and the 2D model of the particulate flow within 1004 head chute followed a predictable path. Further analysis of the simulation highlighted key areas of impact and flow restriction.

The type of raw material running through 1004 head chute is typical of the environment and as discussed for the segregation plate case is highly abrasive due to its silicate mineral form. Volumes in the region of 100k Tonnes/week are expected to travel though this system on a regular basis and this subjects the equipment to a punishing routine.

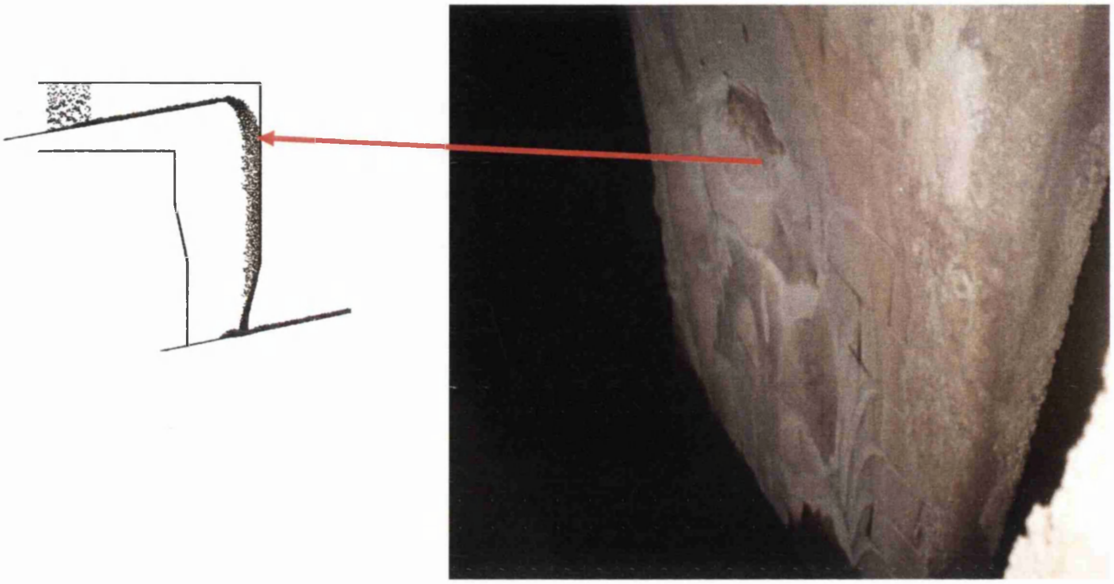

Figure 57: Localised wear in the alumina tiles at the back of 1004 head chute

As shown in *Figure 57*, wear of this nature results in raw material *"hold-up"* due to impact compression, particularly in the cases were moisture is involved. Build up of compacted material eventually collapses in an avalanche and can result in damage of running plant such as the conveyor belt systems. Ultimately an occurrence of this nature leads to plant repair and expensive loss of production during plant down time.

The main focus of the 2D modelling centred on key areas in the sinter plant material supply chain. However, the "Burdening Department" as a whole distributes raw material to a number of other business units within the works environment. The "Granulated Coal Injection Plant" (GCI) processes coal and as an alternative model a project was set up to study the material supply systems involved.

3.4: The Granulated Coal Injection Plant Investigation

The 'Granulated Coal Injection Plant' (GCI) is an important production unit within the integrated steelworks structure. Its sole function is to process imported coal products into a fine granule for blast furnace application. Applying coal in this fashion introduces a cheap hydrocarbon fuel, reducing the dependence on more expensive products.

Consistency of supply from the GCI plant to the blast furnaces is essential in maximising cost efficiency. One of the prominent concerns is directly related to material flow issues into, and around the plant. For this investigation the stating point of the supply line was considered and this was situated between the stock yards and the raw material silos.

With the fundamentals of the 2D DEM program working at a basic level, it was applied to a rudimentary simulation on a material flow problem that occurs as a matter of course in the 'Granulated Coal Injection Plant' (GCI Plant). The nature of the problem was associated with raw material falling onto a conveyor belt and escaping over the sides. Preliminary investigation into this problem seemed to highlighted strong links between material free-fall and the resulting overspill. As stated, the raw material used in the GCI plant is coal with a broad size distribution. This has a tendency to promote water retention, which generates a compact, abrasive and a highly compressive commodity. Material presented in this way and falling from height may block hoppers leading to material avalanche and also cause excessive wear in running plant.

The simulations that were produced in this investigation were only a general representation of material impact but were sufficient to draw conclusions about the problem at hand. As a result of this a solution to the problem was offered and it was derived by the following method:

3.4.1 Background

Coal imported through the deep-water harbour is laid down on the GCI stockyard floor. The coal is then lifted from the ground using machines and deposited into a series of mobile conveyor belt systems. The material is then raised to the end of the mobile conveyor belt and allowed to fall onto a static conveyor through a feed hopper. The static belt then draws the material away to a set of intermediated storage silos before being processed for blast furnace use.

3.4.2: 1401 Raw Material Feed Hopper:

The image shown in *Figure 58* is the conveyor-hopper-conveyor arrangement used in the GCI stockyard. Here one can see a mobile conveyor feeding a square hopper onto 1401 conveyor belt

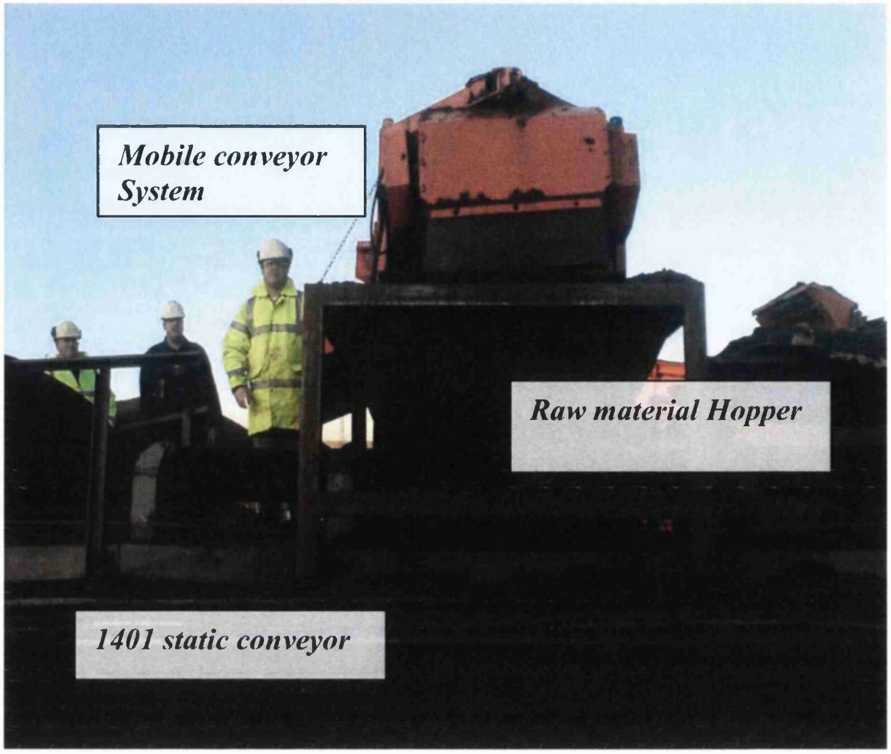

Figure 58: Side on view of a raw material feed hopper with 1401 conveyor running underneath.

3.4.3: Simulations of Particle Freefall and Impact:

To show the reaction of particle impact on a flat moving surface the DEM program was used to generate particles that fell onto one horizontally moving wall. The global damping constants used to create drag forces around the particles were removed and the particles were allowed to bounce vigorously. The idea behind this representation was to exaggerate the point of contact between the particle and the domain and to observe the impact results.

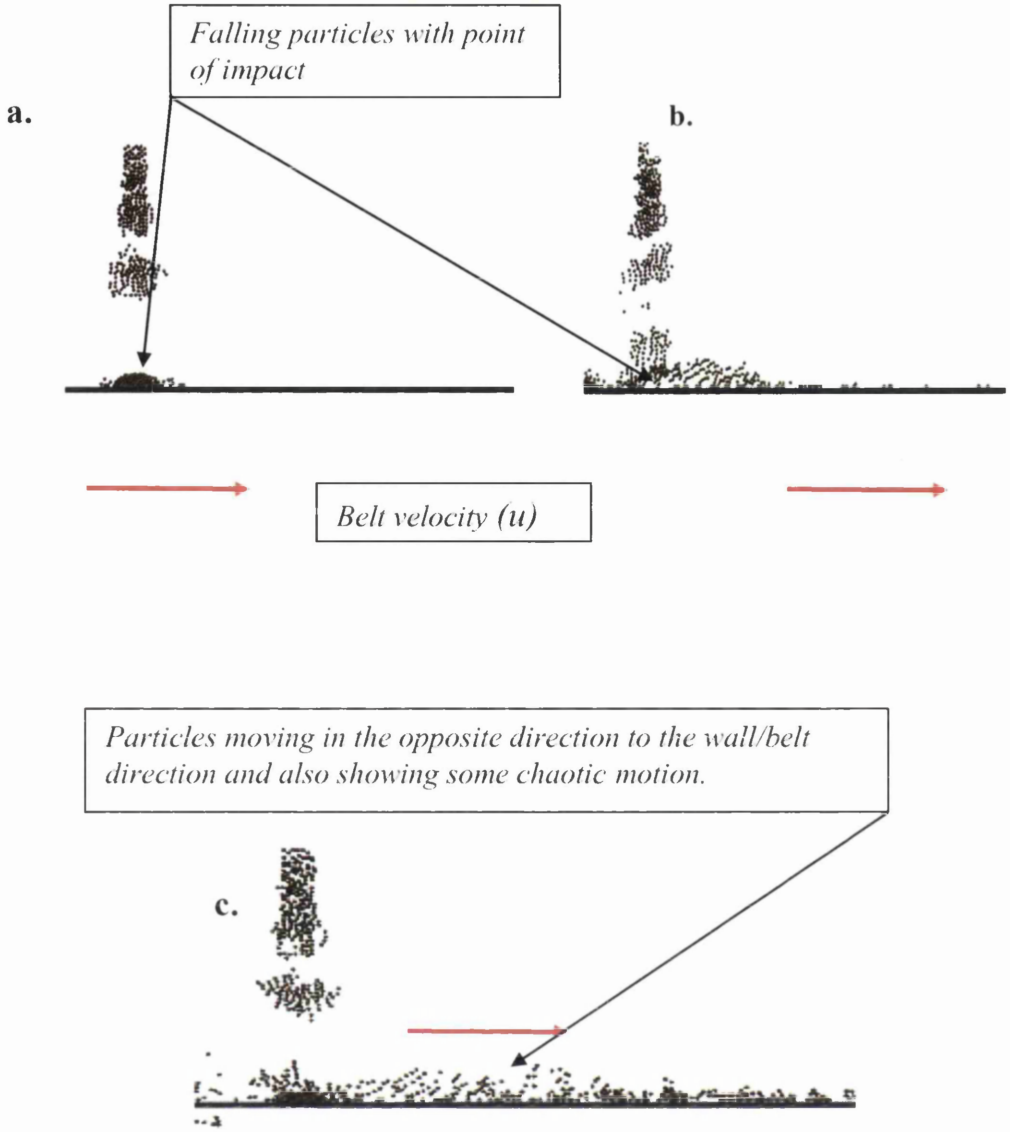

Figure 59 - a,b & c show a simulation of particles falling from height onto a wall.

The slides in *Figure 59* demonstrate a scenario where the particles make contact with the domain and react. The reactions in this case appeared to be forced back into the line of the falling material and spread in both directions away from the impact point. The perpendicular impact could be seen as a direct transfer of kinetic energy to the conveyor belt and could be attributed to the chaotic nature of the particle along the belt.

3.4.4: Smoothing the Material Flow:

Considering the basic observations in *Figure 59*, the material at impact with the boundary reacts in an uncontrolled manner. The chaotic nature of the particle motion could be directly related to the incident angle of the material at the contact point. To smooth the material transition the angle of incident had to be changed at the contact point. To achieve this, a curved wall was introduced between the conveyor wall and the particle flow:

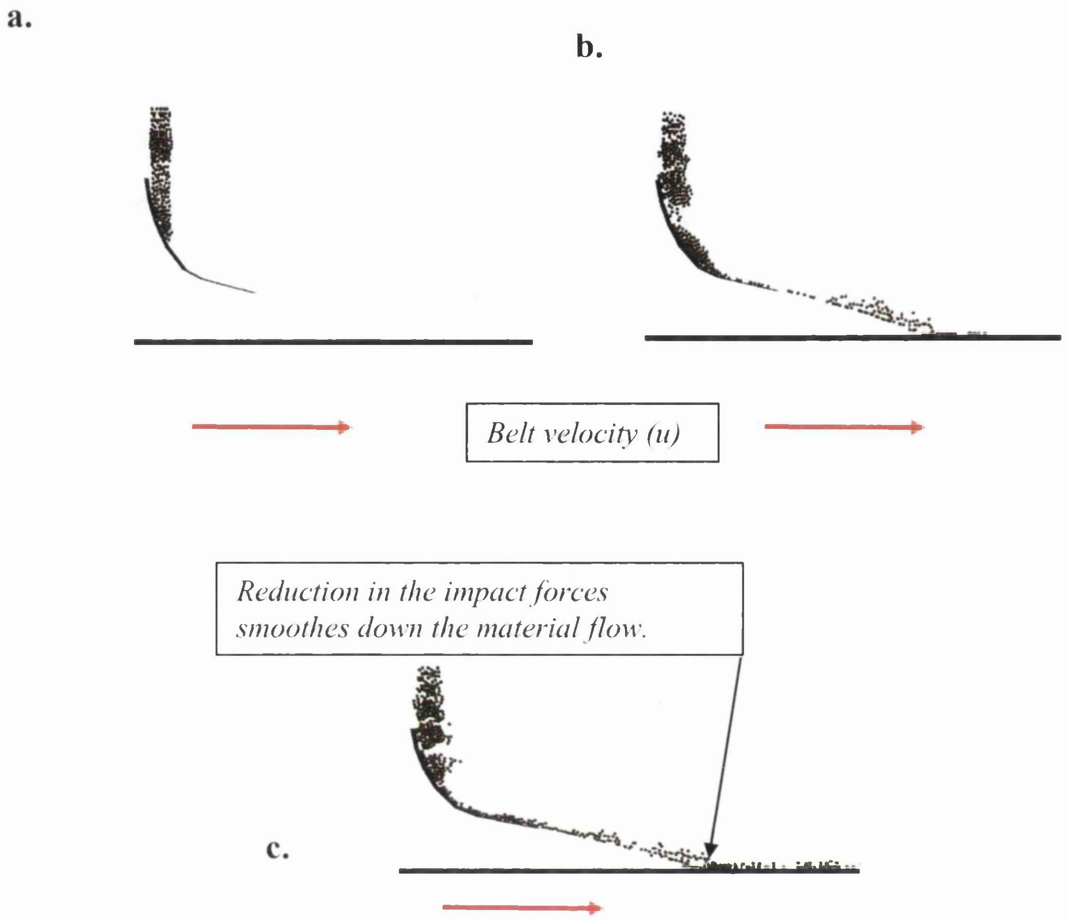

Figure 60 - Slides a,b & c show a curved plate to control the material

Figure 61 - : Angle of incidence A = 0

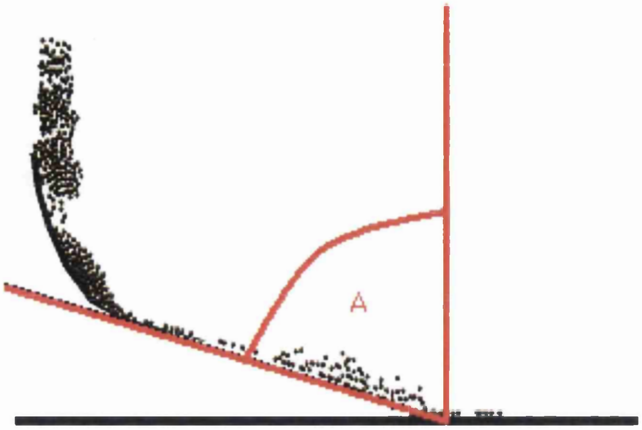

Figure 62 - Angle of incidence A increased

In *Figure 61* the angle of incidence *"A"* is at zero degrees, this encourages the material to bounce into the flow of the falling material and results in zero horizontal velocity at impact. In *Figure 62* the angle of incidence has been increased, this has two direct effects on the material impact:

1. Reduces the component of the vertical impact velocity
2. Increases the component of the horizontal impact velocity

These two factors have the effect of smoothing the material flow through the domain by controlling the directions of the impact velocities. Potentially the material could be transferred through the system more efficiently with higher velocity. This could significantly reduce belt wear, particularly if the horizontal velocity of the material matches that of the conveyor belt.

3.4.5: Chute Design for 1401 Feed Hopper

Using the simulation information the theoretical data was applied to a practical design for on plant implementation. The idea was to produce a prototype curved chute insert that would fit inside one of the existing 1401 feed hoppers to study/improve material transition. The approach adopted in designing the chute insert started with a geometrical study that involved first principles. This eventually moved on, and resulted in a Computer Aided Design (CAD) that verified the initial calculations.

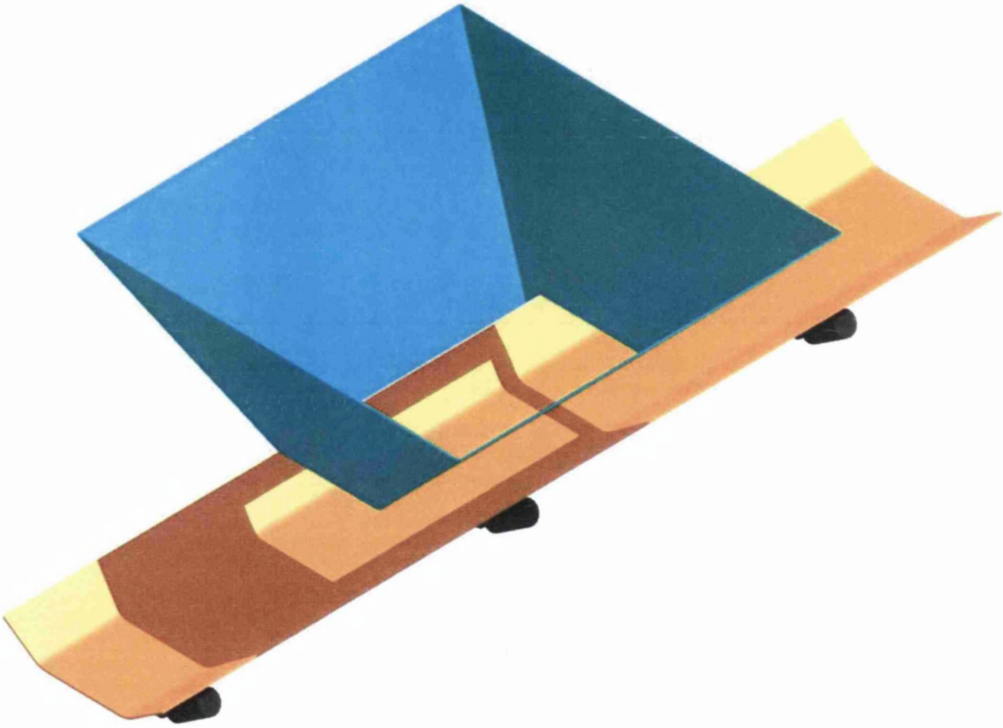

Figure 63 - 3D CAD image of 1401 feed hopper and conveyor

To utilise the 2D DEM program it was essential to use the dimensions generated in *Figure 63* and extract an accurate longitudinal cross-section.

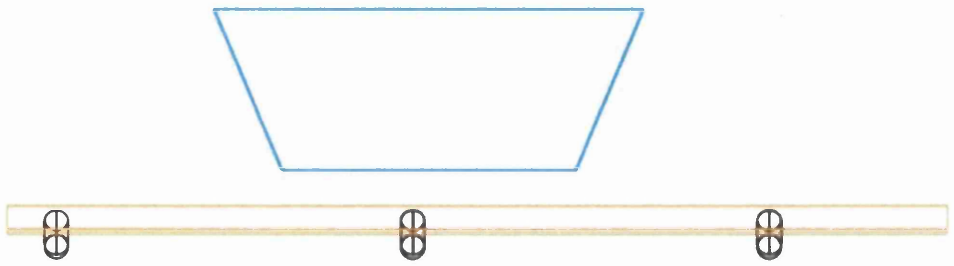

Figure 64 - Side elevation of 1401 hopper and conveyor.

Using the dimensions in *Figure 64* as a guide a theoretical curved chute insert was considered with a radius of curvature being set at 1.5m.

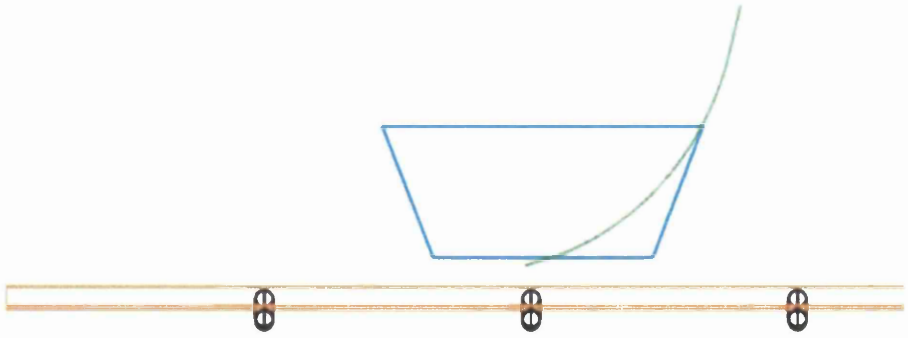

Figure 65 - Side elevation of 1401 hopper and conveyor with curved insert

In *Figure 65* the concept behind the curved insert is shown in the side elevation in 2D. To look at the design in real terms the hopper dimensions were again applied to a CAD program and the exact shape of the curved insert was generated.

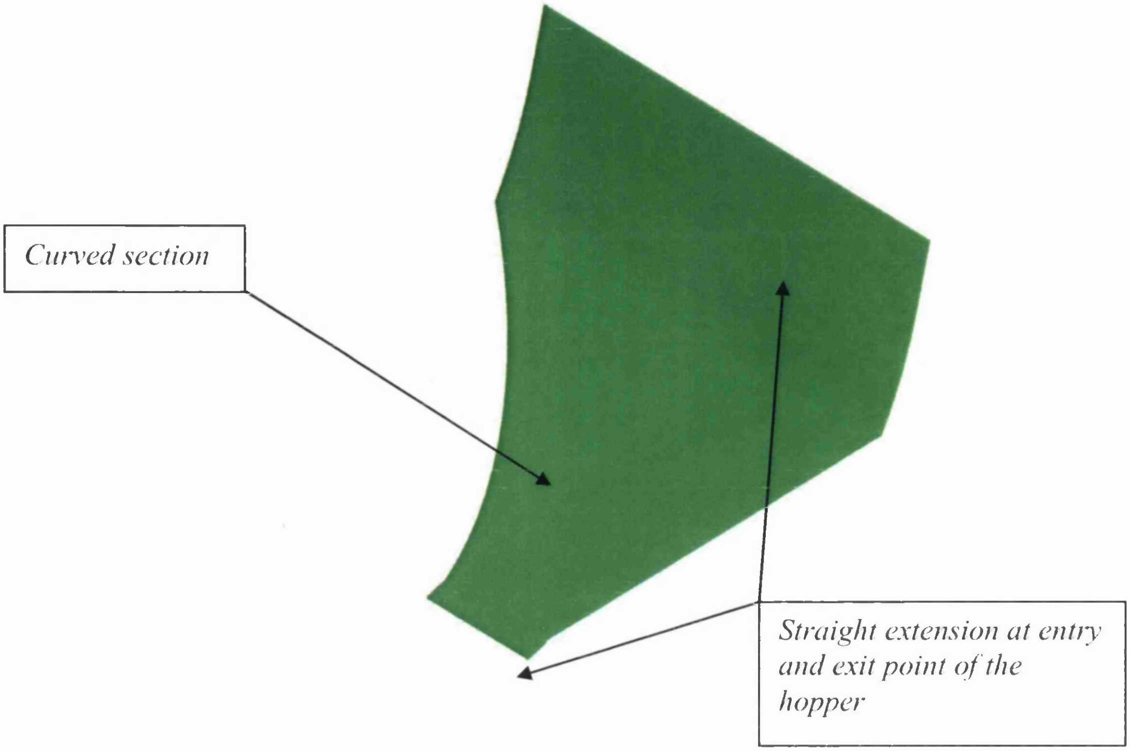

Figure 66 - 3D image of the curved plate.

The sides of the curved chute were shaped specifically to fit snugly against the 45° internal walls of the hopper and the bottom end of the curve was designed to slot through the discharge gap allowing a 0.61m exit hole.

The chute design was then introduced into the original hopper design (as shown in *Figure 63*) and the result was as follows:

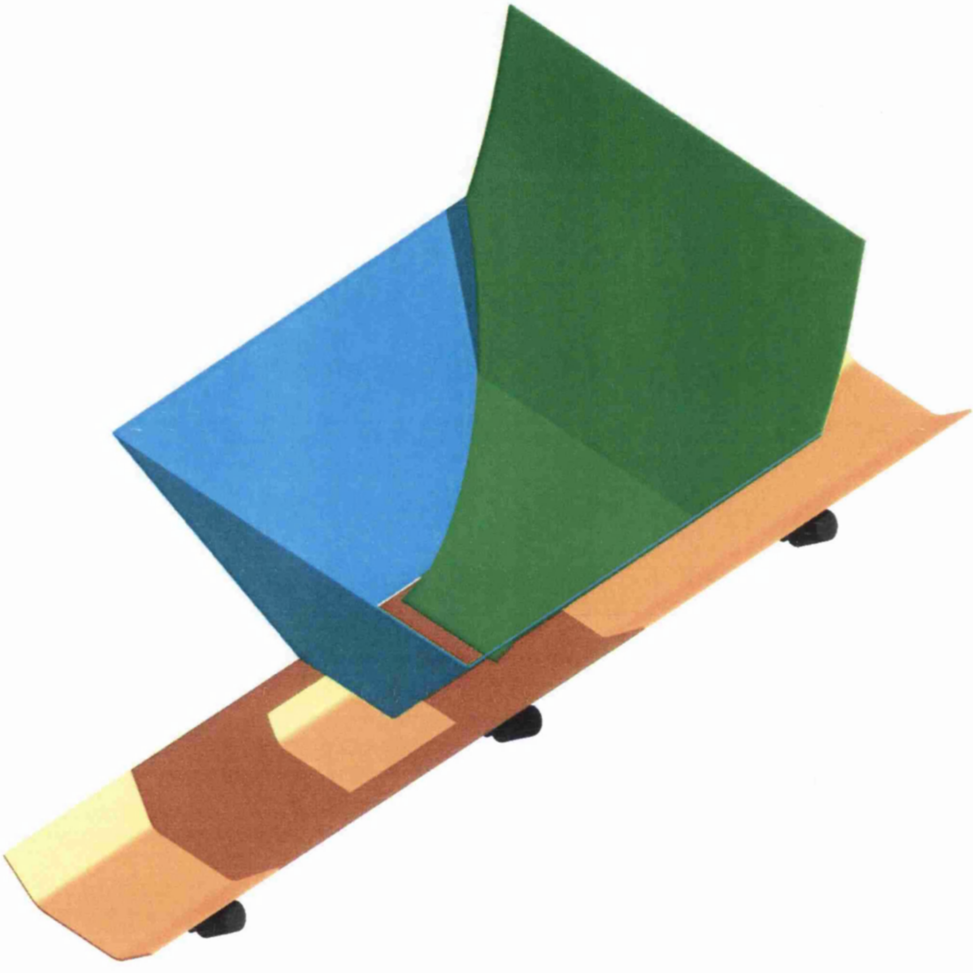

Figure 67 - 3D image of 1401 hopper with curved plate insert

3.4.6: Final Chute design drawing for production

In CAD the hopper was generated first and a curved plate was cut using the sides of the hopper. The resulting shape was then formulated into a final design drawing *(As shown in Figure 68)*.

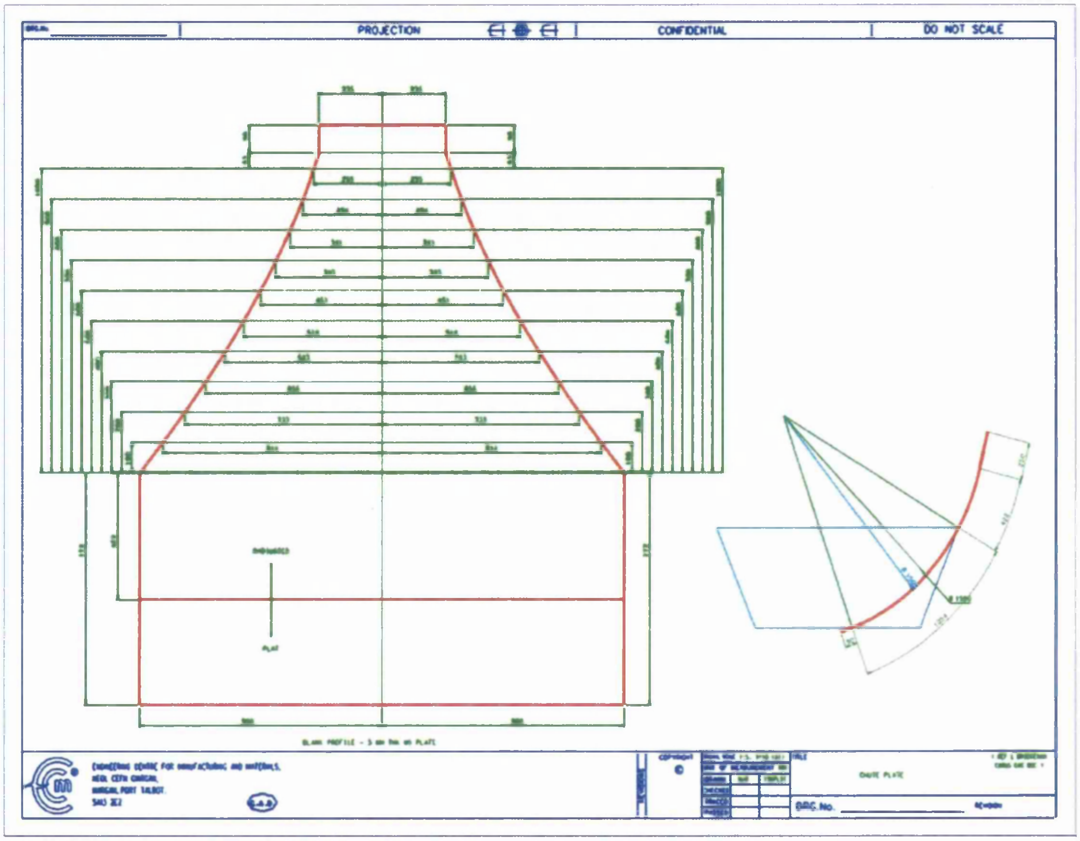

Figure 68 - Final design drawing

3.4.7: Project Experiment and Analysis

The chute insert was fabricated following the design drawing shown in *Figure 68* and the resulting product is shown in *Figure 69.* The chute insert was then fitted into the running plant system for experimental evaluation. The experimental procedure, results and basic observation with conclusions are presented in this sub-section.

Figure 69: The curved chute suspended from the gantry crane.

3.4.7.1: Experimental Procedure

To study the performance of the chute design prior to fitting was a difficult process. Scaling the design down was considered to be an option but the underlying issues would always manifest in mobile conveyor operation and replication of the continuous large mass material flow.

To address this, a full scale hopper was assigned for experimental development and subsequently the chute insert was fitted at a stockyard coal deposit.

Figure 70 - The 8mm curved chute fitted inside 1401 hopper

a. **b.**

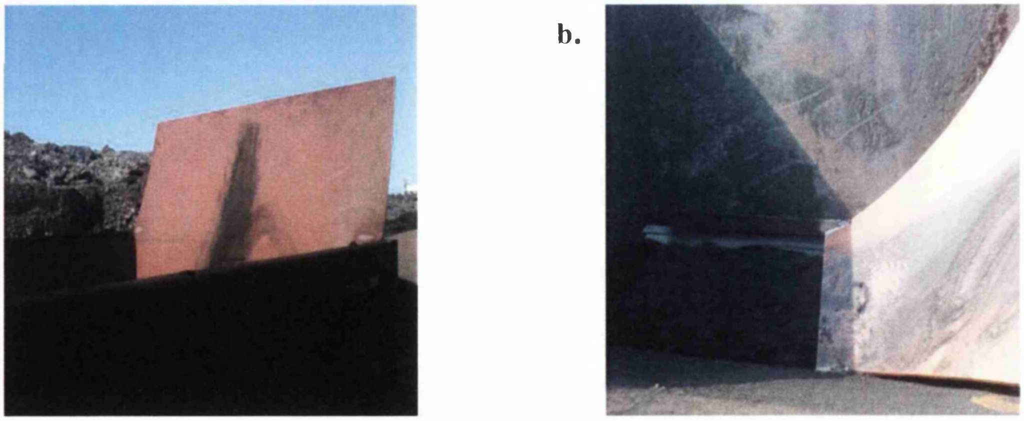

Figure 71 - The curved chute introduced into1401 hopper.

A mobile conveyor was then put into position and material was introduced at a rate of approximately 500 Tonnes/hr.

3.4.7.2: Experimental results

The mobile conveyor was positioned over the central line of the static conveyor and as close as possible to the top part of the chute. As the material started to flow into the hopper and interacted with the chute there was almost an immediate congestion at the exit point. This rapidly built up due to the feed rate of the material and the experiment was terminated.

3.4.7.3: Observations

The concept behind the introduction of curvature was to smooth the material transition and encourage movement in the direction of the conveyor belt, particularly under steady state conditions.

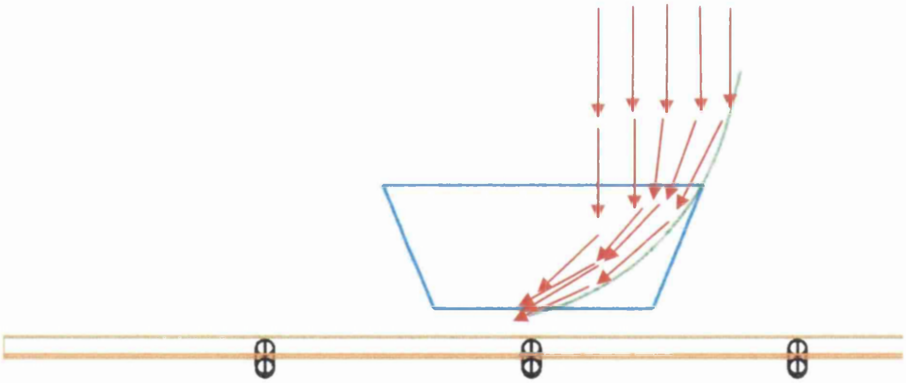

Figure 72 - Predicted steady state flow through the hopper

Steady state however, was never reached. This was essentially due to the orientation of the feed system, naivety in the chute design and a poor understanding of the dynamic nature of the material product.

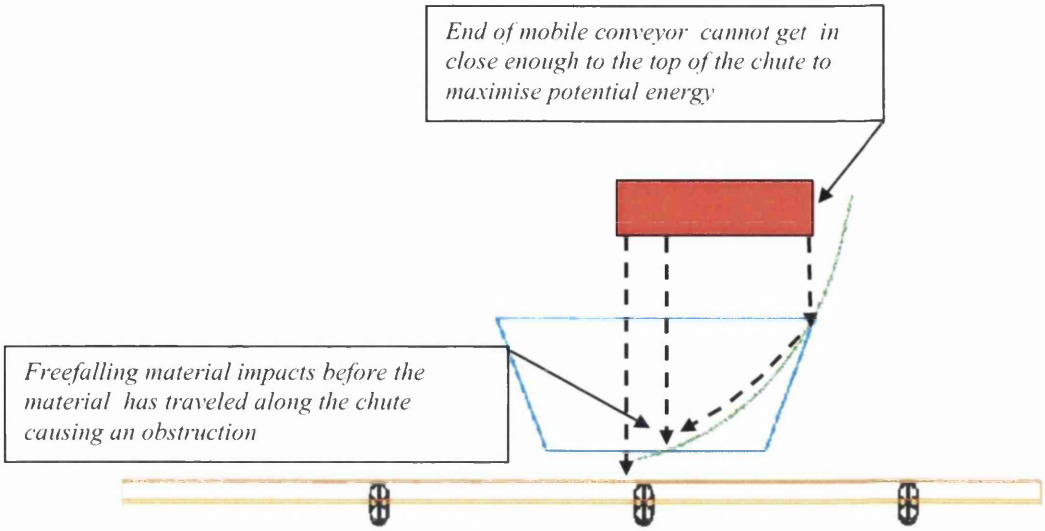

End of mobile conveyor cannot get in close enough to the top of the chute to maximise potential energy

Freefalling material impacts before the material has traveled along the chute causing an obstruction

Figure 73 - Shows the impacts leading to blockage.

In *Figure 73* the points of impact are highlighted in terms of 2D but the experiment also indicated issues outside this regime. From the original source of the obstruction material quickly accumulated and interfered with the intersection line of the hopper sides and the chute. The 45^0 angle of the sides rapidly became congested and the curvature in the chute was rendered useless.

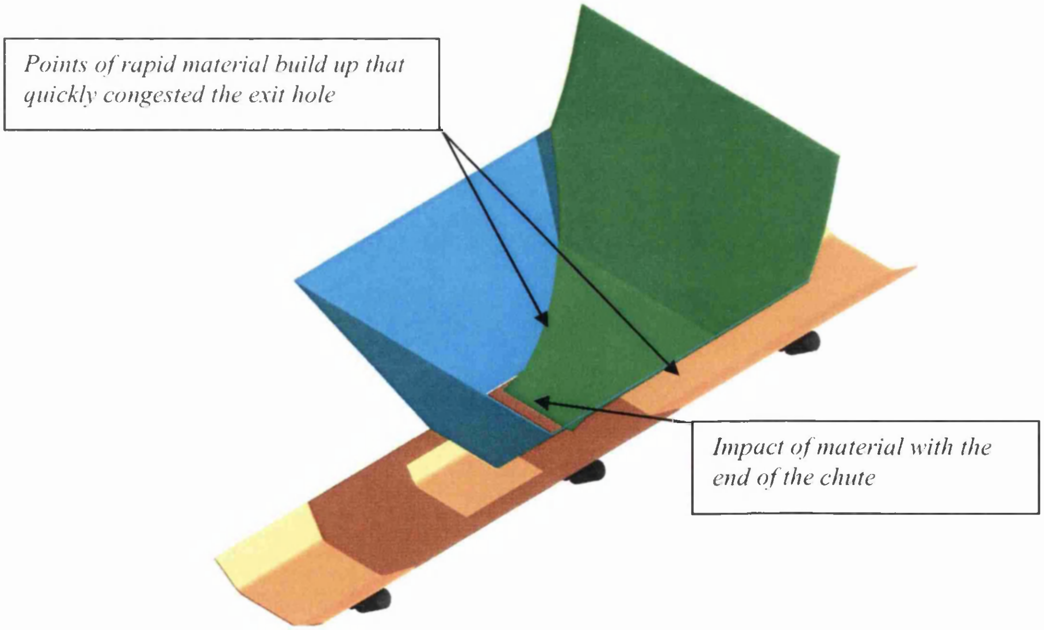

Points of rapid material build up that quickly congested the exit hole

Impact of material with the end of the chute

Figure 74 - Material impacts and points of rapid build up.

3.4.8: Conclusions to the project application

This was an excellent opportunity to apply computer simulation to real on plant situations. Materials in movement through this type of plant exhibit multi variable conditions and are essential in calibrating a computer program. For this hopper investigation the outcomes of the experiment were not as expected and flow was diminished rather that improved. However, the results obtained were extremely enlightening and focus was drawn to the inadequate performance of the 2D simulation model for this case. Essentially 2D calculations had failed to highlight the spread of material and the impact with the internal hopper walls. This perspective would only have been available with the involvement of the *z* coordinate direction, which required 3D analysis.

4: 3D DISCRETE ELEMENT METHOD SIMULATION

In considering the conclusions offered in *3.4.9* regarding the inadequacy of 2D simulation for this project application, this section deals with the development of the Fortran code into a full 3D working model. Discussed in this section are factors relating to:

Sphere-sphere interaction

- *Vector link between spheres*
- *Contact detection and prediction*
- *Damping and frictional force calculation*

Sphere-Boundary interaction

- *Sphere - plane distance calculations*
- *Particle boundary wall contact*
- *Damping and frictional at contact*
- *Parameterisation of a plane surface using Barycentric equations*

Implementation of stereolithography CAD files (STL) to aid boundary generation
Introduction of capillary interaction forces using the Laplace Equation
Energy transfer in a simulation domain and direct comparisons with practical situations

4.1: Introduction

The content of this section focuses on the conversion of the 2D DEM program into a usable 3D alternative. Essentially the particle- particle / particle-boundary interactions in 2D are calculated by summation of forces directed by trigonometric and geometric rules. The same movement in 3D had to be considered in terms of basic vector analysis, which presents little problem when particle-particle contacts are calculated. However things become subtle when having to consider particles encountering a constraint such as a static boundary wall or one that is in motion. In 2D these conditions are realised linearly and parameterised to determine start and end points. In 3D the boundary condition are produced using a combination of three sets of *x, y and z* coordinates to generate an infinite plane that becomes a mathematical barrier. In essence the normal forces in 3D are an extension of the 2D contact force model and integration equations of Walton and Braun[79].

To localise the plane the same coordinates were used to form individual triangles with the normal to each triangular face indicating the internal / external contact area. To limit the contact area to the contact surface, '*Barycentric Equations*' were used as a mathematical tool, along with plane intersection calculations to determine the direction of frictional forces between particle-particle and particle-boundary collisions.

4.2: 3D Inter-Particle Contact Simulation with Sphere – Sphere Interaction

One of the key issues arising from the conversion from 2D into a 3D coordinate system was the obvious change in the particulate shape. In 2D, calculations relay on infinitely thin circular discs to study interactions where as 3D case has the advantage of using spheres that are far more representative of real conditions.

The movement of spheres under gravity in a 3D space can be interpreted as a force vector field and collisions between the spheres determine additional direction changes following Newton's Laws of Motion. In a 2D/3D DEM simulation program the sphere-sphere interactions are monitored using mathematical search algorithms that indicate potential collision candidates, and mechanisms that switch on when contact has been made. In the 3D case particle tracking is achieved by a vector link between spherical centres whose length is set by an input variable called the search radius. If a sphere falls inside the search radius of another sphere then contact is deemed possible.

4.2.1: Vector Link between Spheres

Here contact interaction and detection is considered. The vectorial magnitudes between components are shown to be calculated using the spherical geometry of the element and the corresponding directional cosines.

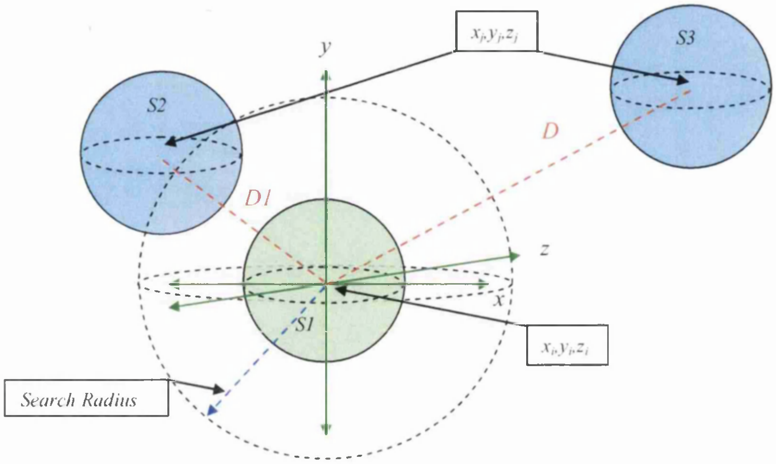

Figure 75: 3D particle-particle search algorithm process.

In the schematic shown in *Figure 75* the '*Find Neighbour*' search algorithm functions off sphere *S1* to determine likely contact candidates. Spheres *S2* and *S3* are moving a distance *D1* and *D* away respectively. The search radii of sphere *S1* and sphere *S2* have combined and at this point, *S3* takes no part in the impact calculations and can be ignored by *S1*. However *S1* now monitors the direction of *S2* at each time step until contact conditions are enforced.

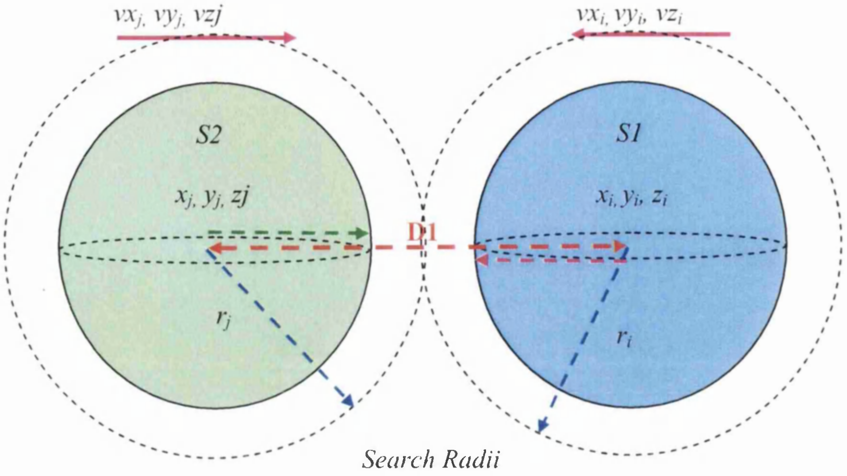

Figure 76 - Particle-particle search radius combination.

Figure 76 shows the point at which the find neighbour search links to an incoming sphere. The program identifies this point by using the sphere radii and the distance between the sphere centres '*D1*'.

In the 3D DEM program:

Vector magnitude between sphere centres

$$D1 = \sqrt{(x_j - x_i)^2 + (y_j - y_i)^2 + (z_j - z_i)^2} \qquad (4.1)$$

$$D_{rad} = D1 - r_i - r_j \qquad (4.2)$$

From *Equations (4.1)* and *(4.2):* If "D_{rad}" is less than the input search radius then the search radii are in contact. If the impact path is followed the boundaries of *S1* and *S2* will interact and a reaction force calculation is then activated. In the DEM program this is termed as the 'Neighbour Search'.

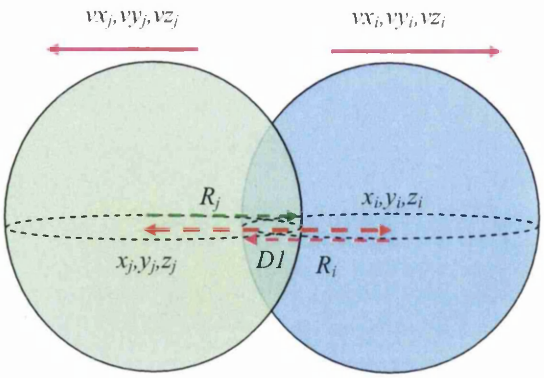

Figure 77 - Particle-particle radii boundary interaction.

In *Figure 77* the schematic diagram shows an overlap in the radial boundaries of the impacting spheres. Prior to the overlap the boundaries came into contact and imposed the following sets of conditions:

$$\delta = r_i + r_j - D1 \tag{4.3}$$

In the DEM program, if δ is greater then zero the spheres are in contact and the sums of the contact forces are calculated to produce a reaction between the spheres and a prediction of the motion after the spheres release. During this exchange the orientation of the combined spheres is determined by the vector linking their relative centres. This is achieved by using the length between the centres *(D1)* as a magnitude and '*Direction Cosines*' as a mechanism to find the vector direction.

4.2.2: Direction Cosines

To implement damping/frictional forces at contact interactions, direction cosines were used to associate appropriate vectors. The magnitude of the individual direction cosines in the x, y and z directions are summed to 1 and can be viewed as unit vectors ($\hat{n}$).

Unit vector: A vector of unit length.

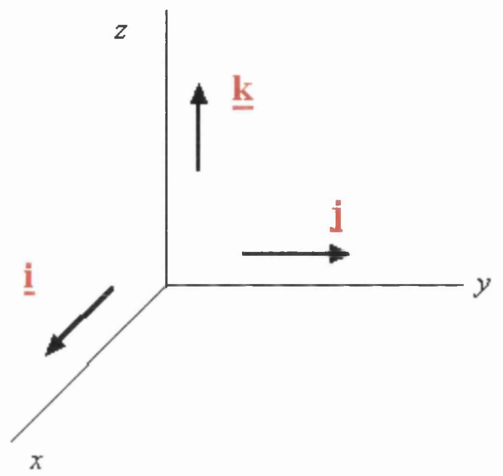

Figure 78 - unit vectors in i, j and k directions

In *Figure 78* the base vectors for a rectangular coordinate system are shown giving a set of three mutually orthogonal unit vectors

This is a Right handed system where coordinates represented by the base vectors follow the right-hand rule.

The Rectangular component of a Vector $\bar{A}$ projected along the x, y, and z directions are A_x, A_y, and A_z, respectively.

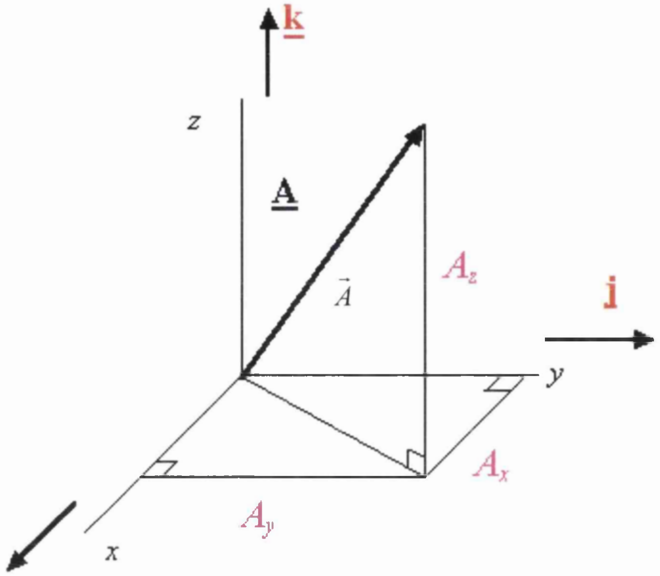

Figure 79 - Unit vectors in the *i*, *j* and *k* directions projected onto the x, y, z axis

$$\vec{A} = A_x i + A_y j + A_z k \tag{4.4}$$

Magnitude of a Vector:

$$|A| = \sqrt{A_x^2 + A_y^2 + A_z^2} \tag{4.5}$$

Direction Cosines: $Cos(\alpha), Cos(\beta), Cos(\gamma)$

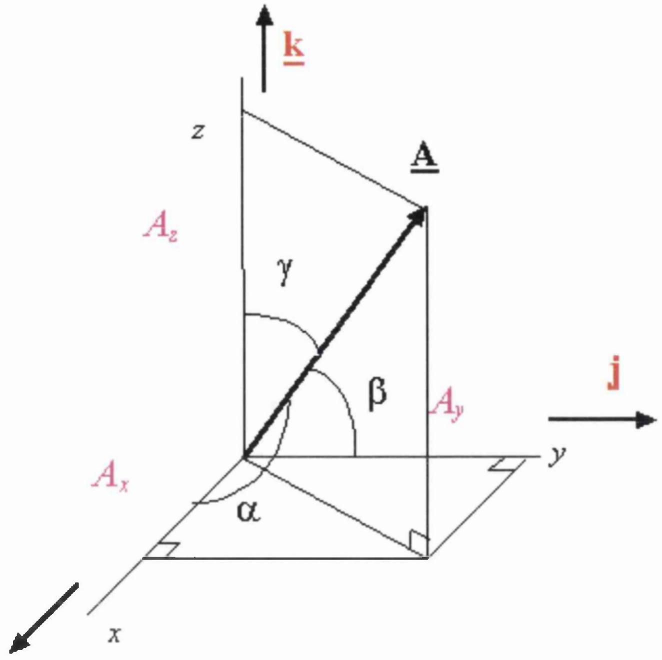

Figure 80 - 'Direction Cosine' angles α, β, γ

$$Cos(\alpha)=\frac{A_x}{|\bar{A}|}, Cos(\beta)=\frac{A_y}{|\bar{A}|}, Cos(\gamma)=\frac{A_z}{|\bar{A}|} \tag{4.6}$$

$$Cos^2(\alpha)+Cos^2(\beta)+Cos^2(\gamma) = 1 \tag{4.7}$$

The Application of "Direction Cosines" in this case was a fundamental mechanism for determining force summation and position relation of translating elements.

4.3: Summation of Forces between Spheres:

The mechanism that drives the simulation program is based on the summation of forces during contact. The principal forces involved in this program are damping and friction, and these are implemented in the following way:

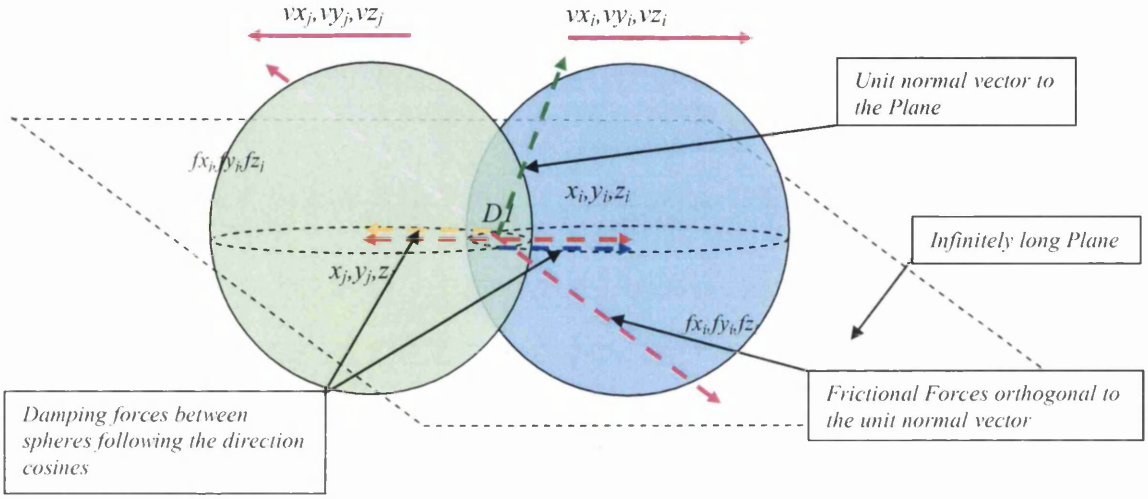

Figure 81 - Direction of the damping/frictional forces at contact.

4.3.1: Damping Forces between Spheres:

In *Figure 82* the direction of the damping force values are shown to be moving away from the contact point and along the direction cosine to the centre of the sphere. The force values are written in the program as; *fxi, fyi, fzi* and *fxc, fyc, fzc*, and are calculated as follows.

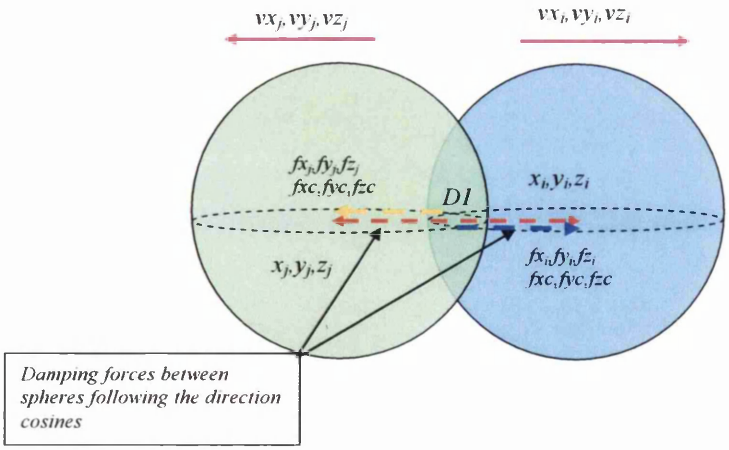

Figure 82 - Shows the direction of the damping force at contact.

$$fk = k\delta \tag{4.8}$$

Where:

k is the spring constant (Nm^{-1}), ($kg\ s^{-2}$)

δ is the surface overlap distance (m)

fk is the product of the above value s (N)

The structure in (4.8) follows that of 'Hooke's Law' where *k* is the spring constant between the spheres and δ is the distance of spherical overlap following the direction cosines *Cos(x), Cos(y), Cos(z)* where:

$$Cos(x) = \left(\frac{x_j - x_i}{D1}\right), Cos(y) = \left(\frac{y_j - y_i}{D1}\right), Cos(z) = \left(\frac{z_j - z_i}{D1}\right) \tag{4.9}$$

Therefore:

$$\begin{aligned} fxi &= -fkCos(x) \\ fyi &= -fkCos(y) \\ fzi &= -fkCos(z) \end{aligned} \tag{4.10}$$

The functions of the components in (4.9) were to generate a harmonic oscillation between the spheres along the vector linking their centers. To do this the components were required to be negative, producing a returning force away from the spherical centers. To achieve a damping effect between the spheres, the harmonic oscillation has to be acted upon to reduce to initial contact amplitude. The method utilized in this program is as follows:

Shows an extrapolated velocity component in the next time frame:

$$\begin{aligned} vnxr &= 1.5(vx_i - vx_j) - 0.5(vxo_i - vxo_j) \\ vnyr &= 1.5(vy_i - vy_j) - 0.5(vyo_i - vyo_j) \\ vnzr &= 1.5(vz_i - vz_j) - 0.5(vzo_i - vzo_j) \end{aligned} \tag{4.11}$$

And:

$$\dot{\delta} = vnxrCos(x) + vnyrCos(y) + vnzrCos(z) \tag{4.12}$$

Where: $\dot{\delta}$ is the derivative of the spherical overlap with respect to time.

Considering spheres of different sizes, the combined masses are dealt with by introducing an '*Effective Mass*' (meff) value, which is critical when dealing with sphere-sphere interaction.

$$meff = \frac{m_i m_j}{(m_i + m_j)} \qquad 4.13$$

Critical damping:

$$cdamp = 2\sqrt{km} \times cedamp \tag{4.14}$$

Where *cedamp* is a function of the coefficient of restitution (*ecoeff*) and is calculated by using an input variable of between 0 and 1 to give a physical interpretation of a rebound.

$$cedamp = \frac{\ln\left(\frac{1}{ecoeff}\right)}{\sqrt{\left(\pi^2 + \left[\ln\left(\frac{1}{ecoeff}\right)^2\right]\right)}} \tag{4.15}$$

Shows the component damping force:

$$\begin{aligned} fxc &= -cdamp \times \dot{\delta} \times Cos(x) \\ fyc &= -cdamp \times \dot{\delta} \times Cos(y) \\ fzc &= -cdamp \times \dot{\delta} \times Cos(z) \end{aligned} \tag{4.16}$$

4.3.2: Frictional Forces between spheres in contact:

In 2D the frictional force direction between discs was calculated using trigonometry and sign changes. However the conversion into 3D simulation required a totally different approach that relied on the application of planes and vectors. To associate a frictional force direction through any sphere-sphere orientation in 3D space the following method was used.

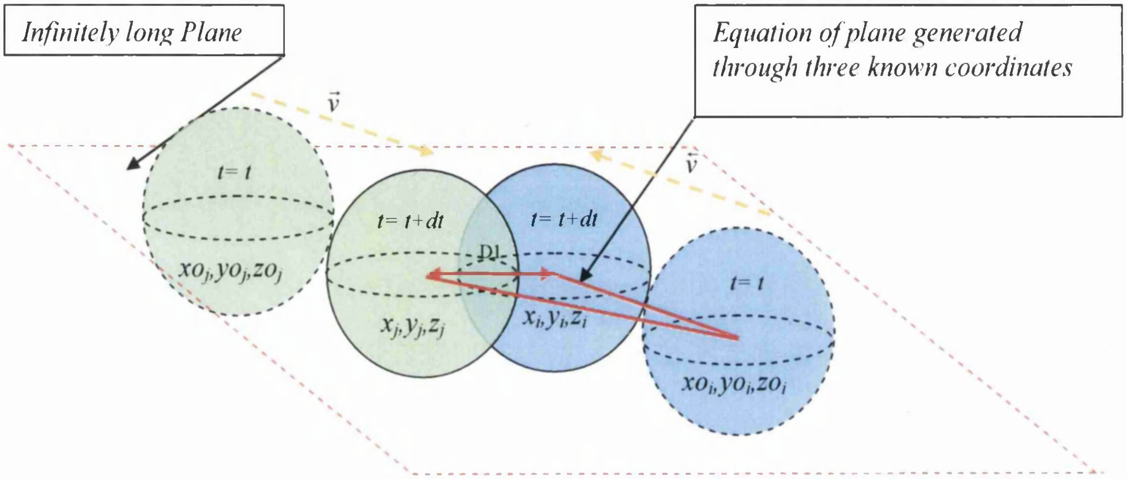

Figure 83 - Three known coordinates used to find a plane.

In *Figure 83* the schematic shows three sets of known coordinates required to generate an infinitely long plane in 3D space. The coordinates from the sphere centres (x_i, y_i, z_i) and (x_j, y_j, z_j) were used along with one of the coordinates from the previous time step (xo_i, yo_i, zo_i). These were then used to find a unit normal to the plane.

$$r \bullet \hat{n} = a \bullet \hat{n} \tag{4.17}$$

Vector Equation of a plane (4.17)

Where:

- r = *Cartesian coordinates x,y,z*
- $\hat{n}$ = *Unit normal vector to the plane*
- a = *Is the first set of 3D coordinates*

To find $\hat{n}$ use data from *Figure 83*:

$$\begin{pmatrix} xo_i - x_i \\ yo_i - y_i \\ zo_i - z_i \end{pmatrix} \times \begin{pmatrix} xo_i - x_j \\ yo_i - y_j \\ zo_i - z_j \end{pmatrix} \tag{4.18}$$

Therefore:

$$\begin{pmatrix} i & j & k \\ xo_i - x_i & yo_i - y_i & zo_i - z_i \\ xo_i - x_j & yo_i - y_j & zo_i - z_j \end{pmatrix} \tag{4.19}$$

So:

$$\begin{aligned} n_x &= ((yo_i - y_i)(zo_i - z_j)) - ((zo_i - z_i)(yo_i - y_j)) \\ n_y &= -((xo_i - x_i)(zo_i - z_j)) - ((zo_i - z_i)(xo_i - x_j)) \\ n_z &= ((xo_i - x_i)(yo_i - y_j)) - ((yo_i - y_i)(xo_i - x_j)) \end{aligned} \tag{4.20}$$

Unit normal component vectors (4.17):

$$\hat{n}_x = \frac{n_x}{\sqrt{(n_x^2 + n_y^2 + n_z^2)}}, \quad \hat{n}_y = \frac{n_y}{\sqrt{(n_x^2 + n_y^2 + n_z^2)}}, \quad \hat{n}_z = \frac{n_z}{\sqrt{(n_x^2 + n_y^2 + n_z^2)}} \tag{4.21}$$

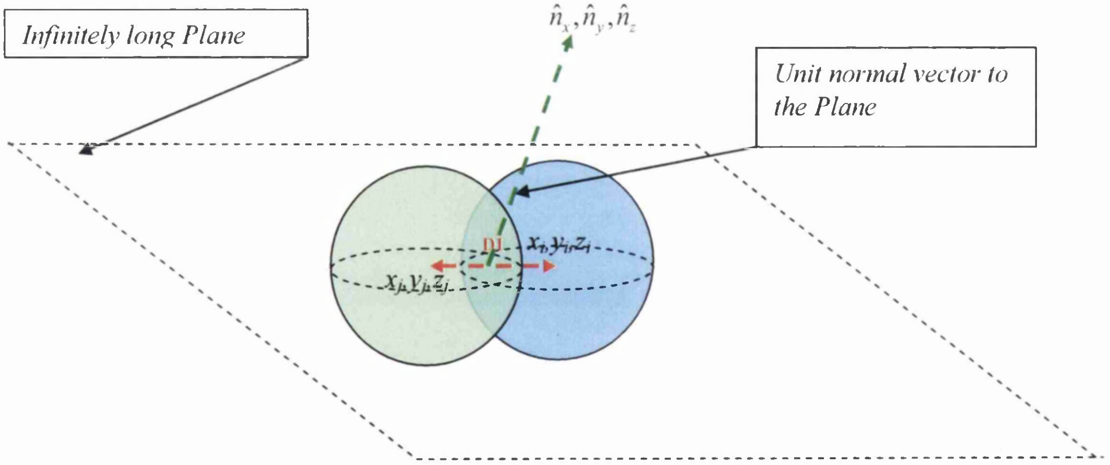

Figure 84 - Unit normal vector ($\hat{n}_x, \hat{n}_y, \hat{n}_z$) to the plane.

The schematic diagram shown in *Figure 84* shows the normal vector to the plane emanating from the vector line between the sphere centres. Taking the cross product of these two vectors produces an orthogonal unit vector which travels along the surface of the plane opposing the direction of the particle motion.

Cross product of sphere centres vector and normal to the plane (4.22):

$$\begin{pmatrix} i & j & k \\ \hat{n}_x & \hat{n}_y & \hat{n}_z \\ Cosx & Cosy & Cosz \end{pmatrix} \tag{4.22}$$

$$\begin{aligned} \vec{f}_x &= ((\hat{n}_y \times Cosz) - (\hat{n}_z \times Cosy)) \\ \vec{f}_y &= -((\hat{n}_x \times Cosz) - (\hat{n}_z \times Cosx)) \\ \vec{f}_z &= ((\hat{n}_x \times Cosy) - (\hat{n}_y \times Cosx)) \end{aligned} \tag{4.23}$$

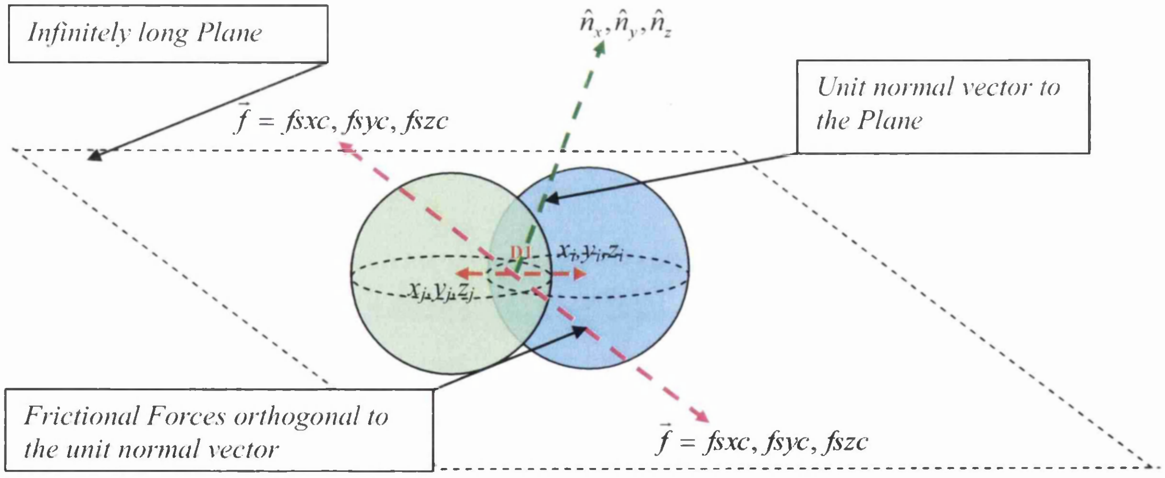

Figure 85 - Direction of the frictional force

The schematic diagram in *Figure 85* shows the direction of the frictional force at contact. The concept behind this method allows the friction to be calculated at any sphere-sphere orientation. The frictional force $\vec{f}$ travels in both directions due to the reactions of each sphere on the other which generates a resultant value.

$$\begin{aligned} fsxc &= fk \times \mu \times \vec{f}_x \\ fsyc &= fk \times \mu \times \vec{f}_y \\ fszc &= fk \times \mu \times \vec{f}_z \end{aligned} \tag{4.24}$$

Where: μ is a frictional input variable.

4.2.3: Addition of forces to simulate motion:

Using the calculated forces at each time step, Newton's third law of motion was applied to produce a resultant component force.

4.2.3.1: Translational motion:

$$\begin{aligned} fx_i &= fx_i + fxi + fxc + fsxc \\ fy_i &= fy_i + fyi + fyc + fsyc \\ fz_i &= fz_i + fzi + fzc + fszc \end{aligned} \tag{4.25}$$

$$\begin{aligned} fx_j &= fx_j - fxi - fxc - fsxc \\ fy_j &= fy_j - fyi - fyc - fsyc \\ fz_j &= fz_j - fzi - fzc - fszc \end{aligned} \tag{4.26}$$

The combined forces fx_i, fy_i, fz_i and fx_j. fy_j, fz_j were brought together to represent the summation of component forces:

Summation of Forces (4.27)

$$\sum \vec{F}_{ij} = (fx_i + fx_j) + (fy_i + fy_j) + (fz_i + fz_j) \tag{4.27}$$

Newton's second law:

$$\sum \vec{F}_{ij} = m_{ij}\frac{\Delta v_{ij}}{\Delta t} \tag{4.28}$$

Rearranging (4.28) in terms of Δv gives a small change in the velocity of the spheres in a time step:

$$\Delta v_x = \Delta t \sum \frac{\vec{F}_x}{m_x} \tag{4.29}$$

$$\Delta v_y = \Delta t \sum \frac{\vec{F}_y}{m_y} \tag{4.30}$$

$$\Delta v_z = \Delta t \sum \frac{\vec{F}_z}{m_z} \tag{4.31}$$

Therefore using "*Δv*":in a basic, speed = (dist/time) relationship:

$$\Delta s_{ij} = \Delta v_{ij} \cdot \Delta t \tag{4.32}$$

Where:

ds_{ij}, dv_{ij}, dt are small changes in distance, velocity and time respectively.

4.2.3.1: Rotational motion:

Rotational motion is apparent at the point of particle-particle/particle-boundary contact and is depending upon the tangential frictional force and the relative impact velocity. For explanation the particle-boundary contact is presented here:

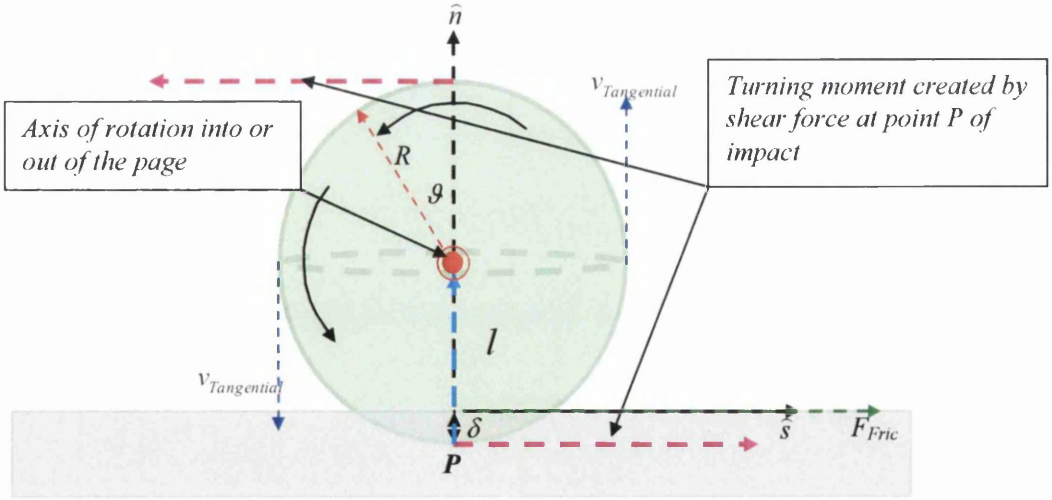

Figure 86: Particle boundary contact showing rotation due to relative motion and friction at contact

$$M = \left|\vec{F}_{Fric}\right|\left|\vec{l}\right| \tag{4.33}$$

$$\vec{M} = \vec{l} \times \vec{F}_{Fric} \tag{4.34}$$

Where M is the moment induced by force $\vec{F}_{Fric}$, and $\vec{l}$ is a vector between the force's point of effect and centre of mass.

The total torque can be acquired from

$$\Delta\omega_x = \frac{M_x}{I_x}\Delta t \tag{4.35}$$

$$\Delta\omega_y = \frac{M_y}{I_y}\Delta t \tag{4.36}$$

$$\Delta\omega_z = \frac{M_z}{I_z}\Delta t \tag{4.37}$$

Where $\Delta\omega x$, $\Delta\omega y$ and $\Delta\omega z$ are changes in rotation speed about each respective axis, I is the moment of inertia for the particle, and Δt is the length of the time step in the simulation for a spherical particle. "I" can be computed from (4.38).

$$I_{ij} = \frac{2}{5} m_{ij} r_{ij}^2 \tag{4.38}$$

Hence, applying ds to the resulting calculation output as the incremental small change in position at each time step dt.

Figure 87 - Simulation of particles falling into a global 3D domain

In the simulation slides shown in *Figure 87*, the particle were generated from a localised zone within the global domain bounded by *xmax,xmin ymax,ymin and zmax,zmin.* The interactions of the particles in contact result in the simulation of movement and the conservations of both energy and momentum.

For the current program consideration was given to typical particulate flow for simulation purposes. The dense media flow allows the application of spherical elements and with correct particle restraints limits the influence of rotational motion on the calculation. For a high mass flow rate with minimal voidage previous work has shown that in practical situations approximately 10% of the particles are able to rotate[80].

4.3: 3D Sphere – Boundary Interaction

The particle movement shown in *Figure 87* had no controlling factor and no local limiting conditions. This allowed the particles to spread randomly throughout the global domain driven by the particle-particle interactions. Although this was a step forwards in converting a 2D program intro a 3D program, it was recognised that to achieve realistic simulations the implementation of a boundary condition to limit/control velocity and direction was a critical success factor. In 2D (as in the sphere-sphere case) the interactions between a disc and a boundary were calculated using trigonometry and geometry with the predicted impact distance deriving from the subtractions of the opposite wall of two right angle triangle.

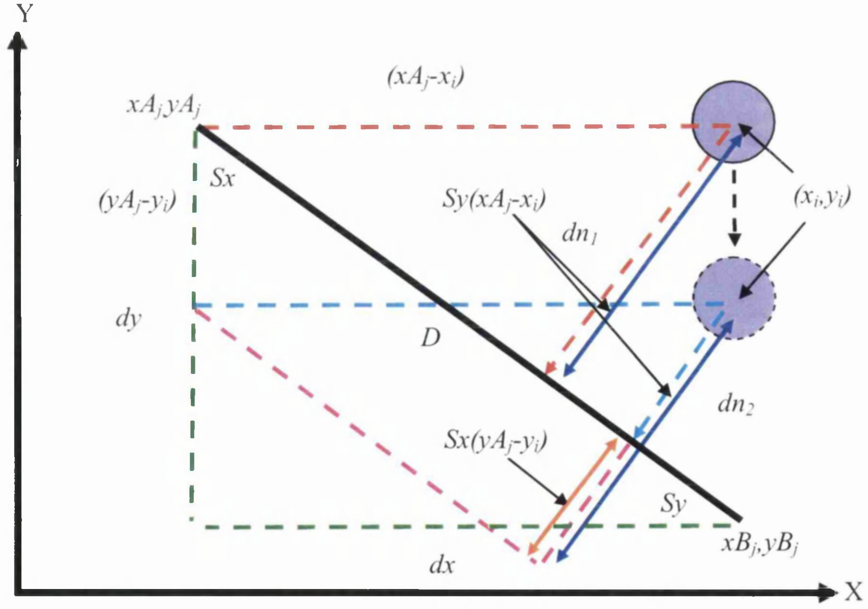

Figure 88 - Shows the trigonometry used to calculate distances $dn1$ and $dn2$

In the schematic diagram shown in *Figure 88* the *dn* values determine the distance to the boundary wall and they follow a direction that was perpendicular to the boundary itself. This method was loosely transferred to the 3D boundary search however; the perpendicular direction was replaced by a 'Normal' to a boundary surface and the distance was found by calculating the vector magnitude from a point in space to a plane.

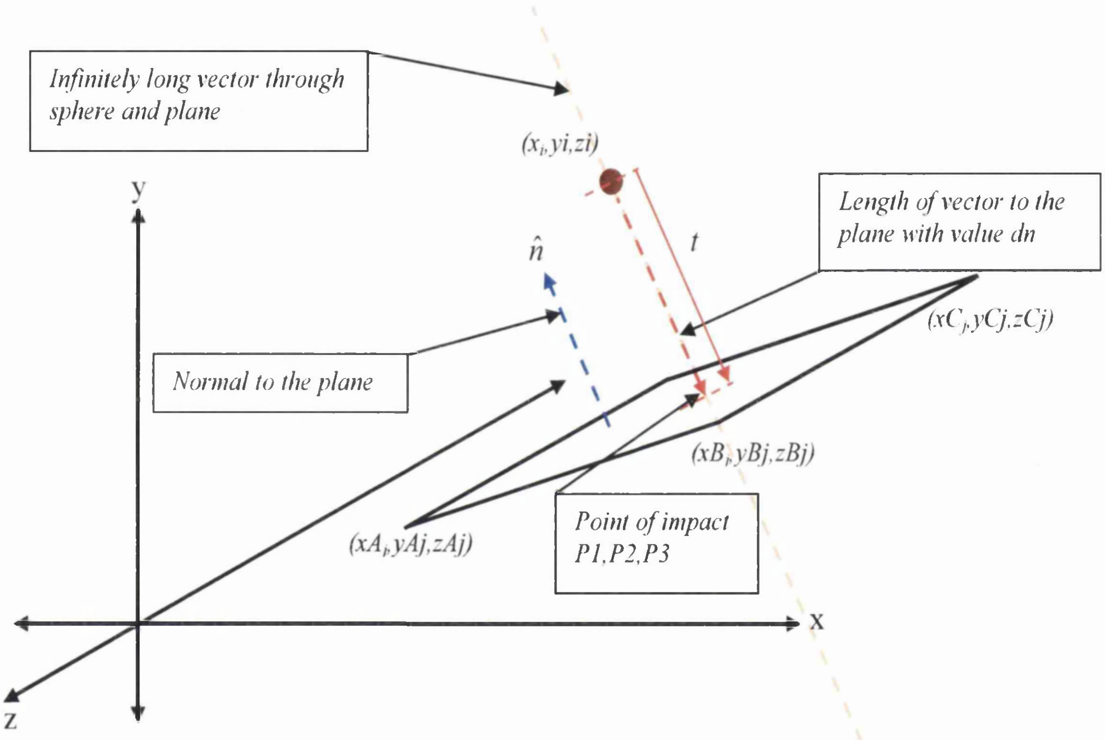

Figure 89 - Vector magnitude used to calculate distances *dn*

The diagram in *Figure 89* shows a particle in a 3D coordinate system at a position x_i, y_i, z_i at a distance *dn* above a plane generated using three coordinates (xA_j,yA_j,zA_j) (xB_j,yB_j,zB_j) *and* (xC_j,yC_j,zC_j). To calculate the perpendicular distance from the particle to the plane, the first step is to find the normal to the plane followed by a calculation to assess the predicted impact point *(P1, P2, P3)*.

4.3.1: Sphere – Plane distance calculation

Using:

Vector Equation of a plane:

$$r \bullet \hat{n} = a \bullet \hat{n} \tag{4.39}$$

Where:

- ➢ r = Cartesian coordinates x,y,z
- ➢ $\hat{n}$ = Unit normal vector to the plane
- ➢ a = Is the first set of 3D coordinates

To find $\hat{n}$ normal to the Plane *(xA* $(xA_j,yA_j,zA_j),(xB_j,yB_j,zB_j),(xC_j,yC_j,zC_j)$ *Figure 89*:

$$\begin{pmatrix} xA_j - xB_j \\ yA_j - yB_j \\ yA_j - yB_j \end{pmatrix} \times \begin{pmatrix} xA_j - xC_j \\ yA_j - yC_j \\ zA_j - zC_j \end{pmatrix} \tag{4.40}$$

Therefore:

$$\begin{pmatrix} i & j & k \\ xA_j - xB_j & yA_j - yB_j & zA_j - zB_j \\ xA_j - xC_j & yA_j - yC_j & zA_j - zC_j \end{pmatrix} \tag{4.41}$$

So:

$$\begin{aligned} n_x &= ((yA_j - yB_j)(zA_j - zC_j)) - ((zA_j - zB_j)(yA_j - yC_j)) \\ n_y &= -((xA_j - xB_j)(zA_j - zC_j)) - ((zA_j - zB_j)(xA_j - xC_j)) \\ n_z &= ((xA_j - xB_j)(yA_j - yC_j)) - ((yA_j - yB_j)(xA_j - xC_j)) \end{aligned} \tag{4.42}$$

Unit normal component vectors:

$$\hat{n}_x = \frac{n_x}{\sqrt{\left(n_x^2 + n_y^2 + n_z^2\right)}}, \quad \hat{n}_y = \frac{n_y}{\sqrt{\left(n_x^2 + n_y^2 + n_z^2\right)}}, \quad \hat{n}_z = \frac{n_z}{\sqrt{\left(n_x^2 + n_y^2 + n_z^2\right)}} \tag{4.43}$$

Using the calculated normal values and the position of the sphere within the coordinate system a vector equation of a line through the sphere into the plane could be found.

Vector equation of a line through sphere and plane:

$$r_1 = \begin{pmatrix} x_i \\ y_i \\ z_i \end{pmatrix} + t \begin{pmatrix} \hat{n}_x \\ \hat{n}_y \\ \hat{n}_z \end{pmatrix} \tag{4.44}$$

Where:

- t acts as the parameterisation of the infinitely long vector line that intersects with the plane and is a length at each time step <u>not</u> the length to the plane.

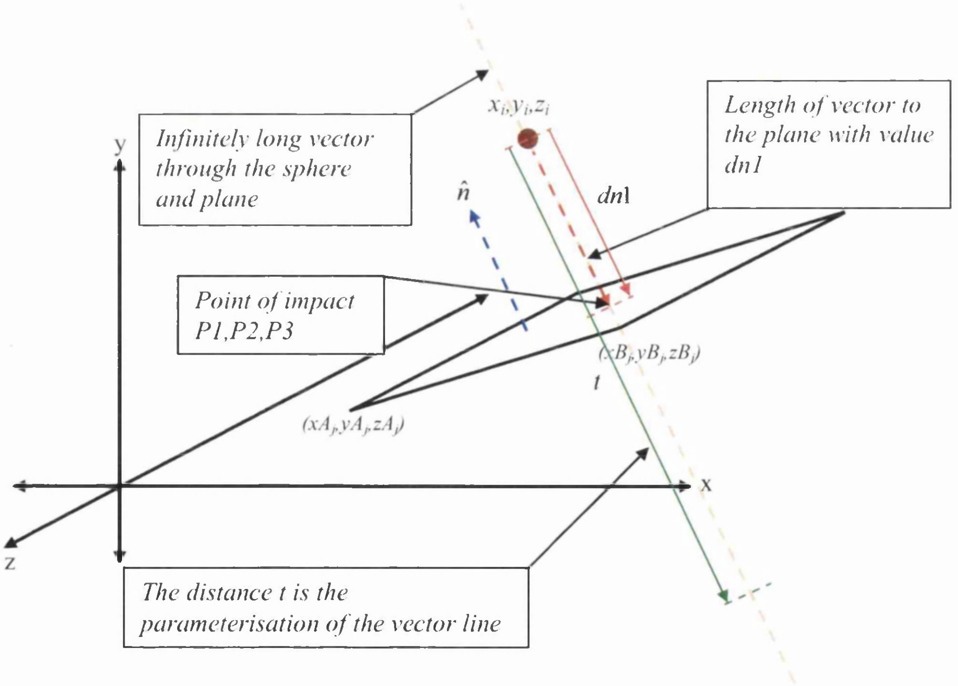

Figure 90 – Parameterisation of vector through sphere and plane

To determine the length t one needs to find the scalar product: $a \bullet n$

Where:

$$a = \begin{pmatrix} xA_j \\ yA_j \\ zA_j \end{pmatrix}, and\_\hat{n} = \begin{pmatrix} \hat{n}_x \\ \hat{n}_y \\ \hat{n}_z \end{pmatrix} \tag{4.45}$$

Therefore:

$$a \bullet \hat{n} = (xA_j \hat{n}_x) + (yA_j \hat{n}_y) + (zA_j \hat{n}_z) \tag{4.46}$$

So:

Length of parametric factor t:'

$$t = \frac{(xA_j \hat{n}_x + yA_j \hat{n}_y + zA_j \hat{n}_z) - (x_i \hat{n}_x + y_i \hat{n}_y + z_i \hat{n}_z)}{(\hat{n}_x^2 + \hat{n}_y^2 + \hat{n}_z^2)} \tag{4.47}$$

Using the value found for *t* the distance from the sphere to the plane can be calculated. From *Figure 90* the distance to the plane is denoted as dn1, and this section of the vector provides the impact point with the plane at P_x, P_y, P_z.

Distance of sphere to the plane:

$$dn1 = \sqrt{\left((t \cdot \hat{n}_x)^2 + (t \cdot \hat{n}_y)^2 + (t \cdot \hat{n}_z)^2\right)} \tag{4.48}$$

And the impact point ***P*** of the vector with the plane is found by:

$$\begin{aligned} P_x &= x_i + (t \cdot \hat{n}_x) \\ P_y &= y_i + (t \cdot \hat{n}_y) \\ P_z &= z_i + (t \cdot \hat{n}_z) \end{aligned} \tag{4.49}$$

Due to the fact that the perpendicular distance dn1 and corresponding impact coordinates on the plane were known, the change in the dn1 value at each time step was used to assess whether a sphere was approaching the plane or moving away from it. Essentially if a sphere moves towards a plane the dn1 value decreases, and at the point when dn1 was less than zero the plane surface was in contact. When this condition was realised it was then used to bring in a 'Wall Search' algorithm.

4.4: Particle-Boundary Wall Contact

In both 2D and 3D simulations the boundary walls can simply be seen as a set of mathematical conditions that govern the motion of a mathematical sphere in a global domain. In a 2D version the constraints are implemented linearly whereas in 3D the constraints take a planar form. However, as discussed in the last section there are strong similarities in both methods, particularly in the calculation of the *dn1* value that determines the point of sphere-boundary contact and the subsequent force interactions.

4.4.1: Sphere-Boundary Wall Interaction

In *Figure 91* the particle contacts the surface of the plane boundary and the interaction forces are highlighted.

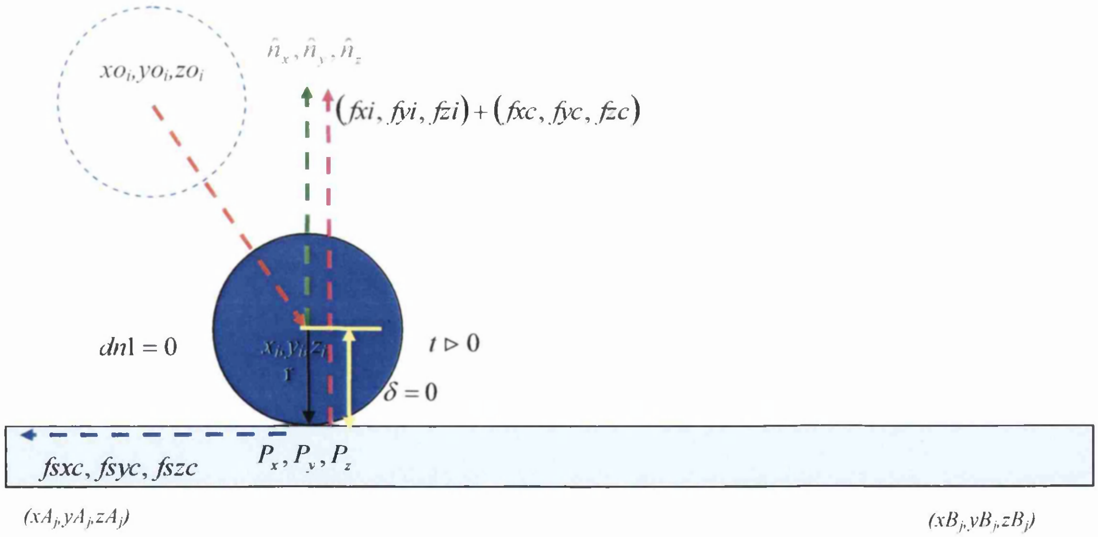

Figure 91 - Sphere in contact with a boundary wall with dn1=0 and t>0

- $(fxi, fyi, fzi) + (fxc, fyc, fzc)$ = *the perpendicular reaction forces*
- $fsxc, fsyc, fszc$ = *the frictional forces opposing the motion of the sphere*
- δ = *the penetration depth of the sphere during contact*

At this point of contact the wall search algorithm activates and the perpendicular reaction forces are calculated to return the sphere through the boundary in a physical manner.

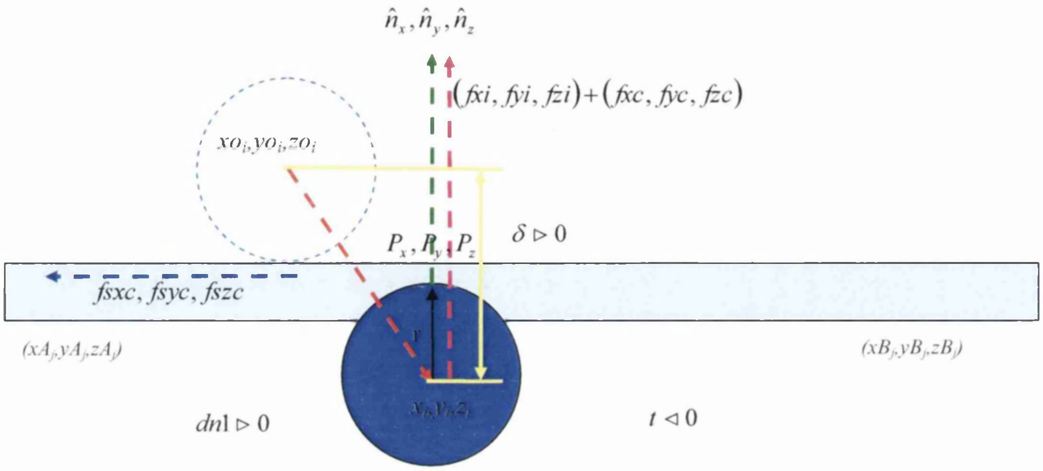

Figure 92 - Sphere breaching a boundary wall with dn1>0 and t<0

In *Figure 92* the sphere breaches the surface with a penetration depth δ being proportional to the impact momentum. The reaction force reduces the velocity of the sphere during the penetration time span by absorbing the energy in a compressive strain until this is returned to propel the sphere back out through the boundary surface. This mechanism follows the same method applied to the sphere-sphere interaction but only considers the mass of the impacting sphere as apposed to the effective mass generated by two moving objects.

Note that in this situation the damping forces here fxi, fyi, fzi and fxc, fyc, fzc follow the normal vector to the plane surface, this is an important factor and drives the calculation to change the direction of the impacting mass.

The other key observation to be made here is that the value of *dn1* always stays positive. This is due to the fact that *dn1* is a calculated distance from the centre of a moving sphere to a plane and does not take account of whether the point is below a boundary or above it. However this is not the case for the value calculated for *t*. As the sphere breaches the boundary surface a negative term is produced and combining these two factors into the conditions during contact, a switching system is provided to determine position.

- i.e. $t > 0$ Not in wall
- $t \leq 0$ In contact with the wall

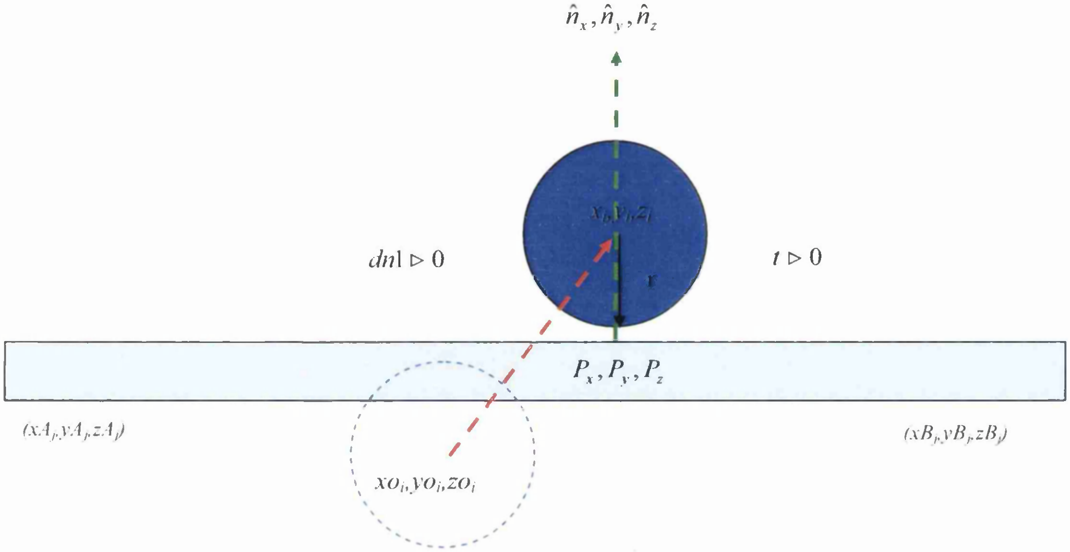

Figure 93 - sphere through a boundary wall with dn1>0 and t>0

4.4.2: Plane-Sphere Frictional Forces

To solve the problem of simulating the friction force that occurs at the interface between material under motion and an engineered structure (i.e. head chute) a similar method to the sphere-sphere interaction was adopted. By utilising a combination of key coordinates it was possible to create an arrangement of intersecting planes that could be used to find a force vector in the required direction of the friction.

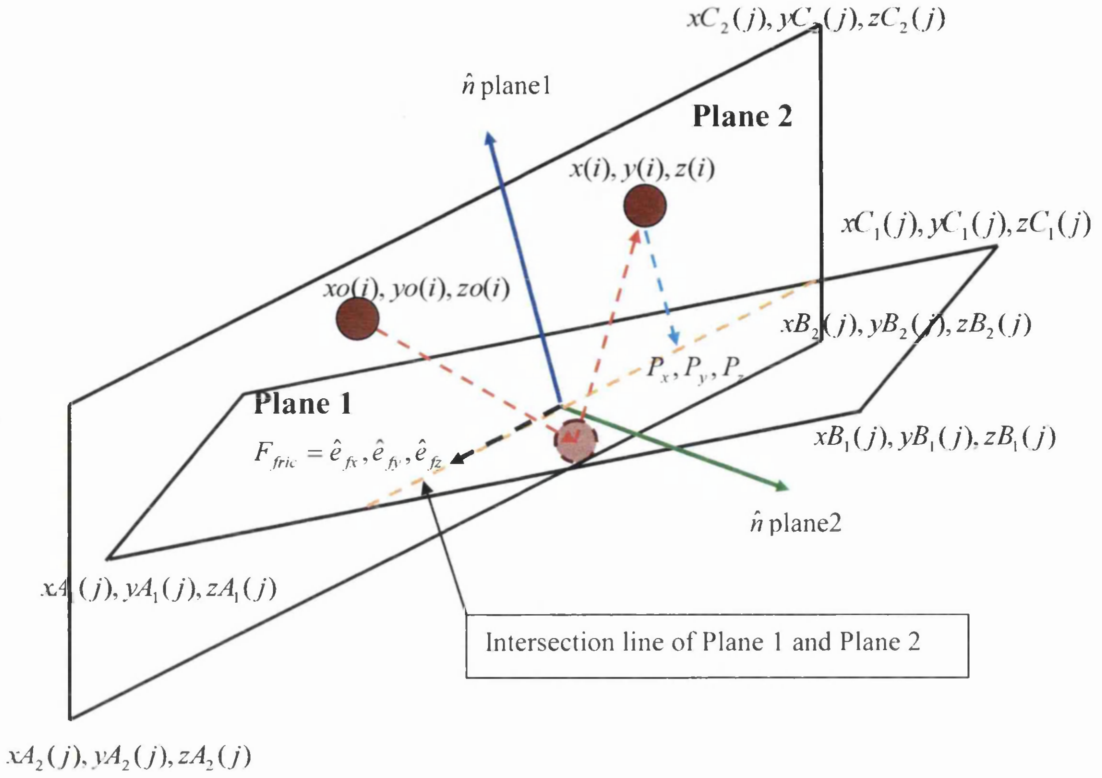

Figure 94 - plane intersection giving a frictional force vector

The schematic diagram in *Figure 94* shows 2 over lapping infinite planes and the line generated by their points of intersection.

Plane 1:

Produced using coordinates:

$$\begin{pmatrix} xA(j) \\ yA(j) \\ zA(j) \end{pmatrix}, \begin{pmatrix} xB(j) \\ yB(j) \\ zB(j) \end{pmatrix} \text{and} \begin{pmatrix} xC(j) \\ yC(j) \\ zC(j) \end{pmatrix} \text{Giving the normal}$$

$$\hat{n}1_x = \frac{n_x}{\sqrt{\left(n_x^2 + n_y^2 + n_z^2\right)}}, \quad \hat{n}1_y = \frac{n_y}{\sqrt{\left(n_x^2 + n_y^2 + n_z^2\right)}}, \quad \hat{n}1_z = \frac{n_z}{\sqrt{\left(n_x^2 + n_y^2 + n_z^2\right)}}$$

Plane 2:

Produced using coordinates:

$$\begin{pmatrix} xo(i) \\ yo(i) \\ zo(i) \end{pmatrix}, \begin{pmatrix} x(i) \\ y(i) \\ z(i) \end{pmatrix} \text{and} \begin{pmatrix} P_X \\ P_Y \\ P_Z \end{pmatrix} \text{Giving the normal}$$

$$\hat{n}2_x = \frac{n_x}{\sqrt{\left(n_x^2 + n_y^2 + n_z^2\right)}}, \quad \hat{n}2_y = \frac{n_y}{\sqrt{\left(n_x^2 + n_y^2 + n_z^2\right)}}, \quad \hat{n}2_z = \frac{n_z}{\sqrt{\left(n_x^2 + n_y^2 + n_z^2\right)}}$$

Therefore, the vector orthogonal to these two normal follows the path apposing the direction of the sphere motion at contact and was representative of frictional vector $\vec{F}_{fric}$.

$$\begin{pmatrix} i & j & k \\ \hat{n}1_x & \hat{n}1_y & \hat{n}1_z \\ \hat{n}2_x & \hat{n}2_y & \hat{n}2_z \end{pmatrix} \tag{4.50}$$

$$\begin{aligned} e_x &= \left(\left(\hat{n}1_y \times \hat{n}2_z\right) - \left(\hat{n}1_z \times \hat{n}2_y\right)\right) \\ e_y &= -\left(\left(\hat{n}1_x \times \hat{n}2_z\right) - \left(\hat{n}1_z \times \hat{n}2_x\right)\right) \\ e_z &= \left(\left(\hat{n}1_x \times \hat{n}2_y\right) - \left(\hat{n}1_y \times \hat{n}2_x\right)\right) \end{aligned} \tag{4.51}$$

$$\hat{e}_x = \frac{e_x}{\sqrt{\left(e_x^2 + e_y^2 + e_z^2\right)}}, \quad \hat{e}_y = \frac{e_y}{\sqrt{\left(e_x^2 + e_y^2 + e_z^2\right)}}, \quad \hat{e}_z = \frac{e_z}{\sqrt{\left(e_x^2 + e_y^2 + e_z^2\right)}} \tag{4.52}$$

$$F_{fric} = \hat{e}_x, \hat{e}_y, \hat{e}_z \tag{4.53}$$

Applying these vector components into the 3D DEM program they formulate in the following manner:

$$\begin{aligned} fsxc &= fk \times \mu \times \hat{e}_x \\ fsyc &= fk \times \mu \times \hat{e}_y \\ fszc &= fk \times \mu \times \hat{e}_z \end{aligned} \tag{4.54}$$

Where:

- fk = the penetration depth δ of the sphere times the spring constant k
- μ = is the coefficient of friction between the surfaces of different media.

4.4.3 Parameterisation of Plane Surface

The disadvantage of generating infinitely large planes limits the practicality of using the program to replicate any simple system where flow occurs. The answer to the problem was to localise the planes into triangles by using the original plane coordinates. This was achieved by the application of a *'Barycentric Equation'*, which is a method of mathematically predicting an impact and is predominantly used in 'Ray Tracing' simulation.

4.4.3.1: Barycentric Equation

Using the calculated impact point (P_x, P_y, P_z) as a position on a plane surface, its relation to a set of triangular coordinates can seen as follows.

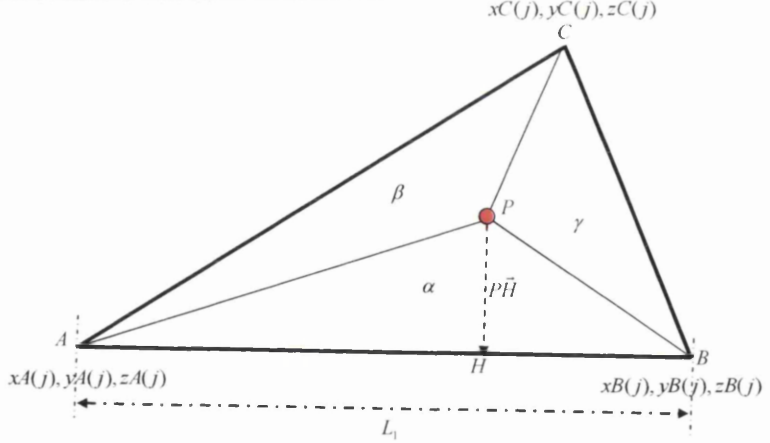

Figure 95 - Three sets of coordinates used to produce a plane

The schematic diagram in *Figure 95* shows a triangle ABC that has been split into three other separate triangles using the impact point (P_x,P_y,P_z) as the centre. The principle behind the 'Barycentric Equation' is that the sum of the areas covered by the three internal triangles equals the total area of triangle *ABC.* If the areas of triangle α, β and γ are normalised then:

Normalisation of internal triangles:

$$\frac{\alpha}{\Delta ABC}+\frac{\beta}{\Delta ABC}+\frac{\gamma}{\Delta ABC}=1 \tag{4.56}$$

4.4.3.2: Calculation Triangular Area

To derive a value for the required triangular area the standard 'Area of a Triangle' equation was used.

Area of a triangle:

$$\Delta_{Area}=\frac{1}{2}Base\times Perpendicular\ height \tag{4.57}$$

Taking $\Delta\alpha$, the shortest distance from *P* to line L_1 was the perpendicular distance from L_1 to *P* denoted as $\vec{PH}$. So to find the area of $\Delta\alpha$ the length of vector $\vec{PH}$ was calculated and applied to (4.47) along with a vector calculation for the base length.

Method

Using the information displayed in *Figure 95*

$$L_1=\left[\begin{pmatrix} xA_j \\ yA_j \\ zA_j \end{pmatrix}+t\begin{pmatrix} xB_j-xA_j \\ yB_j-yA_j \\ zB_j-zA_j \end{pmatrix}\right] \tag{4.58}$$

Because *H* lies on the line L_1 and t has yet to be determined then:

$$L_1=H \tag{4.59}$$

$$H=\begin{pmatrix} P_x \\ P_y \\ P_z \end{pmatrix}+\vec{PH}\longrightarrow\vec{PH}=-\begin{pmatrix} P_x \\ P_y \\ P_z \end{pmatrix}+\left[\begin{pmatrix} xA_j \\ yA_j \\ zA_j \end{pmatrix}+t\begin{pmatrix} xB_j-xA_j \\ yB_j-yA_j \\ zB_j-zA_j \end{pmatrix}\right] \tag{4.60}$$

Note:

To find t: $\vec{PH}\ perp\ to\ L_1$

$$\vec{PH} \bullet \left[\begin{pmatrix} xB_j - xA_j \\ yB_j - yA_j \\ zB_j - zA_j \end{pmatrix} \right] = 0 \tag{4.61}$$

$$\left[-\begin{pmatrix} P_x \\ P_y \\ P_z \end{pmatrix} + \begin{pmatrix} xA_j \\ yA_j \\ zA_j \end{pmatrix} + t \begin{pmatrix} xB_j - xA_j \\ yB_j - yA_j \\ zB_j - zA_j \end{pmatrix} \right] \bullet \left[\begin{pmatrix} xB_j - xA_j \\ yB_j - yA_j \\ zB_j - zA_j \end{pmatrix} \right] = 0 \tag{4.62}$$

$$\left[\begin{pmatrix} -P_x + xA_j \\ -P_y + yA_j \\ -P_z + zA_j \end{pmatrix} \begin{pmatrix} xB_j - xA_j \\ yB_j - yA_j \\ zB_j - zA_j \end{pmatrix} + t \begin{pmatrix} (xB_j - xA_j)^2 \\ (yB_j - yA_j)^2 \\ (yB_j - yA_j)^2 \end{pmatrix} \right] = 0 \tag{4.63}$$

$$t = \frac{-[(xA_j - P_x)(xB_j - xA_j)] - [(yA_j - P_y)(yB_j - yA_j)] - [(zA_j - P_z)(zB_j - zA)]}{(xB_j - xA_j)^2 + (yB_j - yA_j)^2 + (zB_j - zA_j)^2} \tag{4.64}$$

Therefore:

$$\left|\vec{PH}\right| = \sqrt{\left[(xA_j - P_x + (xB_j - xA_j)t)^2 + (yA_j - P_y + (yB_j - yA_j)t)^2 + (zA_j - P_z + (zB_j - zA_j)t)^2 \right]} \tag{4.65}$$

And the 'Base length' of $\Delta\alpha$ is:

$$Bl_{\Delta\alpha} = \sqrt{\left[((xB_j - xA_j))^2 + ((yB_j - yA_j))^2 + ((zB_j - zA_j))^2 \right]} \tag{4.66}$$

Area of $\Delta\alpha$:

$$\Delta\alpha_{Area} = \frac{1}{2} Bl_{\Delta\alpha} \times \left|\vec{PH}\right| \tag{4.67}$$

The same method was also applied to calculating the areas of $\Delta\beta$ and $\Delta\gamma$ to satisfy (4.56).

If (4.56) holds then the sphere trajectory is on a collision course with triangle ABC.

If the sum of the internal triangles is greater than 1 then the sphere will miss triangle ABC.

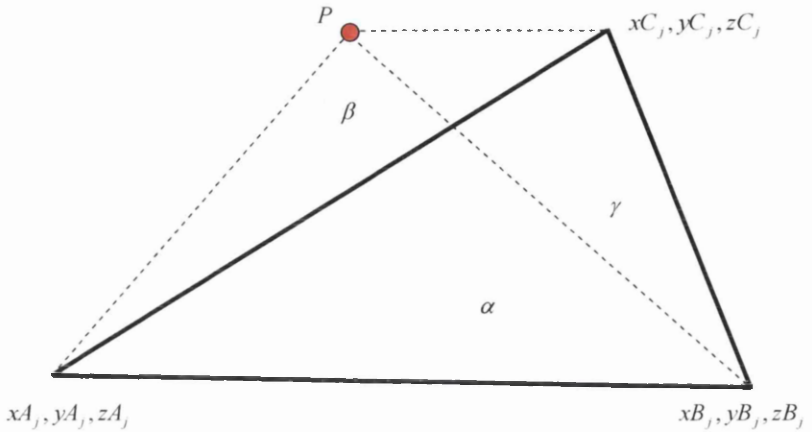

Figure 96: Point P formed outside the triangular section

The schematic diagram shown in *Figure 96* depicts a situation were an element has no relation to the triangular surface bounded by the three coordinates. This result was a foundation for generating 3D localised boundary conditions within a global domain. This enabled the preliminary production of a simulation environment to study dynamic flow situations within a practical arrangement.

4.5: Preliminary 3D Simulation Results

The content of this subsection is a compilation of early 3D localised simulation environments that were all generated by hand built input files. The task of producing these local domains was largely time consuming and impractical in real terms. However, the importance of this step in the modelling was without question and the knowledge gained in coordinate orientations was a critical factor in moving to the next level in program development.

The subject matter attended to here were chosen for their simple design and the relevance to project.

As an addition to the program development, element colour coding was introduced to highlight particles of different radii. Using the minimum and maximum radii and the actual randomly generated radius of a particle, the colour coding was presented as:

- 20% of the min max range: Yellow
- 40% of the min max range: Red
- 60% of the min max range: Green
- 80% of the min max range: Cyan
- 100% of the min max range: Blue

4.5.1: 1004 Head Chute

This part of the plant was discussed in terms of program development for the 2D case in *3.3*. The movement into 3D (as shown in *Figure 97*) provides the simulation with significantly more data but has considerably more visual impact.

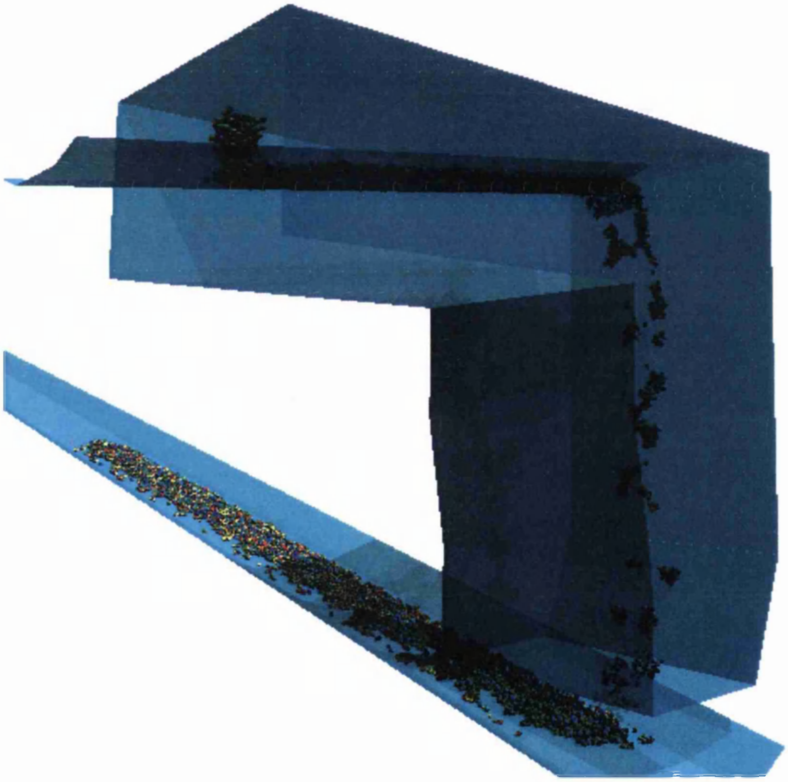

Figure 97: Hand constructed wall configuration to represent 1004 head chute with colour coded element/particles

4.5.2: 1401 Hopper

The simulation slide presented here is the result of the Granulated Coal Injection Plant (GCI) project application addressed in *3.4*. The simulation render shows a particulate generation falling into an open hopper and onto a moving set of walls representing a conveyor belt.

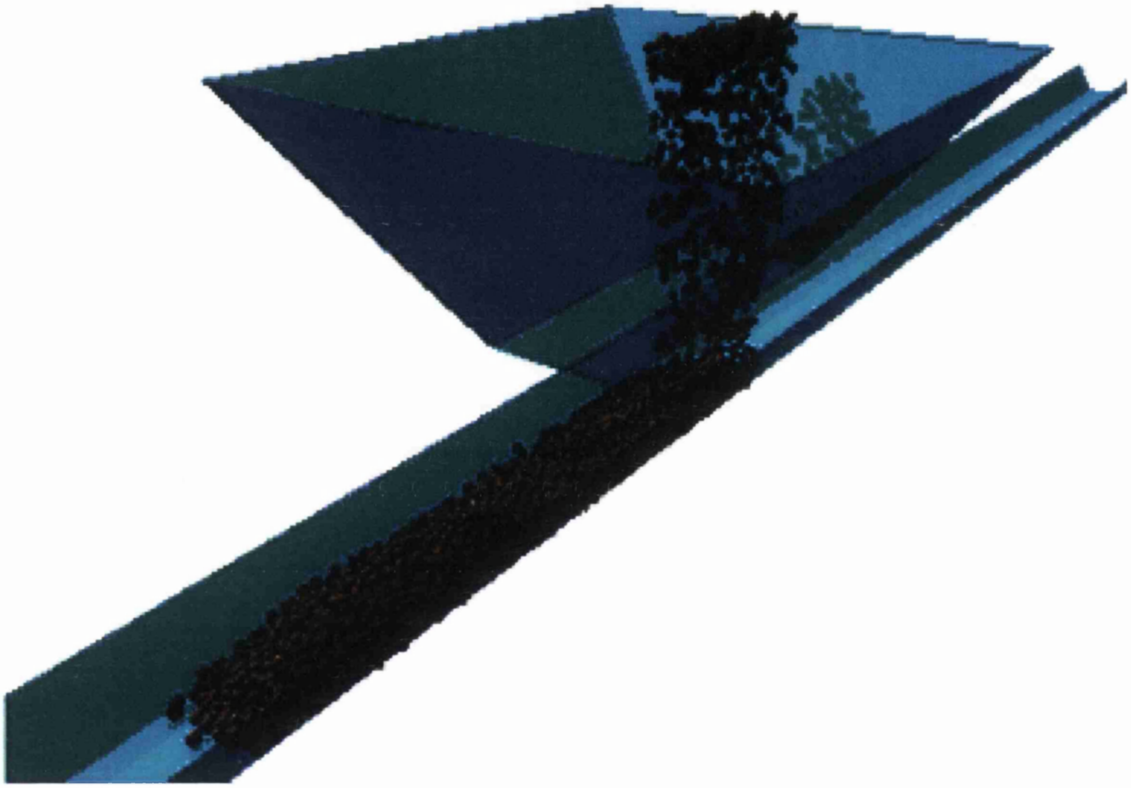

Figure 98: Hand constructed wall configuration to represent 1401 feed hopper

4.5.3: Sinter Plant Segregation Plate

The introduction to this piece of on-plant apparatus was introduced in *1.5* and was a major contributing factor in the DEM investigation technique. Again, terms of data analysis the 3D simulation render offers more information than the 2D counterpart.

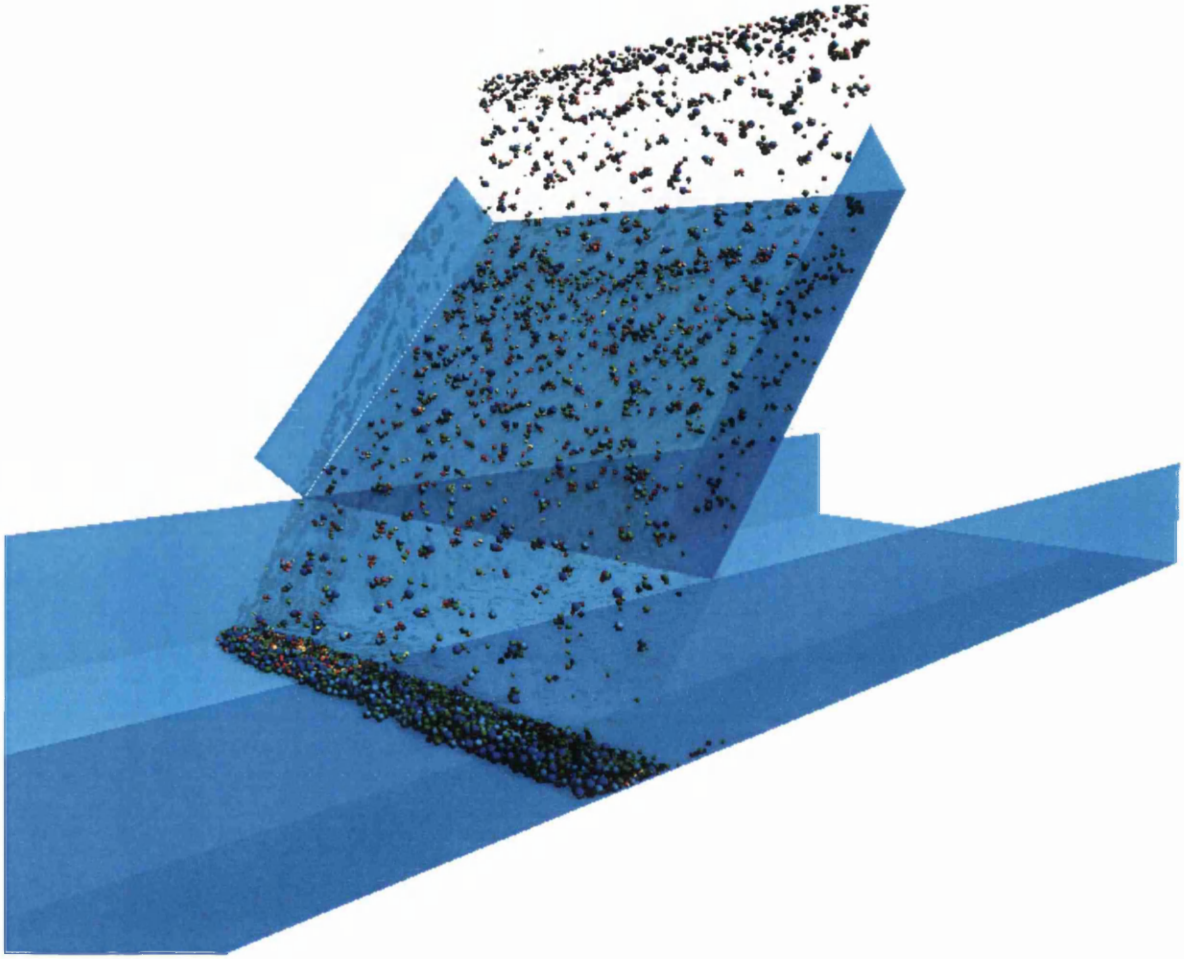

Figure 99: Hand constructed wall configuration to represent the sinter plant segregation plate

To create the above boundary arrangements triangular sections were used to generate planes. Each plane comprised four sets of x, y, z coordinates and the orientation of the coordinates produced the *Unit Normal vectors* associated to each plane. These vectors initiate the contact forces and physical representations are produced. Although the domains discussed here are basic, the simulation media were seen as reasonable representations of the practical situations under investigation. At this stage further development for inter-particle contact was required in terms of the effects of moisture addition. The collections of models studied in this subsection are highly influenced by environmental conditions. Moisture retention is a particular concern and greatly effects particle motion and boundary interaction. To simulate this form of situation capillary forces were introduced and covered in the next subsection.

4.6: Capillary Force

To draw closer to an accurate representation of a granular flow one has to consider as many of the fundamental forces that are present between particulates as practicably possible. For the cases discussed the application of moisture into raw material is both controlled and uncontrolled and previous simulation work on this subject indicates that the adhesion force due to liquid bridges largely affects particulate flow[81]. As an example one of the key factors in efficient Sinter Plant operation is to set a raw material moisture levels to approximately 5% material mass of equivalent water. This is a controlled process but is usually based on trial and error and moisture levels range due to many external variables. The raw material storage facilities for bulk handling of this type are usually exposed to the elements and material moisture levels are highly dependent on weather conditions, drainage and material absorbency. In the case of fine ores and coals, moisture levels strongly determine the handle-ability of the product and its visual appearance, when dry they present themselves as powdery and when saturated they can appear as slurry. The limits of mathematical moisture content for this project were set at 5% material mass of equivalent water to obtain satisfactory results.

- In this subsection, schematic diagrams of the geometric representation of capillary type force are shown.
- A mathematical approach in terms of simple geometry is offered for the production of internal radius of a curved meniscus. This value relates to the capillary force.
- The toroidal approximation to capillary force calculation is used and explained
- A calculation by integration of the void created between two contacting spheres and a virtual toroid is also presented.

4.6.1: Capillary Force Simulation

For this investigation the controlled application of moisture is studied and dealt with by a "Capillary type force" interaction between particles. In this case particles carry a mass percentage of water with them to represent an applied moisture level and when surfaces are close a meniscus is formed by moisture harvest[82]. The normal capillary action is then calculated using the Laplace Equation for capillary force and if the menisci are sufficiently small one can neglect gravitational distortion and buoyancy forces[83].

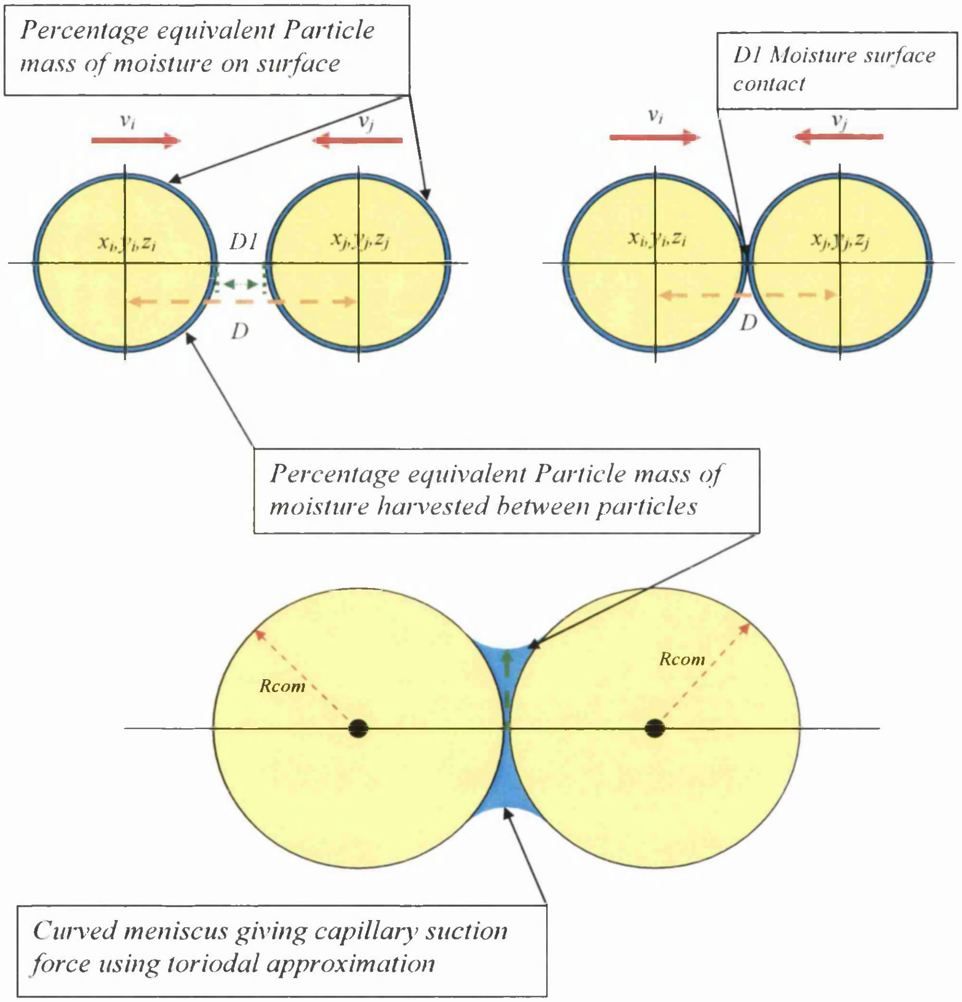

Figure 100: Particles with approach velocity impacting and harvesting surface moisture between surfaces

As shown in *Figure 100* the moisture content between the particles forms a liquid bridge. Surface tension actions provoke the liquid-gas interface to behave like a stretched membrane, which as a consequence, maintains solid particles together.

The capillary force between two or more spherical particles is a complex relationship and is dependent upon the volume of the water addition. There are four main physical descriptions for the quantity of solution between the particles and they are as follows[84][85].

- Pendular: Liquid bridges are formed at the contact points of the particles. Cohesive force act through liquid bridges.
- Funicular: Liquid bridges around contact points and liquid filled pores coexist. Both give rise to cohesion between particles.
- Capillary: Almost all the pores are filled with liquid, but the liquid surface forms menisci and the liquid pressure is lower than the air pressure. This suction results in a cohesive interaction.
- Slurry: The liquid pressure is equal to, or higher than the air pressure. No cohesive interaction appears between particles.

Qualitative arguments agree that cohesion increases with higher water contents to its saturation to a maximum value in the pendular regime[86][87][88].

The image shown in *Figure 100* depicts the meniscus bridge between two spherical particles. The curvature of the meniscus is generated by the difference in the atmospheric pressure with the internal pressure of the liquid and this result's in an attractive interaction force at the particle surface.

Laplace-Young Capillary force equation

$$F_{cap} = 2\pi\sigma y_0 + \pi y_0^2 \Delta P \qquad (4.68)$$

Where:

σ is the surface tension of water at 20^0C ~ 0.073

y_0 s the distance from the centre line between the particles to the lowest point of the meniscus.

ΔP is the pressure difference between the both media (i.e. water and air)

$$\Delta P = \sigma\left(\frac{1}{R_1} - \frac{1}{R_2}\right) \qquad (4.69)$$

The Laplace-Young equation cannot be solved analytically. An alternative approach is to assume the shape of the liquid bridge to be that of a toroid[89][90]

For representation of industrial particulates, size distribution was a simulation requirement and the capillary force values in this situation were calculated by the internal coordinate system of three interacting spheres and the following assumptions:

4.6.1.1: Basic Geometry of a circular toroid

The image in *Figure 100* is shown in 2D coordinates, and the calculations in 3D follow a similar method due to the geometry of the spherical elements. However, if one considers the curved meniscus to be a circular radius the calculations become less complex and in 3D the volume of the meniscus can be seen a the internal structure of a Toroid.

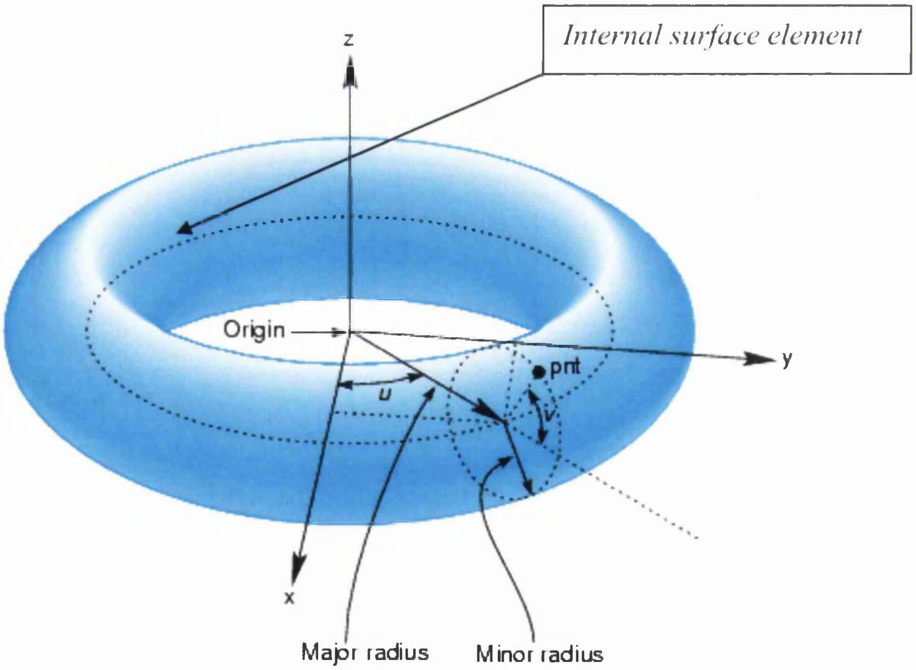

Figure 101: Circular toroid showing major and minor radii

Toriodal Assumptions:

- The internal surface element of the toroid was used as a curved meniscus
- The minor radius produced a toriodal volumes equal to the mass percentage volume of water carried with particle when the major radius = minor radius.
- The minor radius R_k was used as the value R_1 in the Laplace Equation for capillary force. In this case when R_1 is determined it remained constant throughout the contact interaction calculation.
- The Major radius grows as the particle centres encroach and the value R_2 in the Laplace Equation is generated by the Major radius – Minor radius.

The advantage of the toroidal approximation is that the total liquid bridge force may be expressed in terms of a simple closed form expression[91]. A simplistic approach to capillary force due to a liquid bridges can be useful when particles size get small $O(10^{-9})$ as many approximations become invalid at this level[92].

The calculated values are formulated as shown in the following section.

4.6.2: Capillary Force between particles of different size

In this subsection the relationship between interacting spherical elements, the moisture carried with each element and the toroidal approximation for the meniscus are brought together. The schematic diagrams represent a cross-sectional visual image of spherical elements at contact and the corresponding geometric relationships are used to generate a *Normal* attractive force.

The combination of the soft sphere method and the toroidal approximation between different sized particles has an element of novelty associated to it, and its clear success in producing reasonable capillary force prediction can be attributed to the geometric relationship between the contacting particles and the expansion of the toroid during particle interaction.

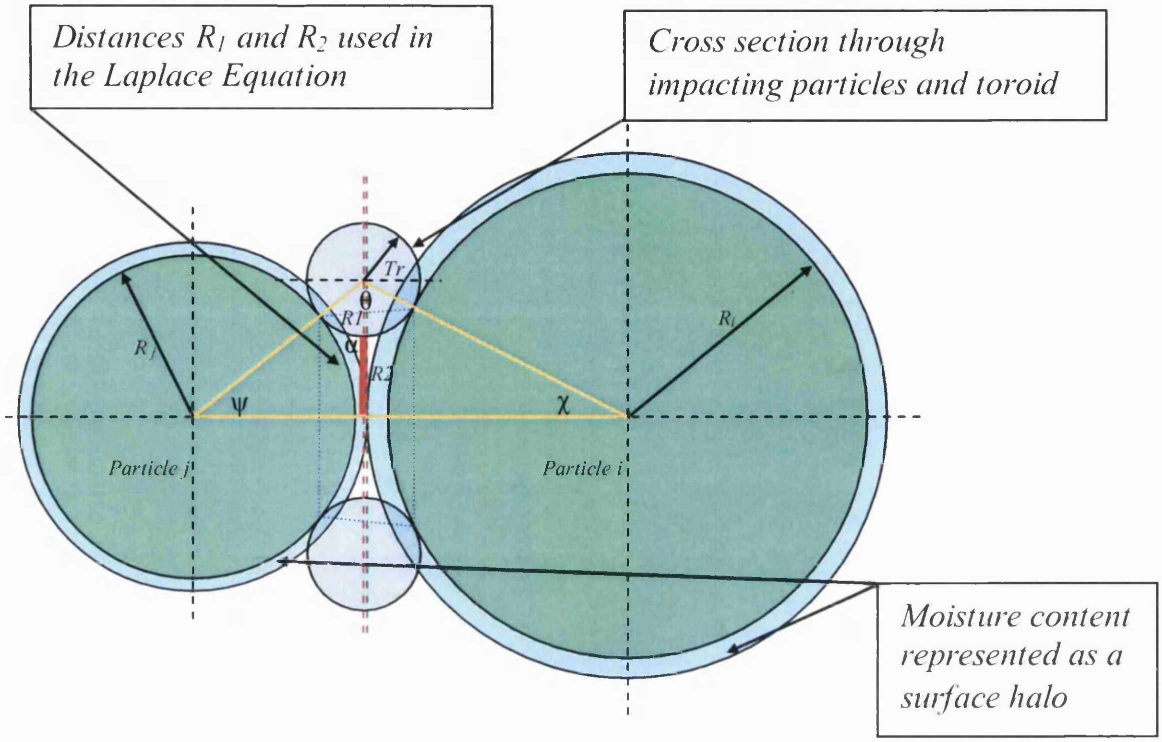

Distances R_1 and R_2 used in the Laplace Equation

Cross section through impacting particles and toroid

Moisture content represented as a surface halo

Figure 102: Particles in moisture-moisture contact switching on the contact algorithm.

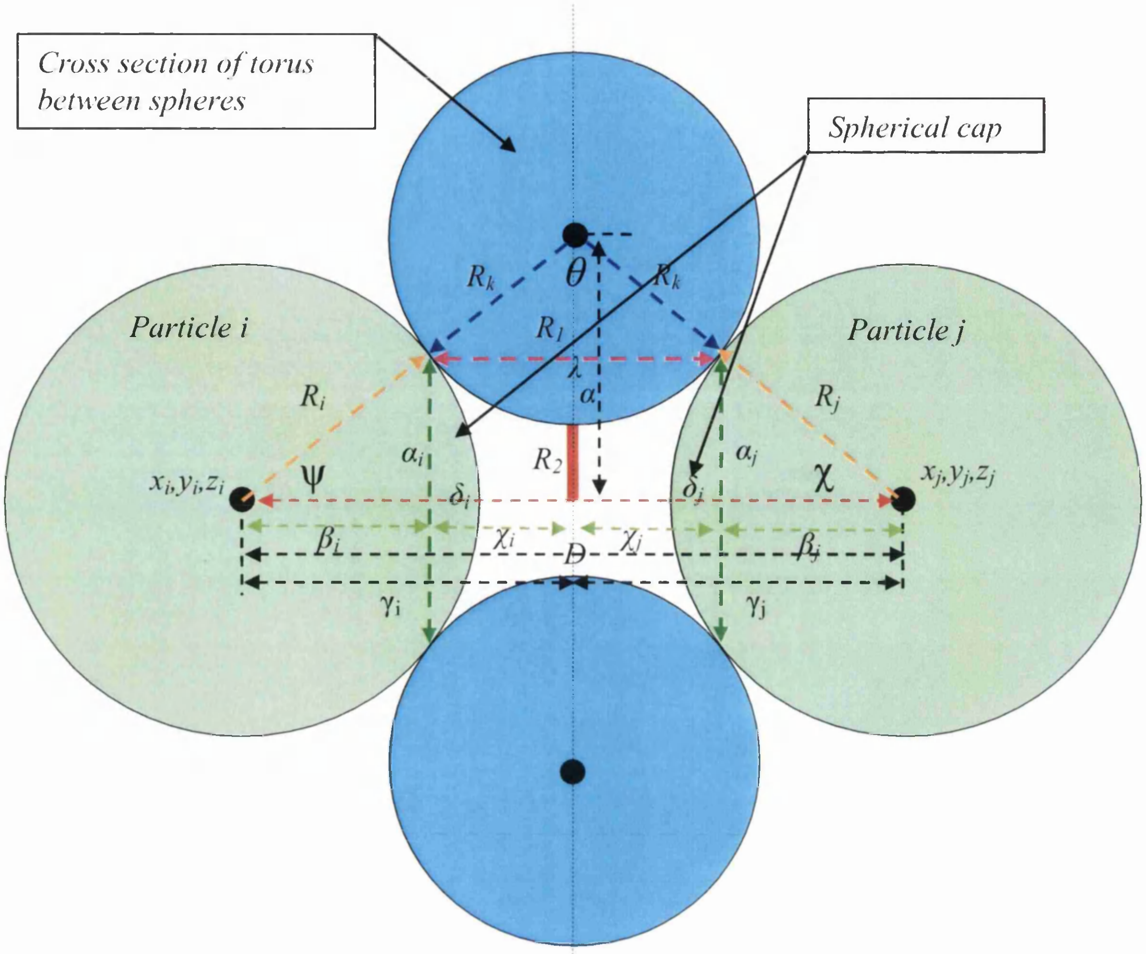

Figure 103: Impacting particles of similar radii showing a symmetric relationship and torus between surfaces

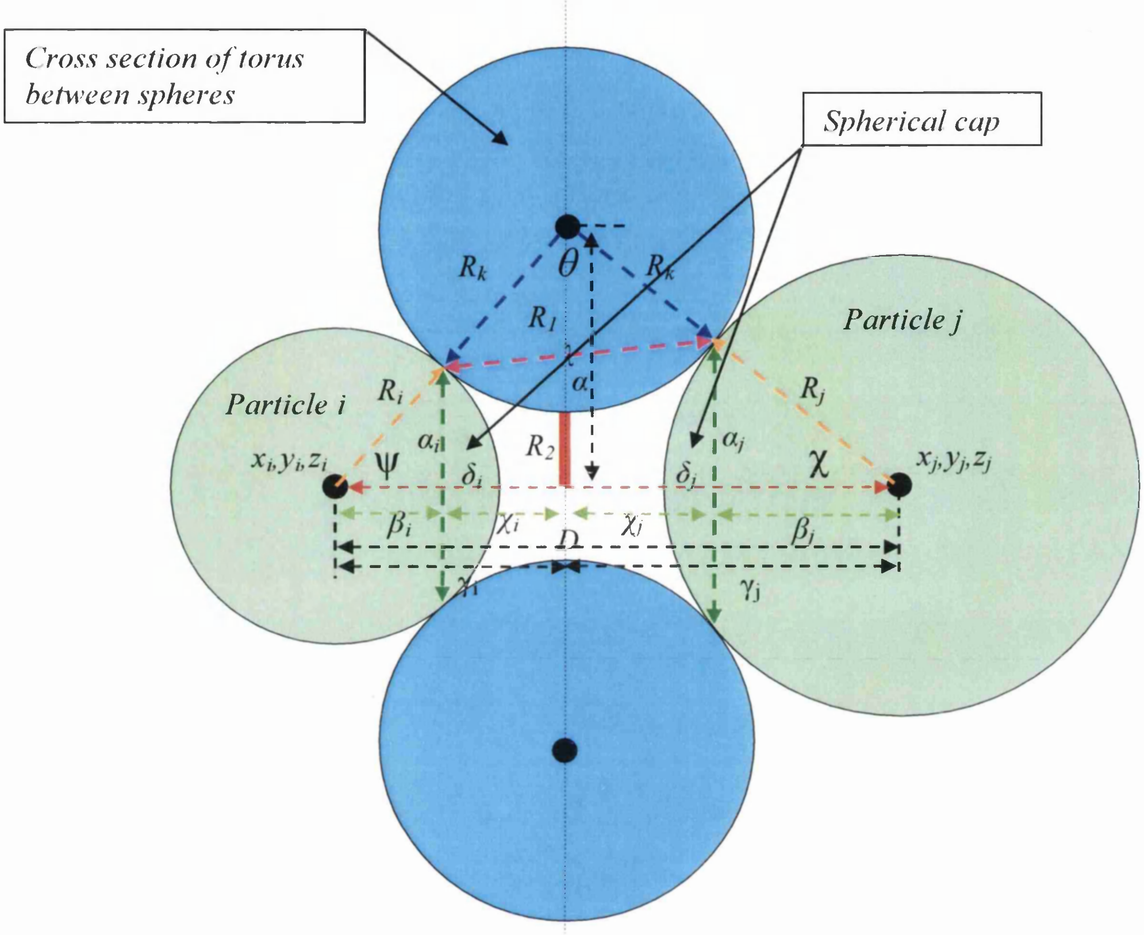

Figure 104: Impacting particles with different radii showing non-symmetric relationship and torus between surfaces

Dimension in *Figures 103 & 104* were determined as follows with *R1* remaining constant:

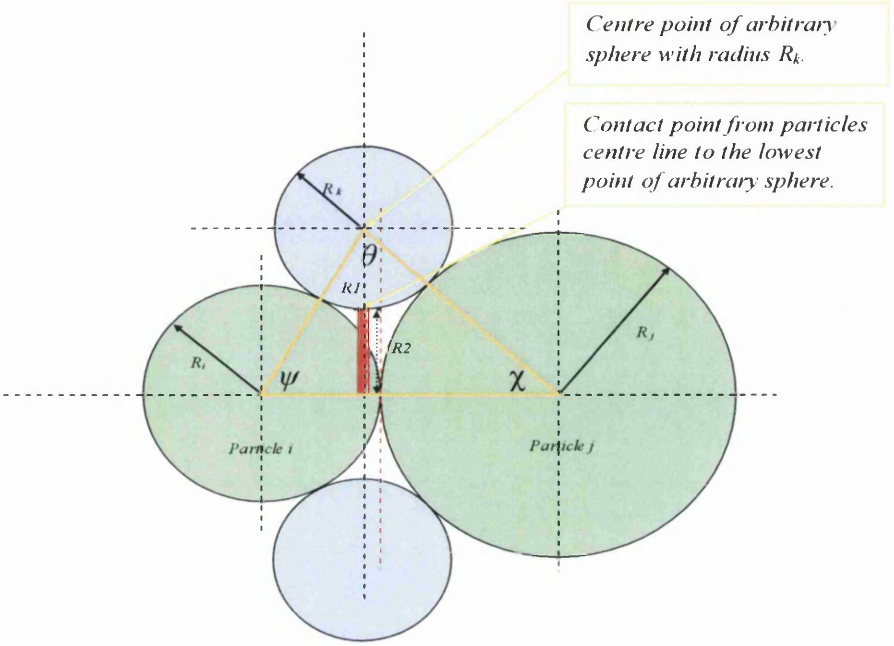

Figure 105: Elements of differing radii with angles χ, θ, ψ exposed

Moisture value = $Mois'$ ~ values btw 0 and 5% of the particle mass

$$\begin{aligned} dx &= x_j - x_i \\ dy &= y_j - y_i \\ dz &= z_j - z_i \end{aligned} \qquad (4.70)$$

$$D = \sqrt{dx^2 + dy^2 + dz^2} \qquad (4.71)$$

$$v_{com} = \frac{4}{3}\pi\left(r_i^3 + r_j^3\right) \qquad (4.72)$$

$$\%v_{com} = Mois' \times v_{com} \qquad (4.73)$$

$$R_k = \sqrt[3]{\frac{\%v_{com}}{2\pi^2}} \quad where: R_k = R_1 \qquad (4.74)$$

Note:

Particle i mass (kg)	M_i
Particle j mass (kg)	M_j
Particle i Volume (m^3)	V_i
Particle j Volume (m^3)	V_j
Particle Density (kgm^{-3})	ρ_p
Moisture Density (kgm^{-3})	ρ_w
Moisture i mass (kg)	M_{wi}
Moisture j mass (kg)	M_{wj}

4.6.2.1: Depth of moisture on particle surface:

When moisture values are introduced into the calculation each spherical element can be seen as carrying a surface quantity of water. The resulting depth of the water is directly related to the mass of the element and the percentage of moisture assigned by the user.

The depth of the surface water is calculated as follows:

$$M_i = \rho_p \cdot V_i \qquad (4.75)$$

$$M_j = \rho_p \cdot V_j \qquad (4.76)$$

$$M_{wi} = \rho_w \cdot V_i \qquad (4.77)$$

$$M_{wj} = \rho_w \cdot V_j \qquad (4.78)$$

Mass of additional moisture:

$$m_{wi} = Mois' \cdot M_i \qquad (4.79)$$

$$m_{wj} = Mois' \cdot M_j \qquad (4.80)$$

New moisture mass with additional moisture

$$Mwi_{new} = M_{wi} + m_{wi} \qquad (4.81)$$

$$Mwj_{new} = M_{wj} + m_{wj} \qquad (4.82)$$

$$Vwi_{new} = \frac{Mwi_{new}}{\rho_w} \qquad (4.83)$$

$$Vwj_{new} = \frac{Mwj_{new}}{\rho_w} \qquad (4.84)$$

New radius for virtual sphere of volumes Vwj_{new} and Vwi_{new}

$$R_{wi} = \sqrt[3]{\frac{3 \cdot Vwi_{new}}{4\pi}} \qquad (4.85) \qquad\qquad R_{wj} = \sqrt[3]{\frac{3 \cdot Vwj_{new}}{4\pi}} \qquad (4.86)$$

Depth of moisture on particle surface:

$$\delta_{wi} = R_{wi} + R_i \qquad (4.87) \qquad\qquad \delta_{wj} = R_{wj} + R_j \qquad (4.88)$$

Combined depth of moisture on particle surfaces for contact algorithm:

$$\Delta_{wij} = \delta_{wi} + \delta_{wj} \qquad (4.89)$$

4.6.2.2: Geometric relationships related to *Figure 103*:

For simplicity the schematic image in *Figure 103* shows element of the same size at contact. This situation is unlikely when a size distribution is applied to the simulation; however, the fundamental geometric rules displayed are legitimate in the case of different sized elements.

To produce numerical values for angles χ, θ *and* ψ a simple rearrangement of the cosine rule was used. The principles to the angular value are as follows:

$$Rl_i = R_i + R_k \qquad (4.90) \qquad\qquad Rl_j = R_j + R_k \qquad (4.91)$$

$$\theta = Cos^{-1}\left(\frac{Rl_i^2 + Rl_j^2 - D^2}{2Rl_i Rl_j}\right) \qquad (4.92)$$

$$\psi = Cos^{-1}\left(\frac{D^2 - Rl_j^2 - Rl_i^2}{2D \cdot Rl_j}\right) \qquad (4.93)$$

$$\chi = Cos^{-1}\left(\frac{Rl_j^2 - D^2 - Rl_i^2}{-2Rl_i Rl_j}\right) \qquad (4.94)$$

$$\alpha = Rl_i \cdot Sin(\psi) \quad (4.95)$$

$$\alpha_i = R_i \cdot Sin(\psi) \quad (4.96)$$

$$\alpha_j = R_j \cdot Sin(\chi) \quad (4.97)$$

$$\beta_i = R_i \cdot Cos(\psi) \quad (4.98)$$

$$\beta_j = R_j \cdot Cos(\chi) \quad (4.99)$$

$$\chi_i = [Rl_i \cdot Cos(\psi)] - \beta_i \quad (4.100)$$

$$\chi_j = [Rl_j \cdot Cos(\chi)] - \beta_j \quad (4.101)$$

$$\delta_i = R_i - \beta_i \quad (4.102)$$

$$\delta_j = R_j - \beta_j \quad (4.103)$$

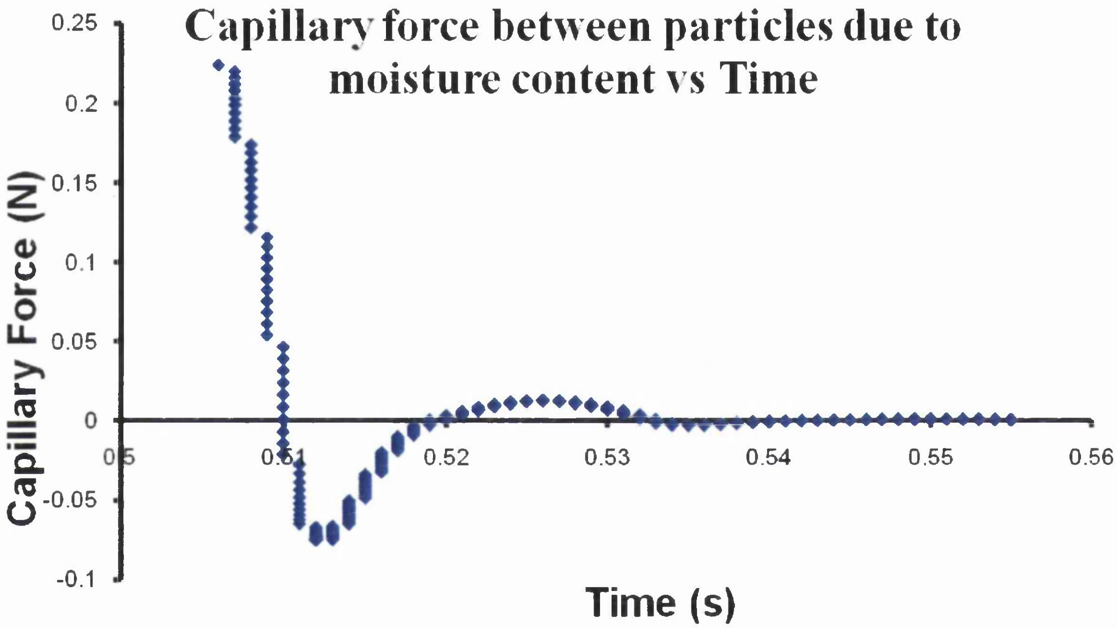

Graph 1: Force deterioration as particles impact

The deterioration of the capillary force shown in *Graph 1* was used as a preventative mechanism to inter-particulate vibration due to the contradiction of the attractive capillary force and the repulsive contact interaction forces. To formulate this damping effect the depth of surface moisture shown in *(4.89)* was used as constant denominator value and a decreasing ratio was produced before surface/surface contact. The key point here is that the repulsive and attractive forces settle to a state of equilibrium until they are broken apart by an external force greater than the meniscus bond.

Note: In this arrangement R_2 will be at its maximum at initial moisture surface contact and this reproduces the spring effect of a capillary force interaction

4.6.2.3: Liquid core volume at the centre of the toroid using integration

The voided space created between the spherical elements and the virtual toroid can be seen as the ideal 3D shape for the moisture to adopt during the contact interaction. The volume calculation of the voided space should match the calculated moisture content of the combined element at interaction. This relationship can be used as a trigger to avoid over saturation where forces become repulsive and the method of obtaining the voided volume can be seen as follows.

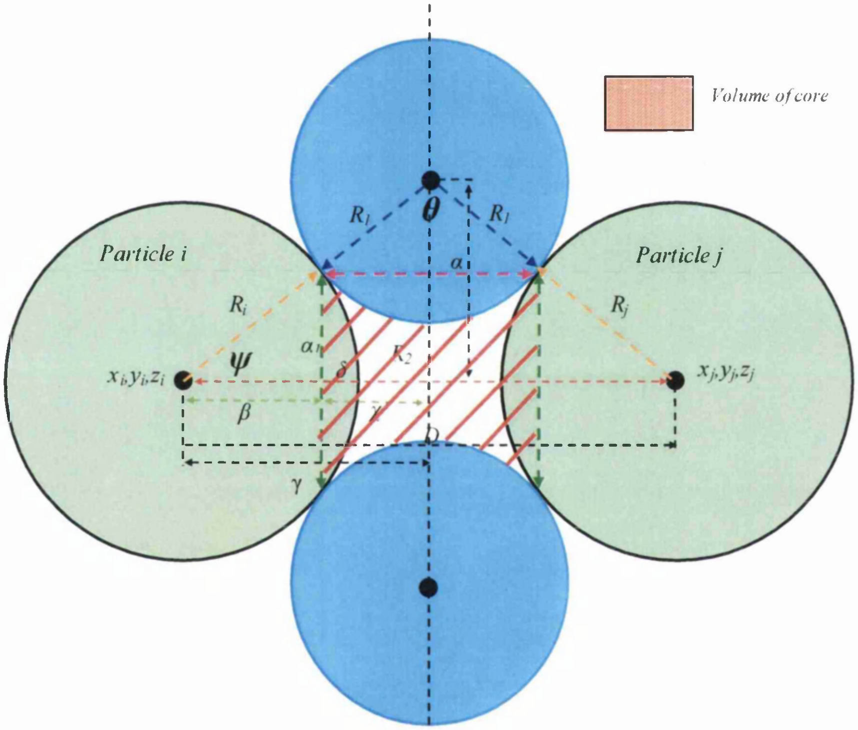

Figure 106: Liquid core developed between impacting spheres and torus

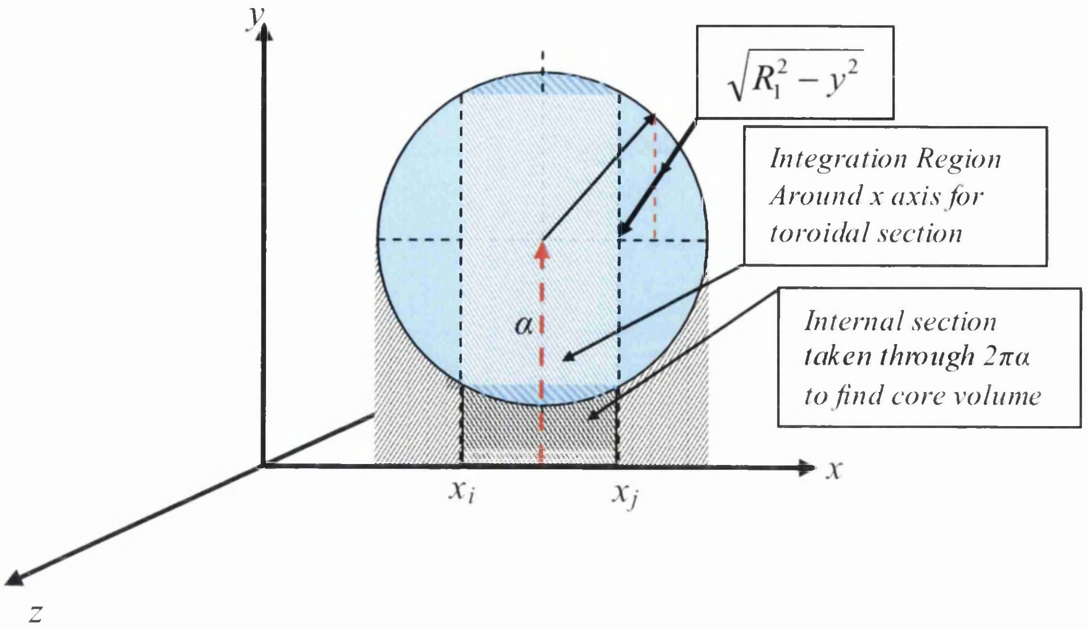

Figure 107: Integration region under sphere of minor radius to calculate the volume of a torus

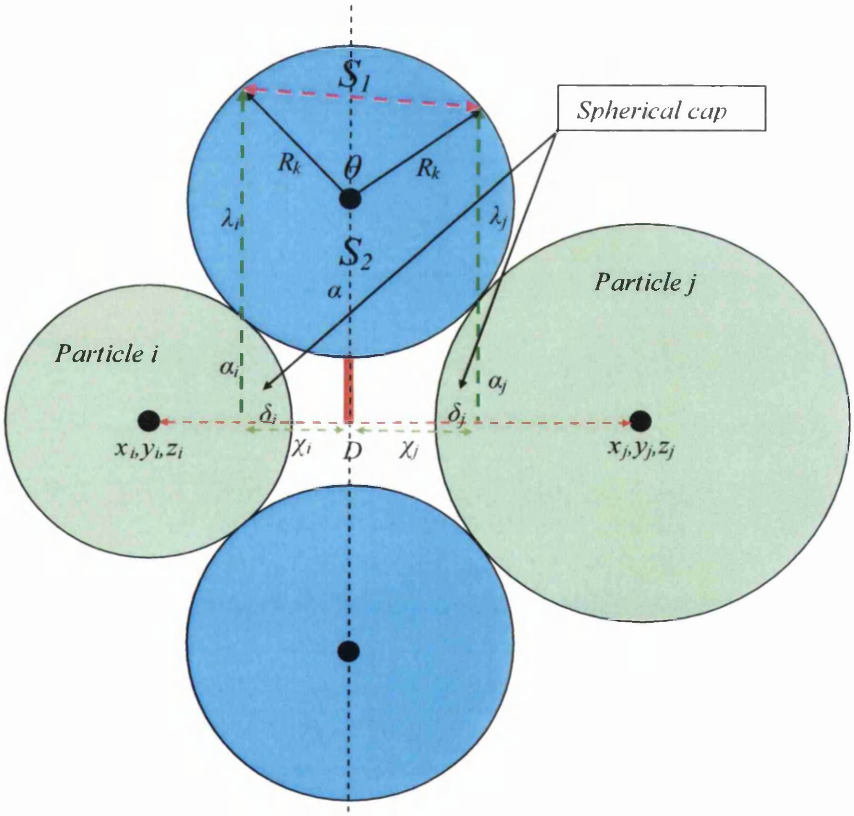

Figure 108: Sections S1 and S2 taken through 2πα to find the volume of the disc shaped centre.

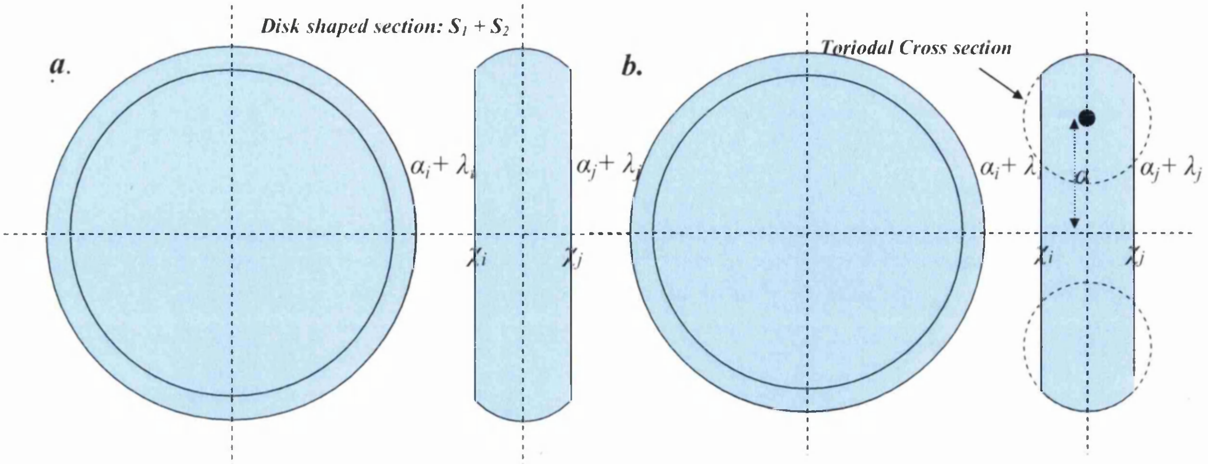

Figure 109: Side and end on view of blue shaded integration region shown in *Fig 107*

The simple shape shown in *Figure 109a* was derived from *Figure 108* and combines S_1 and S_2 for same size particles. The area of the shape was calculated by using the "area of a trapezium" rule with the addition of the area of a spherical cap included.

This area calculation was then taken through 360 degrees (in this case $2\pi\alpha$) and a basic volume calculation was produced. The construction of the equation can be seen in (4.104) where V_{sec} is the volume of the total section.

Volume of Sections S_1 & S_2 through $2\pi\alpha$

$$V_{\sec} = \left\{ \frac{1}{2}\left[\left((\alpha_i + \lambda_i) + (\alpha_j + \lambda_j)\right)(\chi_i + \chi_j)\right] + \left[\left(\frac{1}{2}(\vartheta - Sin\,\vartheta)\right) \cdot R_1^2\right]\right\} 2\pi\alpha \tag{4.104}$$

To determine the voided space between the particles at impact the virtual toriodal shape (as shown in *Figure 101*) had to be removed. *Figure 109b* depicts the cross-sectional view of the key area and the cross-sectional association of the toroid. By using an integral with the limits set at the points of spherical contact a toriodal section can be removed. The following solution shows the volume of a torus V_{torus} by integration and the resulting calculation of the toroidal section.

Volume of toroidal section using integration:

$$V_{torus} = \int_{a_0}^{a_1} \pi\left(\alpha + \sqrt{R_1^2 - y^2}\right)^2 - \pi\left(\alpha - \sqrt{R_1^2 - y^2}\right)^2 dy$$

$$V_{torus} = \int_{a_0}^{a_1} \pi\left(\alpha + \sqrt{R_1^2 - y^2}\right)^2 - \int_{a_0}^{a_1} \pi\left(\alpha - \sqrt{R_1^2 - y^2}\right)^2 dy$$

Let:

$$y = R_1 Sin\vartheta$$

$$\frac{dy}{d\vartheta} = R_1 Cos\vartheta$$

$$dy = R_1 Cos\vartheta \cdot d\vartheta$$

$$V_{torus} = \int_{a_0}^{a_1} \pi\left(\alpha + \sqrt{R_1^2 - R_1^2 Sin^2\vartheta}\right)^2 - \int_{a_0}^{a_1} \pi\left(\alpha - \sqrt{R_1^2 - R_1^2 Sin^2\vartheta}\right)^2 R_1 Cos\vartheta \cdot d\vartheta$$

$$V_{torus} = \int_{a_0}^{a_1} \left[\pi\left(\alpha + R_1\sqrt{1 - Sin^2\vartheta}\right)^2 - \pi\left(\alpha - R_1\sqrt{1 - Sin^2\vartheta}\right)^2 \right] R_1 Cos\vartheta \cdot d\vartheta$$

$$V_{torus} = \int_{a_0}^{a_1} \left[\pi\left(\alpha + R_1\sqrt{Cos^2\vartheta}\right)^2 - \pi\left(\alpha - R_1\sqrt{Cos^2\vartheta}\right)^2 \right] R_1 Cos\vartheta \cdot d\vartheta$$

$$V_{torus} = \int_{a_0}^{a_1} \left[\pi\left(\alpha^2 \cdot R_1 Cos\vartheta + 2\alpha \cdot R_1^2 Cos^2\vartheta + R_1^3 Cos^3\vartheta\right) - \pi\left(\alpha^2 \cdot R_1 Cos\vartheta + 2\alpha \cdot R_1^2 Cos^2\vartheta + R_1^3 Cos^3\vartheta\right) \right] \cdot d\vartheta$$

$$V_{torus} = \pi \int_{a_0}^{a_1} \left(4\alpha \cdot R_1^2 Cos\vartheta\right) \cdot d\vartheta$$

$$V_{torus} = \pi \int_{a_0}^{a_1} \left(2\alpha \cdot R_1^2 \left(1 + Cos2\vartheta\right)\right) \cdot d\vartheta$$

$$V_{torus} = \pi \left[2\alpha \cdot R_1^2 \left(\vartheta + \frac{Sin2\vartheta}{2} \right) \right]_{a_0}^{a_1}$$

$$V_{torus} = \pi \left[2\alpha \cdot R_1^2 \left(\vartheta + Sin\vartheta Cos\vartheta \right) \right]_{a_0}^{a_1}$$

Note:

$$Sin\,\vartheta = \frac{y}{R_1}$$

$$\vartheta = Sin^{-1}\left(\frac{y}{R_1}\right)$$

$$Cos^2\vartheta = 1 - Sin^2\vartheta \rightarrow Cos\,\vartheta = \sqrt{1 - Sin^2\vartheta} \rightarrow Cos\,\vartheta = \frac{1}{R_1}\sqrt{R_1^2 - y^2}$$

Therefore:

$$V_{torus} = \pi\left[2\alpha \cdot R_1^2\left(Sin^{-1}\left(\frac{y}{R_1}\right) + \left(\frac{y}{R_1^2}\right) \cdot \sqrt{R_1^2 - y^2}\right)\right]_{a_0}^{a_1}$$

$$V_{torus} = \pi\left[2\alpha \cdot R_1^2\left(Sin^{-1}\left(\frac{a_1}{R_1}\right) + \left(\frac{a_1}{R_1^2}\right) \cdot \sqrt{R_1^2 - a_1^{\,2}}\right)\right] - \pi\left[2\alpha \cdot R_1^2\left(Sin^{-1}\left(\frac{a_0}{R_1}\right) + \left(\frac{a_0}{R_1^2}\right) \cdot \sqrt{R_1^2 - a_0^{\,2}}\right)\right] \quad (4.105)$$

Where:

$$a_0 = \chi_i \qquad\qquad a_1 = \chi_j$$

By using the result obtained in (4.105) the core volume can be produced by subtracting the toriodal calculation away from the basic volume calculation (as shown in (4.106)). The resulting shape resembles the internal structure of a tyre as depicted in *Figure 110c*

Volume of liquid core between impacting particle carrying moisture:

$$V_{core} = V_{sec} - V_{torus} \quad (4.106)$$

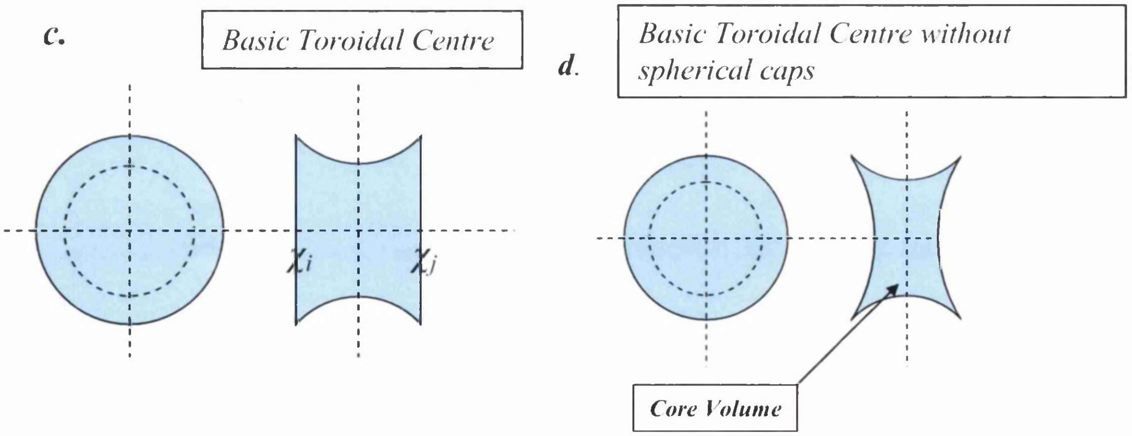

Figure 110: In *Figure 109 a, b,* and here in c & d the degeneration to liquid core volume is shown.

To complete the idealised shape the "spherical cap" volumes (shown in *Figure 109*) are removed and a representation of the core volume is presented.

This geometry and integral used for this representation is applicable to particles of different sizes at contact and the core representation can be seen in *Figure 111*.

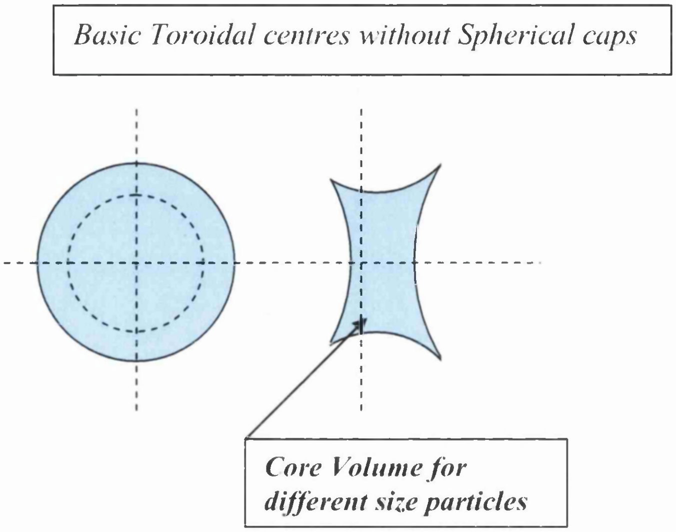

Figure 111: Here the liquid core volume is depicted between different size elements

As indicated in this section the introduction of a capillary type force was of critical importance due to the nature of the simulation requirements. The above method of deriving an attractive force value was based on the geometric relationship between three interconnecting spheres and an integral of a virtual toroidal shape. The integral was used in this case to produce a numerical value for the central core volume of the harvested moisture content between the interacting elements. The geometric relationship of the spheres was ultimately used to determine the internal radial distance from the vector between element centres to the bottom of the meniscus. This value relates to R_2 in the Laplace Equation.

4.6.2.4: Application of capillary force at 1 & 5 wt% moisture and its effects on particle clumping.

To visualise the effects of applying varying degrees of moisture content the following simulation slides were taken from a "Roll Feeder Segregation Plate" flow simulation with initially 1wt% moisture addition and finally 5wt% moisture addition.

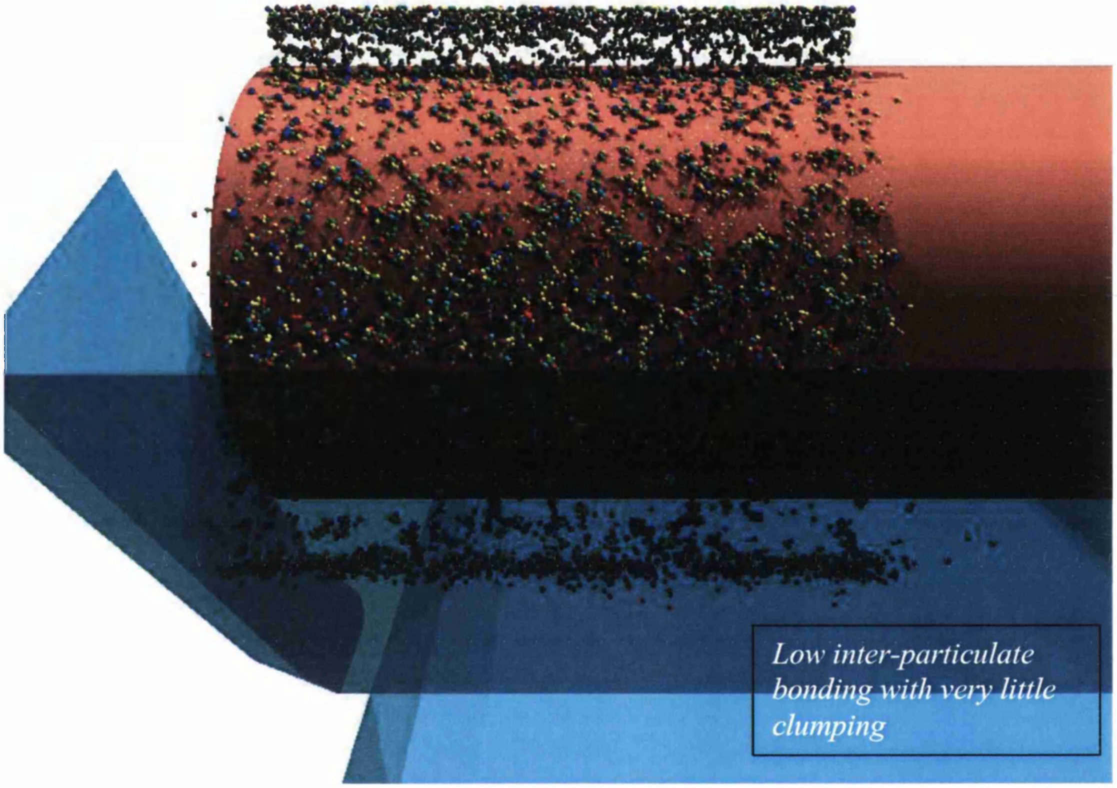

Figure 112: Particulate flow over Roll Feeder with 1wt% moisture

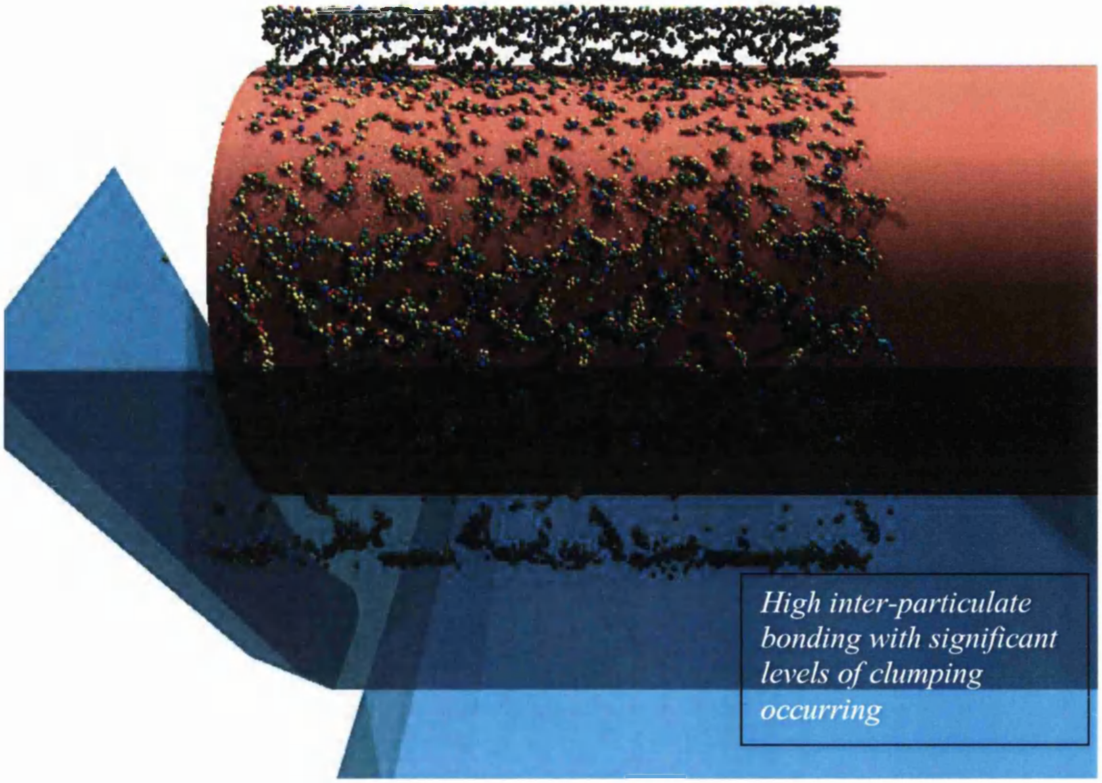

Figure 113: Particulate flow over Roll Feeder with 5wt% moisture

The images shown in Figures 112 & 113 are highly representative of material flows with differing moisture content through the Roll Feeder devise. However, mathematically deriving a stable simulation result required a great deal of trial and error. Extremes in finding the correct method of capillary interaction ranged from inter-element rejection and total bonding that maintained its initial shape.

The following images were produced in a simulation designed to generate an angle of repose from a rectangular box of discrete elements falling under gravity.

As discussed in *4.5* the colouring coding of the elements shows a particulate size distribution in this simulation. The range here was set at a minimum radius of 0.005m and a maximum radius of 0.015 generating 50 thousand elements within the particle generation region.

Note: The particle generation method was completely randomised and the program functioned by placing a particle in an x,y and z coordinate. Particle packing arrangements were not addressed here but could be considered post capillary bonding.

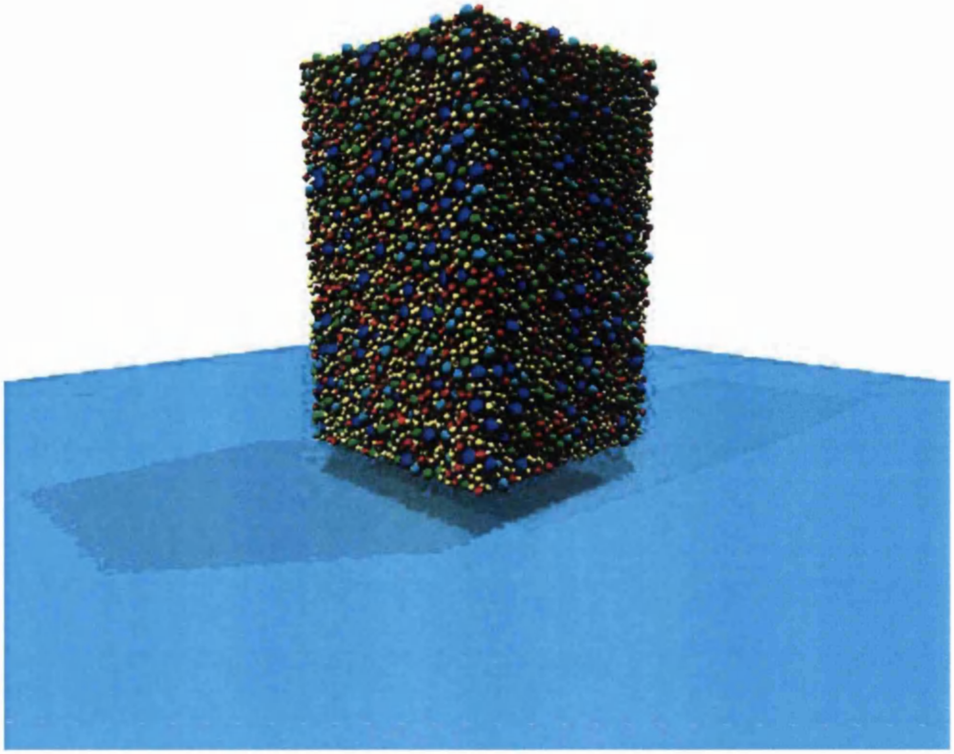

Figure 114: Rectangular box shape used to generate an angle of repose when falling under gravity

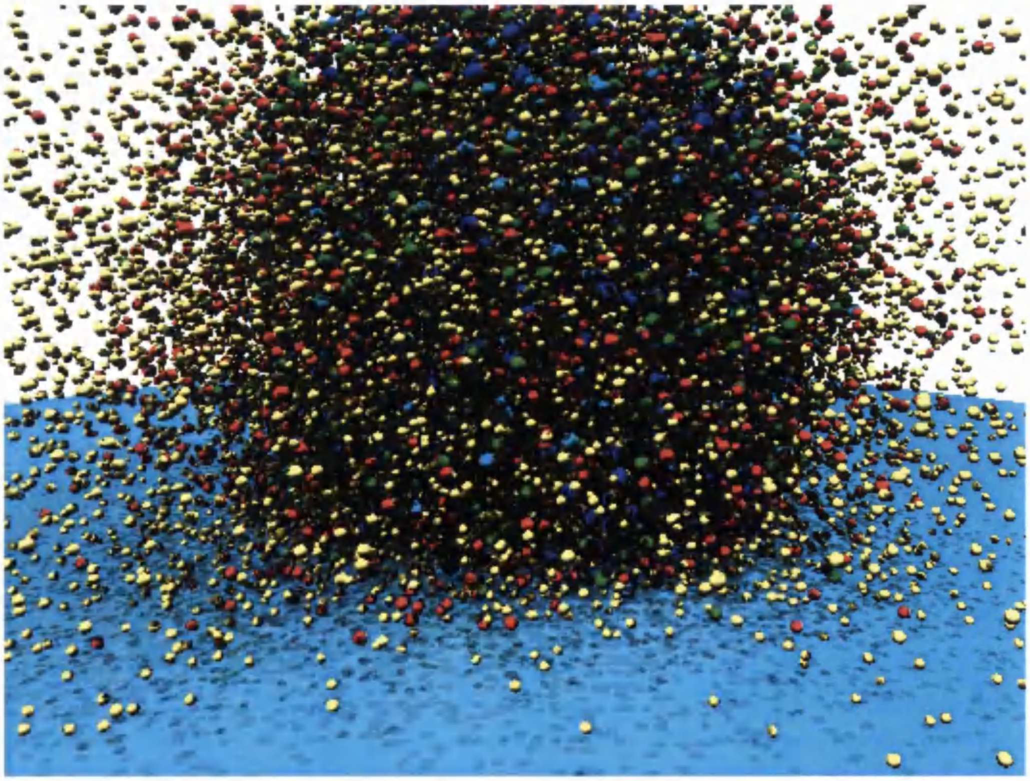

Figure 115: Inter element rejection resulting from high capillary force at contact overlap

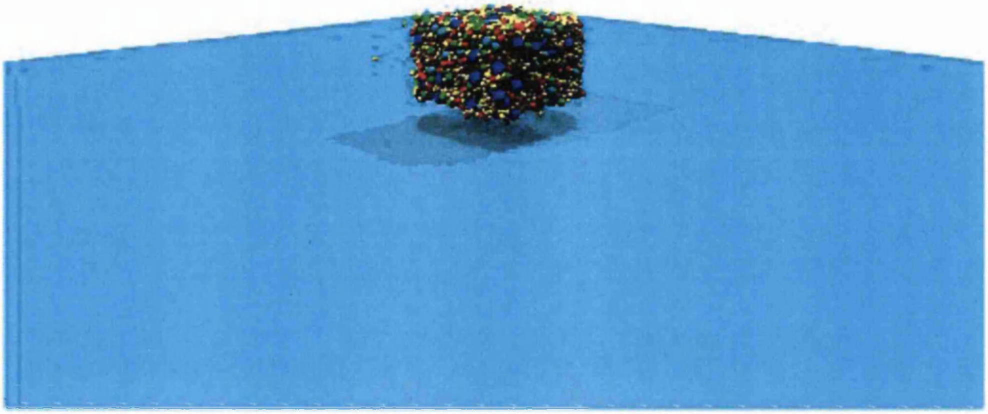

Figure 116: High element bonding due to exaggerated capillary force reducing to zero at surface contact.

In *Figure 115* a high integer multiple was introduced into the Laplace equation to simulate a high bonding condition. However, the contact overlap used in the soft sphere method produced a high negative attractive force at surface penetration (particularly between larger and small elements) and this resulted in an explosive reaction.

In *Figure 116* the same high integer multiple was applied to the capillary equation but on this occasion the force calculation was reduced to zero at surface contact by introducing a ratio of initial moisture surface contact (*as shown in Figure 100*), and the incrementally decreasing distance as the elements approach each other. This resulted in an extremely high attractive force between the elements that remained predominantly positive and produced a rigid cuboid, resembling the primary box shape.

Ultimately, setting the correct input parameters and the method discussed in *Figure 116* the simulation accuracy progressed.

4.7: Implementation of stereolithography (STL) CAD files to generate boundary walls.

For the successful application of a simulation technique of this type into a diagnostic engineering tool, manual boundary wall construction to create a domain was a highly inefficient process. To address this problem stereolithography (STL) files were used as a method of generating multi wall domains with complex nature if required. The basic function of this type of file is explained as follows:

4.7.1: The Function of Stereolithography (STL) CAD files

A Stereolithography (STL) file is formed as an output file for a standard 3D computer design program, for this case 3D Solid Works was used. The basic format of the file is a set of 3D triangular Cartesian coordinates and the corresponding surface unit normal ordered by the right-hand vector rule.

```
facet normal 4.922138e-001 8.525393e-001 -1.757906e-001
    outer loop
      vertex 3.500000e+003 4.400000e+003 4.000000e+003
      vertex 3.500000e+003 4.544338e+003 4.700000e+003
      vertex 3.750000e+003 4.400000e+003 4.700000e+003
    endloop
  endfacet
  facet normal 5.000000e-001 8.660254e-001 1.041605e-016
    outer loop
      vertex 3.500000e+003 4.544338e+003 1.000000e+004
      vertex 3.750000e+003 4.400000e+003 1.000000e+004
      vertex 3.500000e+003 4.544338e+003 4.700000e+003
    endloop
  endfacet
```

Figure 117: A section of an STL file showing the surface (facet) normal and the nine coordinate required for a triangular section

As explained in earlier text the basics behind the 3D current DEM code for boundary interaction is based on the interconnecting triangular sections in *x, y and z* directions. Boundary configurations are read by the Fortran code and are categorised into a results file. The similarities to the format of an STL file makes the two boundary wall input files compatible and interchangeable. As a result of this, an extracted STL can be used to produce a boundary wall arrangement in the current DEM code from a 3D design drawing with any level of complexity.

4.7.2: Implementation of and STL file for the Roll Feeder and Segregation plate

The importance in this type of development can clearly found in the sophistication of the simulation structure that is achievable. This allows a far more representative simulation with high detail and accurate data analysis in key points of interest. Crucially, this method of domain construction can be carried out easily by an expert in the field of 3D design and manipulated with the instruction of an engineer to assess equipment

The results of this development in terms of the segregation plate are as follows:

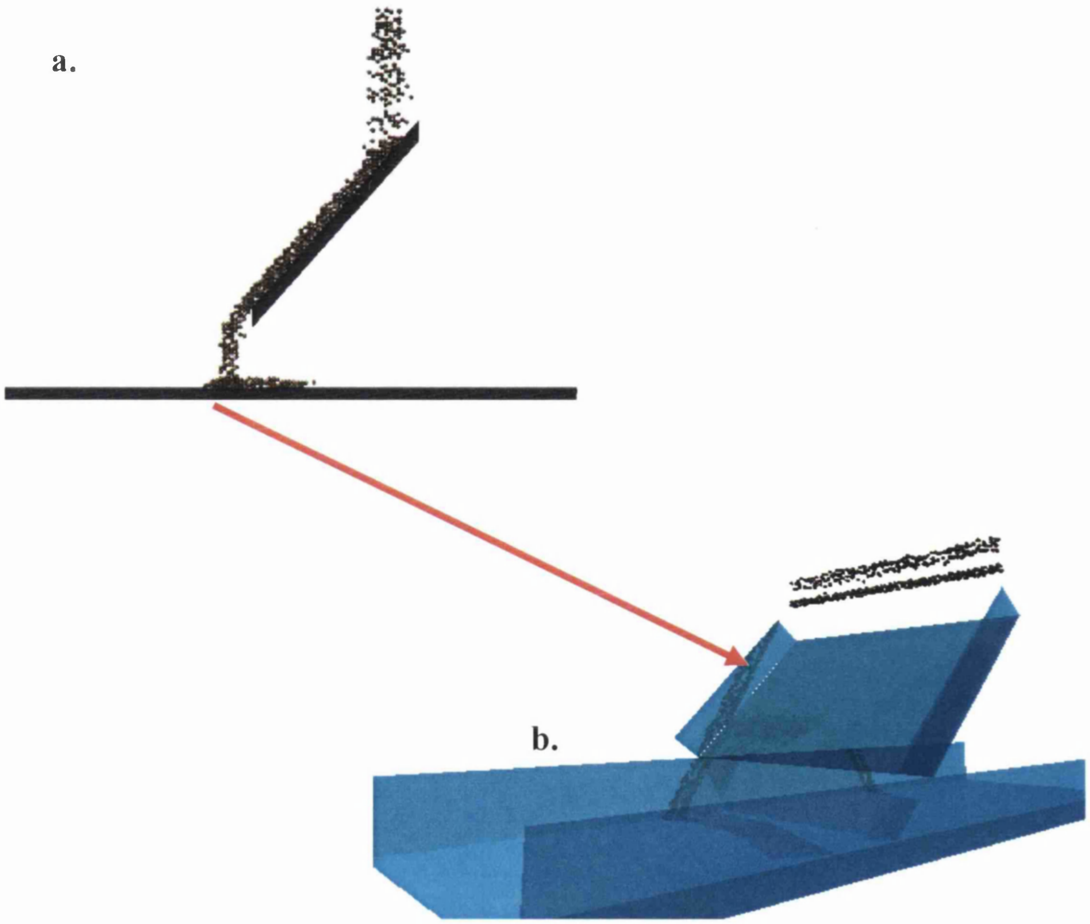

c.

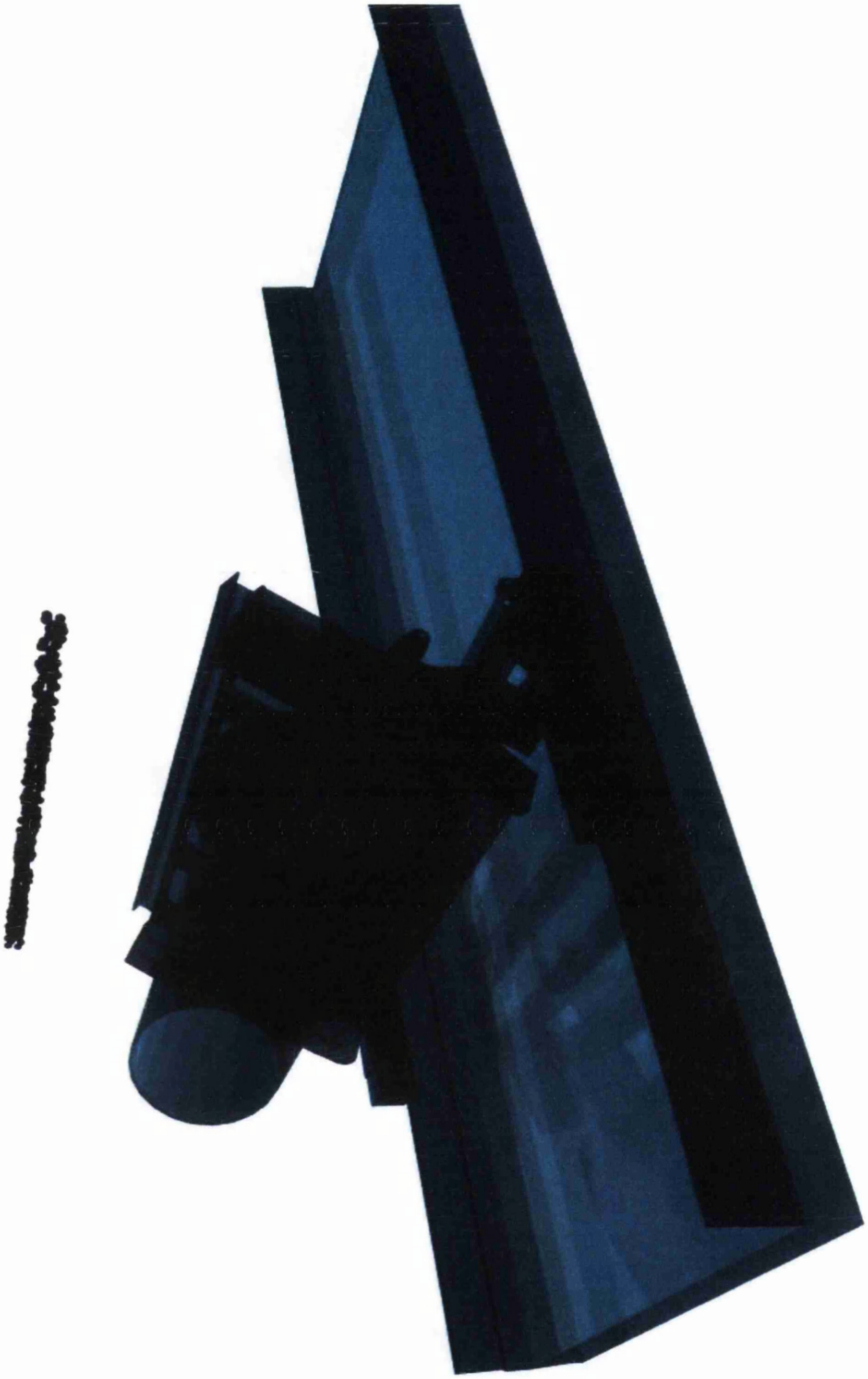

Figure 118: The images shown in a, b and c are the developmental levels in the boundary generation

One of the only drawbacks in using this method of domain generation was that high detail design drawing use large amounts of triangular sections to produce a shape. This had a detrimental effect on the CPU time due to the unnecessary calculation time being devoted to insignificant boundary walls. Limiting the number of sections was achievable by selecting coarse representations and in the main this type of detail was extremely adequate. However, when situations required cylindrical simulation the coarse type representation failed to serve its purpose due to the high detail needed to form a smooth circular surface.

To counteract this problem the following cylindrical generation method was adopted:

4.8: Cylinder Generation

Cylinder generation for this project was an important concept due to the simulation subject matter. The Roll Feeder in the Sinter Plant (as shown in *Figure 118c*) comprises a 4m long cylindrical unit and each conveyor belt assembly runs over a series of cylindrical drum ends. All of these systems rotate and affect the motion of the particulate flow, to replicate this form of transition an independent mechanism was mathematically introduced for rotating cylinders.

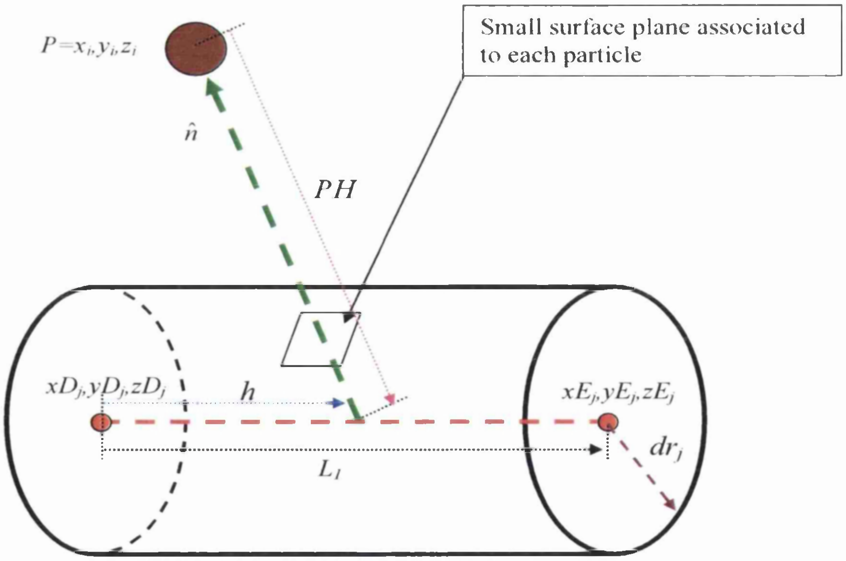

Figure 119: Particle cylinder search mechanism

The schematic diagram in *Figure 119* shows a basic cylindrical geometry and the key values for the cylinder simulation are the positions of the end centres and the cylinder radius.

Where:

L_1 is the distance between cylinder ends

h is the distance from the cylinder start point to the perpendicular contactor on L_1

xD_{ijk} are the coordinates of the cylinder start point

xE_{ijk} are the coordinates of the cylinder end point

dr_j is the cylinder radius

P is the positional coordinates of an impacting element.

PH is the distance from the centre line to the centre of the element

Using the information displayed in *Figure 119* a 3D region can be generated that creates a cylindrical shape. For this program the shape was produced by associating an individual small plane to an impacting element at a circular radial distance from the centre line. Using this basis and the orientation of the vector linking the centre line to the centre of the element, a cross product calculation returns the gradient of the plane. At cylinder-element contact the reaction force follows the surface Normal and the motion becomes physical.

The cylinder generation is presented as follows:

$$L_1 = \left[\begin{pmatrix} xD_j \\ yD_j \\ zD_j \end{pmatrix} + t\begin{pmatrix} xE_j - xD_j \\ yE_j - yD_j \\ zE_j - zD_j \end{pmatrix}\right] \qquad (4.107)$$

Because *H* lies on the line L_1 and t has yet to be determined then:

$$H = \begin{pmatrix} x_i \\ y_i \\ z_i \end{pmatrix} + P\vec{H} \longrightarrow P\vec{H} = -\begin{pmatrix} x_i \\ y_i \\ z_i \end{pmatrix} + \left[\begin{pmatrix} xD_j \\ yD_j \\ zD_j \end{pmatrix} + t\begin{pmatrix} xE_j - xD_j \\ yE_j - yD_j \\ zE_j - zD_j \end{pmatrix}\right] \qquad (4.108)$$

Note:

To find t: $P\vec{H}\; perp\, to\; L_1$

$$P\vec{H} \bullet \left[\begin{pmatrix} xE_j - xD_j \\ yE_j - yD_j \\ zE_j - zD_j \end{pmatrix} \right] = 0 \tag{4.109}$$

$$\left[-\begin{pmatrix} x_i \\ y_i \\ z_i \end{pmatrix} + \begin{pmatrix} xD_j \\ yD_j \\ zD_j \end{pmatrix} + t \begin{pmatrix} xE_j - xD_j \\ yE_j - yD_j \\ zE_j - zD_j \end{pmatrix} \right] \bullet \left[\begin{pmatrix} xE_j - xD_j \\ yE_j - yD_j \\ zE_j - zD_j \end{pmatrix} \right] = 0 \tag{4.110}$$

$$\left[\begin{pmatrix} -x_i + xD_j \\ -y_i + yD_j \\ -z_i + zD_j \end{pmatrix} \begin{pmatrix} xE_j - xD_j \\ yE_j - yD_j \\ zE_j - zD_j \end{pmatrix} + t \begin{pmatrix} (xE_j - xD_j)^2 \\ (yE_j - yD_j)^2 \\ (yE_j - yD_j)^2 \end{pmatrix} \right] = 0 \tag{4.111}$$

$$t = \frac{-[(xD_j - x_i)(xE_j - xD_j)] - [(yD_j - y_i)(yE_j - yD_j)] - [(zD_j - z_i)(zE_j - zD_j)]}{(xE_j - xD_j)^2 + (yE_j - yD_j)^2 + (zE_j - zD_j)^2} \tag{4.112}$$

Therefore:

$$\left| P\vec{H} \right| = \sqrt{\left[(xD_j - x_i + (xE_j - xD_j)t)^2 + (yD_j - y_i + (yE_j - yD_j)t)^2 + (zD_j - z_i + (zE_j - zD_j)t)^2 \right]} \tag{4.113}$$

For particle cylinder contact:

$$r_i + PH - dr_j \leq 0 \tag{4.114}$$

$$\begin{aligned} e_1 &= (xE_j - xD_j) \cdot t \\ e_2 &= (yE_j - yD_j) \cdot t \\ e_3 &= (zE_j - zD_j) \cdot t \end{aligned} \tag{4.115}$$

$$\begin{aligned} e_4 &= (-x_i + xD_j) + e_1 \\ e_5 &= (-y_i + yD_j) + e_2 \\ e_6 &= (-z_i + zD_j) + e_3 \end{aligned} \tag{4.115a}$$

$$e_n = \sqrt{e_4^2 + e_5^2 + e_6^2} \tag{4.115b}$$

$$Cos_x = \frac{e_4}{e_n}, \quad Cos_y = \frac{e_5}{e_n}, \quad Cos_y = \frac{e_6}{e_n}$$

From here the cylinder surface interaction follows the same principles as a plane contact interaction with the corresponding forces associated to it. However, to generate a rotational motion of the cylinder surface the orthogonal vector to L_1 was calculated using a cross product.

$$|L_1| = \sqrt{(xE_j - xD_j)^2 + (xE_j - xD_j)^2 + (xE_j - xD_j)^2} \tag{4.116}$$

$$vC_1 = \frac{xE_j - xD_j}{|L_1|}, \quad vC_2 = \frac{yE_j - yD_j}{|L_1|}, \quad vC_3 = \frac{zE_j - zD_j}{|L_1|} \tag{4.117}$$

$$\begin{bmatrix} i & j & k \\ vC_1 & vC_2 & vC_3 \\ Cos_x & Cos_y & Cos_z \end{bmatrix} \tag{4.118}$$

$$\begin{aligned} eC_1 &= (vC_2 \cdot Cos_z) - (vC_3 \cdot Cos_y) \\ eC_2 &= -[(vC_1 \cdot Cos_z) - (vC_3 \cdot Cos_x)] \\ eC_3 &= (vC_1 \cdot Cos_y) - (vC_2 \cdot Cos_x) \end{aligned} \tag{4.119}$$

The simulated surface velocity of the rotating cylinder can then by applied by introducing it as component of force in the direction indicated by (4.120) i.e.

$$\frac{\lfloor (v_{cyl} \cdot eC_1) - vx_i \rfloor \cdot m_i}{dt}, \frac{\lfloor (v_{cyl} \cdot eC_2) - vy_i \rfloor \cdot m_i}{dt}, \frac{\lfloor (v_{cyl} \cdot eC_3) - vz_i \rfloor \cdot m_i}{dt} \tag{4.120}$$

The cylinder surface direction is determined by the selection of the starting coordinates of the cylinder *(xD$_j$, yD$_j$, zD$_j$)* and the selection of the vector orientation with the "Right Hand Rule".

4.9: Energy Transfer from Particle-Boundary Contact Interaction

The dynamic motion of particulates through bulk handling equipment will be responsible for large amounts of energy transfer to the system if allowed to impact.

Impacting particulates in this case are macroscopic, have mass and varying velocities. Energy transfer under these conditions can be presented in a number of ways:

- Noise generation
- Atmospheric dust production
- Localised wear points at high impact ratios
- Material compaction and avalanche

Energy dissipation of the type discussed above has been approached in earlier sections, however, noise generation and localised wear points are discussed further in terms of kinetic energy transfer:

Where Kinetic Energy E_k is:

$$E_k = \frac{1}{2} m_i \left| \bar{v}_i^2 \right| \tag{4.121}$$

4.9.1: Energy Transfer from a Particle to Flat Inclined Plane

In the situation depicted in *Figure 120* the particle falls under gravity and impacts with the plane surface. Due to the reaction forces and low angle of incidence the particle recovers its potential energy and moves onto the next contact.

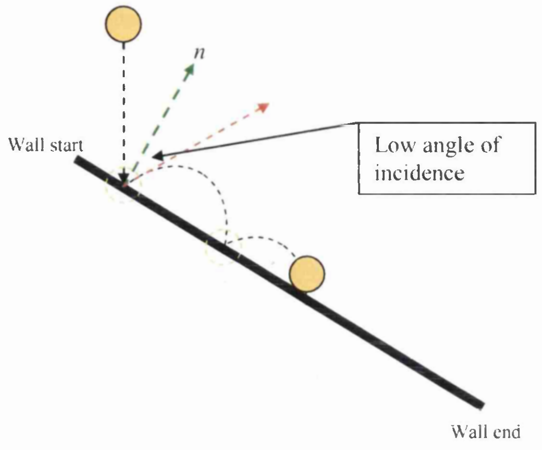

Figure 120: A Particle falling under gravity onto an inclined plane

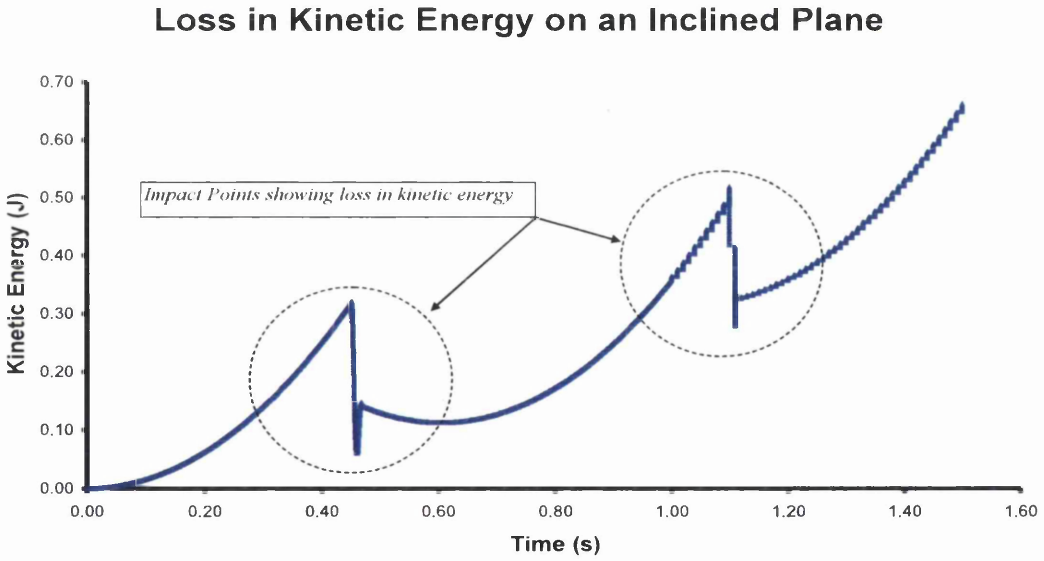

Graph 2: Energy loss on an inclined plane

4.9.2: Energy Transfer from a Particle to Curved Plane

The particle again falls under gravity from the same coordinates as shown in *Figure 121*. However, the initial contact with the curved plane has a large angle of incidence resulting in a low reaction force at the normal to the plane in this position. This results in a glancing contact and the particle is guided to the wall end.

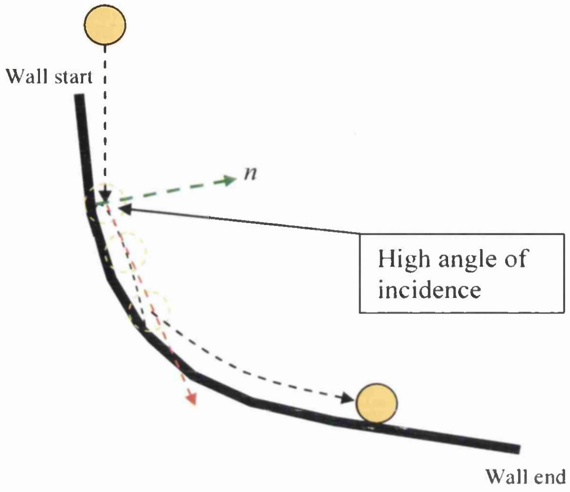

Figure 121: Particle falling under gravity onto a curved plane

The graphical representations of these simple scenarios show a differing interpretation of energy transfer at each impact point. For the inclined plane case the large peaks in the trend line show a high impact due to the low incident angle and in the curved boundary the large incident angle around the normal minimises the particle penetration and guides the particle along.

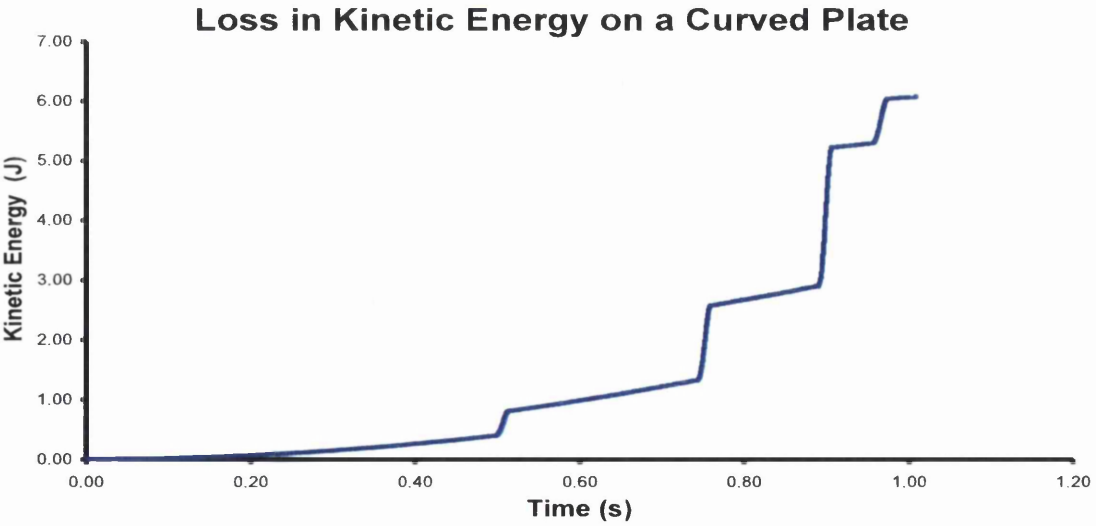

Graph 3: Particle impacting with a curved plane

The curvature in the latter case encourages a smoother transition between the wall ends and maintains the kinetic energy carried with the particle. As the kinetic energy is proportional to the velocity squared the particle in effect retains its velocity and moves more efficiently from point to point.

To look at this phenomenon through a real material handling design a simulation was carried out using 1004 head chute with and without curved inserts. Data was extracted relating to energy transfer and the resulting graph was produced.

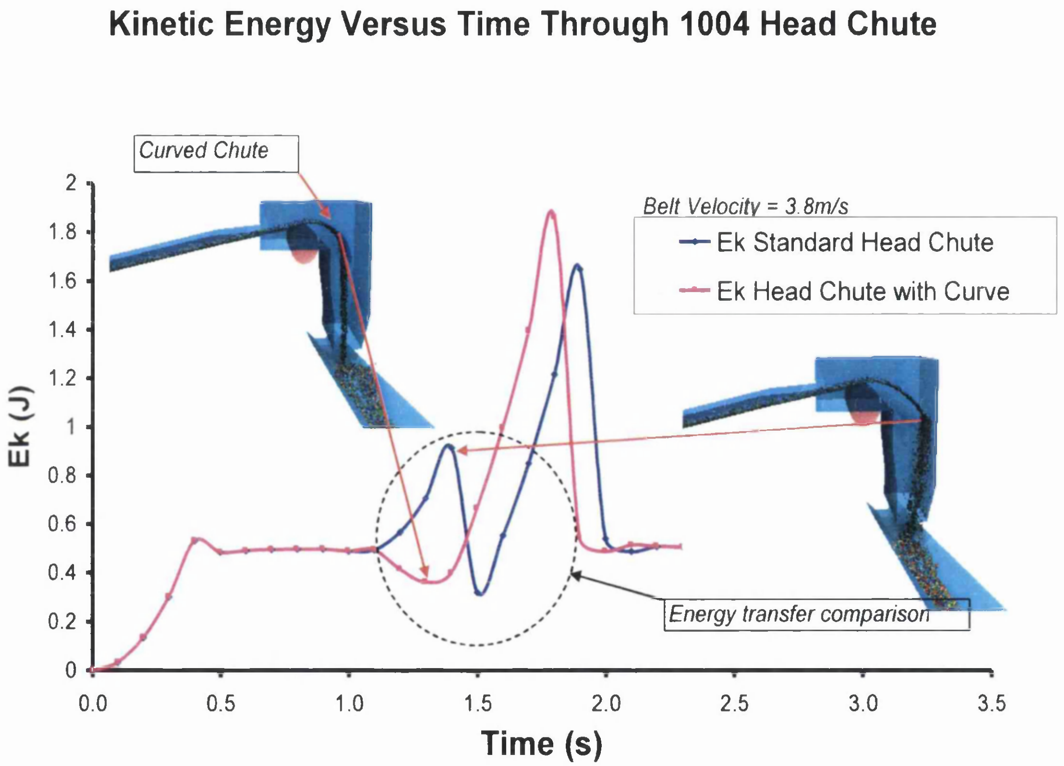

Graph 4: Particle transition through 1004 head chute and corresponding kinetic energy trend

The data threads produced in the 1004 head chute simulation were used in a comparison of controlled and uncontrolled flow. From *Graph 4* the blue trend line is related to the standard head chute as per construction. The pink trend line was produced with data from the controlled flow using a curved chute insert.

Using the energy transfer comparison section and the inset images, one can clearly see that the uncontrolled flow data exhibits large peaks in the blue trend line. This is due to the resultant velocity increase from the end of the conveyor to the back of the head chute wall.

The rapid decrease in the kinetic energy could be attributed to the high impact at the point of boundary contact and the resulting change in momentum.

In comparison the pink trend line takes an immediate drop in kinetic energy as the conveyor is left. This is also an energy transfer but is related to the frictional forces restricting motion over the surface of the curved chute insert. Minimising the drop or maintaining the level of kinetic energy at this point could be a mechanism for determining the efficiency of the insert.

Ultimately, the graphs show that the translational motion of the particulate flow through the simulation domain is controlled better by the influence of the curved insert. The main factor is velocity retention in the particles motion; this reduces impact and allows a smoother transition.

To further quantify the energy transfer at a boundary interface, the global simulation domain was sub divided into cubic sections. The kinetic energy values associated to an impact were recorded at each cubic cell and tabulated for summation.

4.10: Summation of Energy Transfer from an Impacting Particle in boundary contact.

The motion of elements through a simulation domain can be visualised in term of flow patterns and areas that restrict movement by high impact. To numerically quantify the passage of elements though a given 3D region information was drawn from element-boundary contact interaction and the subsequent transfers of kinetic energy. To obtain the data following method was adopted:

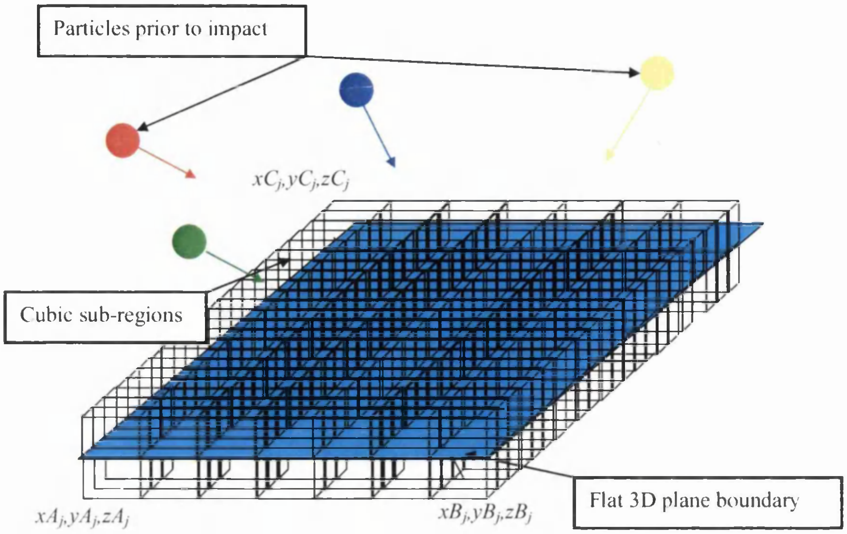

Figure 122: Particle prior to contact interaction with a flat plane

In *Figure 122* the particles are in motion and have varying masses, therefore they carry kinetic energy prior to impact with the flat boundary wall. The boundary plane itself cuts though the global domain and is bounded by a series of interconnecting cubic sub regions.

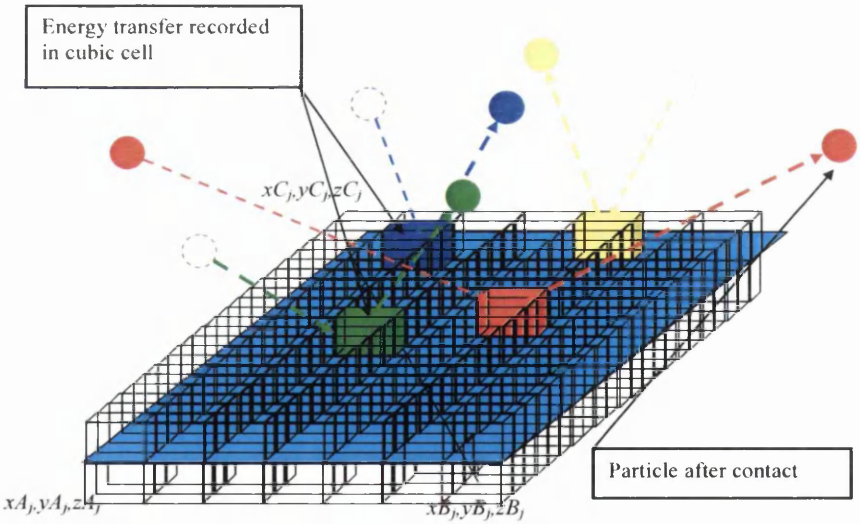

Figure 123: Particles recording a Kinetic Energy transfer at a coordinate grid reference

The schematic shown in *Figure 123* is the post collisional result of the particle impact with the boundary plane. At each contact interaction the particle penetration is converted into a real number quantity relating to the amount of kinetic energy (*using (4.121)*). The kinetic energy value is then recorded within the cubic sub region coordinate and entered into an array. Any subsequent impacts in the same cell are summed together to produce a distribution of energy transfer in any simulation domain to determine the efficiency of particulate transition.

5. PROGRAM VALIDATION AND CALIBRATION

In this section a "simulation model" validation is offered using the influence of frictional forces on how theoretical DEM elements react when formed into heaps. To validate against previous work the angles of repose from the horizontal plane are measured and comparisons were made.

The angles of repose in granular material are a well documented physical anomaly and are apparent in studies involving avalanche, segregation, packing[93] and arching effects in hopper discharge[94]. The major contributing factors to the value of the repose angle can be found in capillary forces generated by small amounts of liquid[94] and the frictional forces between a particle and neighbour and a particle and boundary[95].

The frictional forces addressed in this DEM model have focused mainly on resistance to translational motion and limited attention has been drawn to rotational frictional forces. However, the variations in surface frictional force play a pivotal role in particulate motion and are shown here to affect the angles of repose. In addition variations in particulate diameter also determine the development of a repose angle and this situation was investigated in terms of a set of numerical experiments.

Therefore, for model validation using repose angle:

1. Contact interaction frictional forces were varied numerically.
2. Spherical discrete elements size was altered by using different spherical diameters.

Using the findings from *1 & 2* the results were tabulated for comparisons against published data.

5.1 Experimental Procedure

Practical experimental work was carried out by Zhou *et al*[95] (1999)[96] using a rectangular container with a Perspex viewing window to initiate a particle cascade.

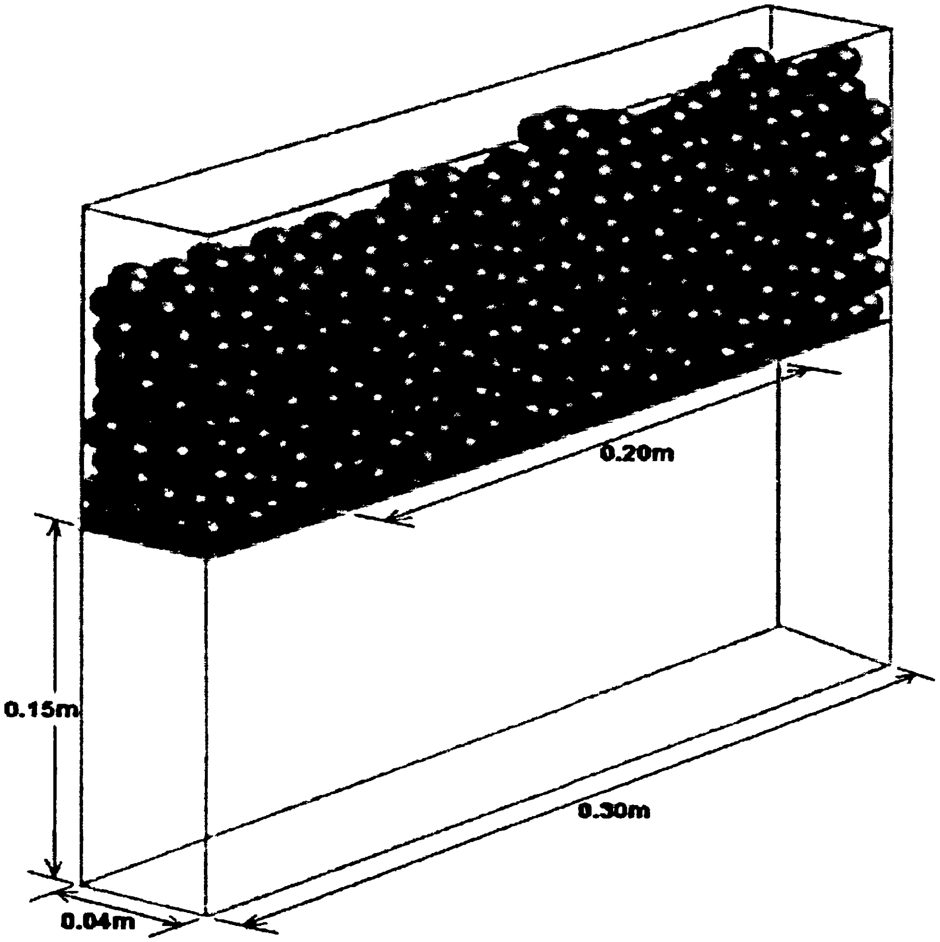

Figure 124: Schematic image of rectangular container with particle packing[95][96]

From the initial conditions shown in *Figure 124* the particles were released and allowed to cascade over a central shelf and this formed a stagnant zone with a corresponding angle of repose.

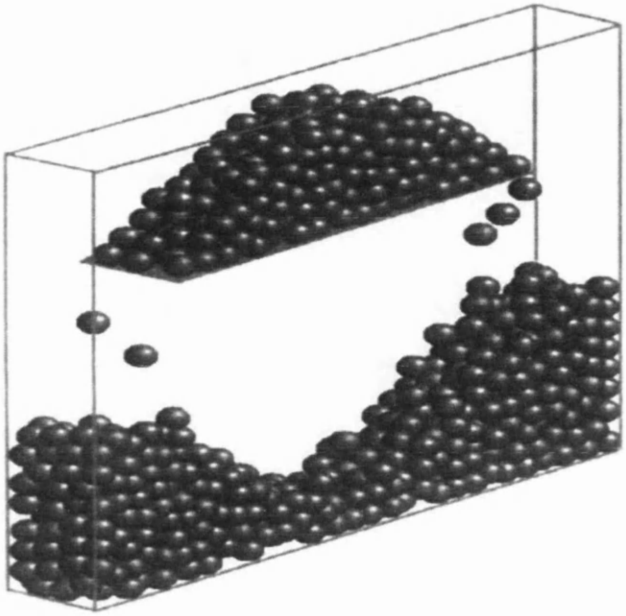

Figure 125: Schematic image of particle cascade over the central shelf producing a stagnant zone[95][96]

5.1.2 Practical results and simulations

The practical experiments used glass beads with diameters of 6mm and 10mm with densities of 2500 kgm^{-3} and a container width of 40mm.

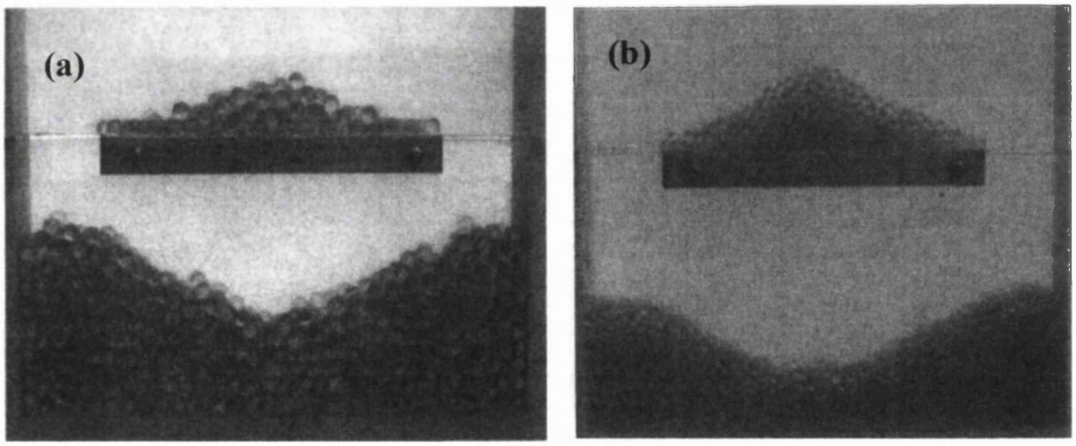

Figure 126: Experimental results showing stagnant zones with (a) 10mm beads and (b) 6mm beads[95]

In *Figure 126* the bead size in (a) and (b) are clearly shown to affect the angle of repose produced at the stagnant zone. The 10mm cascade used 1154 beads and the 6mm cascade used 4000 beads.

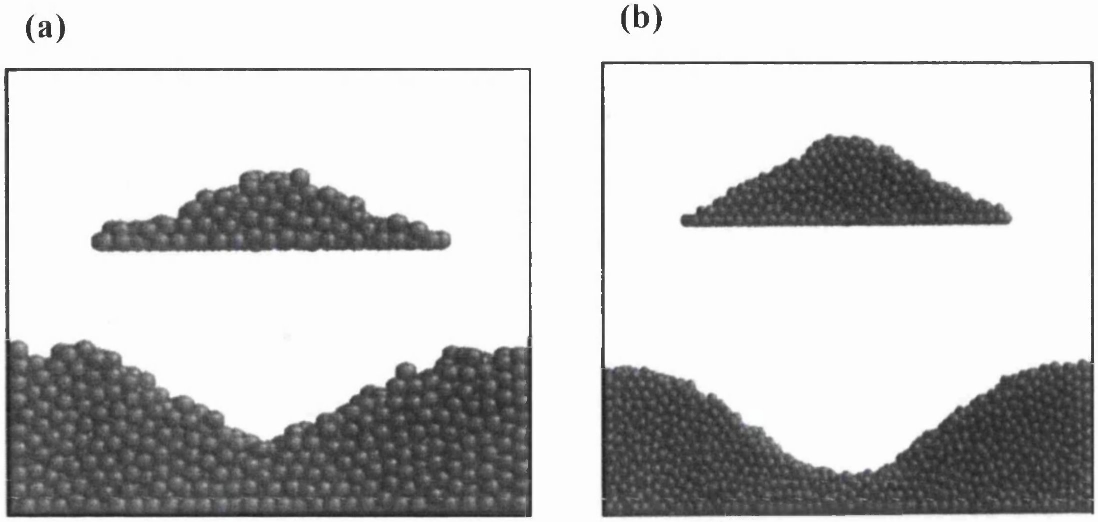

Figure 127: Simulation results produced by *Zhou et al*[95] using 10mm and 6mm particle respectively

The simulation comparisons in *Figure 127* with the practical experimental results are remarkably similar with the angles of repose developed at the stagnant zone showing a realistic angular formation.

Physical parameters used in the simulations where:

Variables		*Values*
Particle density-	ρ	$2500\ kgm^{-3}$
Young's Modulus of particle or wall-	E	$10^6\ Nm^{-2}$
Poisson ratio of particle or wall-	υ	*0.3*
Particle-particle frictional coefficient-	μ_{spp}	*0.4*
Particle-wall frictional coefficient-	μ_{spw}	*0.7*
Particle-particle damping coefficient-	c_{spp}	$0.4\ kgs^{-1}$
Particle-wall damping coefficient-	c_{spw}	$0.7\ kgs^{-1}$

Table 2: Variables used in the simulations shown in *Figure 124*

Where:

$C_{spp} = C_{spw} = C_t = C_n$

5.2 3D DEM Model Comparison

To compare simulation results a rectangular boundary section with 40mm width was produced using an STL file. For this simulation the number of particles (N) was N =2000 and two methods of filling the box section were used and compared:

Method 1: Particles were generated over the top of the central shelf to fill the voided space.
Method 2: Particles were continuously produced at the top centre of the box section until particles spilled over the sides of the shelf and into the bottom of the box.

5.2.1 Angle of repose using particle cascade (Method 1)

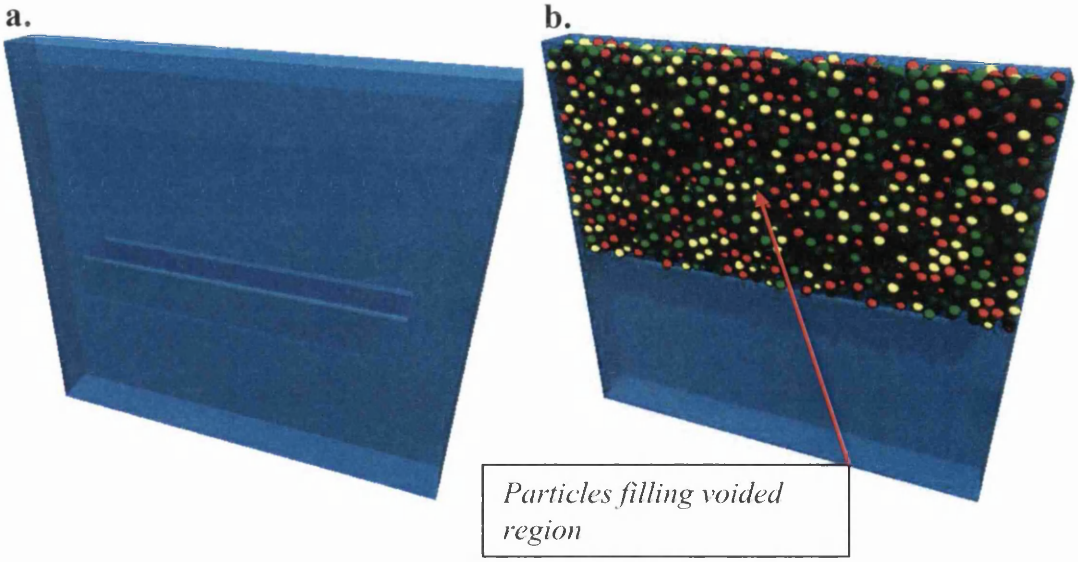

Figure 128: Rectangular box simulation domain with particle generation over central shelf

Note: The variation in particle colour relates to "Particle Size Distribution" (PSD). For this simulation the range was 0.01m ± 0.001m diameter. The object of this was to improve visual interpretation.

At the start of the simulation the particles were allowed to fall under gravity in a cascade generating a stagnant zone on the central shelf.

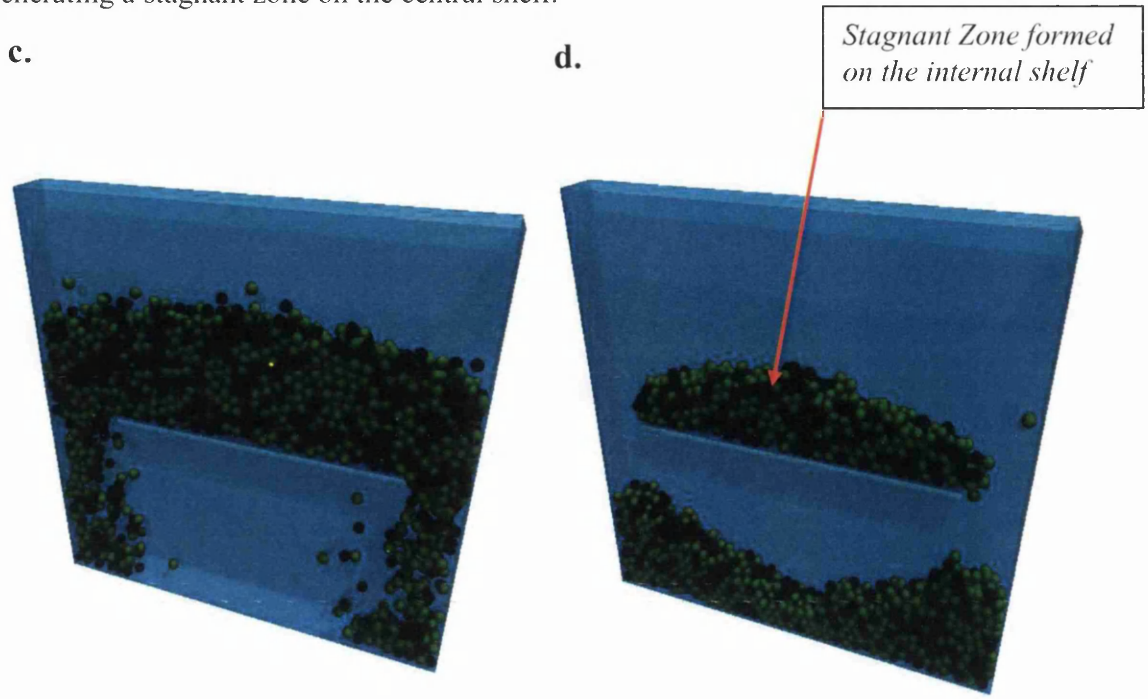

Stagnant Zone formed on the internal shelf

Figure 129: Particle cascade develops a stagnant zone

The above simulation was carried out using the values displayed in Table 2 with particle diameter of 0.01m (10mm) and number of particle $N = 2076$.

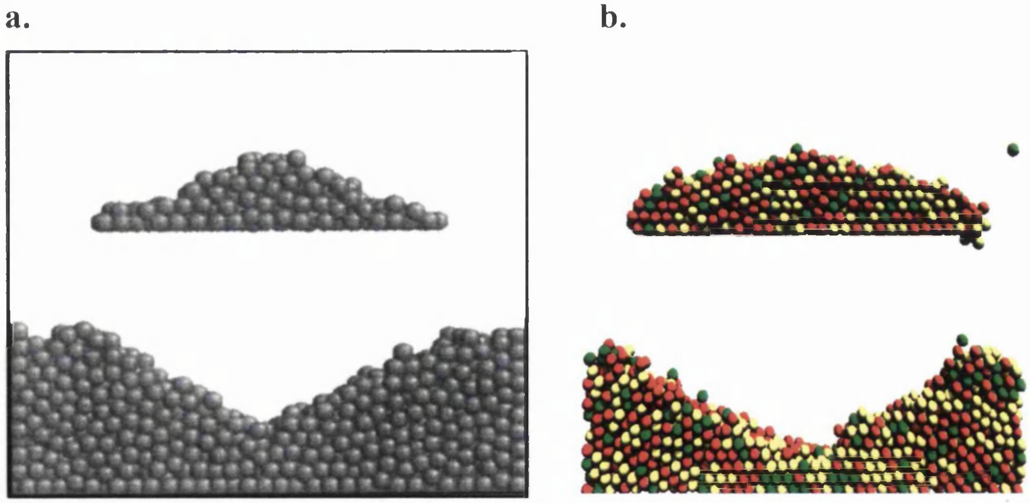

Figure 130: Simulation comparison using Method 1

In *Figure 130* the current DEM simulation model using Method 1 failed to produce a measurable angle of repose (*as shown in "b"*) for comparison with the simulation results produced by Zhou *et al*[95] (*as shown in "a"*)

5.2.2 Angle of repose using particle generation (Method 2)

For Method 2 a particle generation region (*as discussed in 3.2.3*) was opened at the top centre of the simulation domain. Particles were allowed to build-up on the central shelf producing a stagnant zone. Residual particles reaching the end of the shelf fall over the edge and gather in the bottom of the domain. The simulation images in *Figure 131-132* show a particle generation method taking place as opposed to the particle cascade simulation. The particle properties here are the same as expressed in Table 2 and for this simulation the particle generation is terminated at $N \sim 2000$.

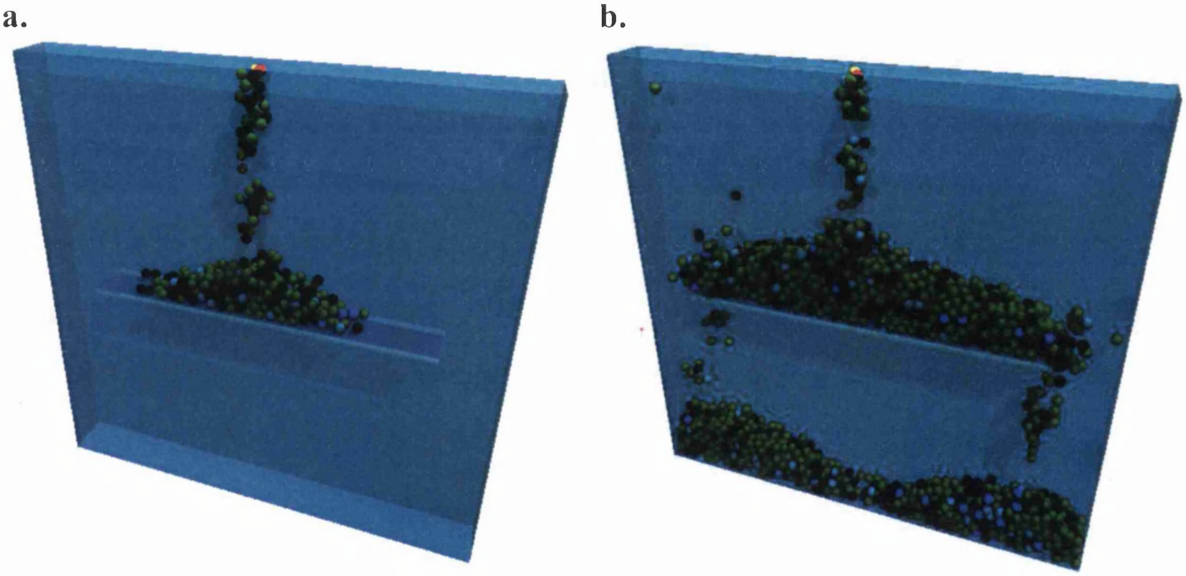

Figure 131: Simulation domain with particle generation collecting on the central shelf and over flowing into the bottom of the domain

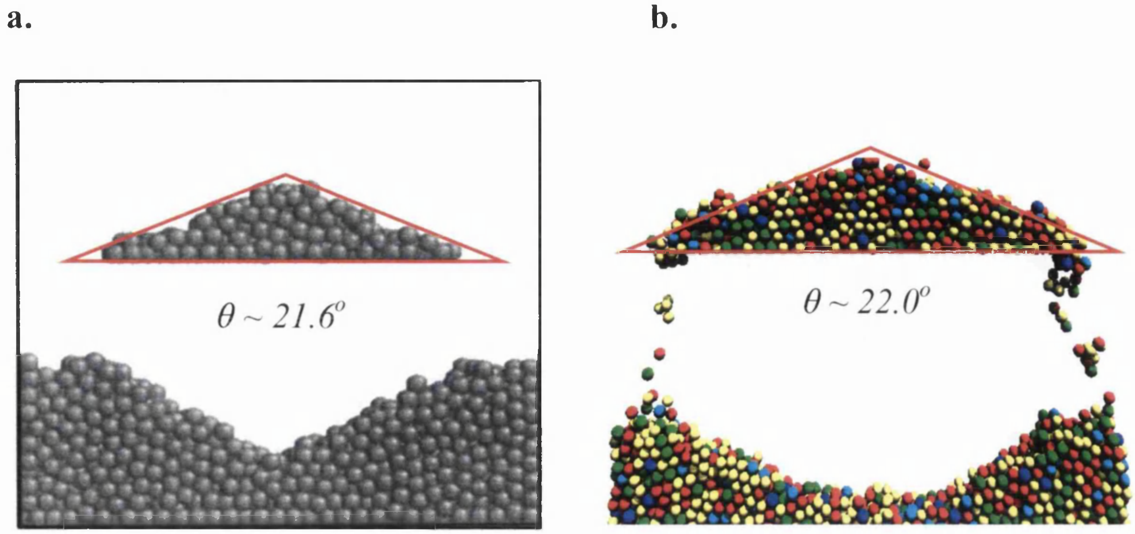

Figure 132: Simulation comparison using Method 2

The simulation slide in *Figure 131a* showed an angle of repose being created on the central shelf almost immediately. As the particles built-up the end of the shelf was reached and the excess particles can be seen to fall into the bottom of the domain. At the point where *N=2000* the particle generation was stopped.

An individual result from the simulations is shown in *Figure 132b* from a front elevation perspective with clear walls. The image shows an angle of repose produced by the falling particles, similar to the theoretic interpretation generated by *Zhou et al*[95] depicted in *Figure 132a*.

To quantify the result the dimensions of the triangular outline superimposed onto the particle heaps were recorded and showed that in:

- *Figure **132a** θ **~ 21.6 degrees***
- *Figure **132b** θ **~ 22.0 degrees***

This indicates that the current DEM program closely matches the results produced by *Zhou et al*[95] in the simulation model.

5.2.3 Frictional forces and angle of repose

In this section frictional forces between particle-particle interactions and particle-boundary interactions are varied with resulting effects on particle build up. Comparisons were made with further work undertaken by *Zhou et al*[95] in 2002 using a predictive equation for angular repose in differing conditions.

$$\vartheta_{rep} = \mu_{s,pp}^{0.27} \times \mu_{s,pw}^{0.22} \times \mu_{r,pp}^{0.06} \times \mu_{r,pw}^{0.12} \times d^{-0.2} \tag{5.1}$$

Using *Equation (5.1)* the following table and resulting graph was produced showing the influence of particle-particle and particle-boundary frictional forces on the angle of repose.

Angle of Repose values produced using equation (*5.1*)				
Sliding Friction PW (μ(spw)	***Ang Rep μ(spp)= 0.2***	***Ang Rep μ(spp)= 0.3***	***Ang Rep μ(spp)= 0.4***	***Ang Rep μ(spp) =0.5***
0	*0.0*	*0.0*	*0.0*	*0.0*
0.1	*15.9*	*17.8*	*19.2*	*20.4*
0.2	*18.5*	*20.7*	*22.4*	*23.7*
0.3	*20.3*	*22.6*	*24.4*	*26.0*
0.4	*21.6*	*24.1*	*26.0*	*27.7*
0.5	*22.7*	*25.3*	*27.3*	*29.0*
0.6	*23.6*	*26.3*	*28.5*	*30.2*

Table 3: Angles of repose using variations in particle-particle / particle wall forces

Where:

$\mu_{s,pp}$ = coefficient of particle-particle sliding friction

$\mu_{s,pw}$ = coefficient of particle-wall sliding friction

$\mu_{r,pp}$ = coefficient of particle-particle rolling friction

$\mu_{r,pw}$ = coefficient of particle-wall rolling friction

As used in:

- *Graphs 4-5*
- *Tables 3-5*

Note: the rolling frictional forces in this graphical analysis are kept constant at 0.05mm.

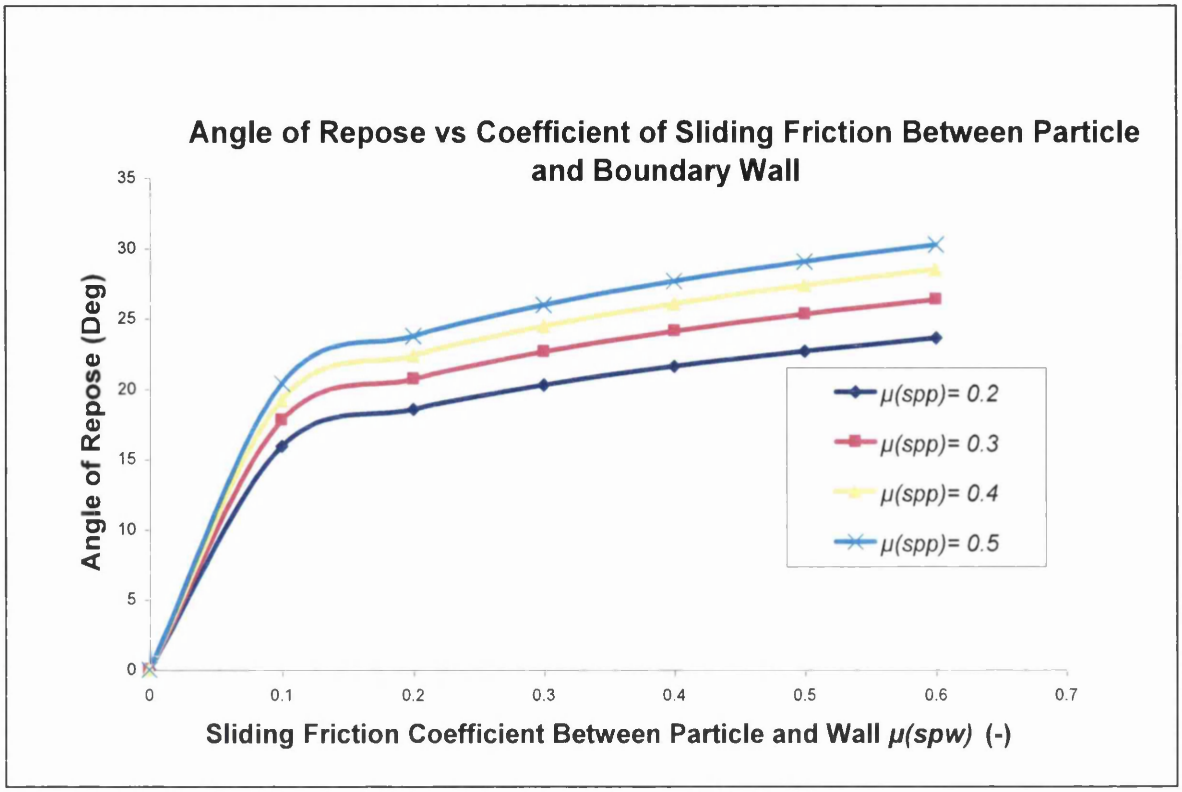

Graph 5: Graph of predicted angle of repose with varying sliding frictional forces (*Zhou et al*[95])

The data displayed in *Graph 5* was the theoretical repose angles values produced using *Equation (5.1)* and these can also be seen in *Table 3*. The table and graph presented here were constructed to replicate the graphical data presented by *Zhou et al*[95] for the effect of particle-particle, particle boundary frictional forces on DEM simulated particle heaps.

To compare the current DEM programs' performances against the values produced in *Graph 5* the following parameters were used (*shown in Table 4*) and were applied to a model with varying frictional forces.

Table 4: Parameters used for angular comparisons

Name of variable	***Symbol***	***Base Value***	***Variable Range***	***Angle of Repose (Deg)***
Number of Particles	*N*	*~2000*	-	
Time Step	Δt	$\sim 5 \times 10^{-5} s$	-	
Particle Diameter	*d*	*10mm*	*2-10mm*	*[38,28]*
Rolling Friction Coefficients	μ_{rpp} μ_{rpw}	*0.05mm* $2\ \mu_{rpp}$	*0-0.1mm* *0-0.2mm*	*[0,34]* *[0,30]*
Sliding Friction Coefficients	μ_{spp} μ_{spw}	*0.4* $1.5\ \mu_{spp}$	*0-0.6* *0-0.6*	*[0,33]* *[0,28]*

5.2.3.1 Program application with varying frictional forces

To relate values from the DEM model to the graphical representation, the parameters shown in *Table (4)* were applied to the current program and the resulting simulations were analysed. The values for the angles of repose produced in this method were tabulated (*Table 5*) and were introduced into *Graph 5* for comparison with the *Zhou et al*[95] trend-lines. This was a simulation experiment and the conclusions were displayed in *Graph 5*

The simulation experiment was carried out as follows:

The program was calibrated for the simulation by setting spin and capillary interactions with the maximum sliding frictions such that the simulation angle of repose represented the maximum parameters in *Table (3).* Frictional forces were then reduced to zero and variable increments were introduced generating angular changes.

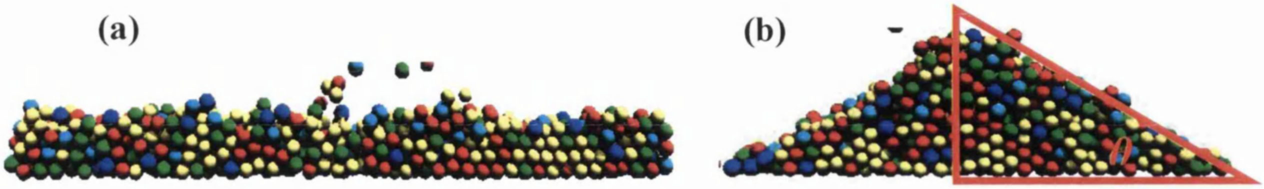

Figure 133: Extremes in the simulation angular results.

In *(a)* the frictional forces were set at zero while in *(b)* the Particle-particle frictional force was set at 0.4 and the particle-wall friction was set at 0.6

The angle of repose in (a) is nonexistent
The angle of repose in (b):

$$\vartheta \cong Tan^{-1}\left(\frac{2.35}{4.05}\right) \therefore \vartheta \cong 30^{0}$$

The same process was conducted over a range of frictional increments and the corresponding table and graph were produced.

Table 5: Simulation results of angle of repose

Angle of Repose Simulation Results				
Sliding Friction PW	***Ang Rep μ (spp) 0.2***	***Ang Rep μ (spp) 0.3***	***Ang Rep μ (spp) 0.4***	***Ang Rep μ (spp) 0.5***
0	*0*	*0*	*0*	*0*
0.1	*16*	*17.8*	*20.4*	*21*
0.2	*18.2*	*19.8*	*22*	*23.5*
0.3	*19.7*	*22.4*	*24*	*26*
0.4	*21.3*	*24.6*	*26.3*	*27.2*
0.5	*22.4*	*25*	*26.8*	*28.7*

Applying the data in *Table 5* to *Graph 6* for comparison with *Graph 5*

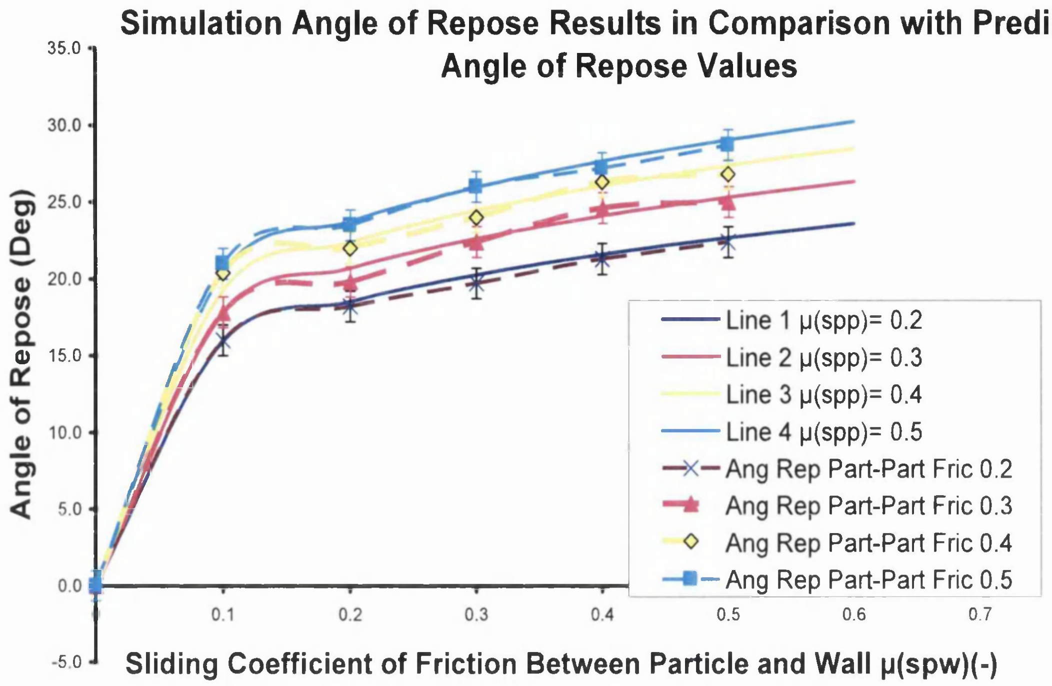

Graph 6: Simulation results displayed against predicted trend lines

Using the current DEM program the same frictional force variations used by *Zhou et al*[95] were applied and the resulting repose angles were recorded and displayed in *Table (5)*. The simulation values were then introduced into the graphical data for *Graph 5* and were displayed in *Graph 6* as dashed lines.

In comparison:

X is related to line 1

▲ is related to Line 2

◇ is related to Line 3

□ is related to Line 4

From *Graph 6* the simulated data closely followed the respective trend lines showing a good correlation with the *Zhou et al*[95] predicted data. This clearly showed that the frictional force changes in the current DEM program functioned in an acceptable manner for validation.

Error bars in Graph 6 were related to visual interpretation of repose angles: ± 1.0 degrees

5.2.4 Particle size and angle of repose

Using *Equation (5.1)* the angle of repose can be shown to decrease with particle size. This is suggested to be due to sliding frictional forces reducing at surface contact as the particulates become larger.

To produce this effect the frictional values in *Equation (5.1)* were kept constant and "*d*" *(particle diameter)* was varied from 1mm through to 10mm.

The simulation using the model program functioned in the same manner and held the coefficients of sliding friction at:

Particle-particle: 0.4
Particle-wall: 0.6

Table 6: Simulation results and predicted angular calculation with varying particle size

Particle Size mm	***AngRep (Predicted (Deg))***	***Ang Rep from Simulation Results (Deg)***
0	*0*	*0*
1	*33.8*	*32.6*
2	*29.4*	*28.6*
3	*27.1*	*26.8*
4	*25.6*	*25.2*
5	*24.5*	*24.6*
6	*23.6*	*24*
7	*22.9*	*23.2*
8	*22.3*	*22.3*
9	*21.8*	*22.4*
10	*21.3*	*21*

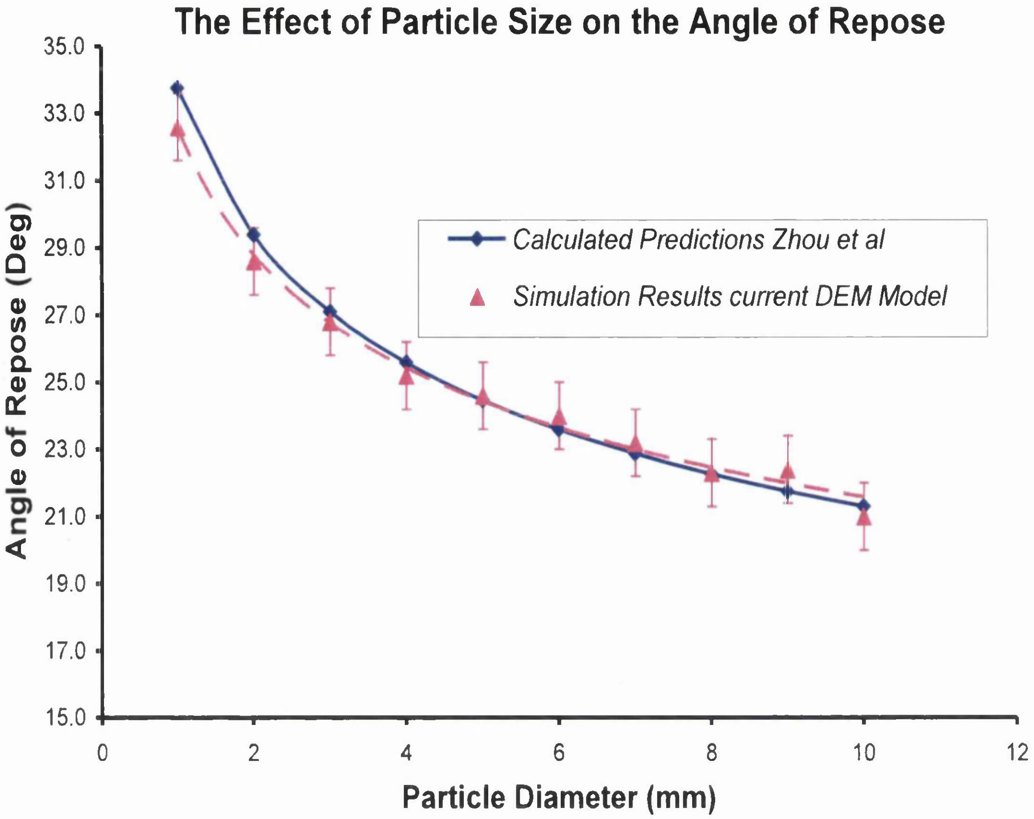

Graph 7: Simulated angles of repose using increasing particle diameter against predicted values.

With respect to particle size affecting repose angle, *Equation (5.1)* was again used with the contact frictional forces held constant. As discussed the value for "*d*" was incremented from 1mm through to 10mm and the predicted values were recorded. Simulations were then preformed using the current DEM model with same incremental changes and the resulting angles of repose were recorded for comparison.

Error bars in Graph 6 were related to visual interpretation of repose angles: ± 1.0 degrees

Graph 7 shows the predicted data trend and the simulated data is transposed over the top. The negative trends in both of the data streams correlated well showing that the angle of repose reduced as the particle diameter *"d"* increased.

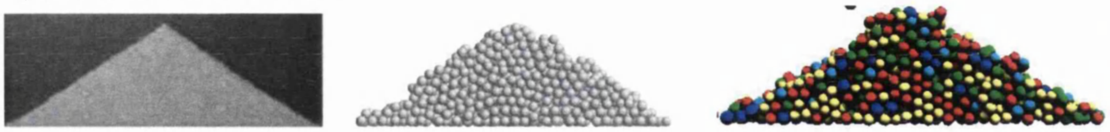

(a) 2mm Particle diameter

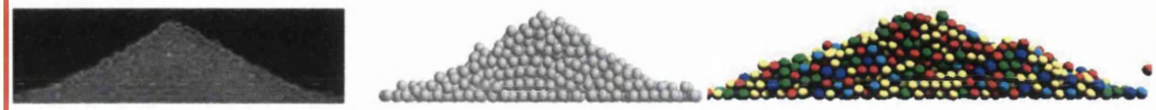

(b) 5mm Particle diameter

Figure 134: Experimental and simulation results by *Zhou et al*[95] and the corresponding current DEM simulation results

Figures 134 (a) and *(b)* are drawn from the experiments and simulations carried out by *Zhou et al*[95] and the corresponding simulations are generated using the current DEM model.

5.3 DEM Model Calibration using "Angle of Repose"

In terms of calibrating a simulation against particulate material properties the angle of repose can be view as a useful value. As shown, material properties vary with particulate size and contact forces. Creating an initial set of parameters prior to running a simulation could significantly improve accuracy and simulation results.

To consider this, bulk material deposits develop an angle of repose when laid on the ground. The angle of repose and general geometry of the deposit can be used to estimate the quantity and how it interacts with the local environment. The information extracted at this stage could be used as a mechanism to determine the correct conditions of a simulation process.

The following images show particulate "Angle of Repose" and the corresponding DEM Initial conditions:

To generate the simulated angles of repose depicted here, it was essential to introduce a capillary force. Angles of repose in simulation terms do not form unless treated in this manner.

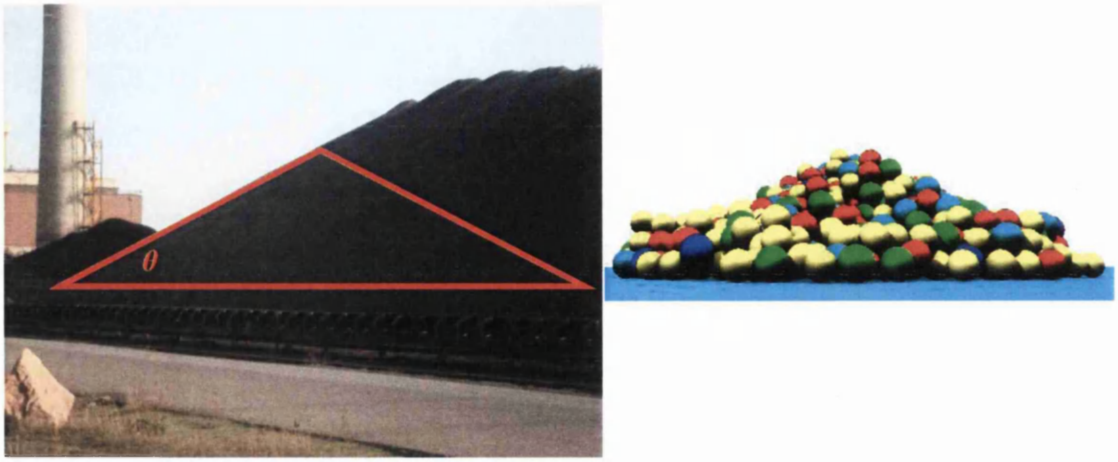

Figure 135: Iron Ore Pellets θ = 27 degrees and DEM simulation θ = 26 degrees

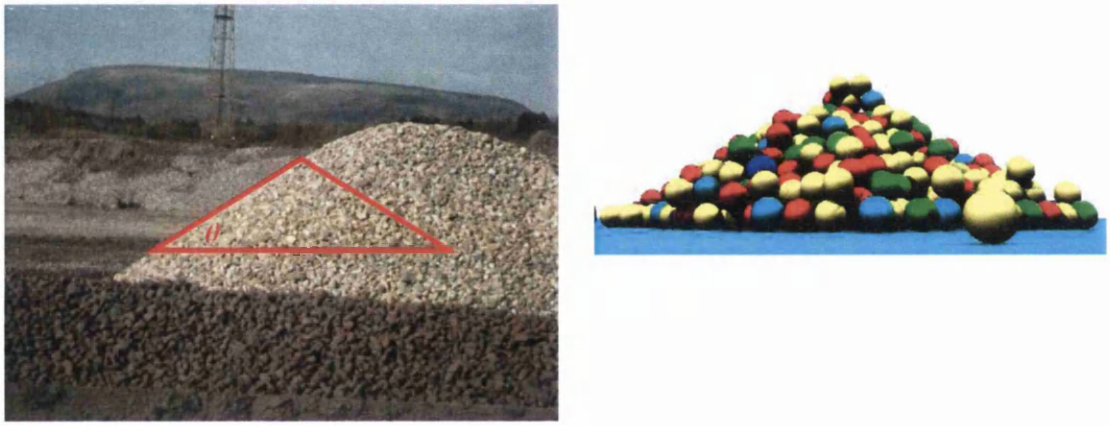

Figure 136: Lime θ = 32 degrees and DEM simulation θ = 31 degrees

Figure 137: Coal θ = 41 degrees and DEM simulation θ = 43 degrees

5.3.1: Benefits of using particulate "Angle of Repose"

The real images shown in *Figures 135-137* are material deposits forming natural angles of repose relating to their particulate size and general condition. If the material is moved without any specific preparation the same angles of repose will be created at another storage point. This knowledge could be used to set the properties of a material to better replicate the translational motion of a flow through a given domain.

The simulation images presented in *Figures 135-137* were produced on a plane surface with no other boundary constraints and a variation of inter-particle/particle-boundary forces.

To generate the differing repose angles considered are 3 main factors:

- *Frictional forces between particle surfaces*
- *Friction at particle and boundary contact*
- *Capillary forces due to moisture content*

Considering the three examples with constant particle diameter of 10mm:

Pellets:

- *Frictional coefficient particle-particle 0.25*
- *Frictional coefficient particle-boundary 0.4*
- *1% moisture addition for capillary force*

Lime:

- *Frictional coefficient particle-particle 0.3*
- *Frictional coefficient particle-boundary 0.5*
- *5% moisture addition for capillary force*

Coal:

- *Frictional coefficient particle-particle 0.4*
- *Frictional coefficient particle-boundary 0.6*
- *10% moisture addition for capillary force*

This concept fits into the simulation process by setting the basic material data in the model and was used when calibrating the simulation conditions for lime in the 633-634 head chute project investigations

6. PROJECT APPLICATIONS USING THE 3D DEM PROGRAM

Over the period of this project there have been a number of opportunities to test and apply the fundamentals of the developed program against real on plant situations and problems. As discussed previously, this type of involvement tended to set different targets and challenges for the DEM models to overcome. This ultimately focused the program structure into a relatively flexible multi-functional version and one that was capable of visually interpreting a solution.

In this section a “Deep Water Harbour” spillage investigation is used as an example of applied modelling.

6.1 Deep Water Harbour Spillage Investigation Introduction and Background

The deep water harbour facility is used to import the raw material products using vessels with displacements in excess of 190,000 tonnes and capable of carrying cargoes of 150,000 tonnes plus into Port Talbot. The grab discharging system is a proven technique, however on some occasions (driver error or grab damage) raw material falls from a traversing grab and gathers on the quay side or fall into the deepwater pocket.

Figure 138: Three harbour ship unloaders working on the Berge Atlantic

The majority of the cargos handled in this way are reclaimed but the loss of cargos over the side of the jetty is pure cargo loss and is very difficult to calculate.

Figure 139: Grab moves along a gantry boom carrying material over to the unloader hopper

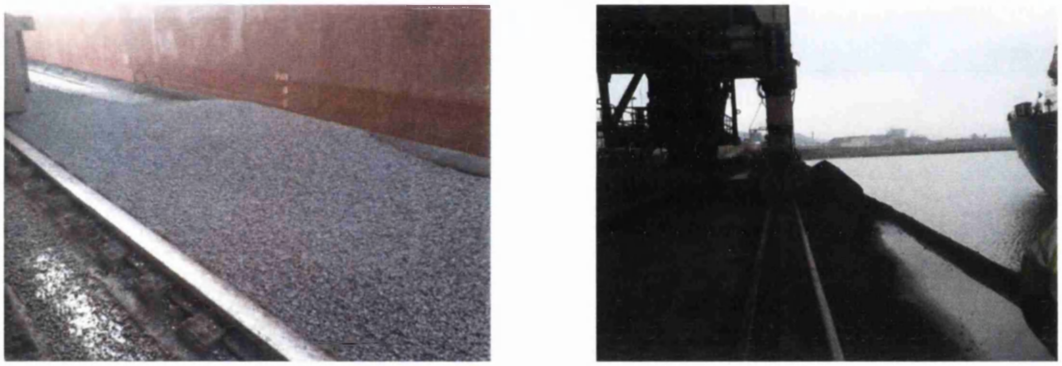

Figure 140: The above images show material deposits on the nearside of the jetty with spillage angles into the harbour

The photographic images shown in *Figure 140* indicate how raw material falling from a travelling grab has a tendency to build to a high level and spill into the harbour following the repose angle. As the unloader travels along the jetty tracks to the next discharge hold the material is reclaimed by contractors. The amount of spillage is small in proportion to the cargo on a vessel but due to the cleaning pattern spillage volumes are particularly hard to quantify. This is an ongoing inefficient process and required investigation.

6.1.1: Suggested spillage solution

The design drawing in *Figure 141* is a CAD representation of the No5 unloaders superstructure, discharge hopper and static conveyor belt system. The suggestion put forward was to utilise the large box section beam on the seaward side of the unloader to filter freefalling material through the gap and back onto the conveyor.

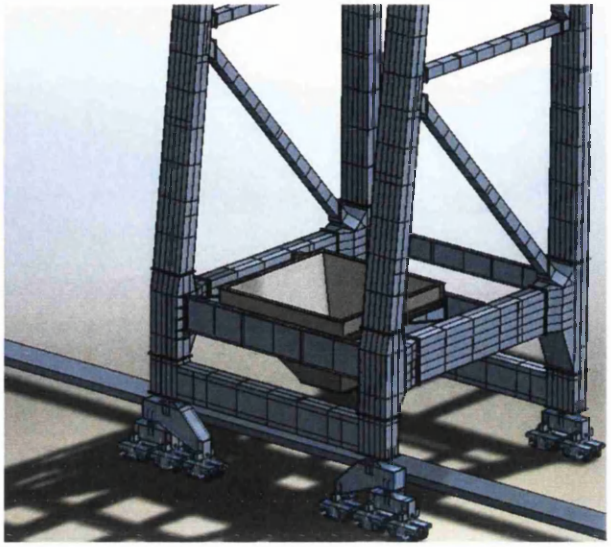

Figure 141: CAD image of No5 unloader showing hopper and conveyor belt system

The idea was to feed an inclined chute over the beam at a given angle that lead onto the conveyor and yet overlapped the nearside of the jetty.

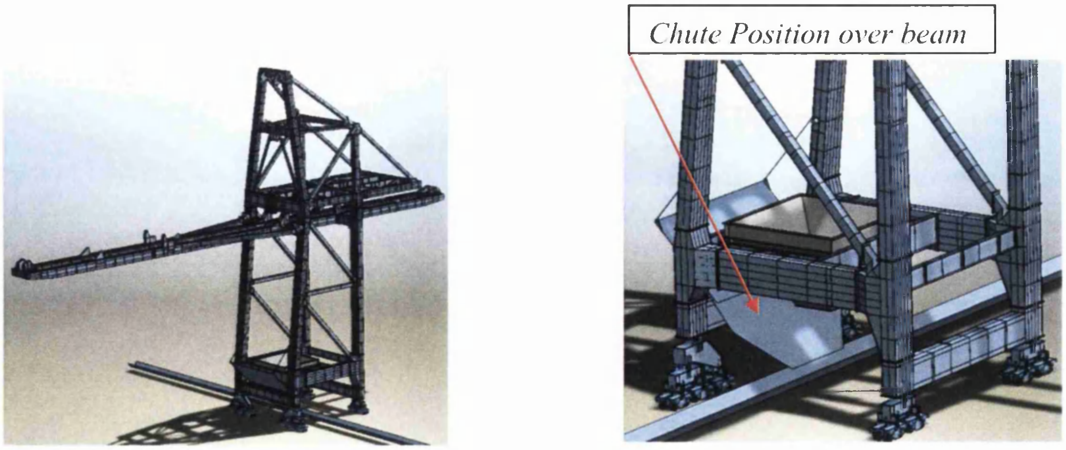

Figure 142: CAD images showing No5 unloader with prototype chute insert

6.1.2: Basic 3D DEM unloader simulations

To complete the harbour spillage investigation a series of simulations were carried out to formulate a visual interpretation of the problem at hand. The simulation domain comprised the basic hopper shell and the key structural box section beams. A particle generation region was opened in a lateral bisecting centre line above the hopper and particles were produced.

The simulation slide in *Figure 143a* shows the particles falling from the generation region and partly falling into the hopper and partly onto the seaward side of the simulation domain. This highlights the impact zone when material is lost in the unloading process and closely resembles the situations of spillage discussed in *6.1*.

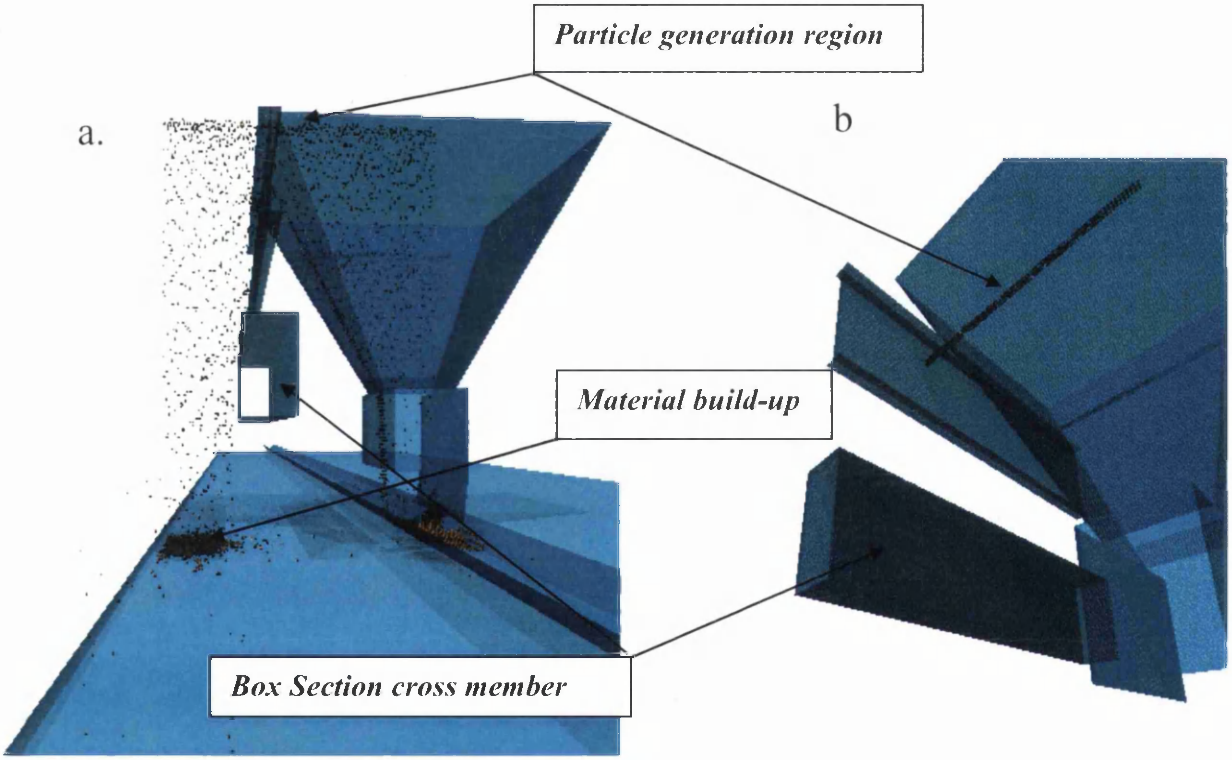

Figure 143: Simulation slides *a & b* show the material freefall without inclined chute

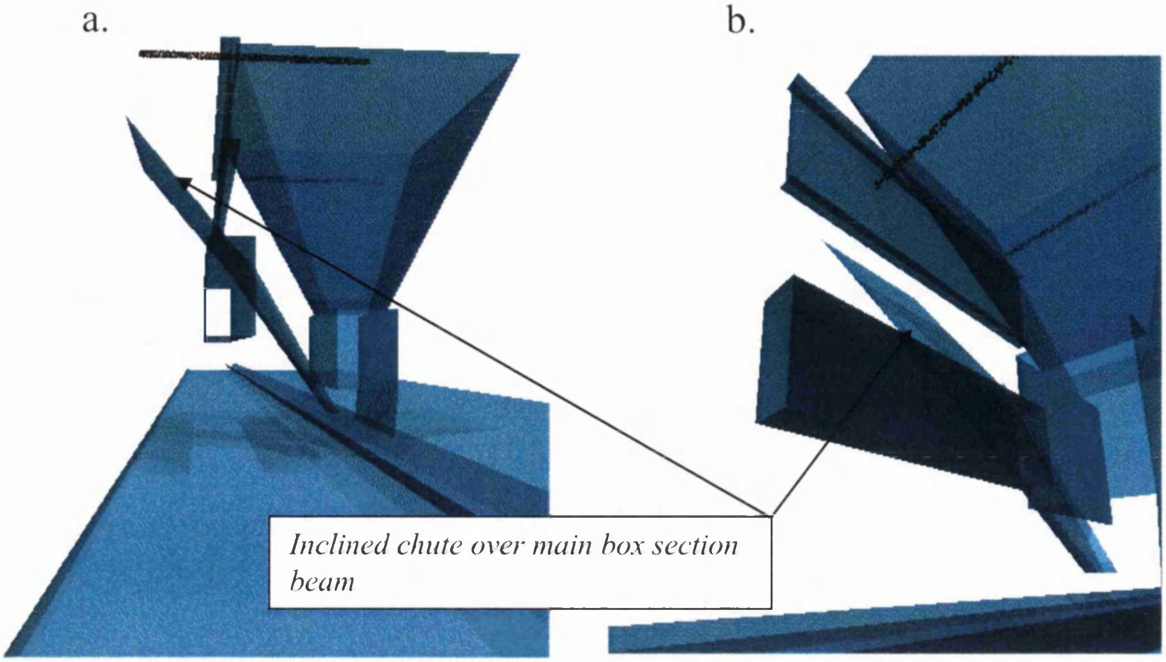

Figure 144: Basic unloader/hopper superstructure with inclined chute

In *Figure 144a & b* an inclined plate suggested as a new feature, sits on top of the main box section beam and extends onto the conveyor belt system. In *"a"* the maximum height of the chute falls in line with the top support of the hopper and this allows an overhang that protects the seaward side of the jetty. With this arrangement and the plate at angles greater than 65 Deg, material spillage from the grab unloaders should be directed away from the jetty impact zone and back onto the conveyor.

To confirm the possibility of making the suggested design change a more refined Solid Works 3D drawing was made with greater detail of small gauge superstructure that could hinder the chute implementation.

The results of which are shown here in *Figures 145 a & b*:

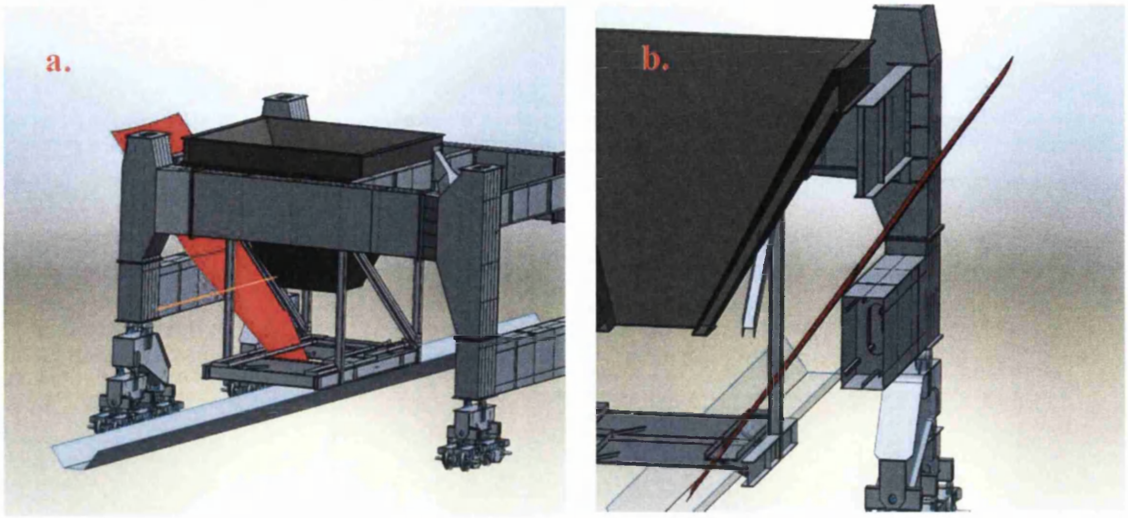

Figure 145:3D solid works drawing of chute design on No5 unloader

The results of the 3D solid works drawings of the chute design on No5 unloader showed that a chute angled at ~50° passed over the main box section beam (with clearance of the "I" section above it) through a maintenance walkway and on to the belt line. The overhang created by the chute on the seaward side had a span of 9m and this would protect the impact zone on the jetty floor from material build-up. The advantages in this application are the possible reduction in valuable raw material loss, minimisation of expensive cleaning operations and prevention of injury due to falling material.

6.1.3: Harbour spillage investigation conclusions

To consider fitting a chute design of this nature, one would have to calculate the additional weights and stresses applied to the unloader. The position and stowage of the chute in adverse weather condition would have to be accounted for due to the rapid environmental changes that occur on a daily basis. The chute over hang is a main feature of the design but limitations would have to be introduced to prevent vessels with high free board connecting with it over the large tidal range.

If the chute functioned as predicted and prevented material loss, valuable cargoes would all be discharged into the relative storage depots.

6.2: Basic Oxygen Steelmaking (BOS) Project Investigation

Basic Oxygen Steelmaking (BOS) essentially strips carbon from a carbon rich hot metal by blowing oxygen though it in an exothermal reaction to produce steel. This process is carried out in a 330 tonne ladle (Converter) and with an oxygen supply lance. Fluxes in the form of lime are also added to ensure the correct steel chemistry.

The application of key raw materials at the stage of the steel making process is a critical one and is responsible for ladle cooling (endothermic reactions) and ladle heating (exothermal reactions). Along with these control methods expensive ores are introduced for secondary steel making processes and metal alloying purposes. The main mechanisms used for transferring the raw materials to the converters are by a conveyor belt and head chute configuration and the transportation of lime is discussed in this section.

6.2.1: Basic Oxygen Steelmaking (BOS) Plant Head Chute Investigation

This BOS plant investigation focussed on 633 to 634 conveyor belt and head chute arrangement and its supply of lime to the converter. The lime product was seen as an ideal candidate for simulation due to its largely homogeneous size distribution and lack of water in suspension due to its chemical reactivity.

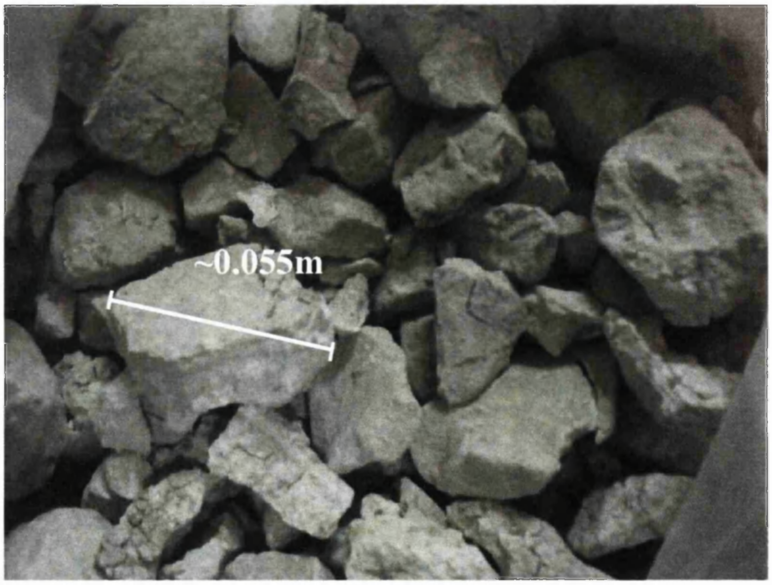

Figure 146: Typical lime sample showing size distribution

For the movement of lime through this system there are two major detrimental factors, they are found in the material degradation at impact (*work required to break contact bonds in inter-particle and particle-boundary breakage is proportional to the kinetic energy at impact*[97]) and the corresponding structural damage at specific high contact areas. The micro particle dust generation from the material impact is not only a health hazard but is lost during converter application via the fume extraction system.

6.2.2: Impact Damage on 633-634 Head Chute

At this particular part of the plant the lime flow rate is approximately 500 T/hour with a material density of between 2000~2400 kgm^{-1}. The nature of the material is highly abrasive and at points of high contact intensity causes significant wear damage due to direct correlation with impact angle as addressed in previous work in this field[98]. The primary areas of concern relating to the damage, are on internal structures and therefore difficult to observe or monitor.

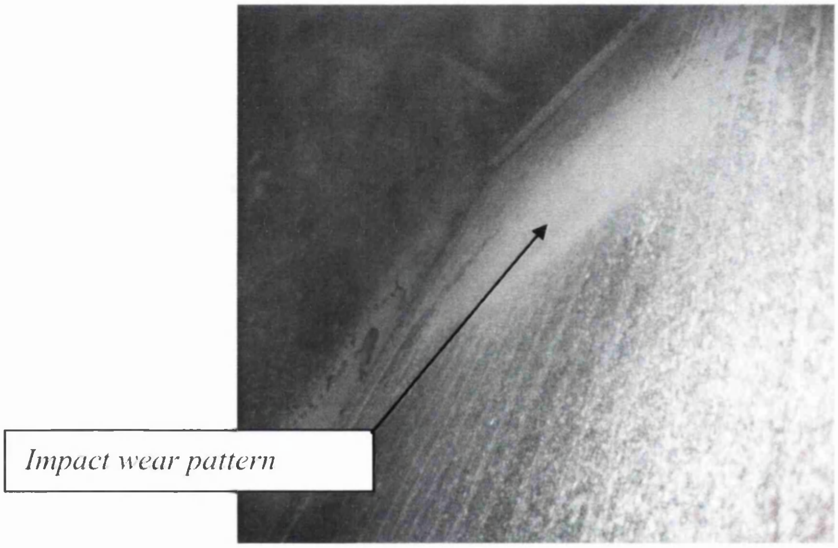

Figure 147: Impact damage on the 633 wear deflector plate

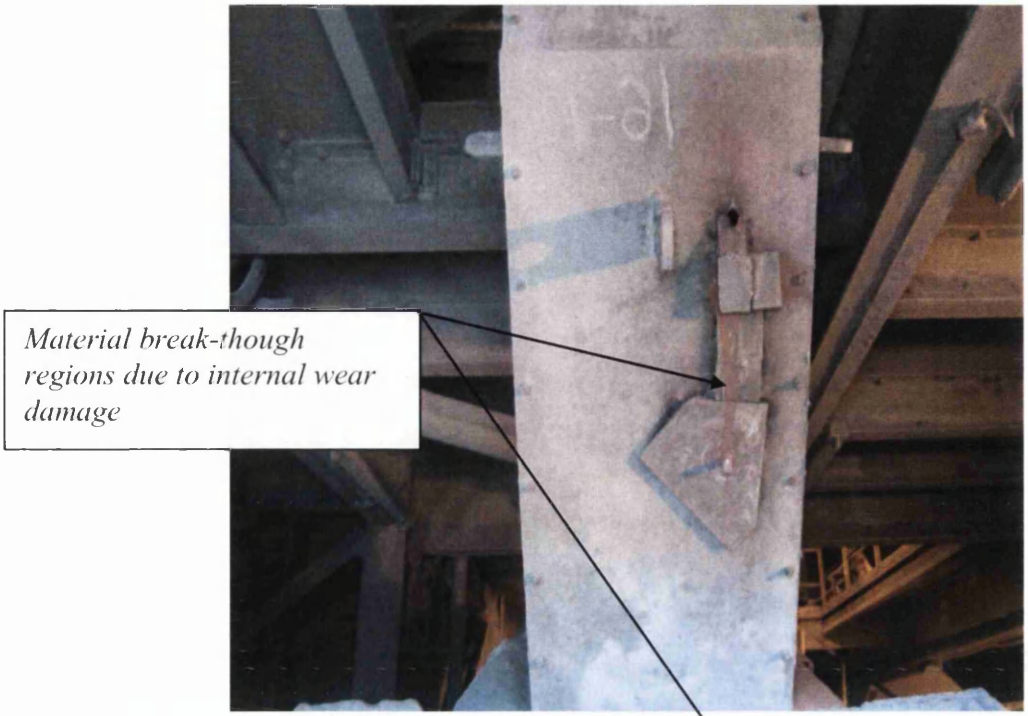

Figure 148: Damage repair due the material break through on the lower section of 633

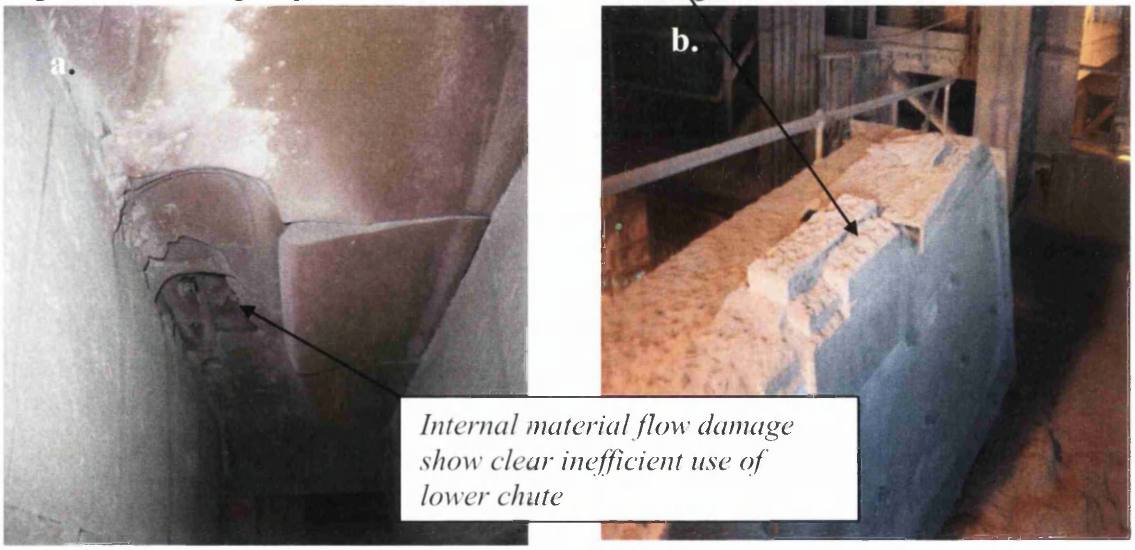

Figure 149: Internal and external flow damage on removed lower 633 head chute

The images in *Figures 147-149* show wear damage due to material flow patterns. The primary impact regions shown in *Figures 147 and 149a* are mainly inaccessible until plant shutdown due to the heavy use of the apparatus. The sustained material impact causes internal structural damage as in *Figure 149a* and eventually wears through the outer skin releasing particulates. The damage shown in *Figures 148* and *Figures 149a & b*, indicate a clearly inefficient process with poor utilisation of equipment.

6.2.3: 633 to 634 conveyor 3D DEM simulations

The conveyor belt and head chute design drawing configuration was converted into a solid works 3D model and the corresponding STL file was applied to the DEM program.

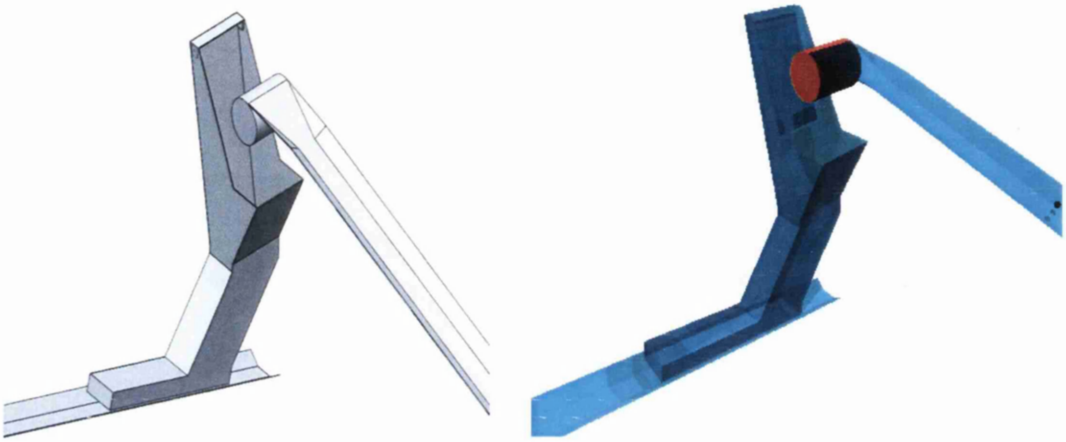

Figure 150: The solid works mesh image and corresponding DEM render

The image in *Figure 147* shows the critical impact point on the first deflector plate, this area was accessible by touch and its minimum and maximum extremities were measured and recorded. The measurements were then transposed onto the solid works image as a "Part" addition, and then used in the simulation as a trajectory guide. The advantages in doing this set the primary contact in 3D space and negated belt velocity calculations that were unreliable.

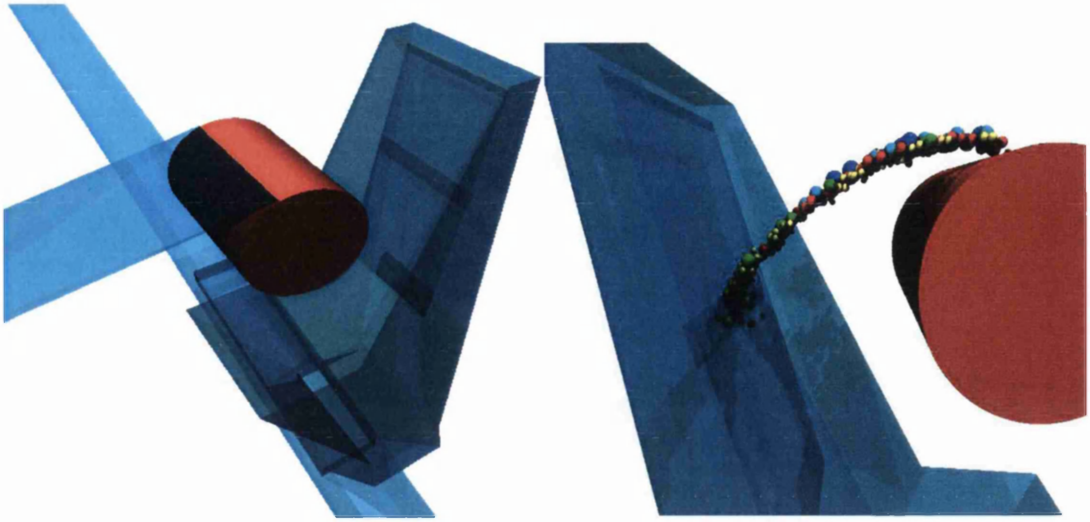

Figure 151: Simulation slides showing impact zone and simple particulate trajectory

6.2.3.1: Head Chute simulations and flow analysis

Using the initial parameters the simulation results were approximately 12 second movies with 42k particles flowing through a system with on average 40 boundary facets controlling the flow. The simulation slides in *Figures 152 to Figures 154* show the simulated predicted flow pattern and the related physical observations.

The time period for the simulation discussed here was approximately 72 hrs on a standard Dell Latitude D810 laptop with Intel Pentium M Processor 2.00GHz, 1.00GB of RAM. The time step used in a simulation of this type was set at 10^{-4} seconds and the program method used Visual Fortran 90.

To run a simulation of the type depicted here (or similar) from first principles, there would be a standard process to implement. For example:

- Identification of problem: Time not applicable
- Solid works 3D drawing and extraction of STL file: Time dependant on complexity but usually 48hrs
- Application into the DEM program and to set up input parameters: Time for this process would be in the order of a few hours.
- Run program and render results in 72hrs

A complete simulation and assessment of the required domain highlighting key feature for practical comparisons could be delivered in one working week with limited cost on a standard desktop system. I terms of an on-site practical comparison one would have to develop/change the domain and invest an unknown time span to study system deterioration for practical analysis and observation. This method of trial and error in many cases is not only extremely expensive in plant down time but generally highly impractical.

Figure 152: 633 head chute with 12.4 second simulation and original deflector plate

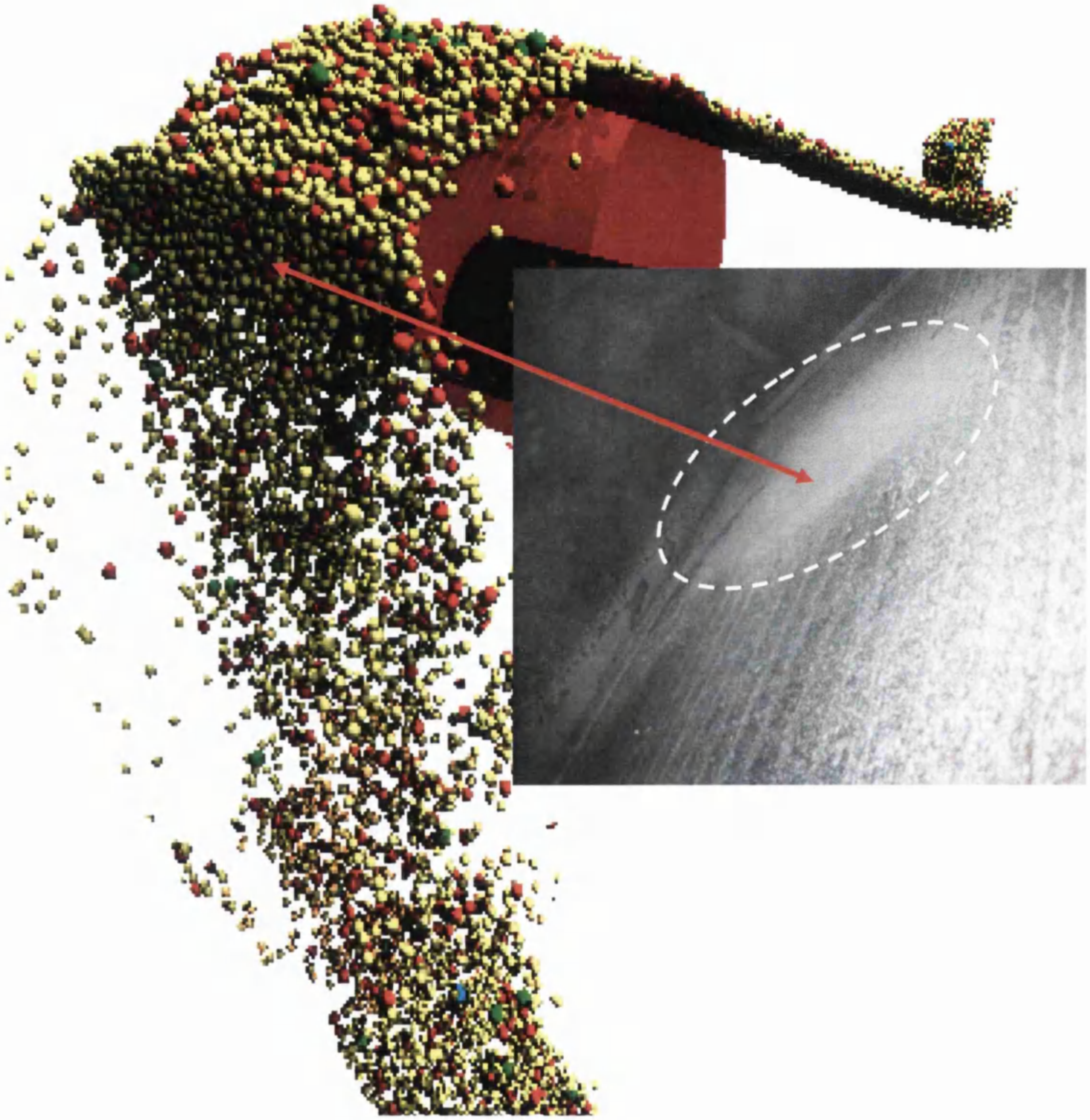

Figure 153: Elliptical impact zone in correlation with wear on impact plate. (Simulation impact plate not shown)

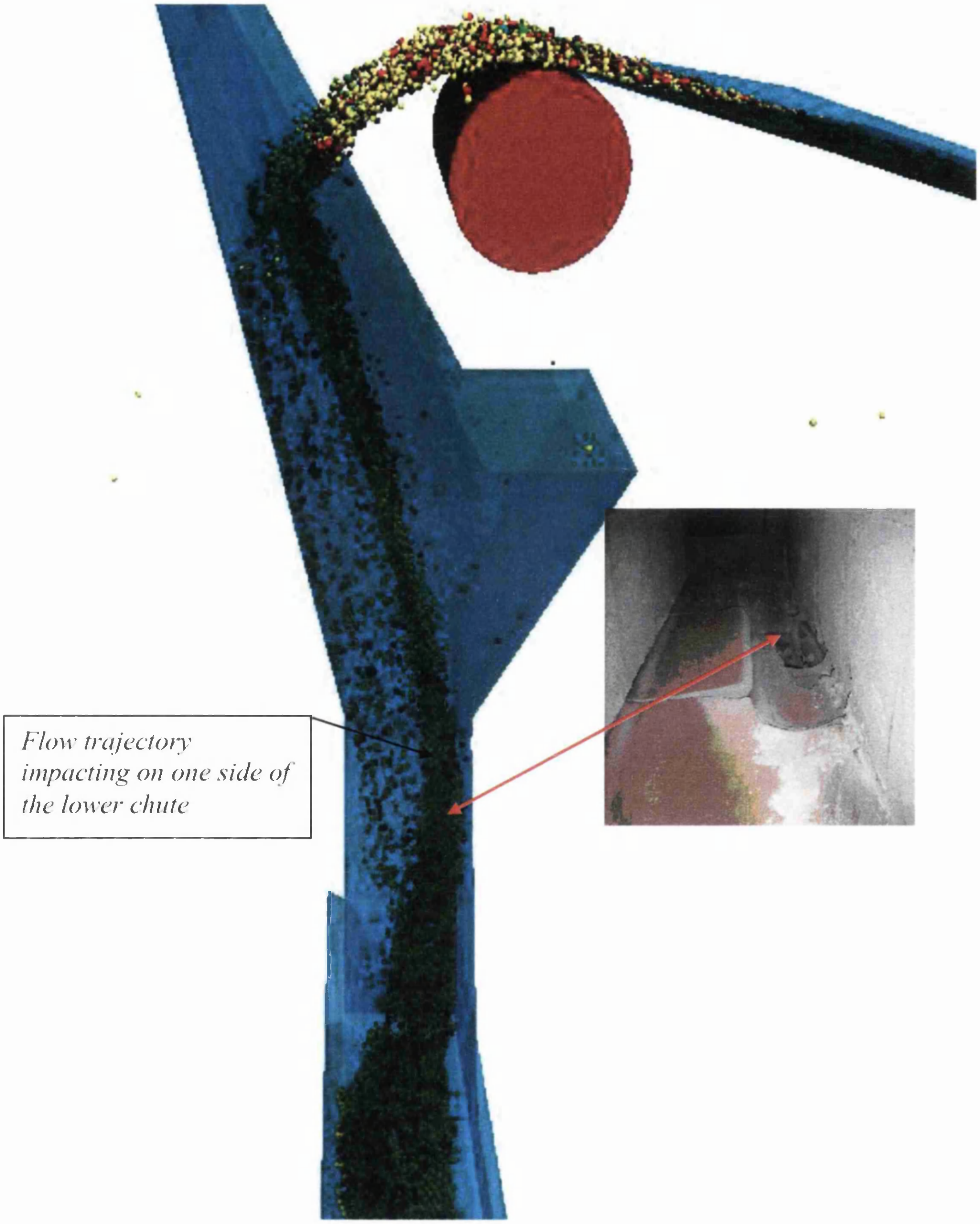

Flow trajectory impacting on one side of the lower chute

Figure 154: Simulation slide showing flow trajectory forced to one side of the bottom section of the chute

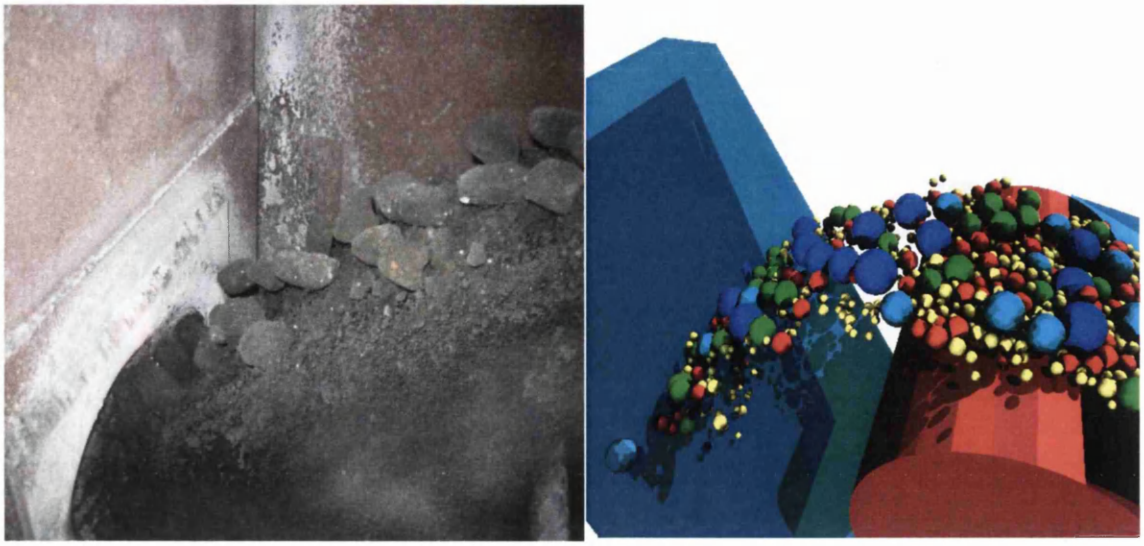

Figure 155: Briquette flow through a head chute and corresponding simulation model

In *Figure 155* the briquette flow shows particulate segregation were the larger elements move to the top. The corresponding DEM simulation predicts a similar reaction although the particle size distribution is not as wide as in reality. Previous work has shown particle size segregation of sintered ore particulates during flow through laboratory scaled chutes using DEM[99].

6.2.3.2: Head Chute simulations and Flow Control

Consolidating the suggestion of smoothing the flow through a given domain a curved chute assembly was designed for implementation into the centre of the 633-634 head chute arrangement. The basics of the design were to control the dynamic flow of the material by reducing high impact, and the limits were built around the original particulate trajectory.

Figure 156: 633-634 Plain head chute with proposed curved inserts

Figure 157: 633-634 Head Chute with curved inserts

6.2.3.3 Key features of curved inserts

As depicted in *Figure 158a* the main function of the curved insert is to manoeuvre material prior to high impact.

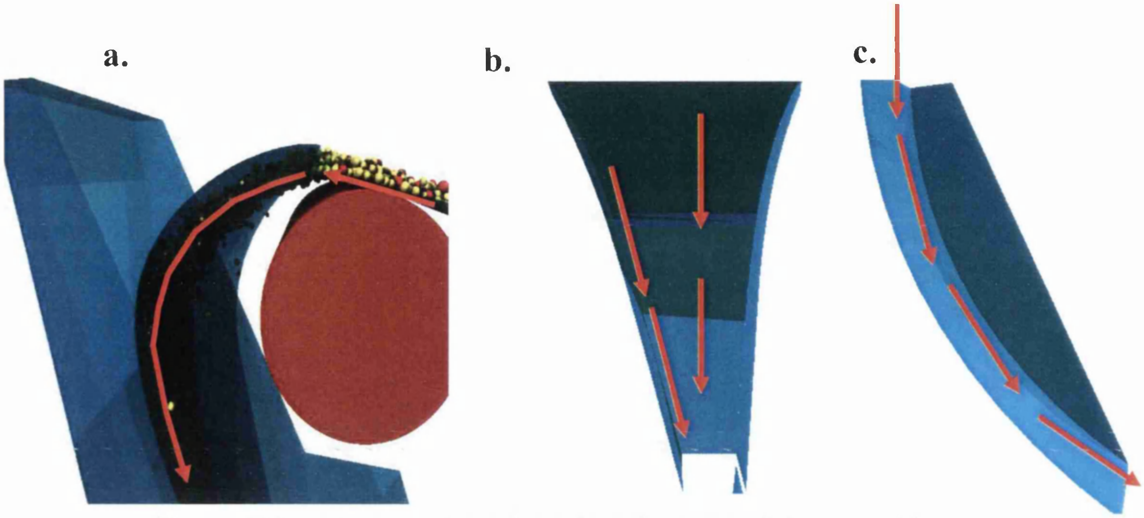

Figure 158: a, b and c show the principle shape of the curved insert

In a. the natural parabolic path of the material flow at the end of the conveyor was mapped and the curve shaped around it

In b. the manoeuvred material is further guided by a high angled flat plate that draws it across the curve to the top of the bottom section.

In c. the material follows a smooth curved plate that introduces it onto the existing head chute surface without severe impact.

7: SIMULATION RESULTS

To assess the effectiveness of a proposed design alteration a quantitative argument must be offered in terms of advantages and disadvantages. In this section a mechanism for visually interpreting system change is discussed and the results of project work simulation are offered.

The main aim of this section is to agglomerate the 3D DEM programming method into practical application and simplistic visual analysis for the design engineer. Addressed here are selections of results from extensive simulations of project work and the outcomes are discussed.

The section comprises:

- A theoretical simulation investigation into the BOS plant 633 head chute design and make comparisons with the existing hopper design and suggested improvement.
- An assessment of the Sinter Plants blended ore supply link. In particular issues of material build up in 886 head chute.
- Basic impact energy transfer on the sinter plant roll feeder and segregation plate.

7.1: Simulation Input Parameters

The simulation input parameters are introduced here to replicate the condition of the particulate material as it moves through a simulation domain. The areas studied in this theoretic investigation (663 head chute, 886 head chute and the Roll Feeder/Segregation Plate) have different material properties and these have to be considered prior to modelling.

As shown in *5.3* the method of material calibration adopted in this project uses the repose angle produced by an individual material type to set the input parameters. The following values were attributed to simulating Lime (as shown in *Figure 146*) and Fines ore (as shown in *Figure 3b*)

Table 7: Input Parameters for simulation results

Inputs/Materials	*Lime*	*Fines Ore 886 HC*	*Fines Ore RF/SP*
Angle of Repose (Deg)	*32*	*38*	*36*
Moisture (wt%)	*5*	*6*	*4*
Density (kgm^{-2})	*2400*	*4000*	*4000*
μ *Particle-Particle*	*0.3*	*0.25*	*0.35*
μ *Particle-Wall*	*0.5*	*0.4*	*0.4*
Particle size Dist (m)	*0.05±0.01*	*0.008±0.002*	*0.008±0.002*
Coefficient of Restitution (-)	*0.3*	*0.1*	*0.1*

Note: In *Table 7* the frictional forces μ vary to generate different repose angles between the Lime and Fines ore. This can be viewed as the interaction of surface asperities of roughness that is generally present at point of material contact.

7.2: Simulation Comparison Results

Simulation comparisons were modelled on the theoretical kinetic energy transfer inside a selection of on-plant equipment. For this project the main focus of research was dedicated to the supply of limestone into the BOS plant and its transition through 633 head chute. Simulations were carried out on the original head chute design and then on a design with a curved chute arrangement in place to control flow. Two chute designs were studied and the corresponding simulation results were used for comparisons.

7.2.1: Original Chute Design of Existing 633 Head Chute

Using the original design drawings a "Solid Works" 3D version of 633 head chute was created. The corresponding STL file was imported into the current 3D DEM program and a simulation of the flow was conducted as shown:

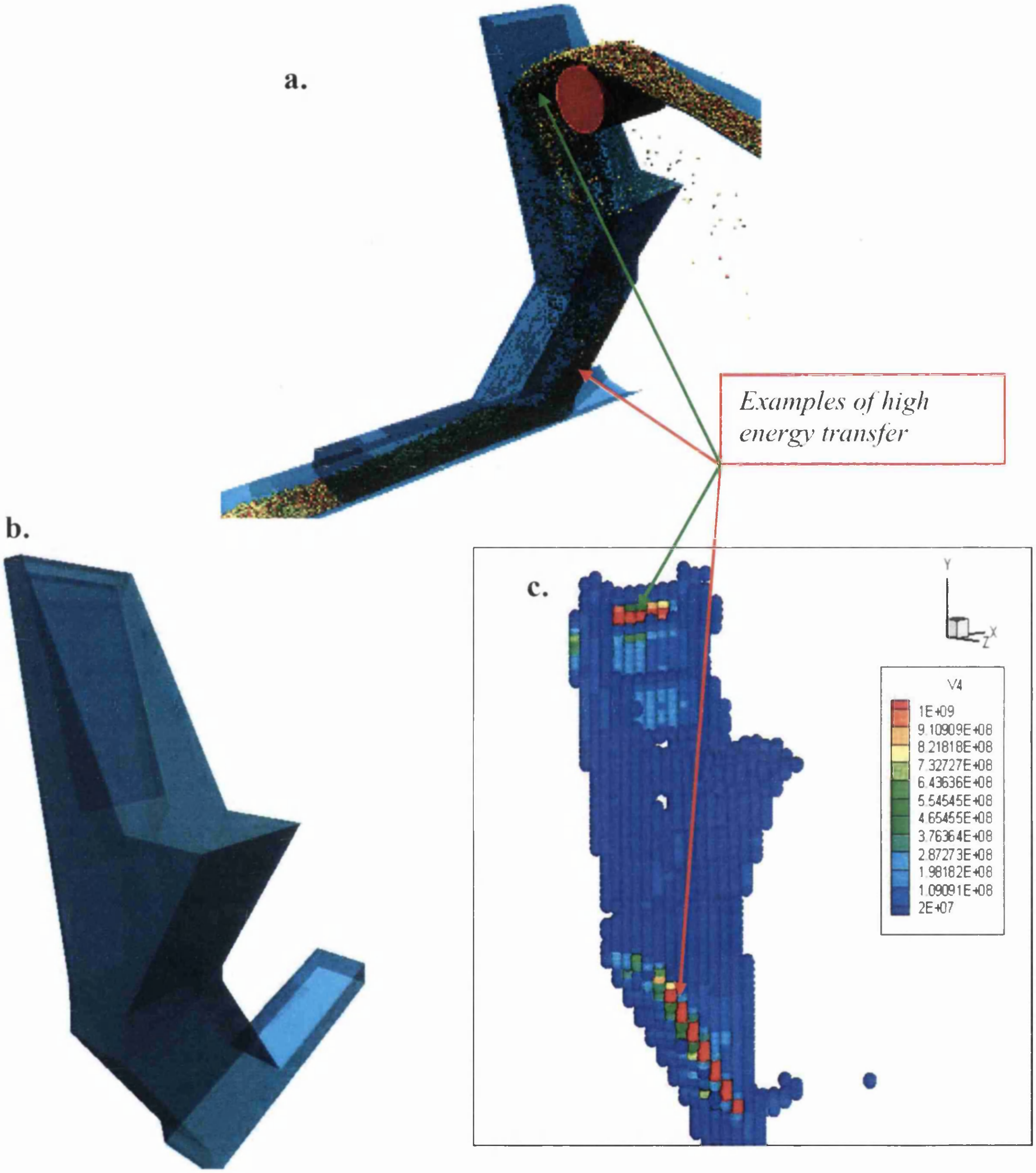

Examples of high energy transfer

Figure 159: Energy transfer inside existing transfer chute with inclined plate

The image in *Figure 159a* is a simulation slide of particle transition through 633 head chute. In the simulation 42k particles were used in a simulation time of 12.4 seconds. Again from *Figure 159a* one can see that the particulate flow follows a predictable path and has a material concentration in two key positions.

The corresponding energy transfer representation shown *in Figure 159c* clearly highlights the intensity of particulate interaction and displays it as an energy distribution map. The findings from the simulation are a direct correlation with deterioration experienced by the existing running plant. This can be seen in the images presented in *Figures 147 & 149.*

Using this model as a simulation basis, design alteration can be introduced and the simulation results studied as a performance comparison.

For this case a combination of curved chute inserts were suggested and the design can be seen as follows.

7.2.1.1: Curved inserts Design Option 1

The principle behind the application of a curved chute assembly was that it would have to be easy to fit into the head chute and easy to remove due to the strategic importance of the running plant. For the initial plans in the design consideration was given to the removal of the primary impact point as shown in *Figures 149 & 155c*. As explained in *6.2.3.3* and *Figure 158a*, the parabolic trajectory of the particle motion after leaving the conveyor belt could be matched with the impact point on the inclined plate and used as a template.

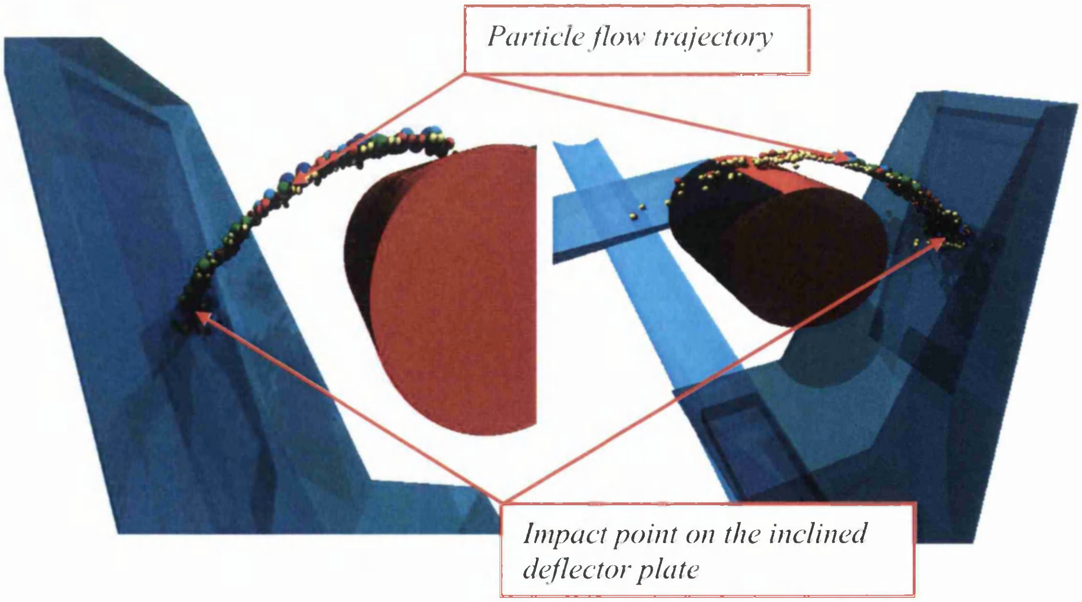

Figure 160: Simulation slides showing impact point on 633 inclined deflector plate and particulate trajectory

In the design proposal, the main emphasis was on the removal of the initial high energy impact point on the inclined deflector plate. To do this, a curved top section unit was created in solid works by superimposing the flow trajectory into the original head chute void and bending a theoretic 3D plate shape from a contact point through the flow.

The idealised function of the curved top section was to collect the particulate flow at early stages when leaving the conveyor, and to smoothly manipulate the flow without dramatic impact. As shown in *Figure 158b* having contained the flow the principle was to direct it to the back of the head chute and onto the bottom curved section.

The design of the bottom section merely linked the flow through the top section onto the gradient of the original bottom chute section.

The curvature of this particular design was specifically designed around the flow and the basic shape can be seen in *Figure 161*. The simulation results for this design are viewed in terms of energy transfer and are displayed in *Figure 162*.

Figure 161: Chute insert design using design "Option 1"

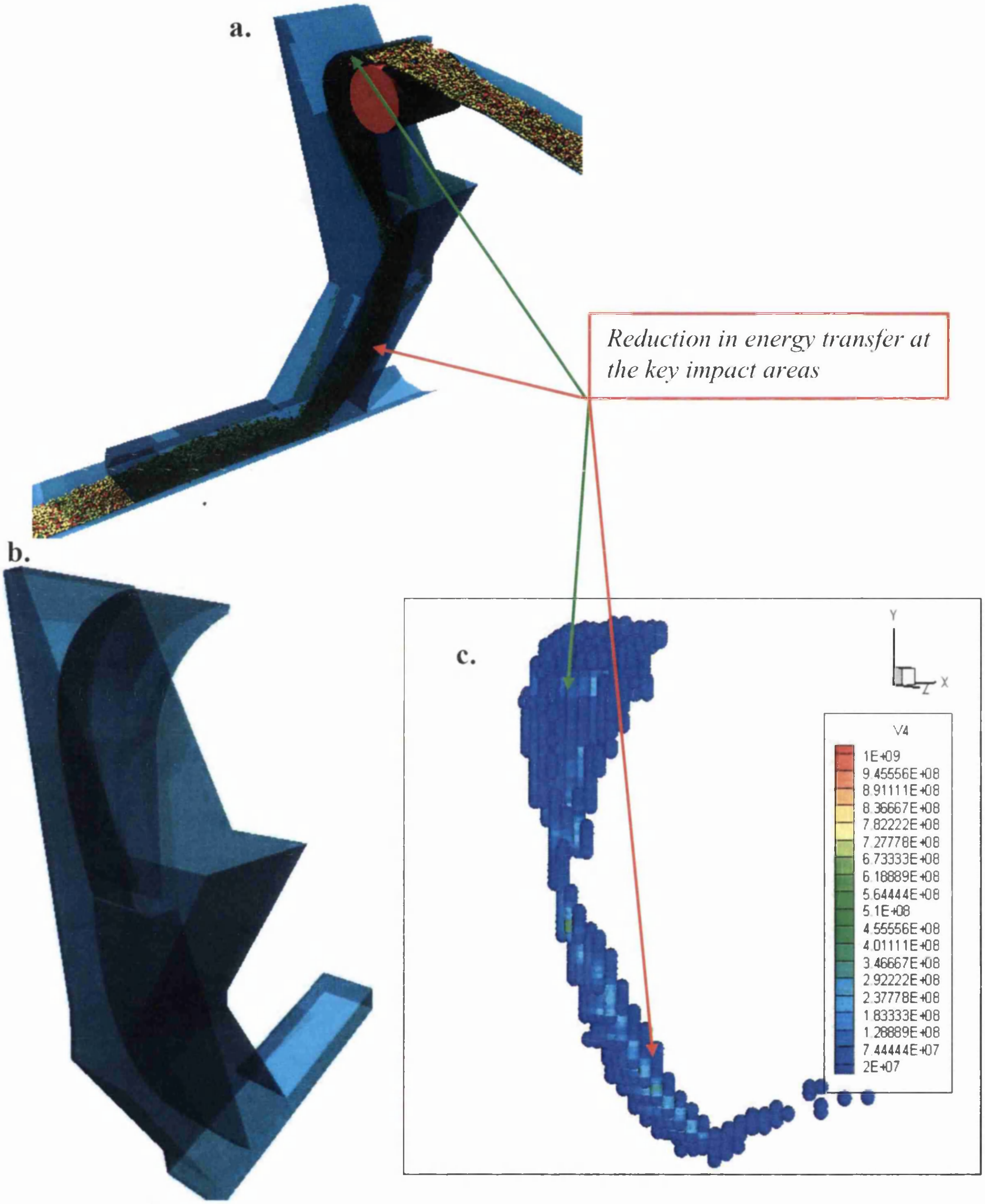

Reduction in energy transfer at the key impact areas

Figure 162: Energy transfer inside Chute with design option 1 curved inserts

The images in *Figure 162a, b and c* show the 633 simulation slide, the chute system with the curved sections and the corresponding kinetic energy transfer plot respectively. In comparison with energy plot shown in *Figure 158c* the energy plot presented here indicates a significant reduction in impact energy transfer at the key impact areas. This suggests a smoother transition of the particulate flow through chute system.

7.2.1.2: Curved inserts Design Option 2

The principle behind option 1 was to match the flow trajectory as closely as possible and in attempting this; the top section of the chute design had a unique curvature. The bottom section of the option 1 design was arranged to maintain a consistent flow through the chute and was independent of the internal structure of the lower section.

In terms of construction and implementation the option 1 design had a number of impracticalities. i.e.:

- Unique top section curvature, therefore difficult/expensive to reproduce
- Large bottom section being difficult to fit and gain access for maintenance.

To address these limiting factors a revision of the problems were considered and Option 2 chute inserts were designed as an alternative.

Figure 163: Option 2 revised curved chute insert design

The fundamental changes to the first chute design were to remove complexities in the shape to make construction easier and more cost effective.

Main alteration features:

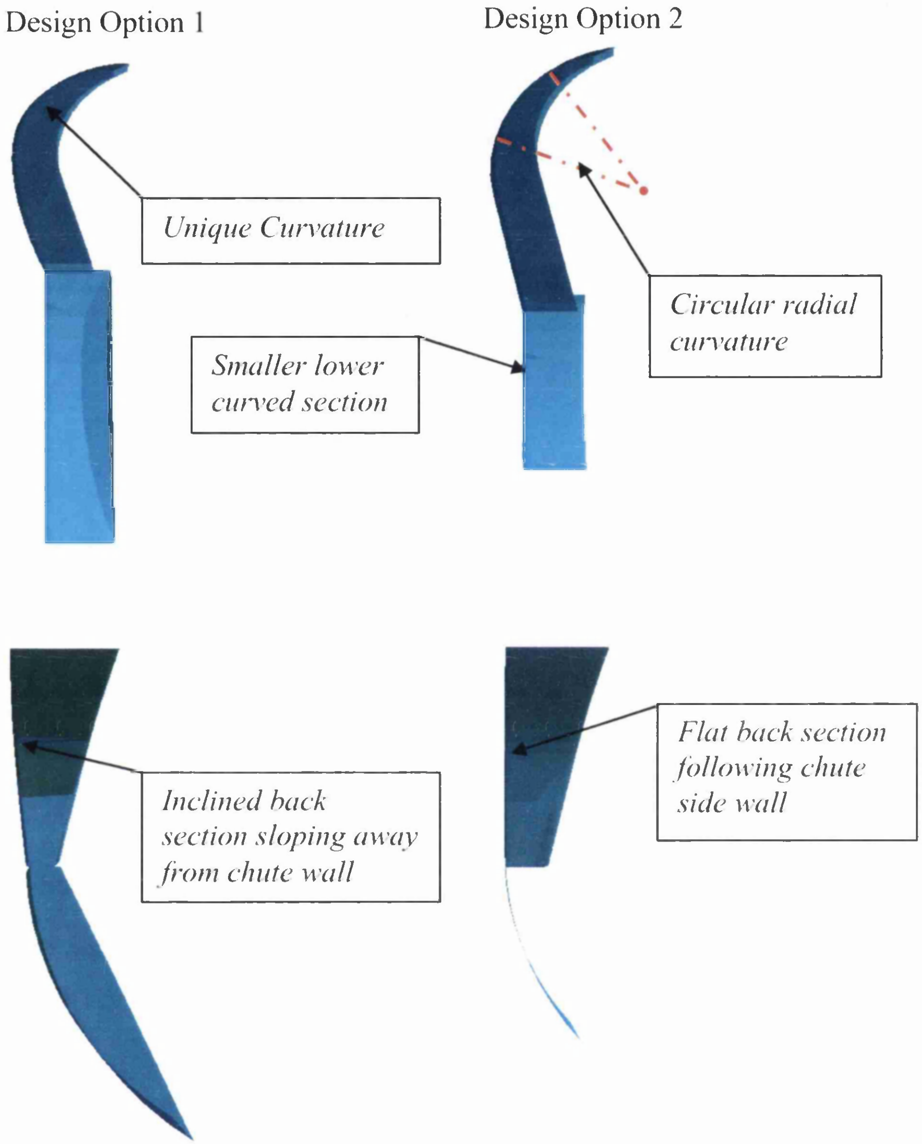

Figure 164: Design comparisons between option 1 and option 2

The images in *Figure 164* show the simplification of the chute design for easier implementation and manufacture. Using the revised chute design a simulation was conducted using the same input parameters. The results are shown in *Figure 165a, b and c.*

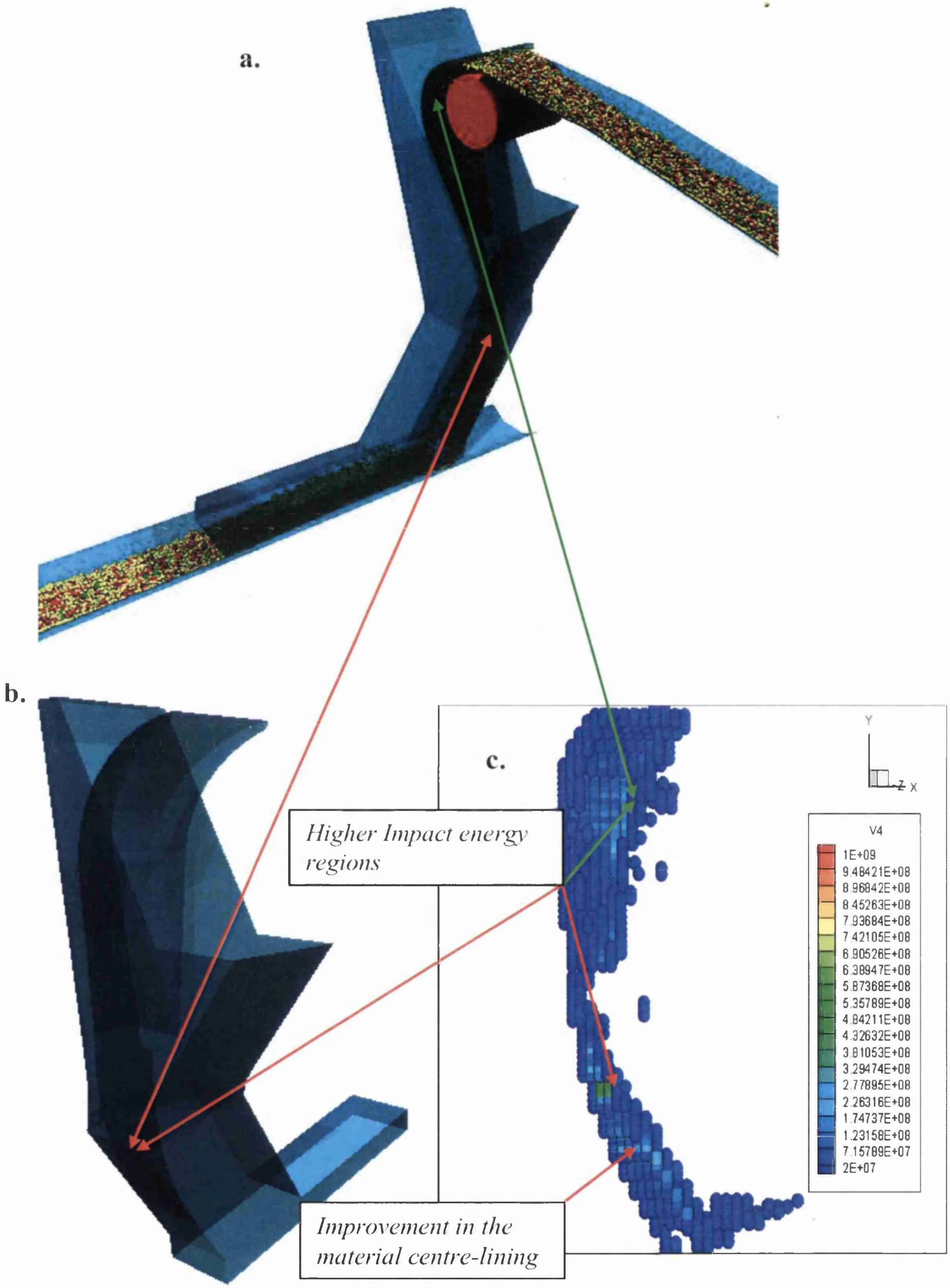

Figure 165: Energy transfer inside Chute with "Option 2" curved inserts

The resulting simulation renders of the "Option 2" chute design show regions of low and medium energy transfer in relation to the maximum energy values found in *Figure 159c*. However, in comparison with Option 1 chute design (*Figure 162c*) higher impact energies are recorded in the key areas highlighted in *Figure 165c*.

7.2.2: Physical Chute Deterioration and energy plot

The photographic image in *Figure 150* showed material breakthrough damage caused by sustained impact and flow intensity. In *Figure 154* the internal simulation flow pattern predicted a movement to one side of the bottom section of the chute and this was verified by energy transfer plots shown in *Figure 159c*. To make a definitive link between the simulation predictions and system deterioration *Figure 156* makes a comparison between the visible damage direction and the trend line produced by the underside energy plot

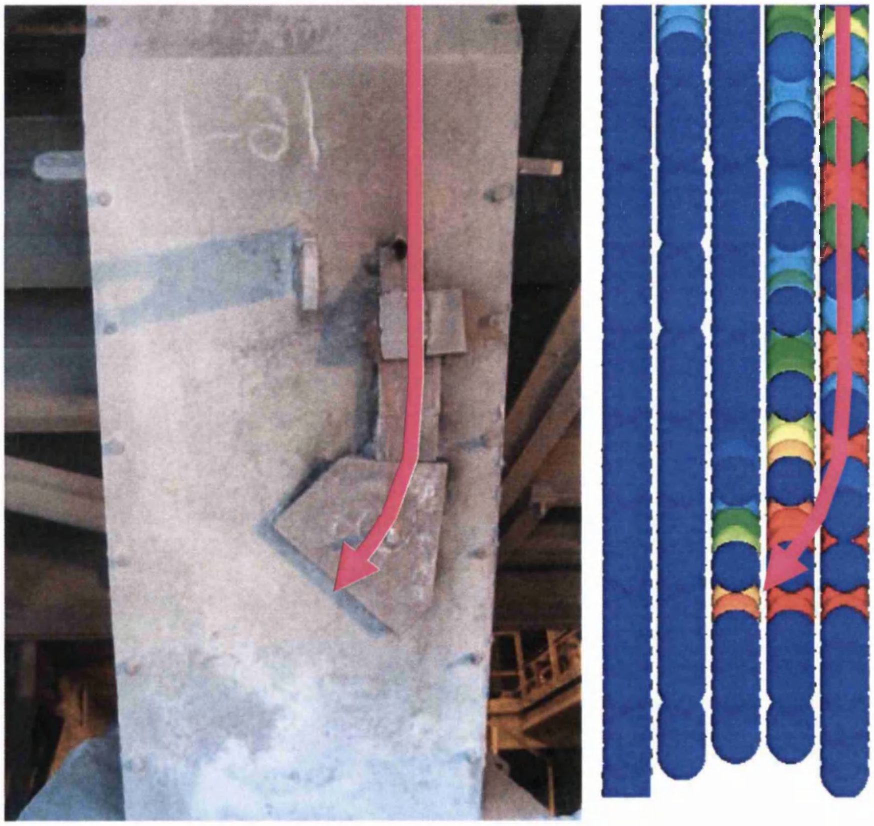

Figure 166: Wear damage on the lower underside section of the 633 head chute and the corresponding simulated prediction

If one compares the trend line of the physical system deterioration with the trend line applied to the simulation prediction the correlation of the two is remarkable. Data of this type could be used to manipulate flow by small initial changes to the flow pattern as material enters a chute.

7.2.3: 633-634 Simulation Concluding Remarks

The images shown in *Figures 159-165* are the DEM simulation renders of a head chute with and without the curved chute inserts and the corresponding energy transfer contour plots. The colours coded slides with legends depict a series contact zones that indicate an energy transfer of varying degrees of impact velocity or sustained boundary interaction.

In *Figure 159* the simulation slides were produced using the original chute design and impact deflector plate arrangement. The slide in *Figure 159c* shows the high energy red colour coded regions depicting high intensity flow at specific points, and a range of energies limited to a small periphery around this region.

In *Figure 162* the original chute design can be seen with the Option 1 curved chute assembly fitted into the internal structure. The slide in *Figure 162c* shows a significant reduction in impact energy transfer but fails to centralise the flow through the bottom curved section. However, this still shows advancement in the dynamic nature of the flow through the head chute but suggests improvements could be made.

In *Figure 165* the Option 1 curved inserts are replaced with the simpler Option 2 arrangement. The corresponding energy transfer plot in *Figure 165c* shows an increase in impact intensity in the highlighted regions in comparison with the Option 1 design. But still shows a marked improvement on the original chute design with the deflector plate. The noticeable improvement over the Option 1 design was the correction in the centre-lining of the flow through the bottom chute section. This progression in performance could increase equipment longevity and reduce maintenance down time.

Using the above information, the Option 2 chute assembly performs well against the two opposing designs and, if implemented, could dramatically reduce material and system degradation.

7.3: Simulation Results on the Roll Feeder and Segregation Plate Impact Wear Investigation

As discussed in Section 1 the Sinter Plant Roll Feeder and Segregation Plate assembly was the primary concern for DEM modelling project. However, due to developmental consideration in the DEM code structure, many of the modelling opportunities were presented in other material flow regions.

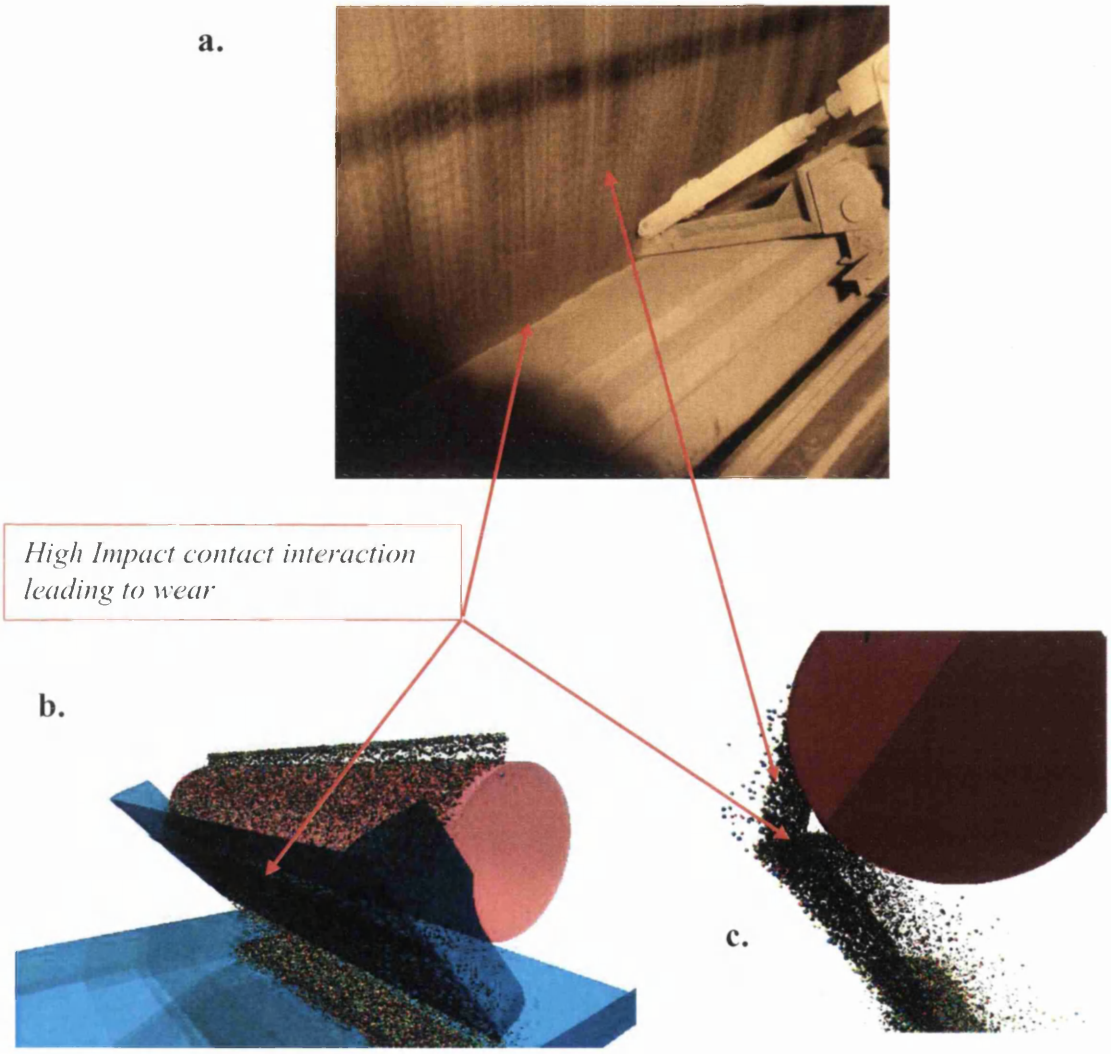

Figure 167: Sinter Plant Roll feeder material distribution showing impact

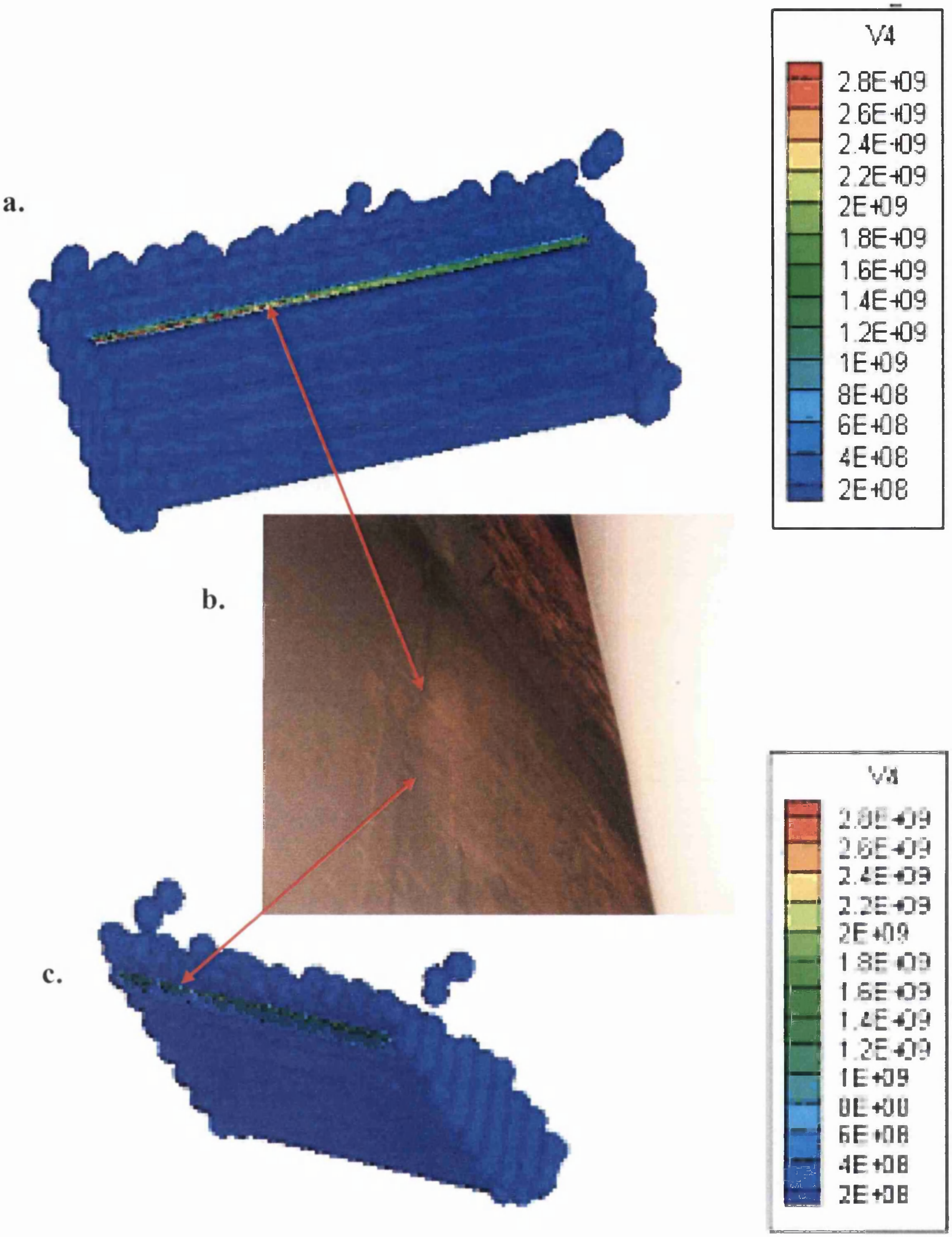

Figure 168: Energy transfer on the sinter plant segregation plate and corresponding wear

The concerns with this piece of apparatus are discussed in Section 1 and attention is drawn to obtaining a satisfactory solution to the wear issues. The photographic images in *Figures 167a & 168b* show material flow off the roll feeder onto the segregation plate and the corresponding contact wear region produced by the sustained impact. The simulation slides taken from a completed “Roll Feeder Segregation Plate” assembly simulation analysis clearly depict a high energy transfer at one specific point of contact. As highlighted in *7.2.1* the initial simulation result could be used as an impact template as a basis prior to studying engineering alternatives. Ultimately, by using the current DEM model reduction of the energy transfer on this plate section could be assessed and strategic design additions implemented to reduce the contact intensity.

8. DISCUSSION

The overriding challenge of this project was to develop a computer modelling technique and to introduce it into the Tata-Corus engineering and design infrastructure. The chosen environment was the "Burdening Department" and the independent business units that are involved in its make-up. Following a detailed research plan, an investigation was started into the processes involved in supplying raw materials, into and around the department and the corresponding effects of supply disruption. The general scope of the research involved a large area, due to plant logistics, but the fundamental conclusions of the study were all directed to basic issues involved in handling bulk materials.

Inevitably, for a project of this type to have credibility one has to consider cost benefits when attempting to implement change. However, the nature of the processes involved rarely offer an opportunity to associate change to an immediate performance related improvement. In the case of a conveyor belt and surface wear situations, the deterioration can be slow, but ultimately belt failures can be catastrophic leading to system shut down. The belt condition are affected by a number of factors such as tension stresses and pinches but wear plays a pivotal role and can take three forms:

- **Abrasive wear:** When material is removed by contact with hard particles. The particles either may be present at the surface of a second material or may exist as loose particles between two surfaces i.e. material spillage traveling back under the conveyor and around the drum ends.

- **Erosive wear:** Is caused by particles that impinge on a component surface or edge and remove material from that surface due to momentum effects. This is typical of an abrasive material falling under gravity onto the conveyor belt surface.

- **Rolling wear:** Conveyor belts in general move through a series of rollers that are in contact with the underneath of the belt, this is where this type of wear occurs.

Limiting or eradicating the effects of these processes could significantly extend the life cycle of a conveyor belt but this could only be realistically viewed on a long term basis.

One would have to extract data relating to time of belt replacement to time of belt removal, repairs carried out over this time period against belt running times and volume/type of material transported. The necessity of this data would have to be questioned considering the general performance of this type of plant.

A large percentage of this project has devoted time to computer program development on domains that handle flowing material. The main activities have been dedicated to energy transfer and how to minimise the transfer in order to amplify efficiency. For a static head chute, the task is merely to change the direction of the flow and the dynamics of the internal interactions are ignored until material punctures the chute wall or spillage occurs. This again has a direct correlation between impact and the wear conditions expressed above. Repairs at this stage are usually temporary until the repair punctures through again and the cycle repeats. Ultimately, the damage becomes severe and the system is rendered useless until an overhaul is carried out. If one accepts the fact that this is an inescapable cycle then improvements would have to be measured by the time span between the sequences of events. This again indicates a long term analysis which is difficult to evaluate over a time limited modelling project. However, to show the observable disruption caused by these material flow issues and the costs that can incur the following examples are discussed.

8.1 Discussion: Raw material import mechanisms and internal supply issues.

Discussed here are:

- Raw material movements through the harbour import facility, with focus on the bulk handing mechanisms and the financial issues related to spillage and system failure.
- The distribution of material into and through the Sinter and GCI Plants.
- The lime supply in the Basic Oxygen Steel (BOS) making department and basic financial implications of material/system degradation.

8.1.1: Raw Material Import Facility

This department is responsible for the unloading of cargo carrying vessels in as short a time as possible with minimum vessel damage. The unloader system of three cranes and a large static conveyor is capable of discharging vessels at a rate of 6000 tonnes per hour depending cargo type. The single conveyor leading off the berthing facility is split by a transfer station into two separate feeds that leads into the stock yards on one line and into the coke plant on the other.

The grab operation system used in the unloading operation is effective but wear and damage issues can relate to material spillage onto the quay side. This type of spillage is small in comparison to the cargo volume but can have a detrimental affect on the unloader mechanics and result in material loss due to build-up. Along with that, one can associate concerns relating to environmental issues and spillage contact with personnel.

Figure 169: Material spillage encroaching onto crane bogies and rails

Drawing attention to the harbour spillage investigation in terms of costs only estimates can be offered due to the lack of quantifying information, but as quoted for spillage loss alone;

In 2006-7 Corus imported £95 million of cargo. If one considers an extreme of a 0.1% to 1% loss of cargo, the cost of the losses could ranges between £95000 and £950000 per annum.

The spillage extent varies with the types and condition of the cargoes being imported. In some cases the material condition will dramatically differ during the total discharge of one vessel and this can impinge on conveyor belt transition from the unloaders. As an example of this type of problem, high moisture content introduced into the cargo at the loading port settles to the bottom of the hold on the seaward passage. In *Figure 3b* the texture of the fine ore is as one would expect to find, however the same material saturated with moisture becomes completely different and resembles slurry. The fluctuation in the material motion from a solid to an almost liquid causes a return flow on inclines and fine particulate flow under the returning conveyor.

Figure 170: Fines ore saturated with moisture on harbour conveyor

The results of moving material in this condition creates large scale spillage problems and back splashing along the conveyor causing end roller burial forcing a shutdown. On the opposite end of the scale, cargoes of coke run through the same system but offer a different set of complications. Coke is a low density robust commodity designed to maintain its integrity under intense conditions. These attributes make it a formidable product when impacting at velocity on the internal structures of a head chute. Damage or disruption to the system to some degree is almost inevitable and the knock on effects of the process are very difficult to predict but can be financially unfavourable.

Examples of recurring situations are when discharging vessels are due to complete cargo in a tidal window of opportunity. If a breakdown occurs the completion times get forced back until deadlines are breached and the vessels stays in berth. The limits on tidal deadlines for large vessels are stringent and may be compromised by only a few minutes. However, the result of this is then transferred to the vessel "changing over" on the berth and this vessel is delayed until the next available tide. The incoming vessel returns to anchor and enforces "demurrage" which is a cost on the vessel charter (Corus) in line with the "Bulk Dry Index" BDI. This cost varies for the vessel size but as an indication the BDI in 2006 for "Cape Size" vessel was between $70000 & $100000 per day. These figures are compiled if the vessel at anchor is constrained by her draft and is unable to berth for an extended period.

In the main, plant breakdowns and failures can be caused by a number of factors, such as electrical, mechanical or human error. Material flow issues are usually low priority compared to continuity of discharge, therefore very little attention is given to material flow problem solving. This project work has confronted and addressed this issue and the current DEM modelling program is highly applicable in this situation for preventing unnecessary spillage and chute optimisation.

8.1.2: Discussion: Sinter Plant and GCI

The stock yards are continuously replenished from the deep water harbour and from there a blended raw mix is processed into sinter in the sinter plant. Coals from the stock yard are also processed in the GCI for blast furnace application. The issues with material distribution in both of these facilities have been discussed, but the importance of supply continuity has to be stressed. Sinter for Port Talbot is a chemically specific, highly reducible component and the alternatives during sinter shortage are the more expensive pellets or rubble.

When these ores are increased per tonne of hot metal the cost of the iron commodity rises. In parallel the GCI supply continuity is vital in satisfying the cheap fuel demand required to maintain a competitive product. Supplementary fuel additions such as oil can be expensive and have a direct bearing on extraction costs.

8.1.3: The lime supply in the Basic Oxygen Steel (BOS) making department

The BOS process is a conversion method for turning iron into steel. The technique involves injecting oxygen into carbon rich molten iron through a lance in an exothermal reaction. This operation strips out the carbon producing a basic steel product. During this routine, chemical alloying agents are introduced along with fluxes in the form of limestone.

The concerns involved in transporting limestone in the BOS environment are discussed in Section 7 and relate to particulate impact causing material and system degradation. The dust generated during this material movement is considerable and is ultimately lost in fume extraction. To quantify this value, an estimate sets this loss in the region of £6000 per day which equates to approximately £2 million per annum.

The purpose of highlighting specific situations and the costs implications within this discussion are to demonstrate the importance of researching the basic systems to enhance efficiency.

8.2: Discussion: Discrete Element Method Modelling Development

To study the dynamics of the bulk handling infrastructure the preferred modelling technique was "Discrete Element Method" simulation due to its previous successes in representing granular flow.

The fundamental breakdown of a DEM model can be viewed in four sections.

1. The Discrete Element: Geometric Shape
2. Contact Detection: Examines the region for particle interaction and determine if contact has been made.
3. Constitutive Forces: Calculate the forces acting on each particle during inter-particle contact and particle boundary contact.
4. Application of Newton's 2nd Law: Summation of the resultant forces associated to the discrete element to determine motion.

Throughout this project spherical elements were used to generate simulations. The decision to follow this course of action was supported by the fact that

Paper Publications verifies that particle shape has little effect on flow and spheres can be used in the simulation process providing the flow is sufficiently dense and the correct parameters are implemented[53].

Spheres are mathematically simple in terms of geometry and this minimises CPU time when using search algorithms.

Element deformation was not considered[62] allowing Linear Spring Dashpot contact interaction to be implemented[64].

However, in terms of improvement the elements could have been a more representative of reality by utilising more sophisticated geometries. Spheres have a tendency to roll or rotate freely and frictional forces can be exaggerated to reduce motion to a state of equilibrium. The most attractive proposition in the field of alternatives was the 3D ellipsoid[32][42][43]. This element shape has been proven to be superior in simulating hopper flow and general particle dynamics in comparison with spheres.

The methods addressed to effectively predict element contact and positions in relation to the searching element were carried out to identify algorithms that would reduce computer processing time. The geometric searching algorithms discussed in Section 2 range from a basic direct search involving all elements to a complex "Alternating Digital Tree"[58][59] mechanism that significantly reduced point detection within a domain. However, the complexities of the more advances searches were further in tune with detecting more elaborate shapes such as ellipsoids and tetrahedra[41][45].
Therefore, the decision to use the spherical element in this case removed the requirement of the more convoluted algorithms and allowed a "Neighbour Search"[57] method to be implemented that satisfied CPU demand.

At the point of inter-element or element boundary contact one has to consider the physical mechanisms of the interaction and introduce them to generate simulation accuracy. The fundamental parameters associated to these types of events can be expressed in terms of frictional and damping forces. Applying these parameters effectively will determine the accuracy of the simulation output results and influence the conditions in the simulation domain. As discussed in Section 2 a "Soft Sphere"[6][7] approach was used in the modelling technique with small contact overlap being allowed that followed Hooke's law during reaction. Ultimately, damping forces were applied as theoretical dashpot assemblies to represent energy transfer and the physical properties associated to the coefficients of restitution. The vectors used to obtain values for the parameters in the 3D modelling method were generated by using a combination of finite difference[3] equations (to find magnitude) and planar intersection (to determine direction).

To depict the effects of the parameters highlighted here the following graphs were produced.

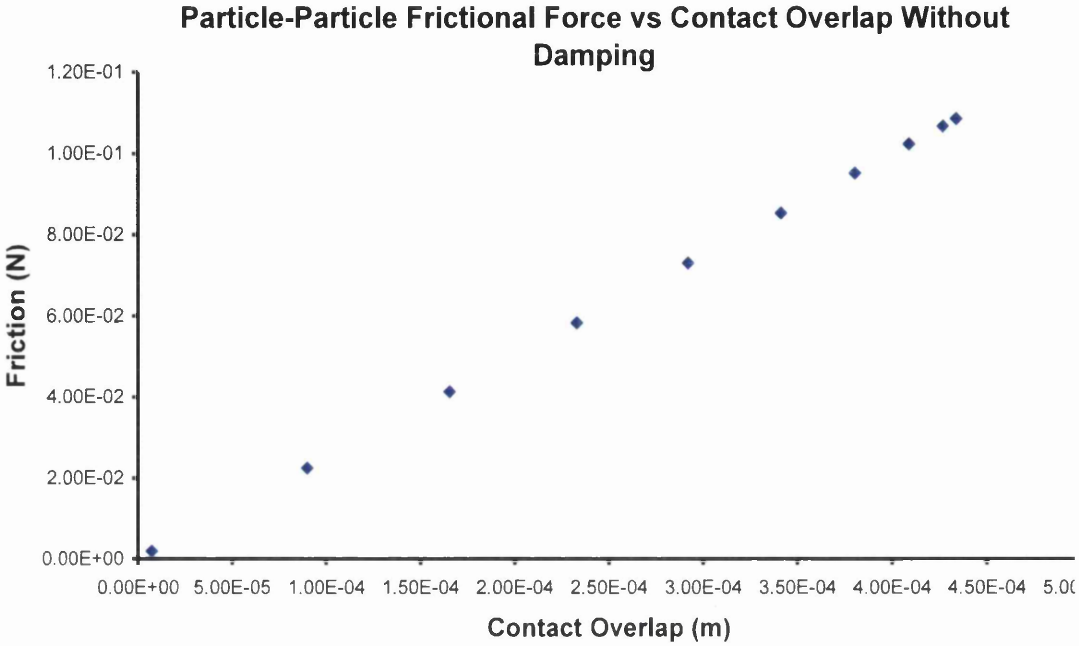

Graph 8: Proportionality of tangential frictional force at Particle-Particle contact overlap with no damping

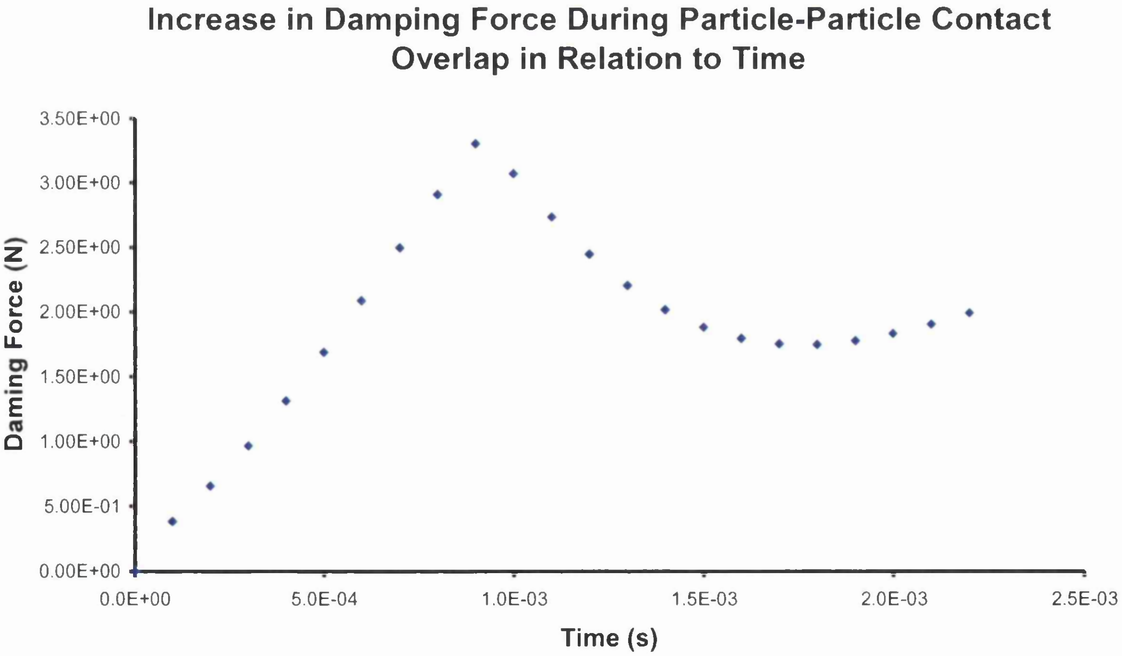

Graph 9: Damping forces in time steps simulating energy transfer in the normal direction at contact

In *Graph 8* the frictional forces exhibited between particle-particle and particle-boundary are shown to be proportional to the contact overlap and are therefore linear. In *Graph 9* the linear damping effect of the dashpot enforced using Equation (2.14) shows a reduction in spring return velocity. This clearly shows how the physical parameters can be manipulated to represent a range of particulate or boundary conditions to simulate the required granular flow.

In order to obtain accurate simulation results the ratio between the element/particulate size distributions and the simulated plant equipment was considered. In latter simulation results the domain/boundary sizes representing the plant equipment were set in the order of metres and all elements/particulates were introduced in size distributions of fractional values of the metre scale. As an example of this the "Roll Feeder Segregation Plate" simulation equipment had an extreme of 4m for the roller and the element size distribution was set between 0.006 ~0.008m. This was viewed as a reasonable ratio between the two key constituents of the simulation and ultimately provided an authentic representation.

An additional inter-particulate force considered during the development of the DEM code was directly related to the involvement of moisture. The effect of capillary action between particles has a profound influence on the dynamics of a practical flowing media and, to a reasonable degree, had to be implemented into the theoretical modelling reproduction.

As explained in Section 4 the effects of moisture between particles was introduced using a capillary type force generated by the Laplace Equation. The function of the equation uses the surface tension of the denser media producing a curved meniscus and the radial values of internal and external curvature. The direction of the force follows the normal inter-element vector which is attractive and apparent between element centres. In terms of magnitude, the force values calculated are small in comparison to contact interaction values and are mainly prevalent when relative particle velocities are small or in quasi-static situation.

The force in this work was simulated by utilising a toriodal approximation to form a suitable meniscus shape between the 3D spherical surfaces of contacting elements. For calculation simplicity the external radius of curvature was produced by using the minor radius of the toroid that was predetermined by the required percentage moisture content.

This value then remained constant over the contact interaction time span until the parameters where breached. This straight forward approach to the external curvature allowed a basic geometric and trigonometric relationship between the elements to be exploited. This resulted in capillary force values calculations between differing size elements with large size distributions.

However the method described in Section 4 was always considered as an approximation in terms of moisture involvement between particulates. To initiate the Laplace Equation a liquid depth was generated at the element surface related to a mass percentage. At liquid-liquid contact, a moisture harvest between the elements occurs and a virtual meniscus can be formed. This method has limitations particularly in the case of multiple element contact interaction, for the case of one particle encountering four contacts at its surface the harvest at liquid overlap would exaggerate the moisture content and elevate the net force between the five interacting elements.

To combat this obvious flaw in the calculation procedure, a mechanism for calibrating a combined mass of elements was sort and the solution was found in the phenomenon of repose angles that are generated on material storage. The basic concept was to simulate the known repose angles of a variety of materials with varying moisture contents and then to introduce them as set of initial parameters. This method of reducing the theoretical computer simulation to practical known values was considered as an ideal vehicle for program validation.

8.3 Discussion: Validation

To acquire suitable program validation comparisons with related paper publications were made in terms of repose angles and how they were affected by varying frictional forces. As explained in Section 5 *Zhou et al*[95] used *Equation (5.1)* to theoretically predict repose angle and compared the results against actual experimental finding using a constructed apparatus (As shown in *Figure 124*).

Using the dimensions expressed in the publicised paper, an exact simulation domain was created using the project program. Simulations were then carried out within the computer generated domain to compare model accuracy and corroboration between graphical data streams.

As shown two methods were used to produce a repose angle in the simulation domain:

- Method 1 used a cascade technique
- Method 2 used a particle generation technique

The simulation results produced in Method 2 showed correlation with the simulations produced by *Zhou et al*[95] and this was the preferred method of validation and in keeping with the granular flow coding structure presented in this work.

Equation (5.1) was then used with suggested parameters to reproduce the graphical analysis displayed by *Zhou et al*[95] and they were expressed in *Graph 5*. Using the project program the same constant values were set in *Equation (5.1)* and the corresponding frictional variables were incrementally introduced. The resulting angular fluctuations were then recorded and compared against the graphical trend-lines. The results of this exercise were again graphical demonstrated in *Graph 6* and the relationship with the predicted data was clearly comparable.

Finally *Equation (5.1)* incorporates an element diameter in its construction and this was used to emphasis the influence of particulate size on repose angle. By setting the frictional coefficients as constant (in this case Part-Part 0.4 and Part-Boundary 0.6) the diameter was varied from 1mm to 10mm. The predicted data trend-line showed that as the elements increased in diameter the repose angle decreased, this trend was evident in the project model and the products of the simulations were shown in *Graph 7*. The results clearly show strong comparisons with the published example in terms of experimental association and theoretical observations. Therefore, the project model was deemed sufficient in producing a reasonable interpretation of theoretical granular flow against flow on a practical scale.

8.4 Discussion: Results using energy transfer

The results shown in Section 7 were generated by the translation of spherical discrete elements through a variety of flow domains and mapping the corresponding contact interaction. The main feature of the extrapolated data was related to particle-boundary events that transferred kinetic energy at impact. The energy transfer at a coordinate system was then summed forming an impact distribution and colour coding was introduced to depict areas of high intensity. The advantage in presenting the simulation results in this manner was that direct correlation with equipment deterioration could be visualised and acted upon if required.

For this project a critical selection process was implemented to highlight key material flow areas that exhibited clear observable system failure or design issues. One of the primary areas of interest was on a limestone supply network into the BOS plant. The initial benefit in using this environment was the material type and condition. Limestone on delivery generally has a good size distribution and has low moisture content. Along with these factors the material is abrasive and when allowed to impact will release energy onto the equipment and eventually puncture a hole though. The areas of damage sustained in this process were used as a footprint of the flow patterns through the region and were ultimately viewed as guide to the reliability of the model performance.

As shown in the results images, setting the flow position at an initial contact wear point causes theoretic flow pattern that proved to be remarkably similar to the practical situation.

8.4.1: Discussion: 633-634 Head Chute Simulation Results

For this project a key objective was the blend of computer simulation with actual conditions experienced in the working environment. As discussed in the *8.4* material flows leave distinct wear patterns that can be used as a damage footprint and these regions are ideal for replication. In the computer modelling of the 633 head chute assembly these factors were considered and physical measurements were taken off the initial deflector plate of the primary impact wear region (*Figure145*).

The central position of the wear region was recorded and applied to a simulation domain using an STL file input as an impact strip (*.Figure 151*). This region was then used to set the flow trajectory by varying conveyor velocity until direct contact was made. This was a useful method of obtaining the correct flow trajectory, as many of the drive motors running conveyors were rated inaccurately compared to the equipment design, and therefore run at different angular velocities.

With the initial conditions in place and the input parameters set for lime products (*As given in 7.1*) a simulation was run over 12.4s and using 42k particles. The simulation was rendered with clear and transparent boundary walls and the first visual results showed an elliptical shaped impact region on a theoretical deflector plate which closely replicated the wear damage on the actual design (*Figure153*).

From this position the particle flow was allowed to follow its own path through the simulation domain and observations were made using different rendering projections. In this case the flow of particles leaving the deflector plate was forced to one side of the bottom section of the chute (*As shown in Figure 154*). This simulation action clearly replicates the situation experienced within the internal structure of the actual chute. The images shown in *Figure 149* are testament to preferential flow through one specific route along the bottom chute section. In terms of quantification the flow trajectory throughout the simulation domain was ultimately mapped using kinetic energy transfer to highlight the key regions of high/sustained impact ratio. The corresponding energy distributions were colour coded with intensity variations ranging from "Red" *High* and "Blue" *Low*. The simulation results using this method (*As shown in Section 7*) produced remarkably accurate plots of predicted wear and damage points.

As a basis a simulation model was run using the STL file from the original 3D "Solid Works" drawing and an energy template was produced with a range of energy distributions (*As shown in Figure 159*). The comparisons between the energy transfer wear predictions and the actual wear were again exceptionally accurate As an example of the simulation success in this format, the trend-lines superimposed onto the images in *Figure 166* shows the definitive simulation wear pattern against the actual path of puncture deterioration expressed as maintenance repair work.

In an attempt to improve the internal flow dynamics of the head chute the intention was to remove material impact opportunity and to manoeuvre the flow. To achieve this two specific "curved chute inserts" were drawn in 3D and fitted into the original chute design for simulation. Using the same input parameters simulations were conducted and comparisons were made between the three alternatives. The results of the simulation are discussed in *7.2.3* which shows that the curved chute inserts have the potential to smooth the material flow, drastically reduce impact wear and encourage better conveyor belt centre lining.

8.4.3: Discussion: Modelling Different Head Chute Designs

Due to design some individual head chutes on material feed lines have a tendency to retain material and ultimately block. DEM assessment to determine the flow dynamics in different arrangements could lead to significant improvements in chute design and efficiency. An example of such a head chute design can be found on the sinter plants blended ore supply line. The head chute design at the end of conveyor uses a "Rock Box" shelf to minimise internal wear. Previous work in conveyor dynamics have shown that curved chute systems replacing rock box design show less wear damage on receiving conveyors[100]

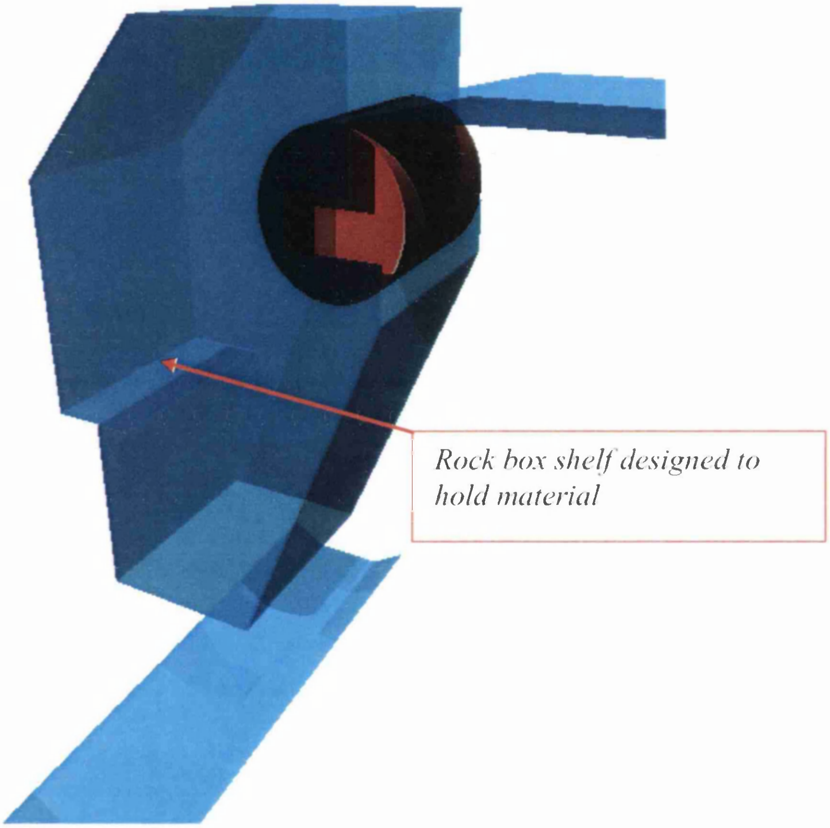

Figure 171: 886 head chute design with rock box shelf

For the sinter plant this type of design presents a problem when large scale material build-up occurs. The moisture in the finer material products allows the growth of the retained material to reach unacceptable proportions. Cleaning or removal of the build-up becomes a difficult process with safety risks attached.

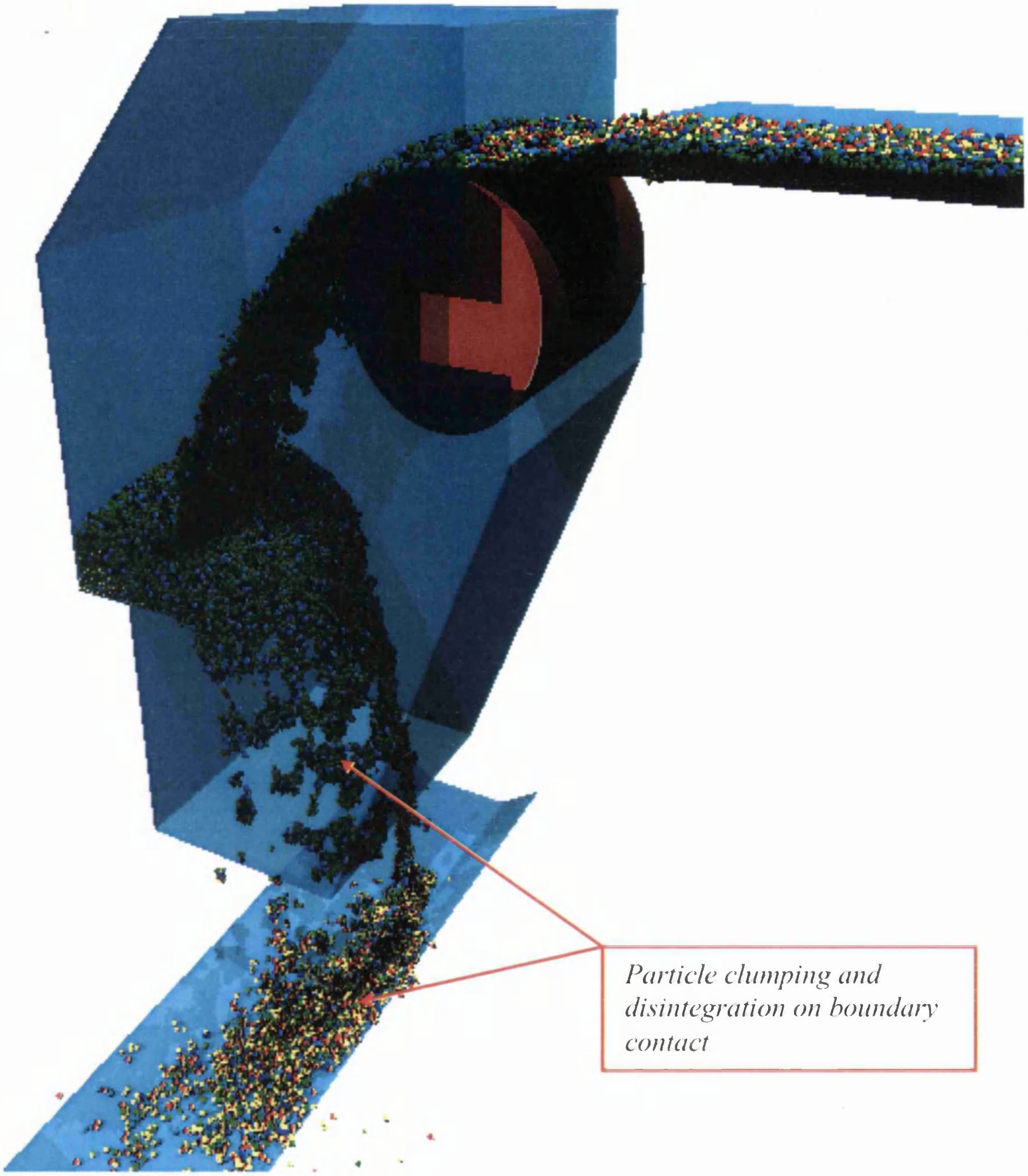

Figure 172: 886 simulation showing material build-up and clumping due to moisture content

The energy plot associated with this simulation offers very little information in boundary interaction due to the protective nature of the material build-up. In this case only the initial boundary contacting particulates leave a kinetic energy footprint and the rest of the energy is dissipated between inter-particle contacts.

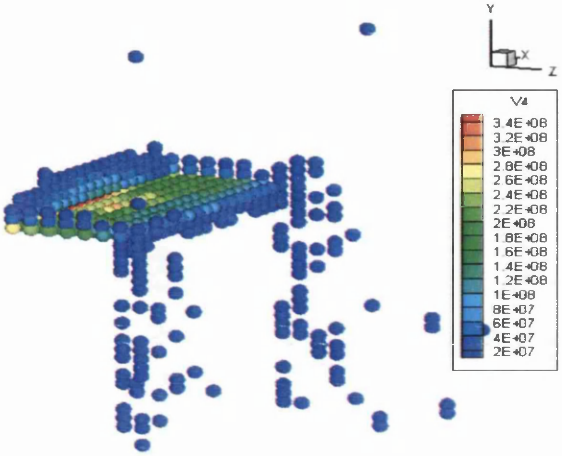

Figure 173: Energy plot between boundary shelf and initial particle impact

To access the data for energy loss due to inter particle contact has not been dealt with in this project but to indicate the principles behind rock box design the contact overlap between the particulate (*Soft sphere model 2.1.1*) can be used as a mechanism for listing high energy impacts

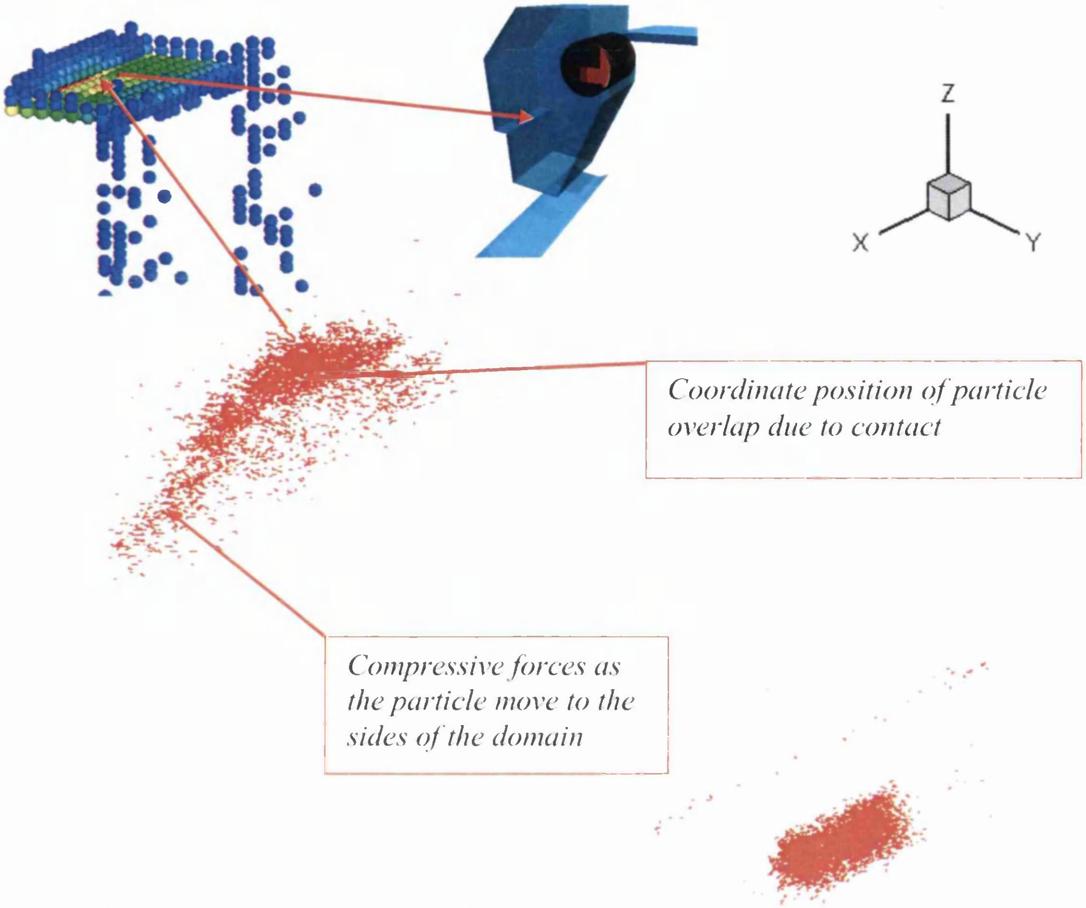

Figure 174: 3D coordinate positions due to high energy contact interaction

The data shown in *Figure 174* is merely a point marker in a 3D coordinate position listed at every high energy contact overlap. The interesting facts produced from this format are the compressive forces within the spreading material and the high energy region developing away from the self surface. Both of the particulate actions indicated in *Figure 174* suggest that the moist material will bond together and coagulate.

To prevent this, a 3D DEM model could be created using the initial simulation shown in *Figure 172* and an alternative internal chute structure offered. This could be the basis of future investigation.

8.4.2: Discussion: Roll Feeder Segregation Plate Simulation Results

Considering the objectives of this project the opening work revolved around the interpretation of flow through the Roll Feeder and Segregation Plate assembly. The application of DEM was a direct result of the nature of material flowing off the rotating feeder and onto the inclined segregation plate. The function of the plate is to primarily segregate material into large and small particulates and to distribute material as smoothly as possible without inter-particle compression. However, due to the nature of the material, surface wear occurs and this presents a number of issues (*As discussed in 1.5, 1.6*).

The modelling of this piece of apparatus has been a fundamental mechanism for simulation development, particularly in the use of STL files and the introduction of rotating cylinders. However, the latter 3D simulations were eclipsed by other simulation work and optimisation of this system has yet to be finalised in terms of simulated predictions.

As shown in *7.3* simulations had produced energy transfer plots that matched actual surface wear conditions. The situation discussed in *7.3* was directly related to intensity of material flow rather than high impact velocities. The simulation in *Figure 175* depicts the point of contact with the material and boundary.

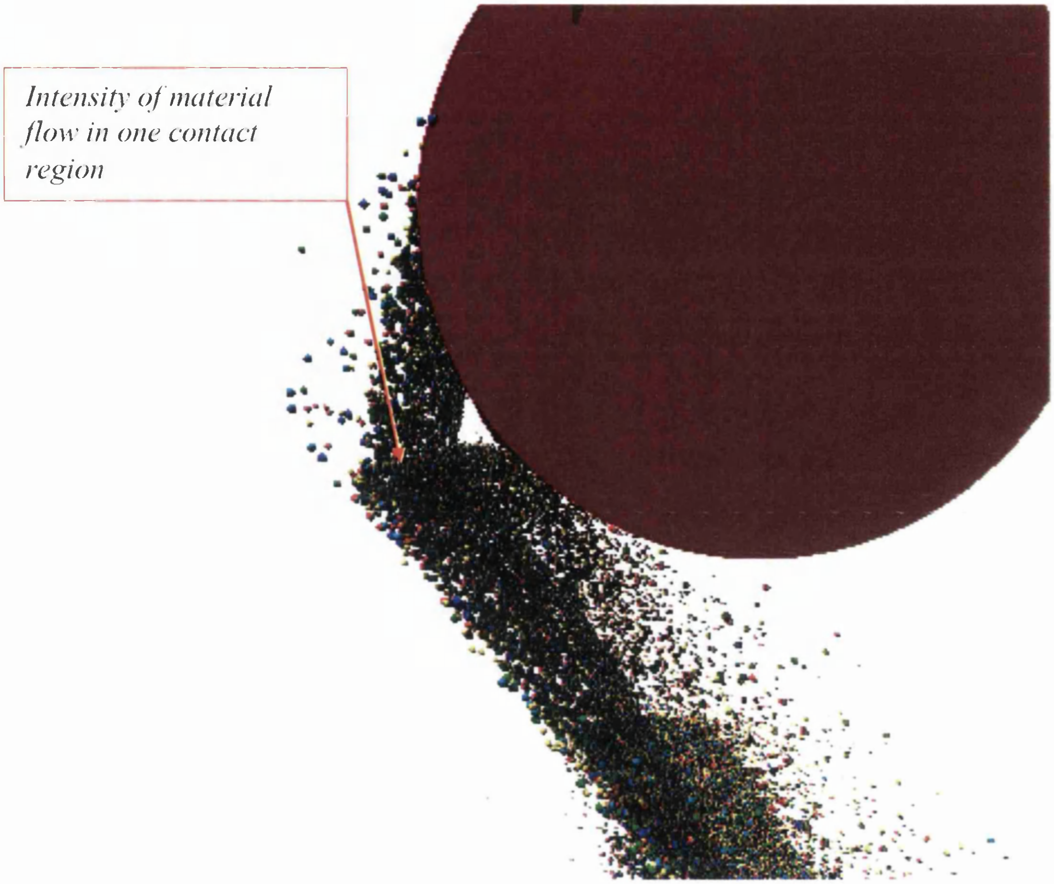

Figure 175: Material flow over the roll feeder concentrated at one contact region

In terms of a solution to the flow concentration at one point, two deflector plates were introduced for simulation to manipulate the flow. This simple design alteration can be seen in *Figure 176*.

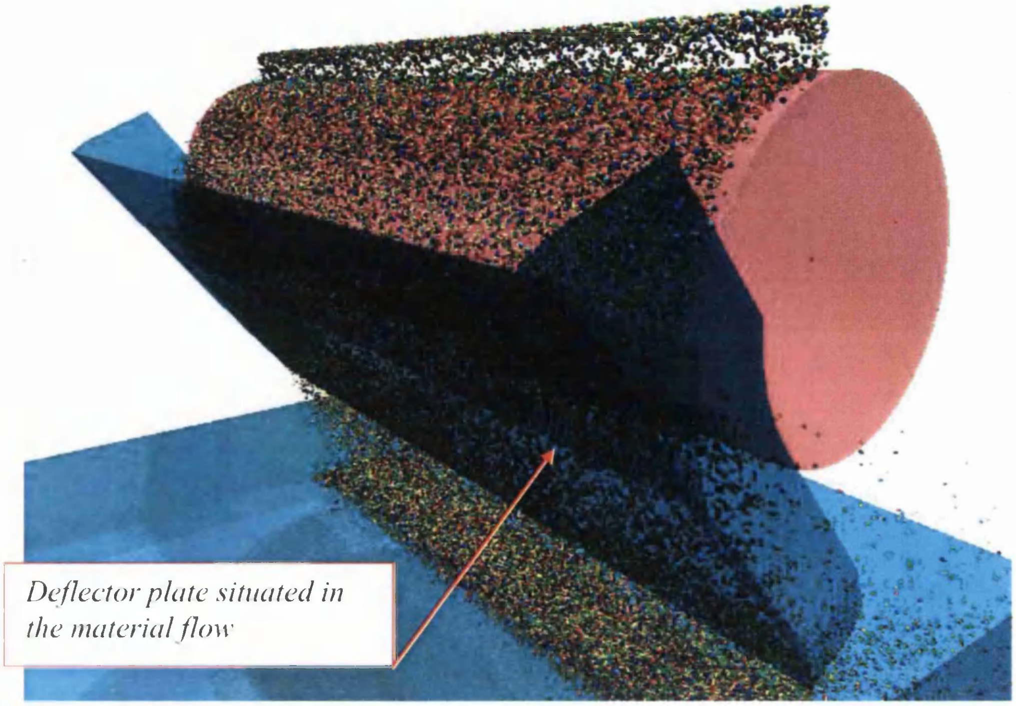

Figure 176: Flow onto the segregation plate broken by two deflector plates

To make comparisons with the situations depicted in *Figures 175-176* the corresponding energy plots were extracted from the data and the following slides in *Figure 173a and 173b* are the results.

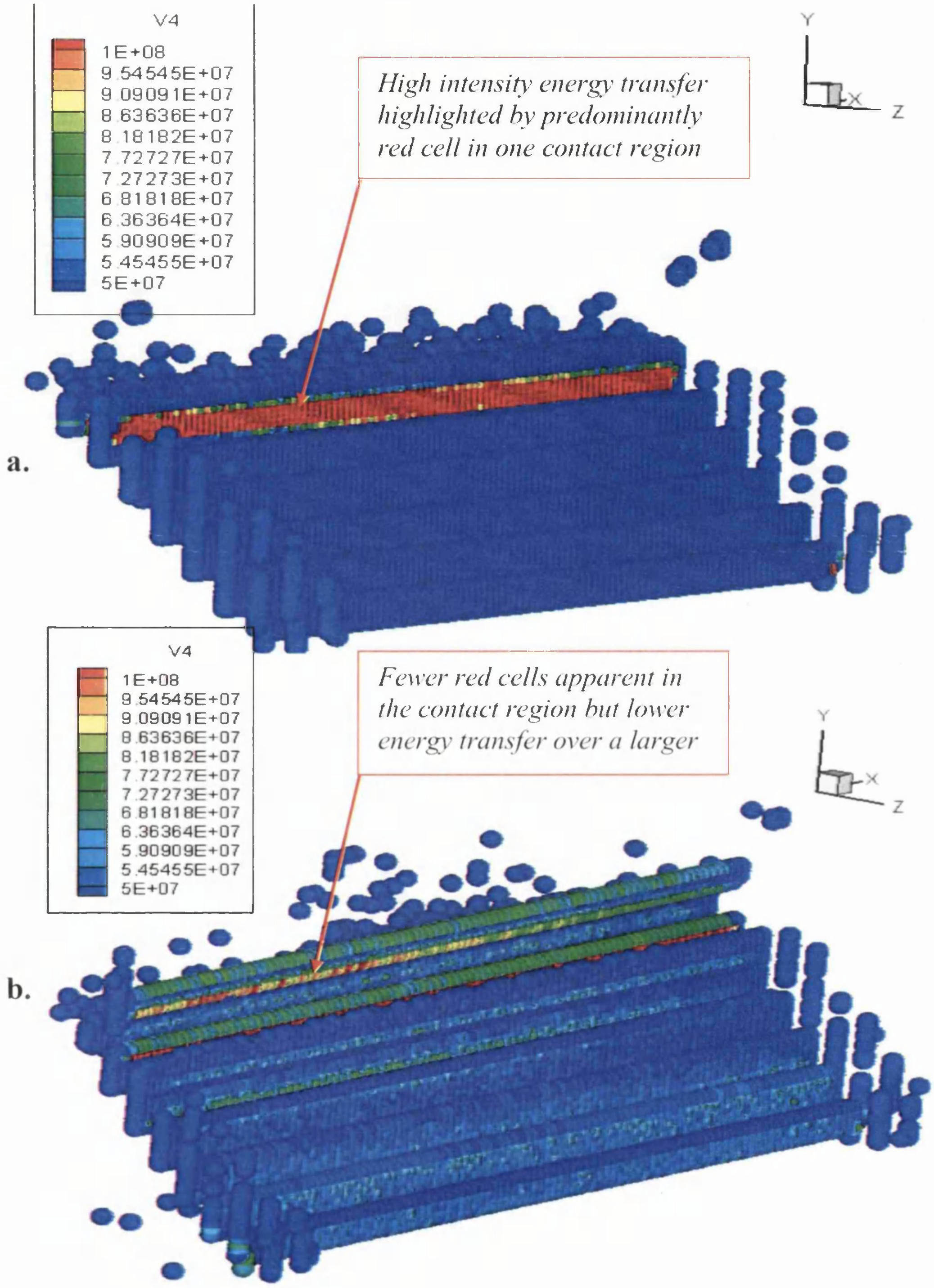

High intensity energy transfer highlighted by predominantly red cell in one contact region

Fewer red cells apparent in the contact region but lower energy transfer over a larger

Figure 177: Energy transfer plot showing the segregation plate with and without deflector plates

To formulate an opinion, the comparisons in the energy plots in *Figure 177a & b* show that the simple defector plate arrangement may significantly reduce the high intensity contact interaction and spread the impact energy over a larger surface area. Further work on this equipment would be a necessity; however the application of the current DEM program for this investigation produced an expected solution.

8.4.4: Discussion: Collaboration with Basic Sound Analysis to Determine Performance Optimisation

In the case of performance assessment of an improved chute system one would have to wait for plant/material deterioration to occur for visual comparisons to be made. Due to the possible time spans involved and the dependence on material volume/type an accurate interpretation of system optimisation may never be reached. In an attempt to address this issue, basic sound intensity investigations were carried out to finger print the noise generated from head chutes when handling different materials. In theory, if the flow though the system were improved the resulting energy transfer would be reduced and the sound intensity levels would drop.

To study this type of change in situation a system design alteration would have to be carried out. However, the same systems and improvements can be assessed using computer simulation with virtual microphones inserted into the simulation domain to predict sound intensity values. In this sub-section the practical data collection is discussed and the method of DEM simulation sound assessment presented.

8.4.4.1: DEM sound intensity simulation used to determine plant optimisation

Considering energy transfer in terms of kinetic energy, one of the transfer mechanisms at impact can be related to sound. During on-plant equipment analysis sound intensity recordings were taken on head chutes that handled a large particulate size distribution in different batches. Using a standard environmental sound recording machine, a range of particulate contact interactions were recorded of different material types. In this example the materials studied were:

Olivine Sand	(0.125mm-0.5mm)
Lime	(5.0mm-60mm)
Briquettes	(Manufactured to approximately 90mm as seen in *Figure 159*)

The sound intensity trends that were obtained for the above materials can be viewed in *Graph 10*.

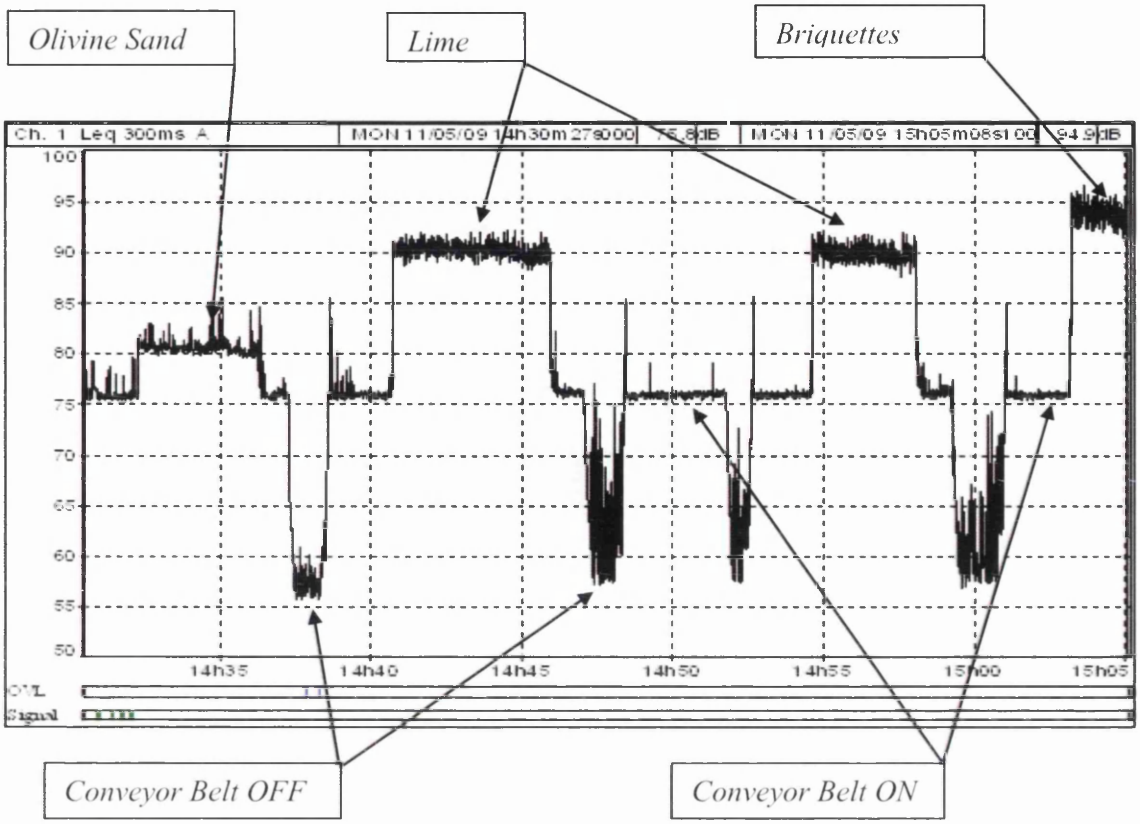

Graph 10: Actual sound intensity readings obtained on equipment analysis

The features shown in *Graph 10* highlight actual periods of varying sound intensity, ranging from low background noise to high energy impact noise. Considering the impact noise regions, the olivine sand recorded an average of ~82dB and the briquettes at the other end of the scale recorded an average of ~93dB. Lime falls between these markers at an average of ~90dB. The energy transfer has a direct correlation with the mass/density of the impacting particle and can be used as a generic pattern for a specific material flow. For this analysis Lime through 633 head chute was the chosen subject and was used for a DEM computer simulation of sound intensity generation.

To produce a predicted sound intensity level a virtual microphone was placed into the simulation domain at a 3D coordinate position. (*As shown in Figure178*)

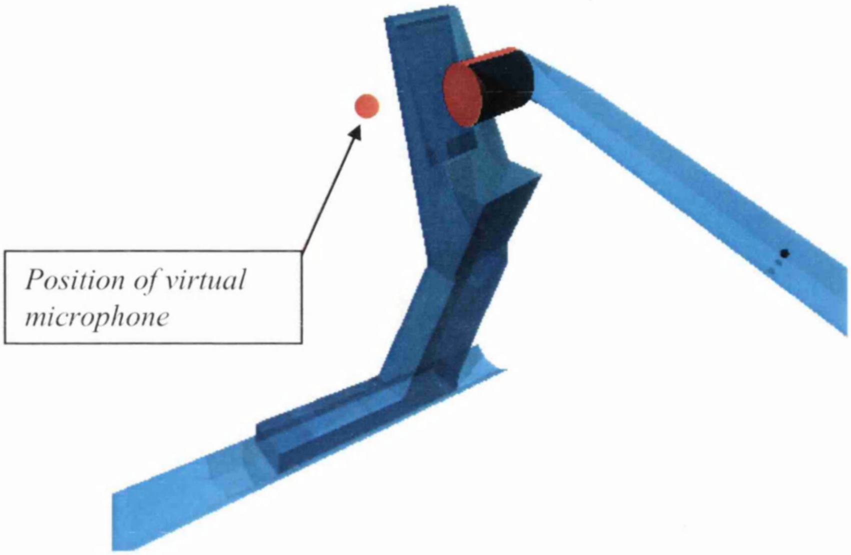

Figure 178: 633 head chute with virtual microphone position

In the above situation when an impacting element makes contact with a boundary condition a kinetic energy value is produced. A vector is then calculated from the point of impact to the position of the microphone and its magnitude recorded. The sound energy simulation is then generated by simply dividing the impact energy by the square of the vector magnitude.

To observe the model results a simulation was conducted using a multiple element flow with initial parameters set for that of Lime. The data produced was applied to *Graph 10* and the results are as follows:

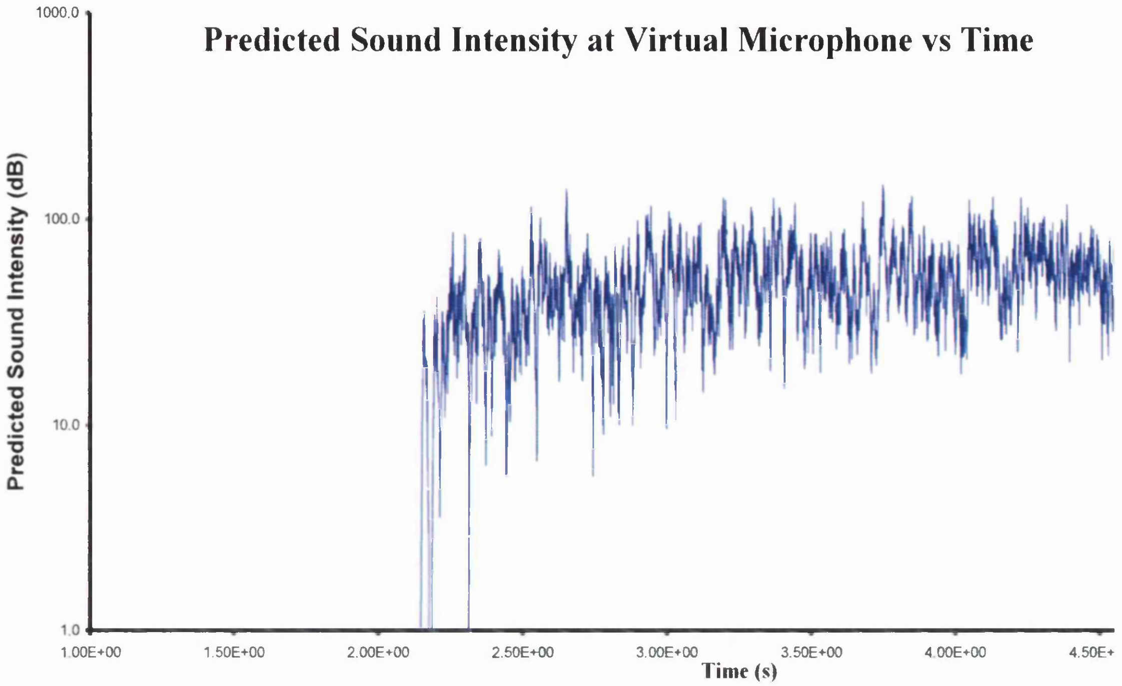

Graph 11: Predicted sound intensity at virtual microphone position

Connecting the data representation in *Graph 10* with the actual date streams produced in *Graph 9* the trends are very similar and the intensity levels are comparable. This suggests that the virtual microphone performs well in predicting sound intensity levels.

Using this simulation technique an examination was made of the standard head chute design (as *shown in Graph10*) with a design implementing a set of curved inserts. The simulations were carried out over 3.5s for Lime and the graphical results are as follows:

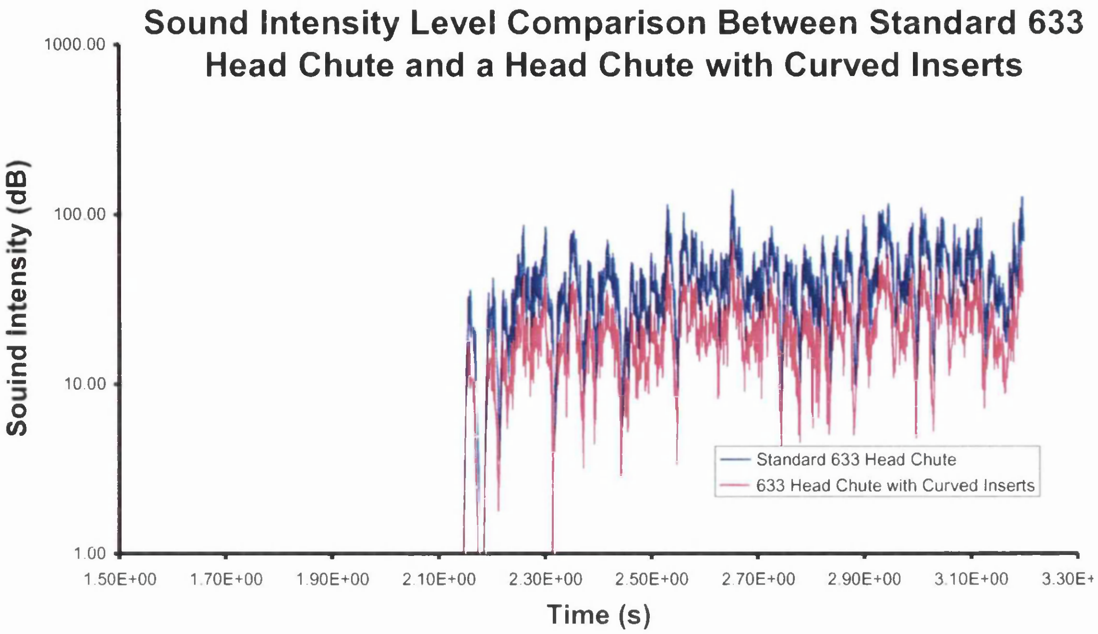

Graph 12: Sound Intensity comparisons between the standard 633 head chute and the head chute with curved inserts

In *Graph 12* the sound intensity levels are clearly different. The standard head chute intensity remains at ~90dB but the intensity level produced by the curved chute inserts has reduced in comparison. This suggests an improvement in the dynamic nature of the theoretical flow through the simulation domain.

In terms of system efficiency the graphical trends shown in *Graphs 10-12* have striking similarities and could be used pre and post design alteration to ascertain the degree of impact energy to determine the level of performance.

The approach of this piece of work was extremely basic and further work in this field would require an in depth knowledge of such energy transmissions and consideration of equipment resonance. However, the concept of studying the performance of a system using sound could clearly be used as a tool to remove excessive contact interaction both in practice and in theory.

9. CONCLUSIONS

- A comprehensive study was made into the mechanisms of supplying bulk mineral particulates as raw material for the iron making process. Included in the investigation were:
  - Importation of raw material products via the harbour import facility
  - Raw material distribution and supply within the plant infrastructure
  - The importance of supply continuity in terms of fuel application
- The conclusion of this investigation was the significance in maintaining a consistent delivery of the required product to replenish departmental stock.

- A 3D Discrete Element Method (DEM) modelling technique was developed to study the dynamic nature of the industrial granular flow. The outcomes of this work were:
  - Assessment of the efficiency of the bulk handling system in terms of computer analysis.
  - Production of a usable 3D non-invasive diagnostic tool to determine wear within a domain by interpreting kinetic energy transfer regions.
  - Reassessment of theoretical engineering developments within a domain by re-mapping energy transfer to measure performance

- The 3D DEM model was successfully validated for simulation accuracy against published papers and theses and its performance in replicating real observable system deterioration on material handling equipment.
- To conduct a modelling exercise on plant equipment material calibration was essential. This was achieved by using the angle of repose created by the material relating to its specific condition.
- The influences of inter-particle and boundary-particle frictional forces play a major role in simulation accuracy by restricting flow and the dynamic transition of particles.
- The introduction of moisture simulation by capillary force action had a profound consequence on the inter-particle bonding relationships, and calculated flow characteristics.

- The application of the attractive capillary force used a "Toroidal Approximation" method that exhibited novelty in contact interaction between elements of differing radii. This approach showed the effects of varying wt% moisture contents in an accurate representation of particle clumping/bonding and dispersion at boundary impact.

10. REFERENCES

---

[1] *R. Goodman, R. Taylor R., & T. Berkke* A MODEL FOR MECHANICS OF JOINTED ROCK: *Journal of Solid Mechanics and Foundation, ASCE, SM3, pp 94, 1968*

[2] *P.A Cundall*: A COMPUTER MODEL FOR SIMULATING PROGRESSIVE LARGE SCALE MOVEMENTS IN BLOCKY ROCK SYSTEMS:, *Proceedings of the Symposium of the International Society of Rock Mechanics, Nancy France, 1, Paper No. II-8, 1971.*

[3] *P.A Cundall, O.D.L Strack*: A DISCRETE NUMERICAL MODEL FOR GRANULAR ASSEMBLIES: *Geotechnique; 29(1): pp 47–65, 1979*

[4] *H.P., Zhou Z.Y, Yang R.Y., Yu A.B.*: DISCRETE PARTICLE SIMULATION OF PARTICULATE SYSTEMS: A REVIEW OF MAJOR APPLICATIONS AND FINDINGS: *Zhu Chemical Engineering Science 63 pp 5728 – 5770, 2008*

[5] *S. Luding, E. Clément, A. Blumen, J. Rajchtenbach, J. Duran*: ANOMALOUS ENERGY DISSIPATION IN MOLECULAR-DYNAMICS SIMULATIONS OF GRAINS:, *The"Detatchment" Effect, Physical Review E 50 (5) pp 4113–4122, 1994*

[6] *Y. Tsuji, T. Kawaguchi, and T. Tanaka*: DISCRETE PARTICLE SIMULATION OF TWO DIMENSIONAL FLUIDIZED BED:. *Powder Technology 77 pp79-87, 1993*

[7] *P. A. Cundall and R. Hart*: NUMERICAL MODELLING OF DISCONTINUA: *Engineering Computations, Vol. 9, pp.101-13.*

[8] *B.P.B. Hoomans, J.A.M. Kuipers, W.J. Breils, and W.P.M. Van Swaaij*: DISCRETE PARTICLE SIMULATION OF BUBBLE AND SLUG FORMATION IN A TWO-DIMENSIONAL GAS FLUIDISED BED: A HARD SPHERE APPROACH: *Chemical Engineering Science 51, p.99, 1996.*

[9] *R.E. Stratton, C.M. Wensrich*: MODELLING OF MULTIPLE INTRA-TIME STEP COLLISIONS IN THE HARD-SPHERE DISCRETE ELEMENT METHOD: *Powder Technology 199 pp 120–130, 2010*

[10] *Y. Matsuda and Y. Iwase*: NUMERICAL SIMULATION OF ROCK FRACTURE USING THREE-DIMENSIONAL EXTENDED DISCRETE ELEMENT METHOD: *Earth Planets Space, 54, 367–378, 2002*

[11] *H. Masuya,. & Y. Kajikawa*: NUMERICAL ANALYSIS OF THE COLLISION BETWEEN FALLING ROCKS AND A CUSHION BY DISTINCT ELEMENT METHOD: , *Computer Methods and Advances in Geomechanics, pp, 493-498, 1991*

[12] *T. C. Halsey and A. J. Levine*: HOW DO SANDCASTLES FALL: *Physical Review Letters 6th of April Volume 80, Issue 14, 1998.*

---

[13] *F. A. Tavarez*: DISCRETE ELEMENT METHOD FOR MODELLING SOLID AND PARTICULATE MATERIALS: *PhD Thesis University of Wisconsin- Madison, February 2006*

[14] *Mohammadi, S.* COMBINED FINITE/DISCRETE ELEMENT ANALYSIS OF IMPACT LOADING OF COMPOSITE SHELLS: *PhD Thesis Department of Civil Engineering, University of Wales Swansea, 1998*

[15] *L. Ogera, M. Ammi, A. Valance, and D. Beladjine*: DISCRETE ELEMENT METHOD STUDIES OF THE COLLISION OF ONE RAPID SPHERE ON 2D AND 3D PACKINGS: *Eur. Phys. J. E 17, pp 467-476, 2005*

[16] *P.W. Cleary, David Hoyer*: CENTRIFUGAL MILL CHARGE MOTION AND POWER DRAW:COMPARISON OF DEM PREDICTIONS WITH EXPERIMENT: *Int. J. Miner. Process. 59, pp.131–148, 2000*

[17] *R.Y. Yang , A.B. Yu , L. McElroy , J. Bao*: NUMERICAL SIMULATION OF PARTICLE DYNAMICS IN DIFFERENT FLOW REGIMES IN A ROTATING DRUM: *Powder Technology (2008), doi: 10.1016/j.powtec.2008.04.081*

[18] *S. Siiria, J. Yliruusi*: PARTICLE PACKING SIMULATIONS BASED ON NEWTONIAN MECHANICS: *Powder Technology 174, pp 82-92, 2007*

[19] *J. Li, C. Webb, S. Pandiella and G. M. Campbell*: A NUMERICAL SIMULATION OF SEPARATION OF CROP SEEDS BY SCREENING - EFFECTS OF PARTICLE BED DEPTH: *Institution of Chemical Engineers Trans IChemE, Vol 80, Part C, June 2002*

[20] *E.P. Honorato and V. Seshadri*: GRANULOMETRIC OPTIMISATION OF RAW MATERIALS FOR ISF CONTINUOUS SEGREGATION SYSTEM IN USIMINAS SINTERING PLANTS: *Iron and Steel Making, vol35, No6, 2008*

[21] *W. R. Ketterhagen, J. S. Curtis, C.R. Wassgren, A. Kong, P.J. Narayan, B.C. Hancock*: GRANULAR SEGREGATION IN DISCHARGING CYLINDRICAL HOPPERS: A DISCRETE ELEMENT AND EXPERIMENTAL STUDY: *Chemical Engineering Science 62, pp 6423 – 6439, 2007*

[22] *J. Li, C. Webb, S.S. Pandiella, G.M. Campbell*: DISCRETE PARTICLE MOTION ON SIEVES—A NUMERICAL STUDY USING THE DEM SIMULATION: *Powder Technology 133, pp 190– 202, 2003*

[23] THE EFFECTS OF PARTICLE SHAPE ON HOPPER DISCHARGE: *P.W. Cleary CSIRO Mathematical and Information Sciences, Clayton Victoria 3169, Australia, Second International Conference on CFD in the mineral process industries CSIRO Melbourne, Australia 6-8 December, 1999*

[24] *Y. Li , Y. Xu , S. Jiang*: DEM SIMULATIONS AND EXPERIMENTS OF PEBBLE FLOW WITH MONOSIZED SPHERES: *Powder Technology 193, pp 312–318, 2009*

[25] *P. A. Langston, U. Tuzun and D.M. Heyes*: DISCRETE ELEMENT SIMULATION OF GRANULAR FLOW IN 2D AND 3D HOPPERS: DEPENDENCE OF DISCHARGE RATE AND WALL STRESS ON PARTICLE INTERACTIONS: *Chemical Engineering Science, Vol. 50, No. 6, pp 967- 987, 1995*

[26] *P.A. Langston, U. Tuzun a, D.M. Heyes*: DISCRETE ELEMENT SIMULATION OF INTERNAL STRESS AND FLOW FIELDS IN FUNNEL FLOW HOPPERS: *Powder Technology 85, pp 153-169, 1995*

[27] *P.A. Langston, U. Tuzun and D. M. Heyes*: *DISTINCT* ELEMENT SIMULATION OF INTERSTITIAL AIR EFFECTS IN AXIALLY SYMMETRIC GRANULAR FLOWS IN HOPPERS: *Chemical Engineering Science, Vol. 51, No. 6, pp 873- 891, 1996*

[28] *S. Humby, U. Tuzun and A.B. Yu*: PREDICTION OF HOPPER DISCHARGE RATES OF BINARY GRANULAR MIXTURES: *Chemical Engineering Science, Vol. 53, No. 3, pp 483- 494, 1998*

[29] *J. Baxter (associate member), H. Abou-chakra, U. Tuzun (Fellow) and B. Mills Lamptey (Associate member)*: A DEM SIMULATION AND EXPERIMENTAL STRATEGY FOR SOLVING FINE POWDER FLOW PROBLEMS: *Trans Icheme, Vol. 78, Part A, October 2000*

[30] *P. W. Cleary*: THE EFFECT OF PARTICLE SHAPE ON SIMPLE SHEAR FLOWS: *Powder Technology 179, pp 144–163, 2008*

[31] *L. Vu-Quoc l, X. Zhang, O.R. Walton*: A 3-D DISCRETE ELEMENT METHOD FOR DRY GRANULAR FLOWS OF ELLIPSOIDAL PARTICLES: *Computer Methods Applied Mechanical Engineering 187, pp 483-528, 2000*

[32] *Chief Investigator: Prof Jeff Loughran (School of Engineering, James Cook University)*: PREDICTIVE MODELLING OF COAL FLOW THROUGH CRITICAL TRANSITIONS - TRANSFER CHUTES: *QPSF Proposal – Technology Diffusion 22nd of April 2005*

[33] *P. Chapellea, H. Abou-Chakrab, N. Christakisa, I. Bridlec, M.K. Patela, J. Baxterb, U. Tuzun, M. Cross*: NUMERICAL PREDICTIONS OF PARTICLE DEGRADATION IN INDUSTRIAL-SCALE PNEUMATIC CONVEYORS: *Powder Technology 143–144, pp 321– 330, 2004*

[34] *X.P Pham, K.S. Varyani*: APPLICATION OF THREE DIMENSIONAL DISCRETE ELEMENT METHOD IN THE PREDICTION OF DECK LOADING DUE TO GREEN WATER EFFECT: *Department of Naval Architecture and Marine Engineering Universities of Glasgow and Strathclyde, 100 Monrose St, Glasgow.*

[35] *K.W. Chu, B. Wang, A.B. Yu, A. Vince*: CFD-DEM MODELLING OF MULTIPHASE FLOW IN DENSE MEDIUM CYCLONES: *Powder Technology 193, pp 235–247, 2009*

[36] *P. McIlvenna and R. Mossad*: TWO DIMENSIONAL TRANSFER CHUTE ANALYSIS USING THE CONTINUUM METHOD: *Third International Conference on CFD in the minerals and process industries CSIRO Melbourne Australia 10-12 December 2003. Editors: P.J. Witt and M.P. Schwarz*

[37] *Y. T. Feng And D. R. J. Owen*: ITERATIVE SOLUTION OF COUPLED FE/BE INTERACTION PROBLEMS DISCRETIZATIONS FOR PLATE-FOUNDATION: *International Journal For Numerical Methods in Engineering, Vol. 39, pp 1889-1901, 1996*

[38] *H. P. Zhu, Y. H. Wu and A. B. Yu*: DISCRETE AND CONTINUUM MODELLING OF GRANULAR FLOW: *China Particuology Vol. 3, No. 6, pp 354-363, 2005*

[39] *X. Lin, Tang-Tat NG*: CONTACT DETECTION ALGORITHMS FOR THREE DIMENTIONAL ELLIPSOIDS IN DEM MODELLING: *International Journal For Numerical and Analytical Methods In Geomechanics Vol.19, pp 653-659, 1995*

[40] *K. Han, Y. T. Feng and D. R. J. Owen*: POLYGON-BASED CONTACT RESOLUTION FOR SUPERQUADRICS: *Int. J. Numerical Methods in Engineering 66 pp 485–501, 2006*

[41] *A.Potapov and C.S. Cambell*: FAST MODEL FOR THE SIMULATION OF NON-ROUND PARTICLES GRANULAR MATTER: *Bulk Solids Handling. Vol 25, 2005*

[42] *Xiang Zhang , Loc Vu-Quoc*: SIMULATION OF CHUTE FLOW OF SOYBEANS USING AN IMPROVED TANGENTIAL FORCE DISPLACEMENT MODEL: *Mechanics of Materials 32, pp115-129, 2000*

[43] *Dr. Graham Mustoe*: A NUMERICAL STUDY OF THE PERFORMANCE AND SAFETY ISSUES FOR ORE PASS SYSTEMS (RP-5): *Colorado School of Mines Engineering Division August 31, 2004*

[44] *G.W. Mustoe, M. Miyata, and M. Nakagawa*: DISCRETE ELEMENT METHODS FOR MECHANICAL ANALYSIS OF SYSTEMS OF GENERAL SHAPED BODIES: *Proceeding of the 5th international conference on computational structures technology, Leuven, Belgium 2000, Edited by: B.H.V. Topping*

[45] *R. Barbosa and J. Ghaboussi*: DISCRETE FINITE ELEMENT METHOD FOR MULTIPLE DEFORMABLE BODIES: *Finite Elements in Analysis and Design, Vol. 7(2), pp 145-58, 1990*

[46] *D. zhao, Erfan G. Nezami, Youssef M.A. Hashash and J. Ghaboussi*: THREE DIMENSIONAL DISCRETE ELEMENT SIMULATION FOR GRANULAR MATERIALS: *Engineering Computations International Journal for Computer Aided Design and Software Vol. 23 No.7, pp 749-770, 2006*

[47] *Qiu, X. and Kruse, D.*: DESIGN CONVEYOR CHUTE USING DISCRETE ELEMENT METHOD: *Fourth U.S. National Congress on computational Mechanics, San Francisco. California August 5-8 1997*

[48] *N. Cho, C.D. Martin, D.C. Sego*: A CLUMPED PARTICLE MODEL FOR ROCK: *International Journal of Rock Mechanics & Mining Sciences 44 pp 997–1010, 2007*

[49] *N. Bell, Y. Yu and P.J. Mucha*: PARTICLE-BASED SIMULATION OF GRANULAR MATERIALS: *University of Illinois at Urbana-Champaign Georgia Institute of Technology Eurographics/ACM SIGGRAPH Symposium on Computer Animation (2005)*

[50] *H.Kruggel-Emden, S.Rickelt, S.Wirtz, V.Scherer*: A STUDY ON THE VALIDITY OF THE MULTI-SPHERE DISCRETE ELEMENT METHOD: *Powder Technology, 2008 doi: 10.1016 powtec2008.04.037*

[51] *F.Y. Fraige, P. A. Langston, Z. Chen*: DISTINCT ELEMENT MODELLING OF CUBIC PARTICLE PACKING AND FLOW: *Powder Technology 186, pp 224–240, 2008*

[52] *H. Abou-Chakra, J. Baxter And U. Tüzün*: THREE-DIMENSIONAL PARTICLE SHAPE DESCRIPTORS FOR COMPUTER SIMULATION OF NON-SPHERICAL PARTICULATE ASSEMBLIES: *Advanced Powder Technology, Vol. 15, No. 1, pp. 63–77, 2004*

[53] *M. Akashi, H. Mio, A. Shimosaka, Y. Shirakawa, J. Hidaka and S. Nomura*: ESTIMATION OF BULK DENSITY DISTRIBUTION IN PARTICLE CHARGING PROCESS USING DISCRETE ELEMENT METHOD CONSIDERING PARTICLE SHAPE: *ISIJ International, Vol. 48, No. 11, pp. 1500–1506, 2008*

[54] *S Mohammadi*: DISCONTINUUM MECHANICS USING FINITE AND DISCRETE ELEMENTS: *WIT Press 2003 ISBN 1-85312-959-3 pp189*

[55] *J. Bonet, J. Peraire*: AN ALTERNATING DIGITAL TREE ADT ALOGORITHM FOR 3D GEOMETRIC SEARCHING AND INTERSECTION PROBLEMS: *International Journal For Numerical Methods In Engineering Vol.31, pp 1-17, 1991*

[56] *Munjiza, A. Owen D.R.J and Bicanic N:* A COMBINED FINITE/DISCRETE ELEMENT METHOD IN TRANSIENT DYNAMICS OF FRACTURING SOLID: *Engineering Computations 12, pp145-174, 1995*

[57] *K.W. Mak*: DISCRETE ELEMENT METHOD SIMULATION OF PARTICULATE SYSTEMS FOR INDUSTRIAL APLLICATION: *Ph.D Thesis*: *Civil Engineering Department University of Wales Swansea, 2003*

[58] *Petrinic, N.*: ASPECTS OF DISCRETE ELEMENT MODELLING INVOLVING FACET TO FACET CONTACT DETECTION AND INTERACTION: *Ph.D. thesis, Department of Civil Engineering University of Wales Swansea UK 1996*

[59] *J. Yu*: A CONTACT INTERACTION FRAMEWORK FOR NUMERICAL SIMULATION AND CONTACT PROBLEMS AND ASPECTS OF DAMAGE AND FRACTURE OF BRITTLE MATERIALS: *Ph.D. thesis, Department of Civil Engineering University of Wales Swansea UK, 1996*

[60] *K. Han, Y.T. Feng And D.R.J. Owen*: PERFORMANCE COMPARISONS OF TREE-BASED AND CELL-BASED CONTACT DETECTION ALGORITHMS: *Engineering Computations International Journal For Computer Aided Design And Software Vol. 24 No.2, pp165-181, 2007*

[61] *C.S. Campbell*: RAPID GRANULAR FLOWS: *Annual Review Fluid Mechanics 22, pp 57–92, 1990*

[62] *P.W. Cleary:* THE FILLING OF DRAGLINE BUCKETS: *Mathematical Engineering in Industry 7, pp 1–24, 1998*

[63] PARTICLE FLOW CODE IN 3 DIMENSIONS, THEORY AND BACKGROUND: *Itasca Consulting Group, Inc., First Edition, November 1999.*

[64] *H. Kruggel-Emden, F. Stepanek, A. Munjiza, Particuology:* A STUDY ON ADJUSTED CONTACT FORCE LAWS FOR ACCELERATED LARGE SCALE DISCRETE ELEMENT SIMULATIONS: *2009, doi: 10.1016/j.partic.2009.07.008*

[65] *R.D Mindlin, H. Deresiewicz:* ELASTIC SPHERES IN CONTACT UNDER VARYING OBLIQUE FORCES: *Varying Oblique Forces. Transactions of ASME, Series E. Journal of Applied Mechanics 20, pp327–344, 1953*

[66] *N. V. Brilliantov, F. Spahn, J.M. Hertzsch, T. Poschel:* THE COLLISION OF PARTICLES IN GRANULAR SYSTEMS: *Physica A 231 pp 417-424, 1996*

[67] *K.F. Malone 1, B. Hua Xu:* DETERMINATION OF CONTACT PARAMETERS FOR DISCRETE ELEMENT METHOD SIMULATIONS OF GRANULAR SYSTEMS: *Particuology 6 pp 521–528, 2008*

[68] *B. C. Vemuri, L. Chen, L. Vu-Quoc and X. Zhang:* EFFICIENT AND ACCURATE COLLISION DETECTION FOR GRANULAR FLOW SIMULATION: *Graphical Models and Image Processing 60, pp 403–422, 1998*

[69] *C.Wellmann, C. Lillie, P. Wriggers:* COMPARISON OF THE MACROSCOPIC BEHAVIOR OF GRANULAR MATERIALS MODELED BY DIFFERENT CONSTITUTIVE EQUATIONS ON THE MICROSCALE: *Finite Elements in Analysis and Design 44, pp 259 – 271, 2008*

[70] *C. Wellmann, C. Lillie, P. Wriggers Computers:* HOMOGENIZATION OF GRANULAR MATERIAL MODELLED BY A THREE-DIMENSIONAL DISCRETE ELEMENT METHOD: *and Geotechnics 35, pp 394–405, 2008*

[71] *A. Di Renzo, Francesco P. Di Maio:* COMPARISON OF CONTACT-FORCE MODELS FOR THE SIMULATION OF COLLISIONS IN DEM-BASED GRANULAR FLOW CODES: *Chemical Engineering Science 59 pp 525 – 541, 2004*

---

[72] *P.W. Cleary, Sawley M.L:* DEM MODELLING OF INDUSTRIAL GRANULAR FLOWS: 3D CASE STUDIES AND THE EFFECT OF PARTICLE SHAPE ON HOPPER DISCHARGE: *Applied Mathematical Modelling 26, pp 89–111, 2002*

[73] *Y. Tsuji, T. Tanaka, and T. Ishida:* LAGRANGIAN NUMERICAL SIMULATION OF PLUG FLOW OF COHESIONLESS PARTICLES IN A HORIZONTAL PIPE: *Powder Tech, 71: pp 239-250, 1992*

[74] *J. Li, C. Webb, S. S. Pandiella and G.M. Campell:* A NUMERICAL SIMULATION OF SEPARATION OF CROP SEEDS BY SCREENING – EFFECTS OF BED DEPTH: *Institute of Chemical Engineering Trans IChemE Vol 80 Part C June 2002.*

[75] *C. Tokorol K. Okaya and J. Sadaki:* A FAST ALGORITHM FOR THE DISCRETE ELEMENT METHOD BY CONTACT FORCE PREDICTION: *Powder Technology, Japan, 40, pp 236-245, 2003*

[76] *K. Maoa, M. Yu Wangb, Z. Xuc, T. Chend:* DEM SIMULATION OF PARTICLE DAMPING: *Powder Technology 142, pp 154– 165, 2004*

[77] *M. Yu Wang, K. Mao, Z. Xu, And T. Chen:* EFFICIENT COMPUTATION OF PARTICLE MOTIONS IN DISCRETE ELEMENT MODELING OF PARTICLE DAMPING: *Corresponding Author. Address: Department of Automation and Computer-Aided Engineering, The Chinese University of Hong Kong, Shatin, NT, Hong Kong. Tel.: +852-2609-8487; fax: +852-2603-6002.*

[78] *H. P. Zhu, Y. H. Wu and A. B. Yu:* DISCRETE AND CONTINUUM MODELLING OF GRANULAR FLOW: *China Particuology Vol. 3, No. 6, 354-363, 2005*

[79] *R. Walton:* NUMERICAL SIMULATION OF INCLINED CHUTE FLOWS OF MONODISPERSE INELASTIC FRICTIONAL SPHERES: *Otis. Mechanics of Materials 16, pp 239-247, 1993*

[80] *D.B. Hastie, P.W. Wypych:* EXPERIMENTAL VALIDATION OF PARTICLE FLOW THROUGH CONVEYOR TRANSFER HOODS VIA CONTINUUM AND DISCRETE ELEMENT METHODS: *Int. J. Mech Mater (2010),doi:10.1016/jmechmat.2009.11.007*

[81] *Y. Muguruma, T. Tanaka, Y. Tsuji:* NUMERICAL SIMULATION OF PARTICULATE FLOW WITH LIQUID BRIDGE BETWEEN PARTICLES(SIMULATION OF CENTRIFUGAL TUMBLING GRANULATOR): *Powder Technology 109 pp 49-57, 2000*

[82] *D. Shi, J.J. McCarthy:* NUMERICAL SIMULATION OF LIQUID TRANSFER BETWEEN PARTICLES: *Powder Technology 184, pp 64–75, 2008*

[83] *Willett, C.D., Adams, M. J., Johnson S.A. and Seville, J.P.K:* EFFECTS OF WETTING HYSTERESIS ON PENDULAR LIQUID BRIDGES BETWEEN RIGID SPHERES: *Powder Technology 130, pp63– 69, 2003*

---

[84] *N. Mitarai and F. Nori.:* WET GRANULAR MATERIALS: *N. Mitarai and F. Nori. Advances in Physics Vol. 55 No's 1-2. January-April 1-45, 2006*

[85] *V. Richefeu, M. Saïd El Youssoufi, E. Azéma, F. Radjaï:* FORCE TRANSMISSION IN DRY AND WET GRANULAR MEDIA: *Powder Technology 190, pp 258–263, 2009*

[86] *L.Scholtes, B. Chareyre, F.Nicot, F. Darve:* MICROMECHANICS OF GRANULAR MATERIALS WITH CAPILLARY EFFECT: *International Journal of Engineering Science 47, pp 64-75, 2009*

[87] *K. Hotta, K. Takeda, K. Ionya:* THE CAPILLARY BINDING FORCE OF A LIQUID BRIDGE: *Powder Technology 10, pp 231–242, 1974*

[88] *Z. Grof, C. J. Lawrence, F. Stepanek:* THE STRENGTH OF LIQUID IN RANDOM GRANULAR MATERIALS: *Journal of Colliod and Interface Science 319, pp 182-192, 2008*

[89] *G. Lian & C. Thornton:* EFFECT OF LIQUID BRIDGE FORCES ON AGGLOMERATE COLLISIONS:. *Powders & Grains 93, 2nd International Conference Micromechanics of Granular Media, pp 59-64, 1993*

[90] *C. Thornton & G. Lian:* MODELLING OF LIQUID BRIDGES BETWEEN PARTICLE IN DEM SIMULATIONS OF PARTICLE SYSTEMS: *2nd International Conference, Discrete Element Methods, pp177-187, 1993*

[91] *Lian, C. Thornton and M. J. Adams.:* A THEORETICAL STUDY OF THE LIQUID BRIDGE FORCES BETWEEN TWO RIGID SPHERICAL BODIES: *G. Journal of Colliod and Interface Science 161, pp 138-147, 1993*

[92] *O.H. Pakarinen, A.S. Foster, M. Paajanen, T. Kalinainen, J. Katainen, I. Makkonen, J. Lahtinen, R. M. Nieminen:* TOWARDS AN ACCURATE DESCRIPTION OF THE CAPILLARY FORCE IN NANOPARTICLE SURFACE INTERACTIONS: *Modelling Simulation Material Science and Engineering 13, pp 1175-1186, 2005*

[93] *N. Standish, A.B. Yu, Q.L. He:* AN EXPERIMENTAL STUDY OF THE PACKING OF COAL HEAP: *Powder Technology 68, 187, 1991*

[94] *N. Mitarai and F. Nori.:* WET GRANULAR MATERIALS: *Advances in Physics Vol. 55 No's 1-2. January-April, 1-45, 2006*

[95] *Y.C. Zhou, B.D. Wright, R.Y. Yang, B.H. Xu, A.B. Yu* ROLLING FRICTION IN THE DYNAMIC SIMULATION OF SAND PILE FORMATION: *Physica A 269, pp 536-553, 1999*

[96] *Y.C. Zhou, B.H. Xu, P. Zulli:* AN EXPERIMENTAL AND NUMERICAL STUDY OF THE ANGLE OF REPOSE OF COARSE SPHERES: *Powder Technology 125, pp 45-54 2000*

---

[97] *R. Moreno-Atanasio, M.Ghadiri:* MECHANISTIC ANALYSIS AND COMPUTER SIMULATION OF IMPACT BREAKAGE OF AGGLOMERATES: EFFECTS OF SURFACE ENERGY: *Chemical Engineering Science 61, pp 2476-2481, 2006*

[98] *B.D. Jana, M.M. Stack:* MODELLING IMPACT ANGLE EFFECTS ON EROSION–CORROSION OF PURE METALS: CONSTRUCTION OF MATERIALS PERFORMANCE MAPS: *Wear 259, pp 243–255, 2005*

[99] *H. Mio, S. Komatsuki, J. Hidaka, M. Akashi, A, Shimosaka:* VALIDATION OF PARTICLE SIZE SEGREGATION OF SINTERED ORE DURING FLOWING THROUGH LABORATORY-SCALE CHUTE BY DISCRETE ELEMENT METHOD: *ISIJ International Vol. 48, No 12, pp. 1696-1703, 2008*

[100] *L.K.Nordell:* PARTICLE FLOW MODELLING: TRANSFER CHUTES & OTHER APPLICATION:
Conveyor Dynamics Inc USA,
http:www.ckit.co.za/secure/conveyor/paper/dem/particle/particle.htm